2018

Diffuse Optical Biomarkers Of Breast Cancer

Jeffrey Martin Cochran
University of Pennsylvania, jeffcochran12@gmail.com

Diffuse Optical Biomarkers Of Breast Cancer

Abstract
Diffuse optical spectroscopy/tomography (DOS/DOT) and diffuse correlation spectroscopy (DCS) employ near-infrared light to non-invasively monitor the physiology of deep tissues. These methods are well-suited to investigation of breast cancer due to their sensitivity to physiological parameters, such as hemoglobin concentration, oxygen saturation, and blood flow. This thesis utilizes these techniques to identify and develop diffuse optical biomarkers for the diagnosis and prognosis of breast cancer.

Notably, a novel DOS prognostic marker for predicting pathologic complete response to neoadjuvant chemotherapy using z-score normalization and logistic regression was developed and demonstrated. This investigation found that tumors that were not hypoxic relative to the surrounding tissue were more likely to achieve complete response. Thus, the approach could enable dynamic feedback for the optimization of chemotherapy. Similar logistic regression models based on other optical parameters distinguished tumors from the surrounding normal tissue and diagnosed whether a lesion was malignant or benign. These diagnostic markers improve the ability of DOS/DOT to accurately localize tumors and could serve as a type of optical biopsy to classify suspicious lesions. Another study carried out the first longitudinal DCS blood flow monitoring over a full course of neoadjuvant chemotherapy in humans; this work explored initial correlations between blood flow and response to therapy and showed how DCS and DOS together can more accurately probe tumor physiology than either modality alone. Finally, still other thesis research included the final construction and initial imaging tests of a DOT instrument incorporated into a clinical MRI suite and the optimization of the DOT reconstruction algorithm. In total, these instrumental and algorithmic advances improved DOT image quality, helped to increase contrast between malignant and normal tissue, and eventually could lead to better understanding of tumor microvasculature.

These contributions represent important steps towards the translation of diffuse optics into the clinic, demonstrating significant roles for optics to play in the diagnosis, prognosis, and physiological understanding of breast cancer.

Degree Type
Dissertation

Degree Name
Doctor of Philosophy (PhD)

Graduate Group
Physics & Astronomy

First Advisor
Arjun G. Yodh

Keywords
Biomarkers, Biopsy, Breast Cancer, Diffuse Optics, Neoadjuvant Chemotherapy, Tomography

DIFFUSE OPTICAL BIOMARKERS OF BREAST CANCER

Jeffrey M. Cochran Jr.

A DISSERTATION

in

Physics and Astronomy

Presented to the Faculties of the University of Pennsylvania in Partial Fulfillment
of the Requirements for the Degree of Doctor of Philosophy
2018

Supervisor of Dissertation

Arjun G. Yodh, Professor of Physics and Astronomy

Graduate Group Chairperson

Joshua Klein, Professor of Physics and Astronomy

Dissertation Committee
Philip Nelson, Professor of Physics and Astronomy
Justin Khoury, Professor of Physics and Astronomy
Alison Sweeney, Assistant Professor of Physics and Astronomy
Ravinder Reddy, Professor of Radiology

DIFFUSE OPTICAL BIOMARKERS OF BREAST CANCER

ABSTRACT

DIFFUSE OPTICAL BIOMARKERS OF BREAST CANCER

Jeffrey M. Cochran Jr.

Arjun G. Yodh

Diffuse optical spectroscopy/tomography (DOS/DOT) and diffuse correlation spectroscopy (DCS) employ near-infrared light to non-invasively monitor the physiology of deep tissues. These methods are well-suited to investigation of breast cancer due to their sensitivity to physiological parameters, such as hemoglobin concentration, oxygen saturation, and blood flow. This thesis utilizes these techniques to identify and develop diffuse optical biomarkers for the diagnosis and prognosis of breast cancer.

Notably, a novel DOS prognostic marker for predicting pathologic complete response to neoadjuvant chemotherapy using z-score normalization and logistic regression was developed and demonstrated. This investigation found that tumors that were not hypoxic relative to the surrounding tissue were more likely to achieve complete response. Thus, the approach could enable dynamic feedback for the optimization of chemotherapy. Similar logistic regression models based on other optical parameters distinguished tumors from the surrounding normal tissue and diagnosed whether a lesion was malignant or benign. These diagnostic markers improve the ability of DOS/DOT to accurately localize tumors and could serve as a type of optical biopsy to classify suspicious lesions. Another study carried out the first longitudinal DCS blood flow monitoring over a full course of neoadjuvant chemotherapy in humans; this work explored initial correlations between blood flow and response to therapy and showed how DCS and DOS together can more accurately probe tumor physiology than either modality alone. Finally, still other thesis research included the final construction and initial imaging tests of a DOT instrument incorporated into a clinical MRI suite and the optimization of the DOT reconstruction algorithm. In total, these instrumental and algorithmic advances improved DOT image quality, helped to increase contrast between malignant and normal tissue, and eventually could lead to better understanding of tumor microvasculature.

These contributions represent important steps towards the translation of diffuse optics into the clinic, demonstrating significant roles for optics to play in the diagnosis, prognosis, and physiological understanding of breast cancer.

Dedication

For Mom,

Proof that love transcends diagnosis

And though I didn't pick the day to turn the page

I know it's not the end every time I see her face

-KW

Acknowledgments

I have been extraordinarily privileged in my life to have the support, friendship, and love of countless incredible people, and as I approach the end of my PhD research, I'd like to highlight some of them who have made my work possible.

The path I've taken in my academic career has been most directly influenced by three excellent teachers and mentors. The first was Dr. Jill Clapper, my middle school English teacher, who set goals far beyond the abilities of pre-teens but somehow always managed to inspire students to accomplish them. She taught me how to critically analyze arguments, how to write effectively, and how to communicate ideas to a variety of audiences. The second mentor was my undergraduate advisor Dr. Steven Doty, Professor of Physics and Astronomy at Denison University. I first met Dr. Doty at my college orientation when he was randomly assigned to me as a faculty advisor. At the time, I was completely undecided on a field of study (I think I listed thirteen possible majors on my pre-orientation survey). Dr. Doty asked me a few questions about my interests and decided that I might enjoy physics. I agreed to take the first semester physics class and never looked back. Dr. Doty then served as my undergraduate research advisor where he taught me how to ask good questions, gave me my first opportunity to publish and present academic research, and pushed me to think more deeply about every concept I encountered. Finally, none of the work presented here would have been possible without the guidance and support of Dr. Arjun Yodh, my PhD Thesis advisor. I was initially drawn to this field by its interdisciplinary nature, requiring not only knowledge of physics, but also engineering, data analysis, and medicine, and I was extremely fortunate to find an advisor with the genuine intellectual curiosity to guide students through every aspect of the work. Dr. Yodh also has a remarkable ability to find and highlight the most interesting results of any research and to determine what new questions those results pose. I am grateful to have had the opportunity to absorb these skills throughout my time here.

I have also been fortunate to work with a number of outstanding colleagues during my time at Penn. The first of these was Dr. David Busch, who introduced me to diffuse optics and served as my day-to-day supervisor when I joined the lab. David's wide range of experience and willingness to help was indispensable, and I have enjoyed working with him ever since. Additionally, this research could not have been done without Dr. Wes Baker, who helped me understand diffuse optical theory; Dr. Han Ban, who imparted his significant knowledge about instrumentation; Dr. Venki Kavuri, who guided me through my early forays into image reconstruction; Dr. Ashwin Parthasarathy, who has always been incredibly supportive of my work; Dr. So Hyun Chung, who collected important data for the analysis presented here; Steve Schenkel, who provided all types of administrative and technical assistance and routinely beat me in fantasy football; and Ken Abramson, who designed or

helped with most of my experiments and was always willing to serve as a sounding board. I am also grateful for my graduate student contemporaries in the Yodh lab, Sanghoon Chong, Tiffany Ko, and Rodrigo Forti, whom I have had the pleasure of collaborating with on a variety of projects, and for all of my other Yodh lab colleagues including Dr. Erin Buckley, Dr. Jennifer Lynch, Dr. Saurav Pathak, Dr. Lin Wang, Dr. Lian He, Dr. Karla Bergonzi, Alex Vandegrift, Maddie Winters, Sarah Grundy, and Julien Menko. I would also be remiss if I did not acknowledge Dot Coleman, who helped us navigate Arjun's busy schedule, and Susan Colleluori, who did everything from help me acquire a hospital ID badge to coordinate our grant reporting.

My work has also brought me in contact with a number of collaborators outside the Yodh lab who have proved vital in furthering my research. First and foremost, I'd like to thank Dr. Bruce Tromberg and Dr. Anaïs Leproux from the University of California, Irvine who have been immensely supportive of my work and have generously included me in their research. I must also thank Dr. Simon Arridge and Dr. Martin Schweiger from University College London, who patiently answered every question I had about image reconstruction; Dr. Mitchell Schnall, who provided access to necessary hospital resources; Dr. David Mankoff, whose feedback helped guide the later stages of my research; and Dr. Julia Tchou, who was extremely helpful with patient recruitment. I would also like to thank Dr. Philip Nelson, Dr. Justin Khoury, Dr. Alison Sweeney, and Dr. Ravinder Reddy for serving on my thesis committee.

The final, and most important, contributors to this research are the patients who donated their time, without any direct benefit to themselves, to further our understanding of breast cancer and to hopefully improve outcomes for future survivors. I am sincerely grateful for your selflessness and courage.

This thesis presents the results of the time I've spent working at Penn; however, I would not not have made it this far into my research without an incredible collection of friends and family members supporting me outside of work. I'd like to thank Colin and Joanna, our first friends in Philadelphia who reassured us that this place could be home, and James, whose love for his friends reminds me that friendship can span great distances. I also could not imagine my time at Penn without the other graduate students from my year: Mehmet, Rachel (and Ryan), Madeleine, Zoey, John, Louis, and Sergey (plus Carolina and Nikunja). When we first met, we spent most of our time together working on problem sets, but as we finished our classes, our relationship transitioned from classmates to family, sharing Sunday dinners, Passover Seders, late-night debates, and painfully terrible 76ers games followed by Golden Tee at Bar. It seems impossible that we were strangers seven years ago. I was again fortunate to meet even more friends at Penn in the following years, including Michele, Anthony, Carl, Nate, Will, Paul, Johanna-Laina, Christina, Frank, and Billy,

who are simultaneously some of the kindest and most entertaining people I've ever met. I can't thank all of you enough for your friendship (and for indulging my need to start a moderately successful flag football team).

Finally, I have been blessed with a truly special family. It is exceedingly rare to receive unconditional love and support from so many people, and I'd like to thank a few individually:

To my mother-in-law, Jeannine, my father-in-law Jim, and my brother- and sister-in-law Matt and Corinne: I became a part of your family while working on this thesis, and you have been there for me constantly, through good times and bad, with words of encouragement and genuine interest. I cannot thank you enough for accepting me as one of your own.

To my brother Matt: To outsiders, it may seem like our relationship is built on obscure movie quotes, inside jokes, and sports, but in reality, we have been best friends for nearly 27 years because of a much deeper connection. Your resolve and commitment to the people and things you love inspires me, and I am constantly buoyed by your unwavering support.

To my dad: For as long as I can remember, I've been told that we act and look alike. Although I'm flattered by the more superficial similarities like our shared demeanor, our interest in science, and the face we make when we're annoyed, my goal has always been to live up to your other qualities: your work ethic, your immense strength, and your love for your family. I can't adequately describe everything you've given to me; I can only say thank you.

To my mom: It has been over three years since you passed away, and yet, I feel your profound impact as strongly as ever. You encouraged me to follow my passion and supported every decision I made, regardless of how long I agonized over it. You were the most generous and nurturing person I've ever met, and it is my sincerest hope that I am able to fulfill that legacy and pass those traits on to your grandchildren. I miss you and love you.

To my wife Kara: Almost ten years ago, I met the most amazing girl in a dingy dorm party at Denison University. In the decade since then, you have become my best friend, my truest confidant, and my wife. Your exceptional courage enabled us to make friends when we moved to a new city, and your limitless empathy has re-defined for me what a relationship can be. You are a brilliant, creative, overly generous person, and you have been the cornerstone of my life since before I could legally drink. Truly, none of this would be possible without you. I love you and am so grateful that you will be Fiona's mom.

To everyone who has helped me along the way, thank you for enabling me to do this work.

Contents

List of Tables

List of Figures

Glossary

Table of Abbreviations

Abbreviation	Meaning
NIR	Near-Infrared
DOS	Diffuse Optical Spectroscopy
DOT	Diffuse Optical Tomography
DCS	Diffuse Correlation Spectroscopy
RTE	Radiative Transport Equation
DA	Diffusion Approximation
DPDW	Diffuse Photon Density Waves
CW	Continuous Wave
FD	Frequency Domain
TD	Time Domain
IRF	Instrument Response Function
PMT	Photo-Multiplier Tube
O.F.	DOT Objective Function
TK0	Zeroth-Order Tikhonov Regularization
TK1	First-Order Tikhonov Regularization
TV	Total Variation Regularization
CT	Computed Tomography
US	Ultrasound
MRI	Magnetic Resonance Imaging
PET	Positron Emission Tomomgraphy
BOLD MRI	Blood Oxygen Level Dependent MRI
DCE-MRI	Dynamic Contrast Enhanced MRI
FEM	Finite Element Method
HbO_2	Oxygenated Hemoglobin
HHb	Deoxygenated Hemoglobin
Hb_T	Total Hemoglobin
S_tO_2	Tissue Oxygen Saturation
DWS	Diffusing Wave Spectroscopy
APD	Avalance Photodiode
ROC	Receiver Operating Characteristic
TCSPC	Time-Correlated Single Photon Counting

Table of Physical Quantities

Symbol	Quantity	Units
n	Index of Refraction	
c	Speed of Light in Vacuum	$cm\,s^{-1}$
v	Speed of Light in Tissue ; $v = c/n$	$cm\,s^{-1}$
μ_a	Absorption Coefficient	cm^{-1}
l_a	Absorption Length; $l_a \equiv 1/\mu_a$	cm
$p(\hat{\Omega}', \hat{\Omega})$	Scattering Phase Function	$cm^{-1}\,sr^{-1}$
$f(\hat{\Omega}', \hat{\Omega})$	Normalized Scattering Phase Function	sr^{-1}
μ_s	Scattering Coefficient	cm^{-1}
l_s	Scattering Length; $l_s \equiv 1/\mu_s$	cm
L	Light Radiance	$W\,cm^{-2}\,sr^{-1}$
μ_t	Transport Coefficient	cm^{-1}
Q	Source Power Density	$W\,cm^{-3}\,sr^{-1}$
Φ	Photon Fluence	Wcm^{-2}
$\vec{J}$	Photon Flux	Wcm^{-2}
S	Source Power Concentration	Wcm^{-3}
g	Anisotropy Factor	
μ_s'	Reduced Scattering Coefficient	cm^{-1}
l_{tr}	Transport Length; $l_{tr} \equiv 1/(\mu_a + \mu_s')$	cm
D	Diffusion Coefficient $D \equiv v\,l_{tr}/3$	$cm^2 s^{-1}$
A	AC Fluence Amplitude	Wcm^{-2}
θ	AC Fluence Phase Shift	rad
z_b	Extrapolated Zero; $z_b \equiv \frac{2}{3} l_{tr} \frac{1+R_{eff}}{1-R_{eff}}$	cm
τ_R	Regularization Hyperparameter	
A	Mie Scattering Amplitude	cm^{-1}
b	Mie Scattering Power	
g_1	Electric Field Auto-Correlation Function	
g_2	Intensity Auto-Correlation Function	
α	Blood Volume Fraction	
D_B	Brownian Diffusion Coefficient	cm^2/s
BFI	DCS Blood Flow Index; $BFI = \alpha D_B$	cm^2/s
AUC	Area Under the Curve - ROC Analysis	
TPR	True Positive Rate	
FPR	False Positive Rate	
PPV	Positive Predictive Value	
NPV	Negative Predictive Value	
$\mathcal{P}_{\mathcal{R}}$	Probability of Response	
$\mathcal{P}_{\mathcal{M}}$	Probability of Malignancy	

Chapter 1

Introduction

1.1 Diffuse Optics

The work in this thesis utilizes diffuse optical technologies to identify and follow various biomarkers of tissue health. Visible light has long been used for diagnostic purposes in medicine [82]. Light in this wavelength range is useful because it provides excellent spatial resolution and is non-ionizing [254]. However, many tissue components, known as chromophores, are strong absorbers of visible light; thus, these traditional optical techniques are largely limited to surface measurements [215]. On the other hand, photons with wavelengths in the near-infrared (NIR) window ($\sim 650-950\,nm$), are able to traverse human tissue with relatively little absorption (see Figure 1.1) due to low levels of NIR absorption of the most prominent tissue chromophores: oxygenated-hemoglobin (HbO_2), deoxygenated-hemoglobin (HHb), water, and lipid [155; 156; 215; 148]. This scenario permits the measurement of deep tissue, between 1 and 4 cm below the surface depending on the tissue type and optical properties [201; 85; 22]. Due to the preponderance of organelles and cells with diameters of $\sim 1\,\mu m$, tissue also strongly scatters photons [148] in the NIR range. The combination of high scattering and low absorption provides the necessary conditions for light transport to obey a diffusion equation in many tissues [202; 196; 267]. This well-known mathematical framework can thus be exploited to probe tissue with light and is the basis of two diffuse optical techniques employed in this thesis: diffuse optical spectroscopy (DOS), also known as near-infrared spectroscopy (NIRS), and diffuse correlation spectroscopy (DCS). These techniques probe tissue optical properties, blood volume, tissue blood oxygen saturation, and tissue blood flow non-invasively, using non-ionizing radiation, and with portable, bedside instruments that permit continuous monitoring [98]. With more spatial information, these monitoring techniques can be utilized to perform three-dimensional

imaging with diffuse light: diffuse optical tomography (DOT) and diffuse correlation tomography (DCT).

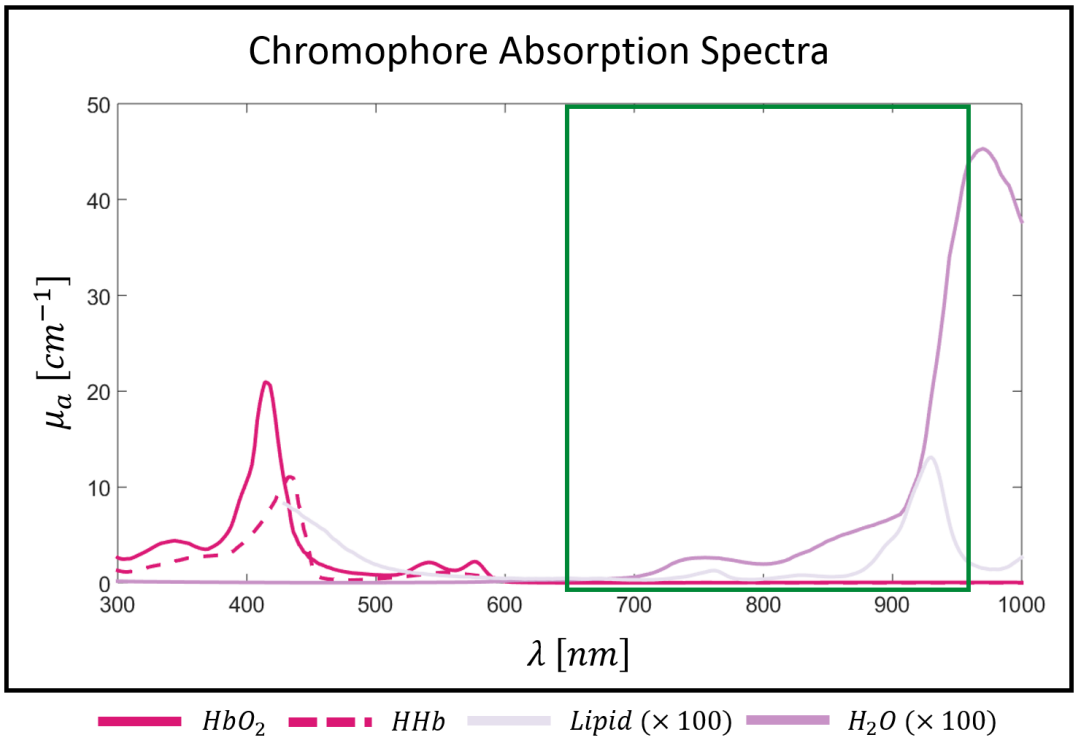

Figure 1.1: Tissue Chromophore Absorption Spectra. The absorption coefficients μ_a (see Section 2.1) due to four different tissue chromophores, oxy-hemoglobin HbO_2, deoxy-hemoglobin HHb, water, and lipid, for typical chromophore concentrations are plotted for wavelengths λ ranging from $300\,nm$ to $1000\,nm$ [215; 148]. Wavelengths between $\sim 650\,nm$ and $950\,nm$ are demarcated by the green box; they have significantly lower absorption in the NIR, thereby creating the so-called physiological window where tissue absorption is low enough to allow depth penetration of greater than several centimeters. Note that the water and lipid spectra are scaled by a factor of $100\times$ so that they are visible relative to the oxy- and deoxy-hemoglobin spectra.

For DOS, DOT, and DCS, near-infrared light is introduced into the tissue, *e.g.*, via fiber couplers or direct illumination, and either the transmitted or reflected light is detected. Then, using the diffusion equation, an inverse problem can be solved to determine the tissue optical properties [87; 203; 267]. In DOS and DOT, multiple wavelengths of light are typically used because the differences in the known absorption spectra of the chromophores [148] (see Figure 1.1) can then be employed to determine the concentrations of HbO_2 and HHb [267; 266]; this information can further be used to determine the total hemoglobin concentration ($Hb_T \equiv HbO_2 + HHb$) and tissue oxygen saturation ($S_tO_2 \equiv HbO_2/Hb_T$). DCS is a qualitatively different NIR technique which interrogates the decay of the temporal auto-correlation function of the measured intensity

(see [33; 32] and references therein). This decay rate depends on the movement of scatterers in the tissue, particularly red blood cells [97; 101; 98; 37], and thus, DCS provides a blood flow index (BFI) that has been demonstrated to be proportional to blood flow [50; 158; 182; 51; 151]. Moreover, combining S_tO_2 measurements from DOS with BFI measurements from DCS offers a new ability to explore tissue oxygen metabolism [69; 97; 101; 273; 54].

1.2 Breast Cancer

Breast cancer is the most common form of cancer among women in the United States, accounting for $\sim 30\,\%$ of all new cancer cases [233]. Approximately 1 in 8 women will develop invasive breast cancer in her lifetime [89]. Breast tumors are most commonly detected via x-ray mammography and determined to be malignant via an invasive needle biopsy [29]. These tumors are classified by which tissues they are affecting (see Figure 1.2). They are then staged and tested for a variety of genetic and hormonal markers to determine subtype [29; 1]. Typically, tumors form *in-situ* in either glandular ducts or lobes, resulting in Ductal Carcinoma or Lobular Carcinoma *In-Situ* (DCIS or LCIS), respectively. As these malignancies grow, they may invade the surrounding tissue to become either Invasive Ductal Carcinomas (IDC) or Invasive Lobular Carcinomas (ILC), at which point the cancer is classified as Stage I. Tumors that have then metastasized to local lymph nodes, such as the axillary or sternal lymph nodes, are considered locally advanced breast cancer (LABC) and are classified as either Stage II or Stage III. Further metastasis to other organs or distant lymph nodes changes the classification to Stage IV [234]. In addition to staging, the biopsied tissue is tested for a series of hormonal and proteomic markers that determine the cancer subtype and inform the treatment regimen. These markers include the estrogen receptor (ER), progesterone receptor (PR), and human epidermal growth factor receptor (Her2) proteins, as well as the Ki-67 antigen [1]. Tumors that are ER-positive, PR-positive, or Her2-positive often receive hormone treatment in addition to other therapies, which has been shown to improve outcome [235]. The majority of breast cancer patients undergo surgical resection of the tumor, followed by an adjuvant chemotherapy and/or radiation regimen. For LABC, though, it is common for subjects to undergo a neoadjuvant chemotherapy regimen prior to surgery. This regimen can lead to improved response; it also permits increased conservation of breast tissue during tumor resection and limits the need for axillary node treatment and surgery [235].

There are several areas of weakness in the current clinical paradigm for both breast cancer detection and breast cancer treatment, which could potentially be addressed by new imaging/monitoring technologies.

A) Ductal Carcinoma In-Situ (DCIS)

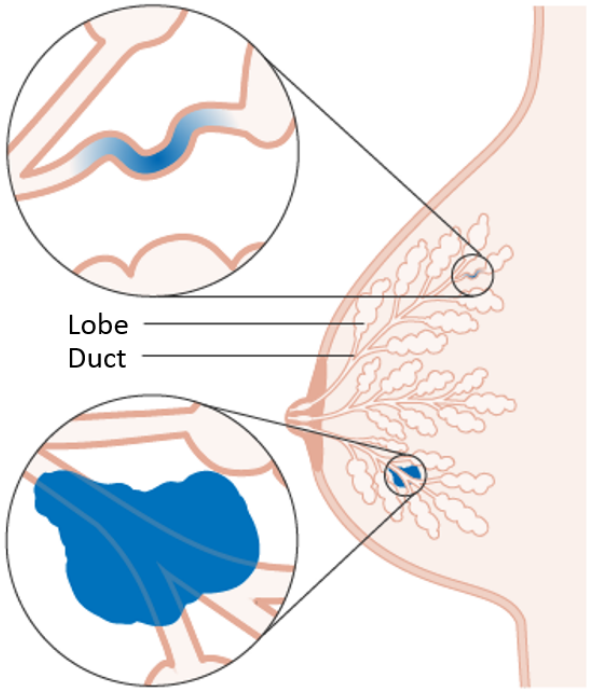

B) Invasive Ductal Carcinoma (IDC) Cancer Research UK

Stage	Characteristics
Stage 0	DCIS or LCIS
Stage I	IDC or ILC
Stage II/III	LABC: Spread to regional lymph nodes
Stage IV	Metastatic Cancer: Spread to other organs

Figure 1.2: Breast Tumors and Staging. A) *In-situ* carcinomas form in either the glandular ducts (DCIS) or lobes (LCIS). They may grow and progress to become invasive carcinomas (IDC or ILC) that affect the surrounding tissue. This diagram is taken from Cancer Research UK [4]. B) In-situ tumors are not considered invasive and are thus classified as Stage 0. Stage I tumors are IDC or ILC with no metastasis beyond the original tumor. Stage II and Stage III disease, also known as locally advanced breast cancer (LABC), are defined as invasive tumors with the spread of malignancies to regional lymph nodes. Stage IV is metastatic disease in which cancer has spread to other organs or distant lymph nodes [234].

1. **Low Specificity of Mammography**. X-ray mammography has a very high sensitivity to breast tumors, *i.e.*, it is very likely to detect malignancies. However, it has a low specificity, *i.e.*, it has limited ability to distinguish malignancies from benign masses (see Section 2.10 for a more detailed discussion of sensitivity and specificity). Thus, mammography has a high false positive rate, prompting many unnecessary invasive biopsies.

2. **Inaccessible Populations**. Women with radiographically dense breasts, some of whom may be at increased risk of breast-cancer [42; 131], are difficult to image with mammography. Additionally, while other modalities such as PET or MRI may be able to complement or augment the diagnostic ability of mammography, they also have logistical constraints, such as ionizing radiation, cost, lack of insurance coverage, and low throughput, which prevent wider adoption.

3. **Monitoring Therapy Response**. Breast cancer treatment regimens have few intermediate markers of cancer progression. Clinicians typically rely on post-therapy radiology or post-surgery pathology to determine the therapy efficacy. This time-delay for acquisition of useful information inhibits a physician's ability to recognize and change ineffective treatment regimens, which are costly and often have significant detrimental side effects.

1.3 Diffuse Optics Applications in Breast Cancer

Diffuse optical techniques are well-suited to study breast cancer for several reasons. First, breast tissue has a particularly low absorption in the near-infrared window due to lower hemoglobin concentrations and higher relative lipid concentrations than most tissue [99; 148]. These factors lead to larger signals and deeper penetration of light into tissue. Also, due to the rapid proliferation of cancer cells and the blood vessels that supply them, there is significant expected contrast between tumors and background tissue in blood volume, blood flow, and oxygen metabolism [119; 57]. For these reasons, and others, DOS [30; 273; 249], DOT [187; 120; 210; 191; 129; 140; 146; 169; 46; 263; 106; 72; 110; 25], and DCS [100; 273; 269; 53; 73] have all been extensively employed to investigate breast cancer.

Furthermore, diffuse optics holds the potential to address some of the weaknesses of the current breast cancer diagnosis and monitoring paradigms discussed in Section 1.2. For example, DOT has shown potential for high specificity in distinguishing malignant tumors from benign lesions, such as cysts and adenomas [67; 72; 165]. Though DOT cannot replicate the high spatial resolution of x-ray mammography [195; 32], it could serve as a complement to mammography that reduces false positive rates and, therefore, the number of unnecessary invasive biopsies. Additionally, diffuse

optics could serve as an alternative modality for patient populations that are inaccessible to current clinical imaging. For example, DOT can successfully image tumors in patients with radiographically dense breasts [164]. Diffuse optical techniques are also generally cost-effective, available at the bedside and free of ionizing radiation [98]; thus, they provide advantages that could help expand the imaged patient population. Finally, the aforementioned logistical advantages position diffuse optics as an ideal modality for repeated, longitudinal monitoring of patients undergoing cancer treatment. Indeed, some potential markers of treatment efficacy, particularly in the neoadjuvant chemotherapy setting, have been identified using both DOS [70; 248; 273; 59; 276; 154; 236; 61; 220; 109; 250; 71; 55; 249; 223] and DCS [273].

1.4 Thesis Contributions and Organization

The work in this thesis is focused on the development of novel biological markers for both cancer diagnosis and for prediction of treatment efficacy using DOS, DOT, and DCS alone, in combination, and with input from structural imaging modalities such as MRI. The remainder of this thesis is organized as follows.

Chapter 2 presents a derivation of the theoretical and mathematical formalism that underlies diffuse optical techniques. This includes the derivation of the diffusion equation (Section 2.2), application of the boundary conditions and techniques required to solve the diffusion equation inverse problem (Section 2.5), algorithms for DOT (Section 2.6), and a brief introduction to DCS (Section 2.9). This chapter also includes a discussion of the statistical methods and models employed throughout the thesis (Section 2.10).

Chapter 3 describes the development of a novel predictor for neoadjuvant chemotherapy response. This new method employs a logistic regression machine learning algorithm and novel, z-score normalized, diffuse optical spectroscopic imaging (DOSI) [30] measurements of tissue oxygen saturation derived from a multi-site clinical trial [249]. This robust response prediction method found that non-hypoxic tumors were more likely to achieve complete response to therapy and, arguably, offers the most impressive evidence to date of the potential of diffuse optics for assessment of cancer treatment efficacy and for guiding cancer treatment adaptations at early time-points. These results have been submitted for publication [75].

Chapter 4 presents a pilot study that employed a subset of patients from the multi-site clinical trial described in Chapter 3; importantly, these patients were imaged at the University of Pennsylvania with both DOSI and DCS. This work represents the first longitudinal DCS monitoring of humans throughout the entire course of a neoadjuvant chemotherapy regimen. The combination of

DOSI and DCS was shown to improve the quantitative accuracy of DCS. Moreover, the data combination provided the ability to quantify tissue oxygen metabolism of the tumors during treatment. The resulting publication showed interesting pilot observations of blood flow differences between responders and non-responders to chemotherapy and rationalized these variations [76].

Chapter 5 describes the application of a z-score normalization and logistic regression scheme for differentiating between malignant and normal tissue, as well as malignant and benign lesions, across a large population of subjects ($n = 222$) measured using DOSI. The models developed from this analysis hold potential to both improve tumor localization with DOS/DOT and to function as an optical biopsy that can determine a probability of malignancy for suspicious lesions identified by mammography. The publication of these findings is currently in preparation.

Chapter 6 describes the construction, optimization, and initial measurements of a high-spatial density DOT instrument that operates concurrently with a clinical MRI. The DOT system utilizes hybrid laser sources to measure absolute optical properties; the structural information from MRI enables improvement of the DOT image quality. These capabilities have been validated in tissue phantoms. The combination of the DOT with clinical MRI systems also presents an opportunity to synthesize DOT biomarkers with hemodynamic properties measured by cutting-edge DCE-MRI methods [237; 238; 92]. A manuscript describing this instrument is also currently being prepared.

Chapter 7 details the novel optimization of a DOT reconstruction algorithm for another high-spatial density DOT instrument, which was described in a recent publication [25]. Modifications to the data weighting method, the inverse problem regularization scheme, and the spatial density of optical data was shown to significantly improve the quality of DOT images.

Finally, Chapter 8 contains a conclusion and some discussion of future directions.

Chapter 2

Diffuse Optical and Statistical Theory

Both of the primary optical techniques presented here, diffuse optical spectroscopy (DOS) and diffuse correlation spectroscopy (DCS), are dependent on the quantification of diffuse light propagation through highly scattering media. The analytical framework for DOS evolved from a special case of the radiative transport equation (Section 2.1), in which certain assumptions about the propagation media and light sources allow for approximation to a diffusion equation (Section 2.2). This diffusion equation can be solved for the optical properties of either infinite (Section 2.4) or bounded (Section 2.5) homogeneous media or for heterogeneous media (Section 2.6) via tomographic reconstruction. The reconstructed optical properties can then be utilized to determine significant physiological properties (Section 2.8). Finally, a blood flow index can be calculated via DCS using a similar diffusive framework (Section 2.9) for temporal auto-correlation.

The various physiological measures produced by DOS and DCS can then be used with statistical and machine learning techniques (Section 2.10) to create useful biomarkers for cancer diagnosis and prognosis.

2.1 Radiative Transport

The radiative transport equation (RTE) is a conservation of energy equation that governs the propagation of electromagnetic radiation in an absorbing and scattering medium. A scalar version of the RTE can be derived from Maxwell's Equations [219] and written as

$$\frac{1}{v}\frac{\partial L(\vec{r},\hat{\Omega},t,\lambda)}{\partial t} + \hat{\Omega}\cdot\vec{\nabla}L(\vec{r},\hat{\Omega},t,\lambda) = \\ -\mu_t(\vec{r},\hat{\Omega},t,\lambda)L(\vec{r},\hat{\Omega},t,\lambda) + Q(\vec{r},\hat{\Omega},t,\lambda) + \\ \mu_s(\vec{r},\hat{\Omega},t,\lambda)\int_{4\pi} L(\vec{r},\hat{\Omega}',t,\lambda)\, f(\hat{\Omega},\hat{\Omega}',\vec{r},t,\lambda)\, d\Omega'. \quad (2.1)$$

Here, the quantities have the following definitions:

- $L(\vec{r},\hat{\Omega},t,\lambda)$ is the light radiance $[Wcm^{-2}sr^{-1}]$ at position $\vec{r}$ and time t, with wavelength λ, propagating in the $\hat{\Omega}$ direction.
- $\mu_a(\vec{r},\hat{\Omega},t,\lambda)$ and $\mu_s(\vec{r},\hat{\Omega},t,\lambda)$ are the absorption and scattering coefficients $[cm^{-1}]$, respectively, at position $\vec{r}$ and time t for light with wavelength λ traveling in the $\hat{\Omega}$ direction.
- μ_t is the transport coefficient $[cm^{-1}]$, which is defined as

$$\mu_t = \mu_a + \mu_s. \quad (2.2)$$

- $Q(\vec{r},\hat{\Omega},t,\lambda)$ is the power per unit volume $[Wcm^{-3}sr^{-1}]$ emitted by sources at position $\vec{r}$ and time t, with wavelength λ, propagating in the $\hat{\Omega}$ direction.
- $f(\hat{\Omega},\hat{\Omega}',\vec{r},t,\lambda)$ is the normalized scattering phase function, which represents the probability density of a photon with wavelength λ propagating in the $\hat{\Omega}'$ direction scattering into the $\hat{\Omega}$ direction at position $\vec{r}$ and time t.

Each term of the RTE describes an aspect of the physics governing photon transport.

2.1.1 Material Derivative

A material derivative describes the time rate of change of a quantity that is subject to some flow velocity v in a given direction $\hat{\Omega}$ [31]. In this case, the measured quantity is the light radiance L, and its material derivative is the left-hand side of Equation 2.1, given as

$$\frac{1}{v}\frac{\partial L(\vec{r},\hat{\Omega},t,\lambda)}{\partial t} + \hat{\Omega}\cdot\vec{\nabla}L(\vec{r},\hat{\Omega},t,\lambda). \quad (2.3)$$

Thus, the left-hand side of Equation 2.1 is simply the rate of change of L at position $\vec{r}$ and time t with wavelength λ in the $\hat{\Omega}$ direction. The terms on the right-hand side of Equation 2.1 then must represent all possible mechanisms for changing the light radiance in the system; these will now be explored.

2.1.2 Absorption and Scattering Loss

In transport theory, the light radiance L in a particular direction $\hat{\Omega}$ can decrease via two mechanisms: 1) the absorption of photons and 2) the scattering of photons into a different direction of propagation. To quantify the amount of absorbed and scattered light, the absorption coefficient, μ_a $[cm^{-1}]$ and scattering phase function $p(\hat{\Omega}', \hat{\Omega})$ $[cm^{-1}sr^{-1}]$ are used.

The absorption coefficient μ_a represents the linear probability density of a photon being absorbed, and it can thus be used to calculate the total power density per unit steradian lost due to absorption

$$\mu_a(\vec{r}, \hat{\Omega}, t, \lambda)L(\vec{r}, \hat{\Omega}, t, \lambda). \tag{2.4}$$

The absorption length l_a, *i.e.*, the mean distance of propagation before a photon is absorbed, can also be can also be calculated by using μ_a and solving for the expectation value of propagation distance, resulting in

$$l_a = \frac{1}{\mu_a}. \tag{2.5}$$

The scattering phase function $p(\hat{\Omega}', \hat{\Omega})$ $[cm^{-1}sr^{-1}]$ is the probability density that a photon traveling in the $\hat{\Omega}$ direction will be scattered into the $\hat{\Omega}'$ direction. For isotropic scattering, $p(\hat{\Omega}', \hat{\Omega}) = 1$ whereas non-isotropic scattering will have a p with an angular dependence, *e.g.*, the Rayleigh scattering phase function $p(\hat{\Omega}', \hat{\Omega}) = \frac{3}{4}\left(1 + \cos^2\left(\Omega' - \Omega\right)\right)$ [43]. Here, we are interested in the loss in light radiance due to scattering, and, as such, we are interested in the probability of light scattering from $\hat{\Omega}$ into any other direction. Thus, we can define the scattering coefficient μ_s as

$$\mu_s(\hat{\Omega}) = \int_{4\pi} p(\hat{\Omega}', \hat{\Omega}) d\Omega', \tag{2.6}$$

which is the integral of the scattering phase function $p(\hat{\Omega}', \hat{\Omega})$ over all possible target solid angles $\hat{\Omega}'$. As with μ_a and absorption, μ_s can also be used to calculate the power density per steradian lost to scattering, given by

$$\mu_s(\vec{r}, \hat{\Omega}, t, \lambda)L(\vec{r}, \hat{\Omega}, t, \lambda) \tag{2.7}$$

and the scattering length l_s, which represents the mean distance a photon will travel before being scattered,

$$l_s = \frac{1}{\mu_s}. \tag{2.8}$$

Given the power densities lost due absorption (Equation 2.4) and scattering (Equation 2.7) and the definition of the transport coefficient μ_t from Equation 2.2, it is apparent that the term

$$\mu_t(\vec{r}, \hat{\Omega}, t, \lambda)L(\vec{r}, \hat{\Omega}, t, \lambda) \tag{2.9}$$

from the right-hand side of Equation 2.1 represents the loss of power density per unit steradian in the $\hat{\Omega}$ direction due to both absorption and scattering.

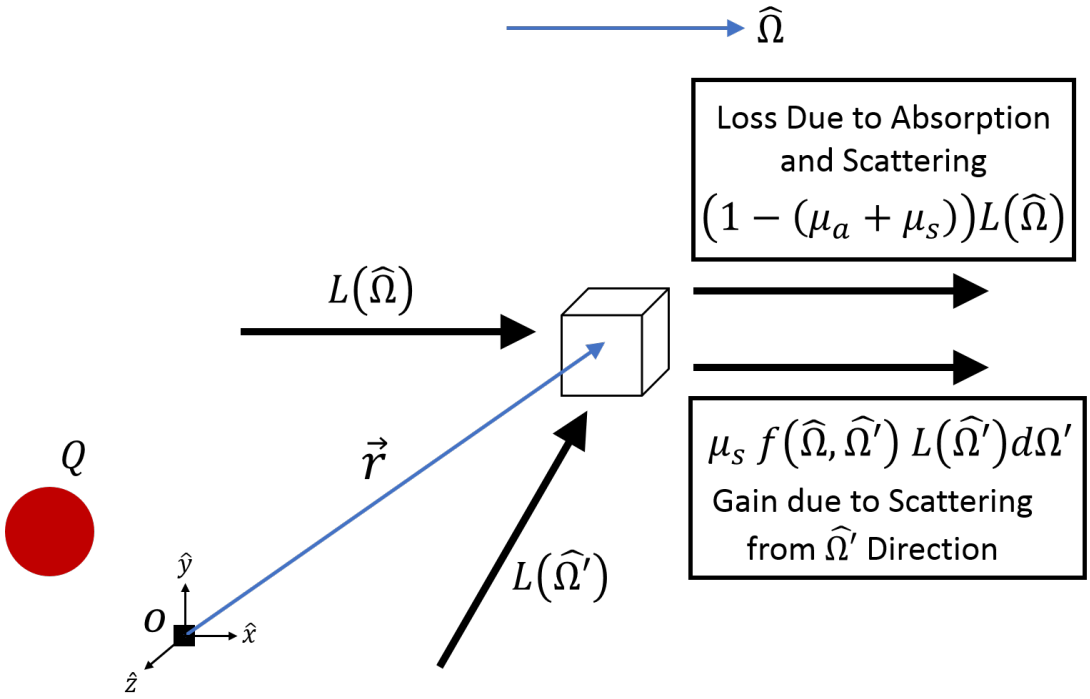

Figure 2.1: Diagram of the change in light radiance in a single, infinitesimal volume element and propagation direction. A single volume element at position $\vec{r}$ and time t experiences an increase in radiance L with wavelength λ, propagating in the $\hat{\Omega}$ direction via two mechanisms: 1) Light Sources Q (Section 2.1.3), and 2) Scattering of light into the $\hat{\Omega}$ direction from another direction $\hat{\Omega}'$ (Section 2.1.4). The volume element experiences a decrease in radiance due to absorption and the scattering of light traveling in the $\hat{\Omega}$ direction into any other direction (Section 2.1.2).

2.1.3 Light Sources

The $Q(\vec{r},\hat{\Omega},t,\lambda)$ term represents the power of light emitted per unit volume by all light sources with wavelength λ in the $\hat{\Omega}$ direction at position $\vec{r}$ and time t. Therefore, this term represents a increase in light radiance due light sources.

2.1.4 Scattering Gain

Section 2.1.2 discussed the loss of light radiance propagating in the $\hat{\Omega}$ direction due to scattering. It is also possible for light traveling in a different initial direction $\hat{\Omega}'$ to be scattered into the $\hat{\Omega}$ direction, resulting in an increase in light radiance along $\hat{\Omega}$. To interrogate this phenomenon, the normalized scattering phase function f is defined as

$$f(\hat{\Omega}, \hat{\Omega}', \vec{r}, t, \lambda) \equiv \frac{p(\hat{\Omega}, \hat{\Omega}', \vec{r}, t, \lambda)}{\mu_s(\vec{r}, \hat{\Omega}, t, \lambda)}. \tag{2.10}$$

Therefore, $f(\hat{\Omega}, \hat{\Omega}')$ represents the fractional probability that a photon that is scattered while propagating along $\hat{\Omega}'$ is scattered into the $\hat{\Omega}$ direction. Given the definition of μ_s in Equation 2.6, it follows that

$$\int_{4\pi} f(\hat{\Omega}, \hat{\Omega}') d\Omega' = 1, \tag{2.11}$$

and thus, as per its name, f is normalized. Given the definition of f in Equation 2.10 and the analogous term for radiance loss due to scattering in Equation 2.7, the final term on the right-hand side of Equation 2.1

$$\mu_s(\vec{r}, \hat{\Omega}, t, \lambda) \int_{4\pi} L(\vec{r}, \hat{\Omega}', t, \lambda)) f(\hat{\Omega}, \hat{\Omega}', \vec{r}, t, \lambda) d\Omega' \tag{2.12}$$

represents the light radiance increase due to photons scattered into the $\hat{\Omega}$ direction from all other directions.

Thus, it has been demonstrated that the RTE in Equation 2.1 can be thought of as an equation of conservation for light radiance along a propagation direction $\hat{\Omega}$.

2.1.5 Assumptions

The scalar RTE from Equation 2.1 provides a significantly simpler framework than Maxwell's Equations for analysis and calculation of photon transport in a variety of interesting media, including Earth's atmosphere [226] and astronomical dust and gas clouds [68]. However, Equation 2.1 is only valid under the following assumptions [219], which allow for the use of geometric optics [137]:

1. The average distance of propagation between photon absorption and scattering events is significantly larger than the wavelength of light.

   $$l_a, l_s >> \lambda. \tag{2.13}$$

   Under this condition, light can be modelled using a far-field, plane wave representation, and the interference between neighboring particles can be neglected in determining the absorption and scattering properties of the particles [42]. For near-infrared light ($\lambda \sim 800\,nm$) in tissue, these quantities are typically in the range of $l_s \sim 0.02\,cm$ and $l_a \sim 10\,cm$, and thus, the condition is fulfilled.

2. The light is unpolarized in the medium of propagation, and thus a scalar radiance can be used instead of a vector representation of the light intensity [137].

3. The index of refraction n is homogeneous throughout the medium. This condition is not necessary to create a scalar RTE, but it does allow for the assumption of constant propagation velocity for light in the medium. If the index of refraction is sufficiently non-uniform, the heterogeneity must be accounted for to properly quantify the photon propagation [83].

The RTE is also an accurate model for the migration of photons through human tissue [128], in which the necessary assumptions are usually met. However, for most relevant tissues, measurement geometries, and boundary conditions, solutions to the RTE require computationally intensive numerical methods [14]. Simplifying the RTE, using a series of approximations that are valid in many biological tissues of interest, leads to a diffusive model of photon propagation, which creates more readily usable analytic solutions and boundary conditions. Section 2.2 will detail the derivation of this diffusion approximation (DA) from the full scalar RTE.

2.2 Photon Diffusion Approximation

The general form of the homogeneous partial differential diffusion equation is

$$\frac{\partial F(\vec{r},t)}{\partial t} - \vec{\nabla}(D(\vec{r})\vec{\nabla}F(\vec{r},t)) = 0, \tag{2.14}$$

where F is a generic function of $\vec{r}$ and t, and D is a spatially dependent diffusion coefficient. This mathematical framework has well-known solutions for a variety of interesting geometries and boundary conditions [9] and has been used to describe, among other processes, the transfer of heat through metal [58] and the mixing of gases [21]. Under typical conditions present in biological tissue, the transport of photons can often be described via a diffusion equation derived from the full RTE [22; 32; 254]. The following sub-sections will describe this derivation and the necessary assumptions required for the diffusion approximation's validity.

2.2.1 Photon Fluence Rate and Flux

Three quantities associated with light radiance and sources must first be defined.

1. Photon Fluence Rate

$$\Phi(\vec{r},t,\lambda) \equiv \int_{4\pi} L(\vec{r},\hat{\Omega},t,\lambda)\, d\Omega \tag{2.15}$$

where Φ, the photon fluence rate, has units of $[Wcm^{-2}]$ and is defined as the integral of the light radiance over all solid angles. Thus, the photon fluence rate can be thought of as the total power per unit area of photons with a given wavelength λ moving radially outward at a specific position $\vec{r}$ and time t.

2. Photon Flux

$$\vec{J}(\vec{r},t,\lambda) \equiv \int_{4\pi} L(\vec{r},\hat{\Omega},t,\lambda)\,\hat{\Omega}\,d\Omega \tag{2.16}$$

where $\vec{J}$, the photon flux, has units of $[Wcm^{-2}]$ and can be thought of as the direction-dependent sum of the radiance with wavelength λ emerging from a volume element at position $\vec{r}$ and time t.

3. Source Power Concentration

$$S(\vec{r},t,\lambda) \equiv \int_{4\pi} Q(\vec{r},\hat{\Omega},t,\lambda)\,d\Omega \tag{2.17}$$

where S, the radiant source power concentration, has units of $[Wcm^{-3}]$ and is the concentration of power emitted radially outward at wavelength λ from a source at position $\vec{r}$ and time t over all solid angles $\hat{\Omega}$.

These physical quantities allow for the simplification of the RTE under certain assumptions.

2.2.2 Assumption 1: Isotropic Medium

The first necessary assumption is that the medium through which the light propagates is isotropic. This condition is typically satisfied for disordered media without an underlying crystalline or semi-crystalline structure, eliminating any orientation-dependence of the permittivity, permeability, and index of refraction [43]. Importantly, this also eliminates the orientation-dependence of the absorption and scattering coefficients, which is represented mathematically as

$$\mu_a(\vec{r},\hat{\Omega},t,\lambda) \rightarrow \mu_a(\vec{r},t,\lambda), \tag{2.18}$$

$$\mu_s(\vec{r},\hat{\Omega},t,\lambda) \rightarrow \mu_s(\vec{r},t,\lambda). \tag{2.19}$$

Thus, throughout the medium, incident photons will be absorbed or scattered with the same respective probabilities, regardless of their direction of travel.

The first step in the diffusion approximation derivation is to integrate the entire RTE over all 4π solid angles, resulting in

$$\begin{aligned}\int_{4\pi} \frac{1}{v}\frac{\partial L(\vec{r},\hat{\Omega},t,\lambda)}{\partial t}\,d\Omega + \int_{4\pi} \hat{\Omega}\cdot\vec{\nabla}L(\vec{r},\hat{\Omega},t,\lambda)\,d\Omega \;=& \\ -\int_{4\pi} \mu_t(\vec{r},\hat{\Omega},t,\lambda)\,L(\vec{r},\hat{\Omega},t,\lambda)\,d\Omega + \int_{4\pi} Q(\vec{r},\hat{\Omega},t,\lambda)\,d\Omega + & \\ \int_{4\pi} \mu_s(\vec{r},\hat{\Omega},t,\lambda)\int_{4\pi} L(\vec{r},\hat{\Omega}',t,\lambda)\,f(\hat{\Omega},\hat{\Omega}',\vec{r},t,\lambda)\,d\Omega'\,d\Omega.&\end{aligned} \tag{2.20}$$

Since $\hat{\Omega}$ is constant relative to the spatial derivative $\vec{\nabla}$, the following equation is true:

$$\hat{\Omega} \cdot \vec{\nabla} L(\vec{r}, \hat{\Omega}, t, \lambda) = \vec{\nabla} \cdot (L(\vec{r}, \hat{\Omega}, t, \lambda)\, \hat{\Omega}). \tag{2.21}$$

Then, by incorporating the relations in Equations 2.18, 2.19, and 2.21, as well as the quantities defined in Equations 2.15, 2.16, and 2.17, Equation 2.20 can be rewritten as

$$\frac{1}{v}\frac{\partial \Phi(\vec{r}, t, \lambda)}{\partial t} + \vec{\nabla} \cdot \vec{J}(\vec{r}, t, \lambda) = -\mu_t(\vec{r}, t, \lambda)\, \Phi(\vec{r}, t, \lambda) + S(\vec{r}, t, \lambda) + \mu_s(\vec{r}, t, \lambda) \int_{4\pi} \left[\int_{4\pi} f(\hat{\Omega}, \hat{\Omega}', \vec{r}, t, \lambda)\, d\Omega \right] L(\vec{r}, \hat{\Omega}', t, \lambda)\, d\Omega'. \tag{2.22}$$

The next assumption will further simplify Equation 2.22 to define a continuity relation.

2.2.3 Assumption 2: Rotational Symmetry in Scattering Phase Function

The second assumption is that the normalized scattering phase function f is rotationally symmetric; therefore, f is dependent only on the angle between the incident and scattering directions, rather than the absolute incident or scattering direction. Mathematically, this means that

$$f(\hat{\Omega}, \hat{\Omega}', \vec{r}, t, \lambda) = f(\hat{\Omega} \cdot \hat{\Omega}', \vec{r}, t, \lambda), \tag{2.23}$$

and

$$\int_{4\pi} f(\hat{\Omega} \cdot \hat{\Omega}', \vec{r}, t, \lambda) d\Omega = 1. \tag{2.24}$$

Using Equation 2.24 and Equation 2.15, the RTE in Equation 2.22 simplifies to a continuity relation for the fluence rate,

$$\frac{1}{v}\frac{\partial \Phi(\vec{r}, t, \lambda)}{\partial t} + \vec{\nabla} \cdot \vec{J}(\vec{r}, t, \lambda) + \mu_a(\vec{r}, t, \lambda)\Phi(\vec{r}, t, \lambda) = S(\vec{r}, t, \lambda), \tag{2.25}$$

which will later be used to simplify the RTE to a diffusion equation.

Physically, this assumption is usually satisfied under the same conditions that the isotropic medium assumption is satisfied, so it is typically valid in the biological tissues of interest.

2.2.4 Spherical Harmonic Expansion

Spherical harmonic series expansion is a useful technique for approximating quantities that have specific angular dependence, like the radiance L in the RTE. Here, L is written as

$$L(\vec{r}, \hat{\Omega}, t, \lambda) = \sum_{l=0}^{N} \sum_{m=-l}^{l} \sqrt{\frac{2l+1}{4\pi}}\, \tilde{\phi}_{lm}(\vec{r}, t, \lambda)\, Y_{lm}(\hat{\Omega}) \tag{2.26}$$

where $Y_{lm}(\hat{\Omega})$ is the spherical harmonic term with angular dependence, $\tilde{\phi}_{lm}(\vec{r},t,\lambda)$ is the spherical harmonic coefficient without angular dependence, and N is the number of terms in the expansion [9]. Given this definition, the photon fluence rate Φ and the dot product of the photon flux $\vec{J}$ and the propagation direction $\hat{\Omega}$ can be calculated using the $l=0$ and $l=1$ spherical harmonic terms, respectively, as follows

$$\Phi(\vec{r},t,\lambda) = \sqrt{4\pi}\,\tilde{\phi}_{00}(\vec{r},t,\lambda)\,Y_{00}(\hat{\Omega}), \tag{2.27}$$

$$\vec{J}(\vec{r},t,\lambda)\cdot\hat{\Omega} = \sqrt{\frac{4\pi}{3}}\left[\tilde{\phi}_{1-1}(\vec{r},t,\lambda)Y_{1-1}(\hat{\Omega}) + \tilde{\phi}_{10}(\vec{r},t,\lambda)Y_{10}(\hat{\Omega}) + \tilde{\phi}_{11}(\vec{r},t,\lambda)Y_{11}(\hat{\Omega})\right]. \tag{2.28}$$

A full derivation of these representations of Φ and $\vec{J}$ can be found in Appendix A.1.

2.2.5 Assumption 3: Light is Nearly Isotropic

The third assumption required for the diffusion approximation is that light propagates approximately isotropically throughout the medium. Mathematically, this translates to

$$\Phi(\vec{r},t,\lambda) \gg \left|\vec{J}(\vec{r},t,\lambda)\right| \tag{2.29}$$

because $\vec{J}$ is a vector while Φ is directionless. Physically, this condition is satisfied in tissue due to multiple scattering; the direction of light propagation is randomized after photons have been scattered many times.

In the spherical harmonic series expansion, only the $l=0$ term Y_{00} is isotropic while the higher order, *i.e.*, $l>0$, terms are increasingly anisotropic. Thus, given the assumption of nearly isotropic light propagation, the series can be truncated without sacrificing accuracy. For media with somewhat less isotropic light propagation, keeping all terms of the radiance expansion where $l\leq 3$, referred to as the P_3 approximation, is necessary [98]. However, for many tissues of interest, keeping only the $l=0$ and $l=1$ terms provides an accurate representation of the radiance. This is referred to as the P_1 approximation.

Given that the P_1 approximation is valid, the spherical harmonic expansion in Equation 2.26 can be truncated at $N=1$, and the spherical harmonic representations of photon fluence rate (Equation 2.27) and flux (Equation 2.28) can be used to express the radiance as

$$L(\vec{r},\hat{\Omega},t,\lambda) = \frac{1}{4\pi}\Phi(\vec{r},t,\lambda) + \frac{3}{4\pi}\vec{J}(\vec{r},t,\lambda)\cdot\hat{\Omega}. \tag{2.30}$$

Thus, under the P_1 approximation, the radiance can be written as a linear combination of the photon fluence rate and the projection of the photon flux into the $\hat{\Omega}$ direction. Substituting Equation 2.30

into the RTE (Equation 2.1) while utilizing the previous assumptions and multiplying both sides by 4π results in

$$\frac{1}{v}\frac{\partial\Phi(\vec{r},t,\lambda)}{\partial t} + \frac{3}{v}\frac{\partial}{\partial t}\left(\vec{J}(\vec{r},t,\lambda)\cdot\hat{\Omega}\right) + \hat{\Omega}\cdot\vec{\nabla}\Phi(\vec{r},t,\lambda) + 3\hat{\Omega}\cdot\vec{\nabla}\left(\vec{J}(\vec{r},t,\lambda)\cdot\hat{\Omega}\right) = \\ -\mu_t(\vec{r},t,\lambda)\Phi(\vec{r},t,\lambda) - 3\mu_t(\vec{r},t,\lambda)\vec{J}(\vec{r},t,\lambda)\cdot\hat{\Omega} + 4\pi Q(\vec{r},\hat{\Omega},t,\lambda) + \\ \mu_s(\vec{r},t,\lambda)\int_{4\pi}\Phi(\vec{r},t,\lambda)\,f(\hat{\Omega}\cdot\hat{\Omega}',\vec{r},t,\lambda)\,d\Omega' + 3\mu_s(\vec{r},t,\lambda)\int_{4\pi}\vec{J}(\vec{r},t,\lambda)\cdot\hat{\Omega}'\,f(\hat{\Omega}\cdot\hat{\Omega}',\vec{r},t,\lambda)\,d\Omega'. \tag{2.31}$$

First, the fluence rate term for the gain due to scattering simplifies as follows

$$\mu_s(\vec{r},t,\lambda)\int_{4\pi}\Phi(\vec{r},t,\lambda)\,f(\hat{\Omega}\cdot\hat{\Omega}',\vec{r},t,\lambda)\,d\Omega' = \mu_s(\vec{r},t,\lambda)\;\Phi(\vec{r},t,\lambda) \tag{2.32}$$

due to the lack of $\hat{\Omega}'$ dependence of the fluence rate and Equation 2.24. To simplify the flux term for the gain due to scattering, $\hat{\Omega}$ is defined, without loss of generality, as pointing along the $\hat{z}$ direction, *i.e.*,

$$\hat{\Omega} = \hat{z}. \tag{2.33}$$

Thus, in spherical coordinates, the dot product between $\hat{\Omega}$ and $\hat{\Omega}'$ is simply

$$\hat{\Omega}\cdot\hat{\Omega}' = \cos\theta', \tag{2.34}$$

where θ' is the polar angle coordinate of $\hat{\Omega}'$. Then, using the definition of $d\hat{\Omega}'$ in Cartesian coordinates (see Equation A.11 in Appendix A.1), the flux term of the gain due to scattering becomes

$$3\mu_s(\vec{r},t,\lambda)\int_{4\pi}\vec{J}(\vec{r},t,\lambda)\cdot\hat{\Omega}'\,f(\hat{\Omega}\cdot\hat{\Omega}',\vec{r},t,\lambda)\,d\Omega' = \\ 3\mu_s(\vec{r},t,\lambda)\int_{4\pi}\vec{J}(\vec{r},t,\lambda)\cdot(\cos\theta'\cdot\hat{z})\;f(\hat{\Omega}\cdot\hat{\Omega}',\vec{r},t,\lambda)\,d\Omega'. \tag{2.35}$$

Given the definition of $\hat{\Omega}$, as seen in Equations 2.33 and 2.34, this term further simplifies to

$$3\mu_s(\vec{r},t,\lambda)\int_{4\pi}\vec{J}(\vec{r},t,\lambda)\cdot\hat{\Omega}'\,f(\hat{\Omega}\cdot\hat{\Omega}',\vec{r},t,\lambda)\,d\Omega' = 3\mu_s\,g(\vec{r},t,\lambda)\,\vec{J}(\vec{r},t,\lambda)\cdot\hat{\Omega}. \tag{2.36}$$

Here g, the anisotropy factor, is defined as

$$g(\vec{r},t,\lambda) \equiv \int_{4\pi} f(\hat{\Omega}\cdot\hat{\Omega}',\vec{r},t,\lambda)\,\hat{\Omega}\cdot\hat{\Omega}'\,d\Omega' \tag{2.37}$$

$$= \int_{4\pi} f(\cos\theta',\vec{r},t,\lambda)\;\cos\theta'\,d\Omega' \tag{2.38}$$

$$= \langle\cos\theta'\rangle, \tag{2.39}$$

and is thus the ensemble average of the cosine of the angle between the incident and scattered propagation directions. Therefore, the anisotropy factor g can be thought of as a measure of the likelihood of a photon scattering in the forward, *i.e.*, the incident, direction. An incident photon will always undergo forward scattering when $g = 1$ while $g = -1$ indicates completely backwards scattering, and $g = 0$ represents isotropic scattering.

2.2.6 Assumption 4: Light Sources are Isotropic

The fourth necessary assumption in the diffusion approximation is that all light sources Q must be isotropic, and therefore

$$Q(\vec{r}, \hat{\Omega}, t, \lambda) \rightarrow Q(\vec{r}, t, \lambda). \tag{2.40}$$

As with the assumption of isotropic radiance, this assumption is valid due to the multiple scattering of photons in the tissue, which randomizes the propagation direction.

Once this assumption is made, using Equations 2.32 and 2.36 to simplify the RTE in Equation 2.31, multiplying both sides of the equation by $\hat{\Omega}$, and integrating both sides of the equation over all solid angles Ω results in

$$\begin{aligned}\frac{1}{v}\frac{\partial \Phi(\vec{r}, t, \lambda)}{\partial t} \int_{4\pi} \hat{\Omega}\, d\Omega \; + \frac{3}{v}\frac{\partial}{\partial t} \int_{4\pi} \hat{\Omega} \left[\vec{J}(\vec{r}, t, \lambda) \cdot \hat{\Omega}\right] \, d\Omega \; + \\ \int_{4\pi} \hat{\Omega} \left(\hat{\Omega} \cdot \vec{\nabla} \Phi(\vec{r}, t, \lambda)\right) \, d\Omega \; + 3 \int_{4\pi} \hat{\Omega} \left(\hat{\Omega} \cdot \vec{\nabla} \left[\vec{J}(\vec{r}, t, \lambda) \cdot \hat{\Omega}\right]\right) \, d\Omega \; = \\ - \left[\mu_t(\vec{r}, t, \lambda) - \mu_s(\vec{r}, t, \lambda)\right] \Phi(\vec{r}, t, \lambda) \int_{4\pi} \hat{\Omega}\, d\Omega \; - \\ 3 \left[\mu_t(\vec{r}, t, \lambda) - g(\vec{r}, t, \lambda) \mu_s(\vec{r}, t, \lambda)\right] \int_{4\pi} \hat{\Omega} \left[\vec{J}(\vec{r}, t, \lambda) \cdot \hat{\Omega}\right] \, d\Omega \; + \\ 4\pi\, Q(\vec{r}, t, \lambda) \int_{4\pi} \hat{\Omega}\, d\Omega. \end{aligned} \tag{2.41}$$

This equation can be simplified by noting the following three vector integral identities:

$$\int_{4\pi} \hat{\Omega}\, d\Omega = 0, \tag{2.42}$$

$$\int_{4\pi} \hat{\Omega} \left[\hat{\Omega} \cdot \vec{A}\right] \, d\Omega = \frac{4\pi}{3} \vec{A}, \tag{2.43}$$

$$\int_{4\pi} \hat{\Omega} \left[\hat{\Omega} \cdot \vec{\nabla} \left(\vec{A} \cdot \hat{\Omega}\right)\right] \, d\Omega = 0, \tag{2.44}$$

where $\vec{A}$ is a generic vector. A full derivation of these identities can be found in Appendix A.2.

With these identities, the RTE can be further simplified to

$$\frac{3}{v}\frac{\partial \vec{J}(\vec{r}, t, \lambda)}{\partial t} + \vec{\nabla} \Phi(\vec{r}, t, \lambda) = -3 \left[\mu_t(\vec{r}, t, \lambda) - g(\vec{r}, t, \lambda)\, \mu_s(\vec{r}, t, \lambda)\right] \vec{J}(\vec{r}, t, \lambda). \tag{2.45}$$

One final assumption must now be made to transform the RTE into a diffusion equation.

2.2.7 Assumption 5: Slow Temporal Variation in Photon Flux

The final necessary assumption is that the the photon flux varies slowly in time, such that

$$\frac{3}{v}\frac{\partial \vec{J}(\vec{r},t,\lambda)}{\partial t} \ll \vec{\nabla}\Phi(\vec{r},t,\lambda) \tag{2.46}$$

$$\ll 3\left[\mu_t(\vec{r},t,\lambda) - g(\vec{r},t,\lambda)\,\mu_s(\vec{r},t,\lambda)\right]\vec{J}(\vec{r},t,\lambda). \tag{2.47}$$

Therefore, in Equation 2.45,

$$\frac{3}{v}\frac{\partial \vec{J}(\vec{r},t,\lambda)}{\partial t} \to 0, \tag{2.48}$$

resulting in a relationship between the photon flux $\vec{J}$ and the spatial derivative of the photon fluence rate Φ of the form

$$\vec{\nabla}\Phi(\vec{r},t,\lambda) = -3\left[\mu_t(\vec{r},t,\lambda) - g(\vec{r},t,\lambda)\,\mu_s(\vec{r},t,\lambda)\right]\vec{J}(\vec{r},t,\lambda). \tag{2.49}$$

Solving for the photon flux $\vec{J}$ results in

$$\vec{J}(\vec{r},t,\lambda) = \frac{-1}{3\left[\mu_t(\vec{r},t,\lambda) - g(\vec{r},t,\lambda)\,\mu_s(\vec{r},t,\lambda)\right]}\vec{\nabla}\Phi(\vec{r},t,\lambda), \tag{2.50}$$

which has the form of Fick's 1st Law of Diffusion [27]. In this case, the diffusing particles are photons, and the term in front of the gradient of Φ is a diffusion coefficient.

With the definition of μ_t (Equation 2.2), this Fick's Law relationship can be rewritten as

$$\vec{J}(\vec{r},t,\lambda) = -\frac{D(\vec{r},t,\lambda)}{v}\vec{\nabla}\Phi(\vec{r},t,\lambda), \tag{2.51}$$

where a diffusion coefficient D $[cm^2 s^{-1}]$ has been defined as

$$D(\vec{r},t,\lambda) \equiv \frac{v}{3\left[\mu_a(\vec{r},t,\lambda) + \mu_s'(\vec{r},t,\lambda)\right]} = \frac{v}{3}l_{tr}(\vec{r},t,\lambda). \tag{2.52}$$

This definition of D also introduces two new quantities. First, D determines the photon transport length l_{tr} $[cm]$, which represents the average random walk step size for a photon [27] and can be expressed as

$$l_{tr}(\vec{r},t,\lambda) = \frac{1}{\mu_a(\vec{r},t,\lambda) + \mu_s'(\vec{r},t,\lambda)}. \tag{2.53}$$

Both of these quantities are also dependent on the reduced scattering coefficient μ_s' $[cm^{-1}]$, which is defined as

$$\mu_s'(\vec{r},t,\lambda) \equiv \mu_s(\vec{r},t,\lambda)\left[1 - g(\vec{r},t,\lambda)\right]. \tag{2.54}$$

Finally, the Fick's Law relationship in Equation 2.51 can be substituted into the fluence rate continuity relation (see Equation 2.25) to arrive at the photon diffusion equation [135]

$$\vec{\nabla} \cdot \Big[D(\vec{r}, t, \lambda) \vec{\nabla} \Phi(\vec{r}, t, \lambda) \Big] - v\, \mu_a(\vec{r}, t, \lambda) \Phi(\vec{r}, t, \lambda) - \frac{\partial \Phi(\vec{r}, t, \lambda)}{\partial t} = -v\, S(\vec{r}, t, \lambda), \tag{2.55}$$

which contains the characteristic relationship between spatial and temporal derivatives for a diffusion equation [27]. The resulting physical process of diffusive photon transport, as well as the validity of the assumptions required for the diffusion approximation, will be discussed in the next section.

2.2.8 Photon Transport and the Validity of Diffusion Approximation Assumptions

In diffusive processes, the diffusing particles make random walks through tissues with an average step size known as the transport length l_{tr} [27]. In photon diffusion, l_{tr} is dependent on the absorption coefficient μ_a and the reduced scattering coefficient μ_s' (see Equation 2.53). The reduced scattering coefficient is, in turn, dependent on both the scattering coefficient μ_s and the anisotropy factor g. With respect to these coefficients, tissue has two important properties for light with wavelengths in the biological window:

1. Tissue is highly scattering [148], and thus,

$$\mu_a \ll \mu_s. \tag{2.56}$$

2. In tissue, g is usually between ~ 0.7 and ~ 0.95 [148], meaning that the scattering has a bias towards the forward direction. Therefore, given the definition of μ_s' (Equation 2.54) and the typical values of g in tissue for the relevant wavelengths,

$$\mu_s' \ll \mu_s. \tag{2.57}$$

Given these relations, it is also clear that

$$l_{tr} >> l_s, \tag{2.58}$$

and therefore many scattering events occur over the length of a single random walk step (see Figure 2.2). This is an important condition for the validity of several assumptions required in the derivation of the diffusion equation. The assumption of isotropic light propagation in Sections 2.2.5 and 2.2.6 is premised on the randomization in photon propagation direction due to multiple scattering. However, a single scattering event does not fully randomize the propagation direction because of

the high anisotropy factor g, which indicates a bias towards forward scattering. Therefore, several of these forward-biased scattering events are required before the photon propagation direction is randomized relative to the incident direction, a condition that is fulfilled by Equation 2.58. Thus, under these optical conditions, which are present in many tissues of interest, near-infrared light will propagate through tissue isotropically, allowing for the approximations made in Sections 2.2.5 and 2.2.6.

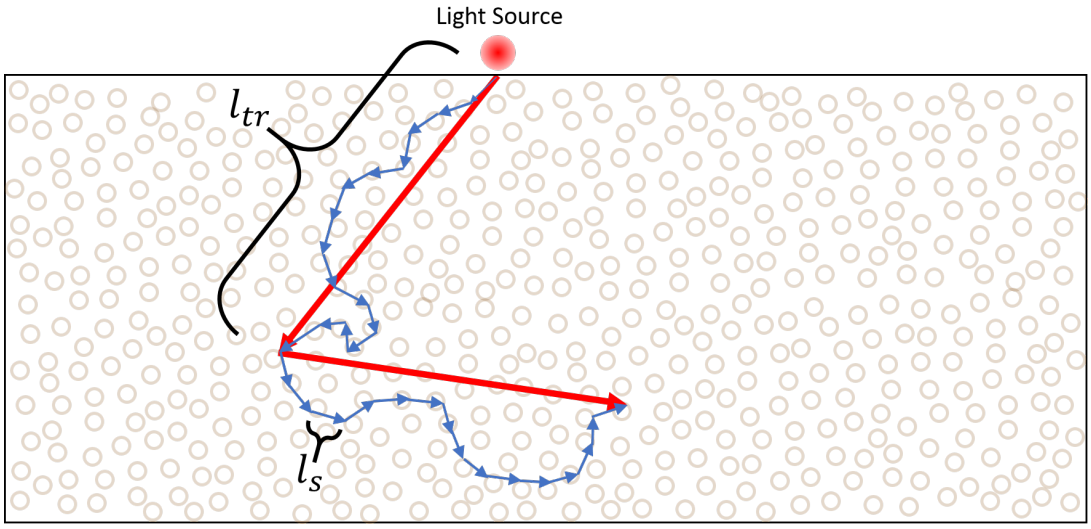

Figure 2.2: Schematic of photon propagation in tissue. A single photon propagates through tissue with a characteristic scattering length l_s. Due to a high anisotropy factor g, each scattering event is biased towards forward scattering, and thus the transport length l_{tr} (Equation 2.53) is greater than l_s. Therefore, a photon will experience multiple scattering events (small blue arrows) over the course of a single random walk step of size l_{tr} (large red arrows). The absorption length l_a is significantly greater than both l_s and l_{tr} under typical conditions; the photon is thus likely to undergo many random walk steps prior to being absorbed. This mechanism of motion is characteristic of diffusion. Note that this figure is adapted from a similar figure in the PhD Theses of David R. Busch [52] and Wesley B. Baker [22].

The final assumption (see Section 2.2.7) is that the photon flux $\vec{J}$ experiences slow temporal variation, allowing for the employment of a steady-state treatment for $\vec{J}$. For this model to be accurate, the photon flux must vary slowly relative to the time it takes for a photon to travel a single random walk step of length l_{tr}. If the photon flux is oscillating with an angular frequency of ω, due to a frequency domain light source (see Section 2.3), then the period of oscillation is defined as

$$T_{flux} \equiv \frac{2\pi}{\omega} = \frac{1}{f}, \tag{2.59}$$

where f $[Hz]$ is the frequency of oscillation. This period T_{flux} must be large relative to the time

for the photon to take a single random walk step, or mathematically,

$$\frac{1}{f} \gg \frac{l_{tr}}{v}, \tag{2.60}$$

Given typical optical properties of tissue for NIR light of $\mu_a = 0.1\,cm^{-1}$, $\mu_s' = 10\,cm^{-1}$, and $n = 1.4$ [148], the time it takes for a photon to travel the transport length is approximately 5×10^{-12} seconds. This means that the condition of slow temporal flux variation is met when $f \ll 200\,GHz$. In typical diffuse optical experiments, the modulation frequency is on the order of $100\,MHz$, and thus, this condition is fulfilled.

2.3 Source Types

The diffusion equation in 2.55 describes how the photon fluence rate is dependent on only the light source S and the absorption and diffusion coefficients μ_a and D, which is also dependent on the reduced scattering coefficient μ_s'. Thus, the general algorithm for diffuse optics is to introduce light from a source into tissue, measure the fluence rate at given detector positions, and solve an inverse problem to determine the optical properties of the tissue.

In diffuse optics, sources are typically lasers or light emitting diodes (LEDs) with wavelengths ranging from $600\,nm$ to $1100\,nm$ [98]. There are three primary methods for using these light sources with varying costs and information qualities.

2.3.1 Continuous Wave

Continuous wave (CW) measurements are performed using an input source with a constant intensity. CW diffuse optical spectroscopy allows for simpler computational methods and fast, low-cost, easy-to-implement detection instrumentation, such as charge-coupled devices (CCD) [80] and photodiodes [232; 188], which permits construction of instruments with many source-detector pairs. However, the detected intensity contains information only about the change in amplitude between source and detector intensity (see Figure 2.3), precluding CW DOS from being able to simultaneously determine μ_a and μ_s' [13; 121]. This is a significant disadvantage, requiring the assumption of a value for μ_s' to determine μ_a, which can result in significant quantitative offsets. This assumed μ_s' value usually takes the form of a population average for a given tissue type, but can also be measured via hybrid diffuse optical instrumentation (see Chapter 6).

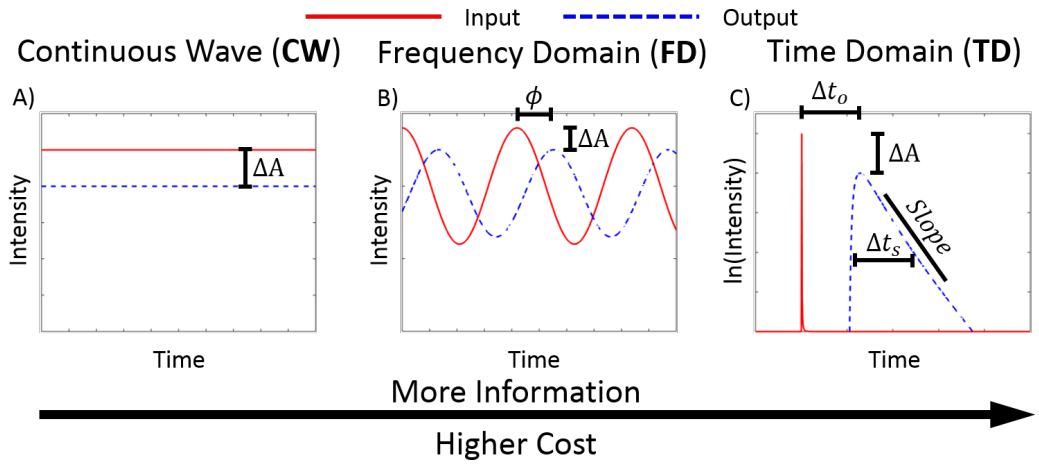

Figure 2.3: Common source and data types used in diffuse optics. Three common types of light sources used in diffuse optics are, in order of increasing information content and cost: A) Continuous Wave (CW) - Light with constant intensity is input into tissue. Thus, the detected signal only provides information about the change in the amplitude (ΔA) of the intensity. This makes it difficult for CW diffuse optics to uniquely determine absolute values of μ_a and μ_s' [13; 121]. B) Frequency Domain (FD) - Source light is modulated with frequency on the order of 100 MHz. The detected signal oscillates at the same frequency but with amplitude attenuation ΔA and a phase shift ϕ, enabling simultaneous determination of μ_a and μ_s' [203; 213; 63]. C) Time Domain (TD) - A short pulse of light ($\sim 100\,ps$) is sent into tissue. The resultant point spread function is measured and fit to analytical solutions to the diffusion equation. The time shift Δt_o between the input and output signals is largely determined by μ_s' while the width (Δt_s) and terminal slope of the point spread function is highly dependent on μ_a [202; 258; 192]. Note that this figure is a modified version of a figure that appears in [98].

2.3.2 Frequency Domain

Frequency domain (FD) instruments utilize near infrared light sources sinusoidally modulated in the radio frequency range ($f \approx 70\,MHz$ to $1\,GHz$). The detected intensity signal oscillates at the same modulation frequency as the source light but does so with amplitude attenuation and a phase shift (see Figure 2.3). Measuring both of these quantities enables the determination of both μ_a and μ_s' [203; 213; 63]. Frequency domain instruments require modulation of either laser diode or LED sources and can include avalanche photodiode (APD) [262; 30; 80], photomultiplier tube (PMT) [179], or heterodyne CCD [25] detection, increasing the cost and complexity of the instrumentation.

2.3.3 Time Domain

Time domain (TD), or time-resolved (TR), instruments use very short ($\sim 100\,ps$) source light pulses, which are temporally broadened during their propagation through tissue. Measurement

and fitting of the resultant point spread functions (see Figure 2.3) provides very dense information content, equivalent to FD measurements performed over a large range of frequencies, which allows for accurate simultaneous determination of both μ_a and μ_s' [202; 11; 258]. However, measurement of the these broadened pulses requires very sensitive time-resolved single-photon counting electronics, in addition to PMT [192; 224; 207; 52] or APD [208] detection, which practically limits the number of source-detector pairs that can be included in a single system.

2.4 Solutions in a Homogeneous Infinite Geometry

2.4.1 Homogeneous Medium Diffusion Equation

The simplest solution to the fluence rate diffusion equation can be found by assuming a homogeneous distribution for the optical properties at a single wavelength, *i.e.*

$$\mu_a(\vec{r}, t, \lambda) \rightarrow \mu_a, \tag{2.61}$$

$$\mu_s'(\vec{r}, t, \lambda) \rightarrow \mu_s', \tag{2.62}$$

$$D(\vec{r}, t, \lambda) \rightarrow D. \tag{2.63}$$

Note that for inhomogeneous media, the measured μ_a and μ_s' from a homogeneous analysis will be an average of these properties across the measured tissue, weighted by the probability that a photon visits a given region [98; 22]. The diffusion equation (Equation 2.55) can then be simplified to

$$D\,\nabla^2\Phi(\vec{r}, t) - v\,\mu_a\Phi(\vec{r}, t) - \frac{\partial\Phi(\vec{r}, t)}{\partial t} = -v\,S(\vec{r}, t), \tag{2.64}$$

where the constant D has been brought outside of the derivative. A frequency domain (FD) source term provides an important example solution to Equation 2.64. The source term S for a point source emitting a single wavelength can be written as

$$S(\vec{r}, t) = S_o\left(1 + M\,e^{\imath\omega t}\right)\delta(\vec{r} - \vec{r}_s), \tag{2.65}$$

where S_o is the average power emitted by the source $[W]$, M is the modulation depth of the sinuosoid, which can vary from 0 to 1, ω is the angular frequency, such that $f = \omega/(2\pi)$ is the oscillation frequency in Hz, and $\vec{r}_s$ is the position of the point source. Note that in practice, physical quantities will be the real part of any complex representation. A solution for the fluence rate given this FD source term is particularly useful because it can also be applied to both CW

and TD representations. A CW point source is simply the FD source with $\omega = 0$, and a pulsed TD source is the Fourier transform of the modulated FD source [11].

Given this source, the fluence rate Φ can be written as the sum of a continuous wave DC component and an AC component oscillating with angular frequency ω, as follows:

$$\Phi(\vec{r}, t) = \Phi_{DC}(\vec{r}) + \Phi_{AC}(\vec{r}, t) \tag{2.66}$$

$$= \Phi_{DC}(\vec{r}) + U(\vec{r})\, e^{\imath\omega t}. \tag{2.67}$$

If the representation of Φ in Equation 2.67 is substituted into the diffusion equation (Equation 2.64), the time-dependent and time-independent terms can be separated as

$$D\nabla^2\Phi_{DC}(\vec{r}) - v\,\mu_a\Phi_{DC}(\vec{r}) - \frac{\partial\Phi_{DC}(\vec{r})}{\partial t} = -vS_o\delta(\vec{r} - \vec{r}_s), \tag{2.68}$$

$$D\nabla^2\left(U(\vec{r})e^{\imath\omega t}\right) - v\,\mu_a U(\vec{r})e^{\imath\omega t} - \frac{\partial\left(U(\vec{r})e^{\imath\omega t}\right)}{\partial t} = -vS_o\,M\,e^{\imath\omega t}\delta(\vec{r} - \vec{r}_s). \tag{2.69}$$

By taking the time derivatives for both the DC and AC components and dividing through by $e^{\imath\omega t}$ in Equation 2.69, these equations can be simplified to

$$\left(\nabla^2 - k_o^2\right)\Phi_{DC}(\vec{r}) = -\frac{vS_o}{D}\delta(\vec{r}, \vec{r}_s), \tag{2.70}$$

$$\left(\nabla^2 - k^2\right)U(\vec{r}) = -\frac{vS_oM}{D}\delta(\vec{r}, \vec{r}_s), \tag{2.71}$$

where k_o and k are defined as

$$k_o \equiv \sqrt{\frac{v\mu_a}{D}}, \tag{2.72}$$

$$k \equiv \sqrt{\frac{v\mu_a + \imath\omega}{D}}. \tag{2.73}$$

These equations are similar to Helmholtz differential equations [98] and thus have known solutions that take the form of damped, oscillating wave patterns [9]. In diffuse optics, these fluence rate waves are known as diffuse photon density waves (DPDW), and this propagation of the photon energy density demonstrates typical wave propagation characteristics [196; 36; 32; 195].

In order to solve these differential equations for the form of Φ_{DC} or U, boundary conditions that correspond to the geometry of the medium must now be imposed.

2.4.2 Infinite Homogeneous Geometry - Boundary Condition

The simplest geometry to consider is an infinite homogeneous medium with a point source at the origin of the coordinate system. This solution is not particularly practical for tissue applications,

but the solution is an instructive demonstration of the form taken by diffuse photon density waves. Note that for any analysis involving a point source, the solution will, by definition, simply be a convolution of the Green's function solution and the source power term [9], *e.g.* S_oM in Equation 2.71. In practice, the sources used will not be true point sources, and thus a convolution between the mathematical form of a source's spatial extent and the Green's function must also be performed.

In an infinite geometry, the only boundary condition that must be imposed on the diffusion equation in Equation 2.71 is that $\Phi \to 0$ as $\vec{r} \to \infty$. This greatly simplifies the process of determining solutions to the diffusion equation.

2.4.3 Infinite Homogeneous Geometry - Frequency Domain

Given the boundary condition that fluence rate falls to 0 as $\vec{r}$ approaches ∞, the solution to the diffusion equation takes the form of a spherical wave disturbance propagating outwards from the source position [58], such that

$$U(\vec{r}) = \frac{v\, S_o\, M}{4\pi\, D\, |\vec{r}|} e^{-k|\vec{r}|}. \tag{2.74}$$

Given the definition of U, the full form of the AC fluence rate can thus be written as

$$\Phi_{AC}(\vec{r}, t) = \frac{v\, S_o\, M}{4\pi\, D\, |\vec{r}|} e^{-k_r|\vec{r}|}\, e^{\imath(\omega t - k_i|\vec{r}|)}, \tag{2.75}$$

where k_r and k_i are the real and imaginary components, respectively, of k (Equation 2.73). The full solution for the fluence rate will also include a DC component (see Equation 2.66), but the AC component is sufficient for solving for the homogeneous optical properties. This expression for Φ_{AC} can be simplified to

$$\Phi_{AC} = A(\vec{r}) e^{\imath(\omega t - \theta(\vec{r}))}, \tag{2.76}$$

where

$$A(\vec{r}) = \frac{v\, S_o\, M}{4\pi\, D\, |\vec{r}|} e^{-k_r|\vec{r}|}, \tag{2.77}$$

$$\theta(\vec{r}) = k_i|\vec{r}|. \tag{2.78}$$

A schematic and spatial map of A and θ can be found in Figure 2.4. The real and imaginary components of k are dependent on the optical properties of the tissue and can be written as

$$k_r = \left(\frac{v\mu_a}{2D}\right)^{1/2} \left[\left(1 + \left(\frac{\omega}{v\mu_a}\right)^2\right)^{1/2} + 1\right]^{1/2}; \tag{2.79}$$

$$k_i = \left(\frac{v\mu_a}{2D}\right)^{1/2} \left[\left(1 + \left(\frac{\omega}{v\mu_a}\right)^2\right)^{1/2} - 1\right]^{1/2}. \tag{2.80}$$

Thus, if the index of refraction n for tissue is known or assumed via a population average [148], these components of k can be used to solve for the optical properties μ_a and μ_s' [112; 22], which take the form

$$\mu_a = \frac{\omega}{2v}\left(\frac{k_r}{k_i} - \frac{k_i}{k_r}\right); \tag{2.81}$$

$$\mu_s' = \frac{2v}{3\omega} k_r k_i - \mu_a. \tag{2.82}$$

A full derivation of these representations of μ_a and μ_s' can be found in Appendix A.3.

In order to solve for the optical properties of the medium, however, k_r and k_i must be able to be determined uniquely. This is not practically possible for a measurement from only a single source-detector pair because the $S_o\, M$ factor in Equation 2.77, which is determined not only by the true average power and modulation depth of the source, but also factors such as fiber coupling and detector efficiency, cannot be consistently calculated [113]. This limitation can be overcome, though, by acquiring data at multiple source-detector separations. In that scenario, k_i is the slope of the fitted line for θ vs $|\vec{r}|$ and $-k_r$ is the slope of the fitted line for $\ln(A\,|\vec{r}|)$ vs $|\vec{r}|$ (see Equations 2.78 and 2.77). Additionally, measurements using sources with multiple modulation frequencies can be performed in lieu of multiple source-detector separations. This technique, however, does not allow for the simple linear fitting provided by multiple source-detector separations. Instead, a non-linear fitting algorithm must be performed (see Sections 2.6.6 and 3.2.2).

2.4.4 Infinite Homogeneous Geometry - Continuous Wave

The CW solution to the diffusion equation in any geometry is simply a special case of the FD solution with $\omega = 0$. Thus, the fluence rate can be determined, using the DC diffusion equation (Equation 2.70), to be

$$\Phi_{CW}(\vec{r}) = \Phi_{DC}(\vec{r}) = \frac{vS_o}{4\pi D\,|\vec{r}|} e^{-k_o|\vec{r}|}, \tag{2.83}$$

where $k_o = \sqrt{(v\mu_a)/D}$ (Equation 2.72). This Φ_{CW} is insufficient to uniquely determine both μ_a and μ_s' [13; 121], and unlike in the frequency domain case, the non-uniqueness of the optical properties cannot be overcome by performing measurements at multiple source-detector separations. Thus, CW instruments must assume one of the optical properties, usually μ_s', in order to solve for the other, usually μ_a. This technique allows CW instruments to solve for the concentrations of tissue

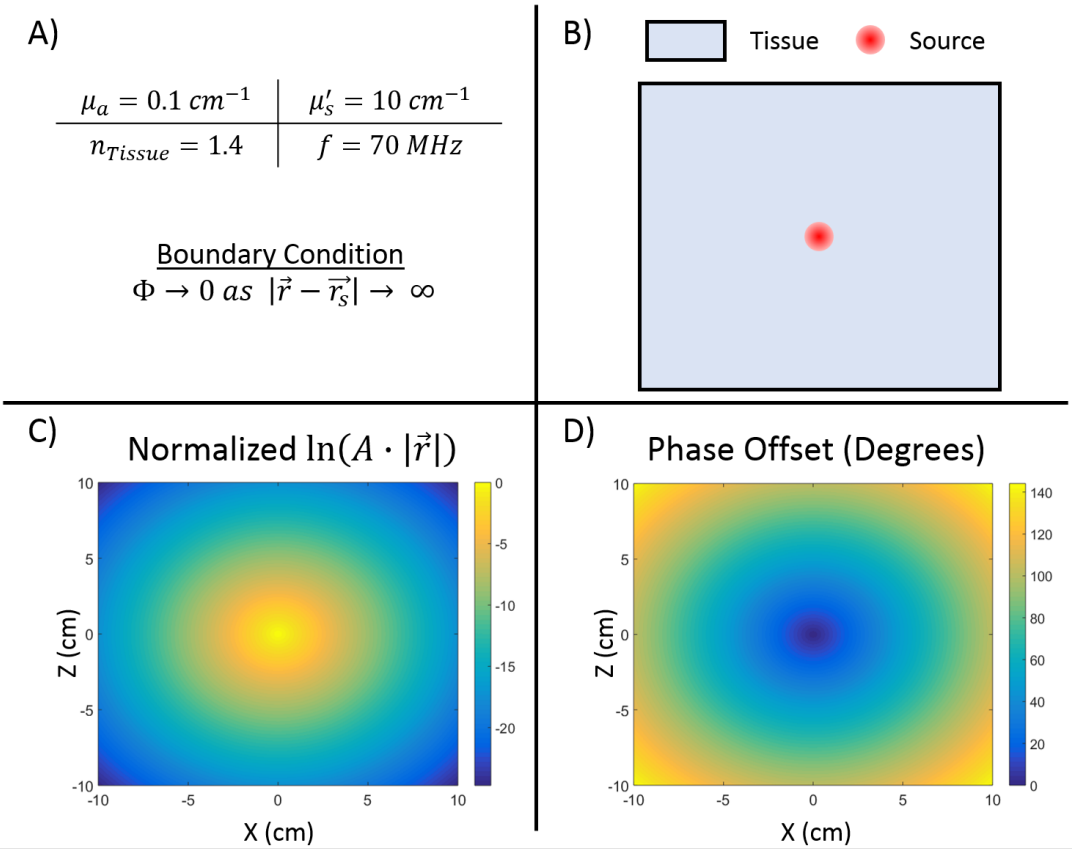

Figure 2.4: Frequency Domain Fluence Rate in the Infinite Homogeneous Geometry. A) Tissue and source properties used for this example, along with the boundary condition necessary to solve the differential equation in the infinite geometry. B) Schematic of an infinite homogeneous medium with a source at the origin of the coordinate system. C) Plot of the normalized natural log of the amplitude of the fluence rate multiplied by the distance from the origin ($\ln[A|\vec{r}|]$) in the $y = 0$ plane of the infinite medium. The slope of the linear fit of this quantity vs $|\vec{r}|$ yields $-k_r$ (see Equation 2.77). D) Plot of the phase offset in degrees of the fluence rate in the $y = 0$ plane of the infinite medium. The slope of the linear fit of this quantity vs $|\vec{r}|$ yields k_i (see Equation 2.78).

chromophores (*e.g.*, oxy- or deoxy-hemoglobin) that contribute to absorption (see Section 2.8), but the use of an assumed μ_s' value introduces significant error to the calculation of μ_a.

2.4.5 Infinite Homogeneous Geometry - Time Domain

Time-domain photon propagation obeys the time-dependent photon diffusion equation (see Equation 2.55) with a source term S of the form

$$S(\vec{r}, t) = S_o \delta(t - t_s)\delta(\vec{r} - \vec{r}_s). \tag{2.84}$$

Here, S is an infinitely short point source light pulse at position $\vec{r}_s$ that occurs at time $t = t_s$. Note that this source term is the Fourier transform of the source term in the AC diffusion equation (Equation 2.71). Therefore, the Green's function solution to the full time domain diffusion equation with this source term is also the Fourier transform of the Green's function solution to the frequency domain diffusion equation (Equation 2.74). As such, the photon fluence rate in the time domain can be written as

$$\Phi(\vec{r}, t) = \frac{vS_o}{(4\pi Dt)^{3/2}} \exp\left[-\frac{r^2}{4Dt} - v\mu_a t\right]. \tag{2.85}$$

The full calculation of the time domain solution using the Fourier transform can be found in Appendix A.4.

For time domain instruments, measurements of the fluence rate are made at many time points, and then this fluence rate data is fit to Equation 2.85 to determine μ_a and μ_s' [202; 258; 52; 190]. The data collected at multiple time points allows for the simultaneous determination of both optical properties using only a single source-detector separation, providing an advantage unavailable to CW or FD instruments. As discussed earlier, the primary disadvantage of TD instruments is the relative cost of the instrumentation necessary to make measurements with sufficient temporal resolution.

In practice, the pulsed laser source, which can reasonably be modeled as a delta function, is not the light directly entering the tissue. The light must usually travel through optical fibers, switches, and other instrumentation, which broadens the previously very narrow pulse. This broadening due to the instrument is referred to as the Instrument Response Function (IRF). The true light source that enters the tissue is actually a convolution of the initial pulse and the IRF. Thus, the measured fluence rate must be fit to a convolution of the IRF and the time domain Green's function. This will be discussed further in Section 6.3.2.

2.5 Solutions in Homogeneous Bounded Geometries

In almost all practical applications, an infinite geometry is not an accurate model for the tissue being measured. Instead, there is usually an interface between the diffusive tissue and a non-diffusive medium, *e.g.*, air. The two most common geometries used in diffuse optics are:

1. Semi-Infinite - A geometry that contains both a diffusive and non-diffusive region divided by an infinite planar interface.

2. Infinite Slab - A geometry that contains a diffusive region of a fixed depth that extends to infinity in both planar dimensions with non-diffusive regions bounding both the "shallow" and "deep" interfaces of the diffusive region.

In these geometries, sources and detectors are typically placed on one or, in the case of transmission slab measurements, both of the interfaces. Thus, fitting the measured fluence rate at the detectors requires a solution to the diffusion equation that is accurate near the tissue boundaries, which, in turn, requires the application of appropriate boundary conditions.

2.5.1 Partial Flux Boundary Condition

The inward flux of light J_{in} at time t and a position $\vec{r}_i$ on the tissue interface can be defined as

$$J_{in}(\vec{r}_i, t) \equiv \vec{J}(\vec{r}_i, t) \cdot \hat{z} \tag{2.86}$$

$$= \int_{\hat{\Omega}\cdot\hat{z}>0} L(\vec{r}_i, \hat{\Omega}, t)\hat{\Omega}\, d\Omega \cdot \hat{z}. \tag{2.87}$$

Here $\hat{z}$ is the direction opposite the normal of the tissue surface (see Figure 2.5), and Equation 2.87 is simply the definition of $\vec{J}$ in terms of the radiance L from Equation 2.16, except here, the $\left(L\,\hat{\Omega}\right)$ term is only integrated over the solid angle hemisphere pointing into the tissue. Using the P_1 approximation for the radiance L, and noting that $\hat{\Omega}\cdot\hat{z} = \cos\theta$, allows this equation to be rewritten as

$$J_{in}(\vec{r}_i, t) = \int_{\theta=0}^{\pi/2}\int_{\varphi=0}^{2\pi} \cos\theta\sin\theta \left[\frac{1}{4\pi}\Phi(\vec{r}_i, t) + \frac{3}{4\pi}\left(J_x(\vec{r}_i, t)\sin\theta\cos\varphi + J_y(\vec{r}_i, t)\sin\theta\sin\varphi + J_z(\vec{r}_i, t)\cos\theta\right)\right] d\varphi\, d\theta. \tag{2.88}$$

Here, the Cartesian coordinate definition of $\hat{\Omega}$ (A.11) was used to separate $\vec{J}$ into Cartesian components. The J_x and J_y terms go to 0 when the integration over φ is performed, leaving

$$J_{in}(\vec{r}_i, t) = \int_{\theta=0}^{\pi/2} \frac{1}{2}\Phi(\vec{r}_i, t)\cos\theta\sin\theta + \frac{3}{2}J_z(\vec{r}_i, t)\cos^2\theta\sin\theta\, d\theta \tag{2.89}$$

$$= \frac{1}{4}\Phi(\vec{r}_i, t) + \frac{1}{2}J_z(\vec{r}_i, t). \tag{2.90}$$

For diffusive media, this inward flux J_{in} is due almost exclusively to back reflections of light traveling from within the tissue. This state is caused by two conditions

1. Under the conditions necessary for the application of the diffusion equation, sources on the interface of the tissue can be modeled as isotropic point light sources approximately one transport length l_{tr} from the interface [113] because of the randomization of propagation direction caused by multiple scattering (see Section 2.2.8). Thus, all light sources are inside the tissue in this model.

2. Light that leaves the tissue is rarely reflected back into the tissue because the outside medium generally has very low scattering.

Therefore, the inward photon flux J_{in} can also be written as

$$J_{in}(\vec{r}_i, t) = \int_{\hat{\Omega}\cdot\hat{z}<0} R_F(\hat{\Omega}) L(\vec{r}_i, \hat{\Omega}, t) \hat{\Omega}\, d\Omega \cdot (-\hat{z}), \tag{2.91}$$

where $R_F(\theta)$ is the Fresnel reflection coefficient for unpolarized light incident at an angle θ from $\hat{z}$ [135; 22]. Note that because the semi-infinite and infinite slab geometries are symmetric about $\hat{z}$, the Fresnel reflection coefficient is not dependent on φ. Here, J_{in} is dependent on the dot product between the integral and $-\hat{z}$, rather than $\hat{z}$, because the projection of the incident radiance L onto the normal axis is parallel to $-\hat{z}$ direction. The simplest way to perform this integral is to define

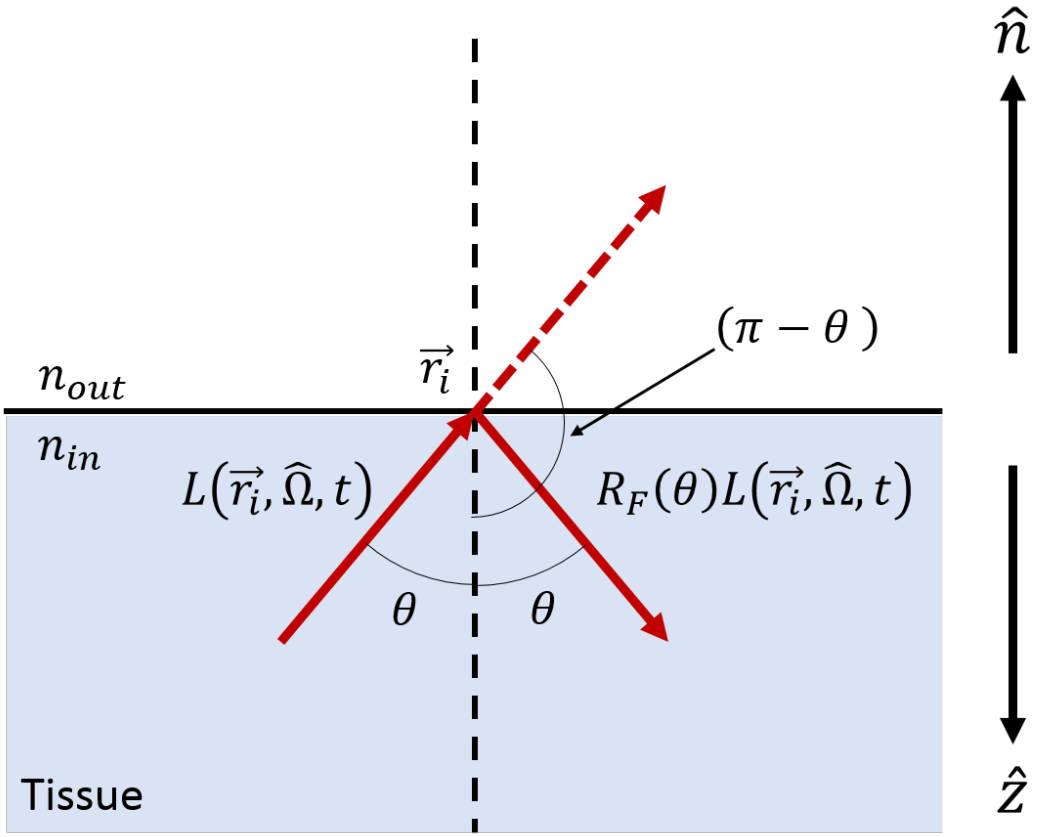

Figure 2.5: Geometry of Reflected Radiance for Partial Flux Boundary Condition. When all light sources are inside a diffusive medium, the inward photon flux will be due entirely to light reflected back into the tissue by the tissue interface. Here, the light radiance L incident on the interface from the tissue side is traveling in direction $\hat{\Omega}$ which has a polar angle $(\pi - \theta)$. The light reflected back into the tissue is L multiplied by the Fresnel reflection coefficient R_F, which is dependent on the angle θ and the indices of refraction outside and inside the tissue.

θ to be the angle between $\hat{z}$ and the incident light and integrate over the hemisphere where θ goes from 0 to 2π. With this convention, the polar angle of $\hat{\Omega}$ is $(\pi - \theta)$ (see Figure 2.5). The,n using

the P_1 approximation and performing the integration over φ, the integral can be expressed as

$$J_{in}(\vec{r}_i,t) = -\int_{\theta=0}^{\pi/2} R_F(\theta)\cos(\pi-\theta)\sin(\pi-\theta)\left[\frac{1}{2}\Phi(\vec{r}_i,t) + \frac{3}{2}J_z(\vec{r}_i,t)\cos(\pi-\theta)\right] d\theta. \quad (2.92)$$

The integral can be further simplified using the trigonometric identities for cosine and sine of $(\pi-\theta)$ [5], such that

$$J_{in}(\vec{r}_i,t) = \frac{1}{4}\Phi(\vec{r}_i,t)R_\Phi - \frac{1}{2}J_z(\vec{r}_i,t)R_J, \quad (2.93)$$

where

$$R_\Phi = 2\int_{\theta=0}^{\pi/2} R_F(\theta)\cos\theta\sin\theta\, d\theta, \quad (2.94)$$

$$R_J = 3\int_{\theta=0}^{\pi/2} R_F(\theta)\cos^2\theta\sin\theta\, d\theta. \quad (2.95)$$

Equations 2.90 and 2.93 provide two representations of J_{in} which can be set equal to each other and rearranged to solve for Φ, such that

$$\Phi(\vec{r}_i,t) = -2J_z(\vec{r}_i,t)\left[\frac{1+R_J}{1-R_\Phi}\right]. \quad (2.96)$$

For simplicity, a new term R_{eff} is often defined as

$$R_{eff} \equiv \frac{R_\Phi + R_J}{2 - R_\Phi + R_J}. \quad (2.97)$$

R_{eff} can be calculated either by numerically integrating the expressions in Equations 2.94 and 2.95 or using the common approximation [128]

$$R_{eff} \approx -1.440\left(\frac{n_{in}}{n_{out}}\right)^{-2} + 0.701\left(\frac{n_{in}}{n_{out}}\right)^{-1} + 0.668 + 0.0636\left(\frac{n_{in}}{n_{out}}\right), \quad (2.98)$$

where n_{in} and n_{out} are the indices of refraction inside and outside the medium, respectively.

This allows the boundary fluence rate relationship (Equation 2.96) to be written as

$$\Phi(\vec{r}_i,t) = -2J_z(\vec{r}_i,t)\left[\frac{1+R_{eff}}{1-R_{eff}}\right]. \quad (2.99)$$

Finally, the $\hat{z}$-component of the Fick's Law diffusion relationship (Equation 2.51) and the definition of the diffusion coefficient D (Equation 2.52) are employed to rewrite Equation 2.99 entirely in terms of Φ, where

$$\Phi(\vec{r}_i,t) = z_b\frac{\partial\Phi(\vec{r}_i,t)}{\partial z}. \quad (2.100)$$

Here, z_b is defined as

$$z_b \equiv \frac{2}{3} l_{tr} \frac{1 + R_{eff}}{1 - R_{eff}}, \tag{2.101}$$

where l_{tr} is the transport length (Equation 2.53). This relationship is the partial flux boundary condition, in which the fluence rate at the interface is directly proportional to the spatial derivative along the dimension normal to that interface. This is an exact boundary condition for these geometries, given the assumption of no photon flux into the tissue from outside. However, this boundary condition can be practically difficult to use for determining analytical solutions to the diffusion equation. Therefore, it is convenient to employ the extrapolated-zero boundary condition, an approximation of the partial flux boundary condition.

2.5.2 Extrapolated-Zero Boundary Condition

The extrapolated-zero boundary condition, which has been demonstrated to be accurate in tissue [135], can be derived by approximating the fluence rate Φ near the tissue interface with a first-order Taylor series expansion along the $\hat{z}$-axis. The fluence rate can thus be expressed as [39]

$$\Phi(z) = \Phi(z = 0) + \frac{\partial \Phi(z)}{\partial z} z. \tag{2.102}$$

The partial flux boundary condition provides an expression for $\partial\Phi/\partial z$ in terms of Φ on the interface, which can be substituted into the Taylor expansion to create the relation

$$\Phi(z) = \Phi(z = 0) \left[1 + \frac{z}{z_b}\right], \tag{2.103}$$

where z_b is defined as in Equation 2.101. From this relation, it is apparent that Φ will equal 0 when $z = -z_b$, or mathematically,

$$\Phi(z = -z_b) = 0. \tag{2.104}$$

Therefore, under the extrapolated-zero boundary condition, there is a point outside the tissue region at which the fluence rate falls to 0, and the distance of this point from the interface is dependent on the characteristic transport length l_{tr} of the tissue and the indices of refraction on both sides of the interface, via the Fresnel reflection coefficients. A graphical schematic of this boundary condition can be found in Figure 2.6.

2.5.3 Semi-Infinite Homogeneous Solution - Partial-Flux Boundary Condition

Solving for the Green's function solution to the diffusion equation in the semi-infinite geometry requires the use of the method of images [49; 202; 113]. The Green's function solution will be a

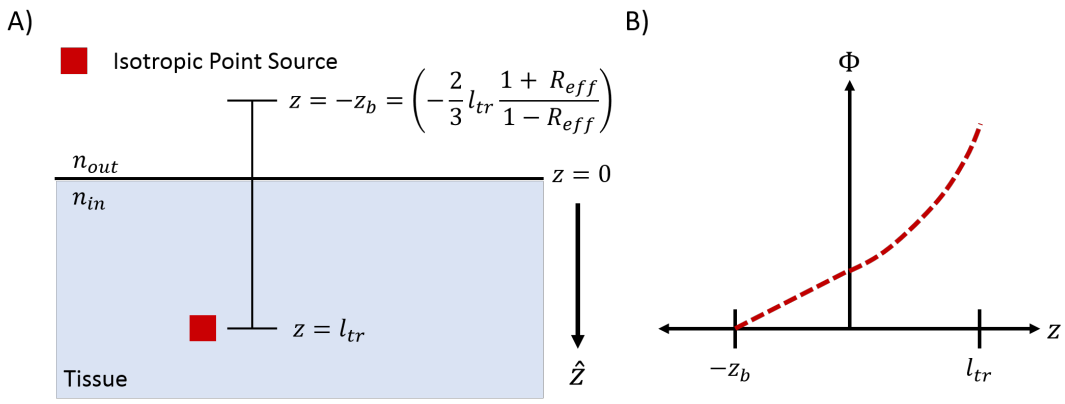

Figure 2.6: Fluence Rate near Tissue Interface - Extrapolated-Zero Boundary Condition. A) Schematic of the Tissue Interface. In a diffusive medium, a source on the boundary is well-modeled by an isotropic point source at a distance of l_{tr} into the tissue. Under the extrapolated-zero boundary condition, a point that is a distance of z_b outside the tissue is set to have a fluence rate of 0. This quantity z_b is determined by both l_{tr} of the diffusive medium and R_{eff}, which is dependent on the indices of refraction n inside and outside the tissue via the Fresnel reflection coefficient. B) Plot of Fluence Rate versus Depth. Given the Taylor expansion used for the extrapolated-zero boundary condition, the fluence rate outside the tissue decreases linearly with a slope of $\partial\Phi(z = 0)/\partial z$ until the fluence rate goes to 0 at $z = -z_b$.

superposition of infinite geometry Green's function solutions arising from the real light source and a number of image sources that satisfy a given boundary condition.

First, semi-infinite and slab geometries are both conveniently described using the cylindrical coordinate system, whereby z is the depth, ρ is the radial distance from the origin along the interface, and φ is the azimuthal angle. In practice, φ will not usually be important due to the symmetry of these geometries about the longitudinal ($\hat{z}$) axis. Therefore, given Equation 2.74, the frequency domain, infinite homogeneous medium Green's function G_o^I for a light source at position $(\rho = 0, z = l_{tr})$ expressed in cylindrical coordinates is

$$G_o^I(\rho, z) = \frac{v}{4\pi D r_1} \exp\left[-k r_1\right], \tag{2.105}$$

where r_1 is defined as

$$r_1 = \sqrt{(z - l_{tr})^2 + \rho^2}. \tag{2.106}$$

Using the method of images, the generic Green's function solution G_o^B for a bounded medium will be

$$G_o^B = G_o^I(\rho, z) + G_o^C(\rho, z), \tag{2.107}$$

where G_o^C is a correction term to find the full bounded Green's function G_o^B. For a semi-infinite medium constrained by the partial-flux boundary condition, G_o^C can be written as

$$G_o^C = \frac{v}{4\pi D r_2} \exp\left[-k r_2\right] - \frac{2}{z_b} \int_0^\infty \frac{v}{4\pi D \sqrt{(z + l_{tr} + u)^2 + \rho^2}} \exp\left[-k\sqrt{(z + l_{tr} + u)^2 + \rho^2} - \frac{u}{z_b}\right] du, \quad (2.108)$$

where

$$r_2 = \sqrt{(z + l_{tr})^2 + \rho^2}, \quad (2.109)$$

and u is the result of an integral substitution. This correction term is derived by enforcing the partial-flux boundary condition on G_o^B and using an image source at position $z = -l_{tr}$. The full derivation [22] can be found in Appendix A.5. The first term in G_o^C can be thought of as an image source at position $z = -l_{tr}$, and the integral can be thought of as continuous line distribution of image sinks, *i.e.*, negative sources, spanning the distance from $z = -l_{tr}$ to $z = -\infty$. The amplitude of these image sinks falls to 0 as z goes to $-\infty$ due to the e^{-u/z_b} term. A schematic can be found in Figure 2.7. The sum of $G_o^I + G_o^C$ will clearly be a solution to the diffusion equation because it satisfies the partial-flux boundary condition (see Appendix A.5) and because each of the individual terms is a solution to the diffusion equation. Therefore, by the superposition principle, their sum is a solution as well [103]. Although this is an exact Green's function solution for the semi-infinite medium obeying the partial-flux boundary condition, it can be cumbersome to use in practice due to the infinite line of image sinks. This challenge can be overcome by using the extrapolated-zero boundary condition.

2.5.4 Semi-Infinite Homogeneous Solution - Extrapolated Zero Boundary Condition

The extrapolated-zero boundary condition states that there is a plane at $z = -z_b$ where the photon fluence rate is 0. Thus the correction term G_o^C is simply the infinite homogeneous Green's function for an image sink at $z = -(2z_b + l_{tr})$ with identical amplitude to the isotropic point source at $z = l_{tr}$ (see Figure 2.8), and the full Green's function takes the form

$$G_o^{SI}(\rho, z) = \frac{v}{4\pi D}\left[\frac{e^{-k r_1}}{r_1} - \frac{e^{-k r_b}}{r_b}\right], \quad (2.110)$$

where

$$r_1 = \sqrt{(z - l_{tr})^2 + \rho^2}, \quad (2.111)$$

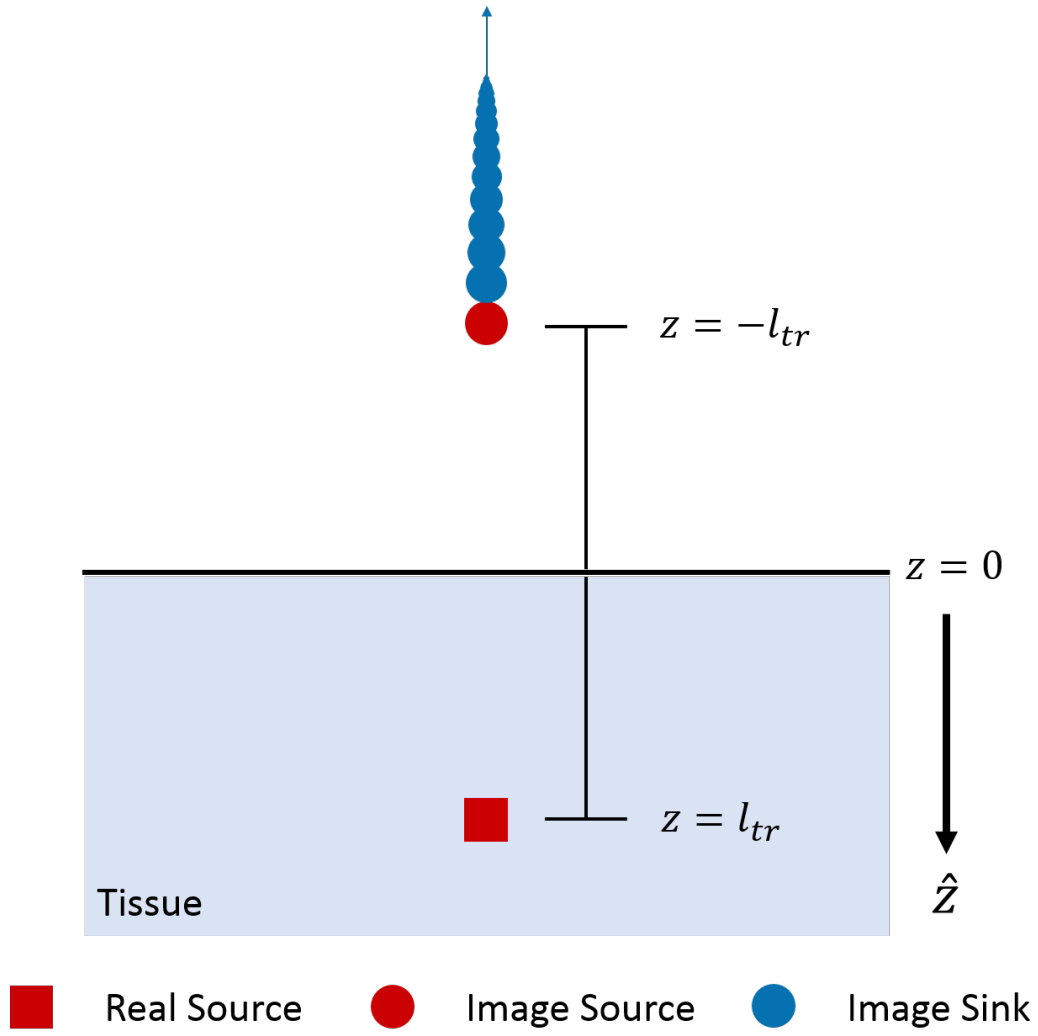

Figure 2.7: Semi-Infinite Geometry and Partial-Flux Boundary Condition. A Green's function solution to the diffusion equation for a semi-infinite homogeneous geometry can be determined using the partial-flux boundary condition and the method of images. The full Green's function is a superposition of infinite homogeneous Green's functions for 1) a real source at position $z = l_{tr}$, 2) an image source at position $z = -l_{tr}$, and 3) an infinite series of image sinks ranging from $z = -l_{tr}$ to $z = -\infty$, with amplitudes falling to 0 as z approaches $-\infty$. This produces an exact, but difficult to use, Green's function solution for the semi-infinite homogeneous geometry.

$$r_b = \sqrt{(z + 2z_b + l_{tr})^2 + \rho^2}. \tag{2.112}$$

The two infinite homogeneous Green's function both individually satisfy the diffusion equation, and the fact that they are mirror images about the $z = -z_b$ plane satisfies the extrapolated-zero boundary condition. This solution is much easier to use in practice than the partial-flux boundary solution because it contains only two terms and does not require the integration of an infinite image

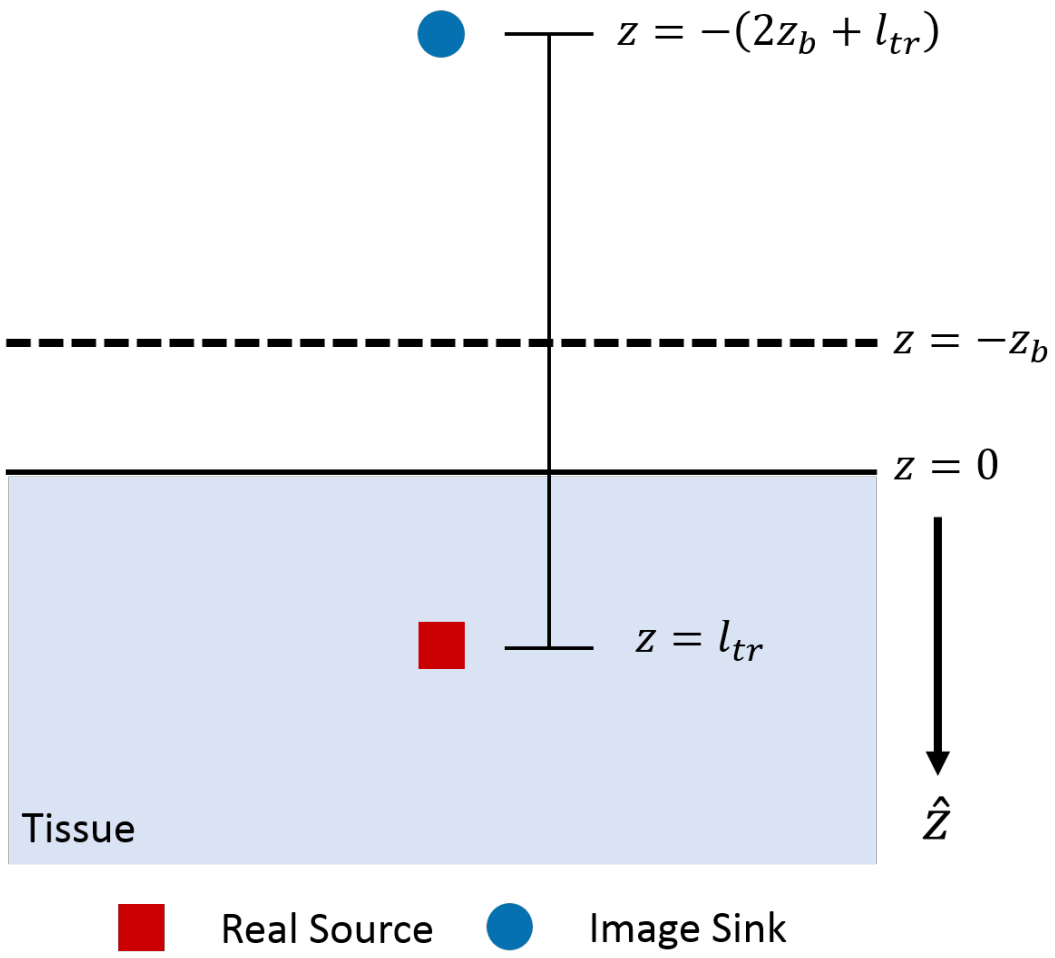

Figure 2.8: Semi-Infinite Geometry and Extrapolated-Zero Boundary Condition. A Green's function solution to the diffusion equation for the semi-infinite homogeneous geometry can be determined using the extrapolated-zero boundary condition and the method of images. This Green's function is a superposition of the infinite homogeneous Green's functions for 1) a real source at position $z = l_{tr}$ and 2) an image source at position $z = -(2z_b + l_{tr})$. Though an approximation, the solution produced by the extrapolated-zero boundary condition is typically very accurate [135] and much easier to use than the partial-flux boundary condition solution.

sink.

2.5.5 Infinite Slab Homogeneous Solution - Method of Images

The infinite slab geometry is a commonly used geometry for diffuse optical imaging of breast cancer using parallel source and detector plates [81; 278; 25; 8]. In this geometry, the tissue has a finite thickness d along the $\hat{z}$ dimension but is infinite in the $\hat{x}$ and $\hat{y}$ directions. Like the semi-infinite

geometry, the infinite slab also obeys the extrapolated-zero boundary condition; however, there are now two tissue interfaces, and thus, there is an extrapolated-zero plane on each side of the tissue (see Figure 2.9).

These two extrapolated-zero boundary conditions necessitate an infinite series of image sources and sinks, resulting in a Green's function solution of the form

$$G_o^{Slab}(\rho, z) = \frac{v}{4\pi D} \sum_{m=-\infty}^{\infty} \left[\frac{e^{-kr_{+,m}}}{r_{+,m}} - \frac{e^{-kr_{-,m}}}{r_{-,m}} \right], \tag{2.113}$$

where

$$r_{\pm,m} \equiv \sqrt{(z - z_{\pm,m})^2 + \rho^2}, \tag{2.114}$$

and the image source positions $z_{+,m}$ and image sink positions $z_{-,m}$ can be defined as

$$z_{+,m} \equiv 2m(d + 2z_b) + l_{tr}, \tag{2.115}$$

$$z_{-,m} \equiv 2m(d + 2z_b) - 2z_b - l_{tr}. \tag{2.116}$$

Here, d is the thickness of the slab along the $\hat{z}$ dimension. Although the exact Green's function under the given boundary conditions is an infinite series, the amplitudes of the series terms in the region of interest, *i.e.*, the tissue, decrease as $|m|$ increases because the image sources and sinks are placed increasingly farther from the tissue. For example, the amplitude of the fluence rate due to the nearest $|m| = 5$ image is approximately four orders of magnitude smaller than the real source amplitude. Thus, the infinite series can be truncated after relatively few terms, providing a tractable solution to the diffusion equation.

2.5.6 Time Domain Solutions - Semi-Infinite and Infinite Slab

As with the infinite homogeneous solution, the time-domain Green's functions for the semi-infinite and infinite slab will be Fourier transforms of the frequency-domain Green's functions. These can be calculated using the method used in Appendix A.4 to derive the time-domain Green's function for the infinite homogeneous geometry. The resulting time-domain Green's functions for a point source at position $(\rho = 0, z = l_{tr})$ and time t_s are

$$g_o^{SI}(\rho, z, t) = \frac{v \exp\left(-v\mu_a(t - t_s)\right)}{(4\pi D(t - t_s))^{3/2}} \left[\exp\left(\frac{r_1^2}{4D(t - t_s)} \right) - \exp\left(\frac{r_b^2}{4D(t - t_s)} \right) \right], \tag{2.117}$$

$$g_o^{Slab}(\rho, z, t) = \frac{v \exp\left(-v\mu_a(t - t_s)\right)}{(4\pi D(t - t_s))^{3/2}} \sum_{m=-\infty}^{\infty} \left[\exp\left(\frac{r_{+,m}^2}{4D(t - t_s)} \right) - \exp\left(\frac{r_{-,m}^2}{4D(t - t_s)} \right) \right], \tag{2.118}$$

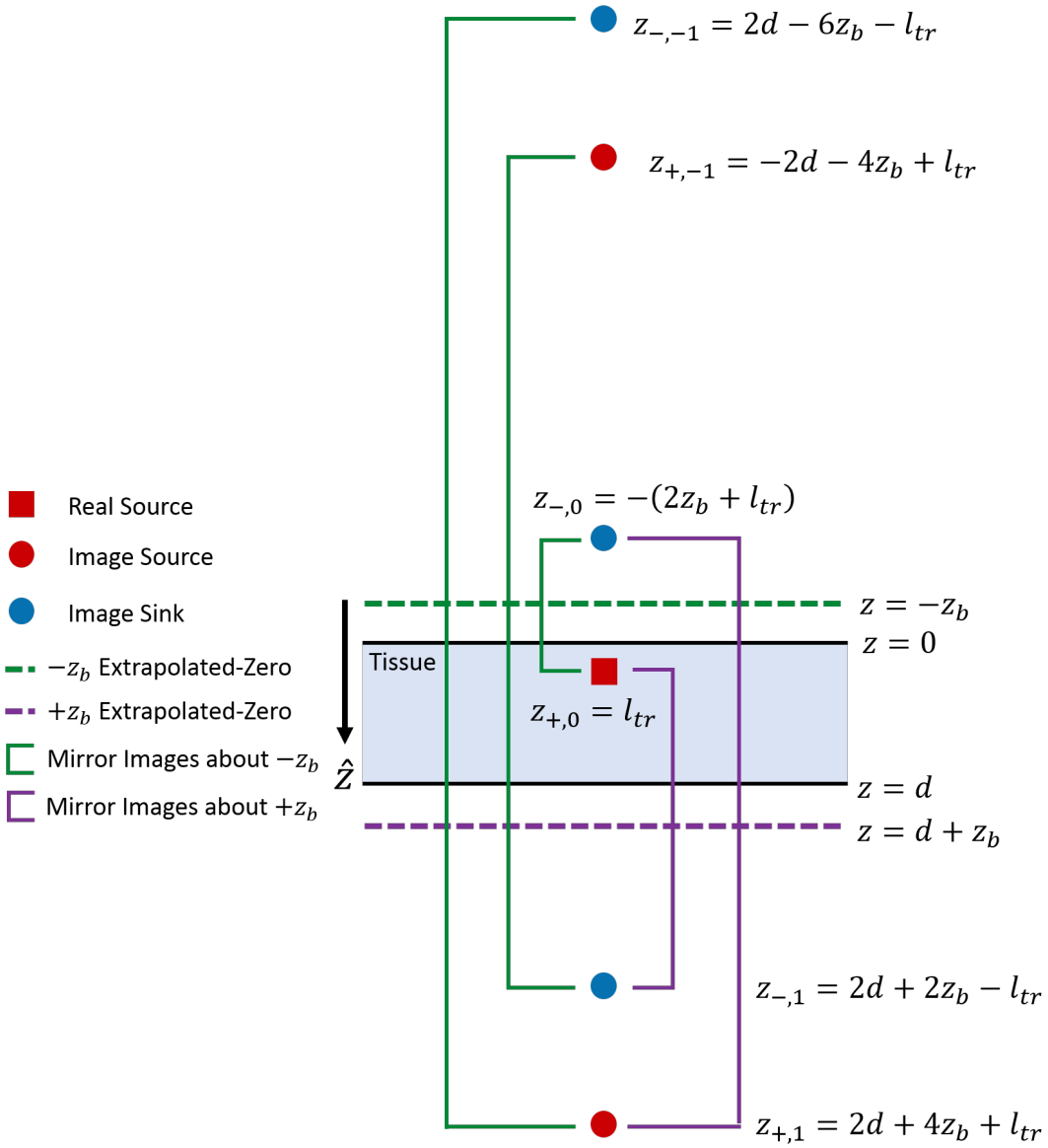

Figure 2.9: Infinite Slab Geometry and Extrapolated-Zero Boundary Condition. A Green's function solution to the diffusion equation for the homogeneous infinite slab geometry can be determined using the extrapolated-zero boundary condition and the method of images. Unlike the semi-infinite geometry, the infinite slab has two tissue interfaces, and therefore requires the extrapolated-zero boundary condition to be applied on both sides of the tissue. The full Green's function solution is a superposition of the infinite homogeneous Green's functions for 1) a real source at position $z = l_{tr}$ and 2) an infinite series of image sources at positions $z = 2m(d + 2z_b) + l_{tr}$ and image sinks at positions $z = 2m(d + 2z_b) - 2z_b - l_{tr}$ where m goes from $-\infty$ to ∞. Note that the $m = 0$ "image" source is actually the real isotropic point source. These image sources and sinks form a recursive series wherein each set of sources and sinks complement previous sinks and sources to force the fluence rate to zero at one of the two extrapolated-zero planes.

where r_1, r_b, and $r_{\pm,m}$ are defined as in the frequency-domain Green's functions. As with the infinite homogeneous medium, to fit the measured fluence rate, convolutions between these Green's functions and both the source profile term and instrument response function must be performed.

2.5.7 Solving for Optical Properties in Bounded Geometries

The Green's function solutions for semi-infinite and infinite slab geometries in Sections 2.5.4 and 2.5.5 enable the calculation of photon fluence rate in the tissue for a given source and homogeneous optical property distribution.

A convolution of the Green's function solution with the spatial source profile of the light source, or, in the case of time-domain measurements, the spatial and temporal light source profiles, provides solutions to the fluence rate diffusion equation. Therefore, the amplitude term of the frequency domain fluence rate U can be expressed as

$$U(\vec{r}) = \int G(\vec{r}', \vec{r}_s) S(\vec{r} + \vec{r}_s - \vec{r}')\, d^3 r', \tag{2.119}$$

where $\vec{r}_s$ is the source position and for an oscillating source,

$$S_{AC}(\vec{r}, t) = S(\vec{r}) e^{\imath \omega t}. \tag{2.120}$$

In the time-domain, the fluence rate can be expressed as

$$\Phi(\vec{r}, t) = \int g(\vec{r}', \vec{r}_s, t', t_s) S(\vec{r} + \vec{r}_s - \vec{r}', t + t_s - t')\, d^3 r'\, dt'. \tag{2.121}$$

where $S(\vec{r}, t)$ is the full source term.

For point sources, these convolutions would simply be the Green's function multiplied by the constant amplitude S_o of the source. For sources that have a spatial extent, or temporal broadening in the time-domain, the full convolution must be performed.

Equations 2.119 and 2.121 now provide the calculated fluence rate at any point in the tissue, including on the boundary. In diffuse optics applications, detectors are typically placed on a tissue interface, and thus, these calculated fluence rates at these interfaces enable an optimization problem which compares calculated and measured light intensities and optimizes for the absorption coefficient μ_a and reduced scattering coefficient μ_s'. However, it is still necessary to convert the fluence rate to the quantity that is actually measured by detectors. For a fiber-coupled detector with the fiber optic placed on the tissue surface, the detected intensity I is an integral of the radiance L over the detection area and the solid angle range over which light can enter the fiber. Given the P_1 approximation, the radiance can easily be expressed in terms of the fluence rate (Equation 2.30). The actual intensity detected by the fiber is not only dependent on the fluence rate, though,

but also on quality of contact between the fiber and tissue, the width, numerical aperture, and transmission coefficient of the fiber, and the sensitivity of the detector [135; 72; 22]. The detected intensity can thus be expressed as

$$I(\vec{r},t) = C(\vec{r},t)\Phi(\vec{r},t), \tag{2.122}$$

where $C(\vec{r},t)$ is the coupling coefficient at time t for a detector at position $\vec{r}$. Though C could be calculated theoretically for a given tissue and optical fiber, in practice, C is dependent on many factors that are difficult to measure or predict, making calculation impractical. C must thus be treated as an unknown that needs to be fit or normalized away via phantom or other reference measurements (see Section 7.2.4 for one such strategy).

Once these coupling coefficients are accounted for, an optimization routine can now be performed which compares the calculated intensity from the Green's function solution, due to a source and guessed optical properties, to the actual measured intensity. The guessed optical properties are then updated, and a new predicted intensity is calculated. This algorithm is then performed repeatedly until a sufficiently good fit is obtained. The optical properties that provide this fit are then predicted to be the optical properties of the tissue. In practice, for the instruments and studies in this thesis, this fitting algorithm is performed either by the MATLAB function *fminsearchbnd* [3] or via a non-linear iterative solver called TOAST [227], which enables three-dimensional imaging of heterogeneous media and will be discussed in more detail in Section 2.6.

2.6 Diffuse Optical Tomography for Heterogeneous Media

2.6.1 Perturbation from the Homogeneous Medium

Solutions to the diffusion equation for homogeneous media are useful for many scenarios in diffuse optics where average tissue optical properties are sufficient, including in the brain [65; 45], muscle [64; 256], and breast [30]. However, to perform three-dimensional imaging of the optical properties, known as Diffuse Optical Tomography (DOT), the diffusion equation needs to be solved for heterogeneous media, and thus, the optical properties need to be calculated at many positions in the tissue. Even for instruments that use many source and detector positions, this three-dimensional imaging creates under-determined systems of equations, which can be difficult or impossible to solve analytically. However, for geometries that have analytical solutions to the diffusion equation in homogeneous media, these heterogeneous media solutions can be found via a perturbative method, wherein the optical properties are assumed to have a small spatially-dependent perturbation from

the homogeneous properties, such that

$$\mu_a(\vec{r}) = \mu_a^o + \delta\mu_a(\vec{r}), \tag{2.123}$$

$$D(\vec{r}) = D^o + \delta D(\vec{r}). \tag{2.124}$$

Here, μ_a^o and D^o are the homogeneous absorption and diffusion coefficients, and $\delta\mu_a$ and δD are the spatially-varying perturbations in the absorption and diffusion coefficients. Note that these are generally small perturbations, such that $\delta\mu_a \ll \mu_a^o$ and $\delta D \ll D^o$. Under these conditions, the fluence rate solution in the heterogeneous medium can be expressed as a perturbation from the solution in the homogeneous medium. The two most common representations of this perturbation in the solution are the Born method and the Rytov method. With the Born method, the AC part of the fluence rate solution U is written as

$$U(\vec{r}) = U_o(\vec{r}) + U_{sc}(\vec{r}), \tag{2.125}$$

where U_o is the solution in the homogeneous medium, and U_{sc} is the perturbation, or scattering term, due to the optical property perturbation.

The Rytov method expresses the heterogeneous solution U as

$$U(\vec{r}) = U_o\, U_{sc} \tag{2.126}$$

$$= e^{\phi_o}\, e^{\phi_{sc}} = e^{\phi_o + \phi_{sc}}. \tag{2.127}$$

Here, again, U_o is the homogeneous medium solution, and U_{sc} represents the perturbation to U_o while ϕ_o and ϕ_{sc} are the exponential representations of the homogeneous and perturbation terms, respectively. Using the Rytov approximation, the frequency domain diffusion equation for the heterogeneous medium at a single wavelength can be written as

$$\nabla \cdot \left[\left(D^o + \delta D(\vec{r})\right) \nabla \left(U_o U_{sc}(\vec{r})\right)\right] - \left[v\left(\mu_a^o + \delta\mu_a(\vec{r})\right) + \imath\omega\right]\left(U_o U_{sc}(\vec{r})\right) = -v S_o M \delta(\vec{r}, \vec{r}_s). \tag{2.128}$$

This equation has been solved for the ϕ_{sc} term [225; 10; 15; 197; 195] using the homogeneous medium diffusion equation, Green's Theorem [9], and several approximations relating to the assumption of a small perturbation. The full derivation can be found in Appendix A.6, and the discretization of the medium into a series of volume elements, known as voxels, results in a matrix equation of the

form

$$\begin{bmatrix} \phi_{sc}(\vec{r}_{s_1}, \vec{r}_{d_1}) \\ \phi_{sc}(\vec{r}_{s_2}, \vec{r}_{d_2}) \\ \vdots \\ \vdots \\ \vdots \\ \phi_{sc}(\vec{r}_{s_M}, \vec{r}_{d_M}) \end{bmatrix} = \begin{bmatrix} W^A_{1,1} & \dots & W^A_{1,N} & W^S_{1,1} & \dots & W^S_{1,N} \\ W^A_{2,1} & \dots & W^A_{2,N} & W^S_{2,1} & \dots & W^S_{2,N} \\ \vdots & & \vdots & \vdots & & \vdots \\ \vdots & & \vdots & \vdots & & \vdots \\ \vdots & & \vdots & \vdots & & \vdots \\ W^A_{M,1} & \dots & W^A_{M,N} & W^S_{M,1} & \dots & W^S_{M,N} \end{bmatrix} \begin{bmatrix} \delta\mu_a(\vec{r}_{n_1}) \\ \vdots \\ \delta\mu_a(\vec{r}_{n_N}) \\ \delta D(\vec{r}_{n_1}) \\ \vdots \\ \delta D(\vec{r}_{n_N}) \end{bmatrix}. \tag{2.129}$$

Here, $\vec{r}_{s_i}$ is the position of the source in the i^{th} source-detector pair, $\vec{r}_{d_i}$ is the position of the detector in the i^{th} source-detector pair, M is the total number of source-detector pairs, $\vec{r}_{n_j}$ is the position of the j^{th} voxel, and N is the total number of voxels. Note that the maximum value of M is the number of source positions N_s multiplied by the number of detector positions N_d; however, in practice, some possible combinations of source and detector positions will not be used due to insufficient signal or signal-to-noise ratio. $W^A_{i,j}$ and $W^S_{i,j}$ are the absorption and scattering weight factors, respectively, and are defined as

$$W^A_{i,j} \equiv \frac{U_o(\vec{r}_{n_j}, \vec{r}_{s_i}) G_o(\vec{r}_{d_i} - \vec{r}_{n_j}) v\, \Delta V}{D^o U_o(\vec{r}_{s_i}, \vec{r}_{d_i})}, \tag{2.130}$$

$$W^S_{i,j} \equiv \frac{\left(\nabla U_o(\vec{r}_{n_j}, \vec{r}_{s_i})\right) \left(\nabla G_o(\vec{r}_{d_i} - \vec{r}_{n_j})\right) v\, \Delta V}{D^o U_o(\vec{r}_{s_i}, \vec{r}_{d_i})}. \tag{2.131}$$

Here, G_o is the homogeneous medium Green's function for a given geometry, and ΔV is the volume of a single voxel. For simplicity, Equation 2.129 can be written as

$$\vec{\phi} = \mathbf{W}\vec{\mu}, \tag{2.132}$$

where $\vec{\phi}$ is the ϕ_{sc} vector, $\vec{\mu}$ is the optical property perturbation vector, and $\mathbf{W}$ is the weight matrix.

This matrix equation can be solved for the heterogeneous optical property vector using the heterogeneous fluence rate measurements and the weight matrix $\mathbf{W}$ (see Section 2.6.2). In the frequency domain, the heterogeneous part of the fluence rate ϕ_{sc} can easily be written in terms of the amplitude A and phase θ of the AC fluence rate U. If a measurement of a homogeneous medium similar to the heterogeneous measurement is made, either via a phantom normalization or a difference reconstruction, the data set will contain both the measured homogeneous fluence rate U_o and the measured heterogeneous fluence rate U. These quantities can be further decomposed into the homogeneous amplitude A_o and phase θ_o and the heterogeneous amplitude A and phase θ.

First, note that

$$\ln\left(\frac{U}{U_o}\right) = \ln\left(\frac{e^{\phi_o}e^{\phi_{sc}}}{e^{\phi_o}}\right) \tag{2.133}$$

$$= \phi_{sc}. \tag{2.134}$$

Then, given the definition of the AC fluence rate in Equation 2.76, the following relationship also holds

$$\ln\left(\frac{U}{U_o}\right) = \ln\left(\frac{Ae^{\imath\theta}}{A_o e^{\imath\theta_o}}\right) \tag{2.135}$$

$$= \left[\ln(A) - \ln(A_o)\right] + \imath\left[\theta - \theta_o\right]. \tag{2.136}$$

Therefore the ϕ_{sc} term can be expressed using the differences between the log-amplitudes and phases of the heterogeneous and homogeneous measurements, such that

$$\phi_{sc} = \left[\ln(A) - \ln(A_o)\right] + \imath\left[\theta - \theta_o\right]. \tag{2.137}$$

Thus, difference measurements of phase and amplitude, combined with the matrix equation in Equation 2.129, provide a framework for performing three-dimensional tomography of the optical properties μ_a and μ_s', via D, and the corresponding tissue chromophore concentrations.

2.6.2 Reconstructing Optical Properties

Because the weight matrix $\mathbf{W}$ in Equation 2.132 maps the optical properties of the tissue $\vec{\mu}$ onto the measured output $\vec{\phi}$, it is referred to as the forward operator, and solving for $\vec{\phi}$, given $\vec{\mu}$, is called the forward problem. The algorithms underlying DOT are premised on solving the inverse problem, wherein the optical properties $\vec{\mu}$ are determined given a set of measurements $\vec{\phi}$.

The simplest method to solve the inverse problem is to invert $\mathbf{W}$, such that

$$\vec{\mu} = \mathbf{W}^{-1}\vec{\phi}. \tag{2.138}$$

However, $\mathbf{W}$ is an $M \times N$ matrix, where M is the number of source-detector pairs and N is the number of reconstruction voxels. Due to logistical limitations, $M \ll N$, meaning that $\mathbf{W}$ is not a square matrix, and the system of equations is undetermined. Thus, $\mathbf{W}$ is not generally invertible. A simple inverse solution is therefore not practical for solving this equation with a unique solution. Many methods have been developed for overcoming this limitation including discrete algebraic inversions [225; 124; 123; 24], analytic linear subspace techniques [123; 175; 176; 159], and non-linear iterative algorithms [228; 15; 12; 174; 84]. All of these techniques, in combination with regularization (see Section 2.6.5), provide additional constraints to reduce the ill-posedness of the

problem. Here, the focus will be on the non-linear iterative methods, a flow chart for which can be found in Figure 2.10. Note also, that throughout this section, the vector of measurements $\vec{\phi}$ will be the measured amplitude and phase for a series of source and detector position combinations. However, these algorithm can also be performed such that $\vec{\phi}$ is the amplitude and phase measured at a single source-detector pair but for a series of modulation frequencies. This will not provide heterogeneous spatial information but will provide improved quantification of μ_a and μ_s' at a single position [30] (see Section 3.2.2).

2.6.3 DOT Initialization and Forward Problem

The first step in iterative reconstruction algorithms for DOT is initialization, whereby an initial optical property distribution $\vec{\mu}$ is set. The simplest initial optical properties are homogeneous distributions of the absorption and diffusion coefficients μ_a^o and D^o. In this case, the initial $\vec{\mu}$ would be a 0-vector since there are no heterogeneous perturbations $\delta\mu_a$ and δD from the homogeneous distribution.

Heterogeneous optical property distributions can also be chosen for initialization. This is particularly useful in the case that *a priori* structural knowledge can be used to identify disparate tissue regions, with distinct optical properties (see Section 2.6.7). Regardless of what type of distribution is chosen, it is important that the initial optical properties are chosen to be reasonably close to the true values; otherwise the iterative algorithm may not converge to a meaningful solution [194].

These initial conditions are then used to solve the forward problem, utilizing the appropriate weight matrix W, which is dependent on the homogeneous fluence rate, Green's function, and optical property distributions, as well as the voxel volume (see Equations 2.130 and 2.131). This forward problem results in a calculated fluence rate vector $\vec{\phi}_c$.

2.6.4 DOT Objective Function

The goal of the iterative reconstruction algorithm is to minimize an objective function Ψ of the form

$$\Psi = \chi^2 + \tau_R R, \tag{2.139}$$

where χ^2 is a function comparing the calculated fluence rate $\vec{\phi}_c$ to the measured fluence rate $\vec{\phi}_m$, R is regularization term that compensates for the ill-posedness of the inverse problem, and τ_R is the regularization hyper-parameter, which calibrates the relative weight of the χ^2 and R terms. The various forms of the regularization term will be discussed in Section 2.6.5.

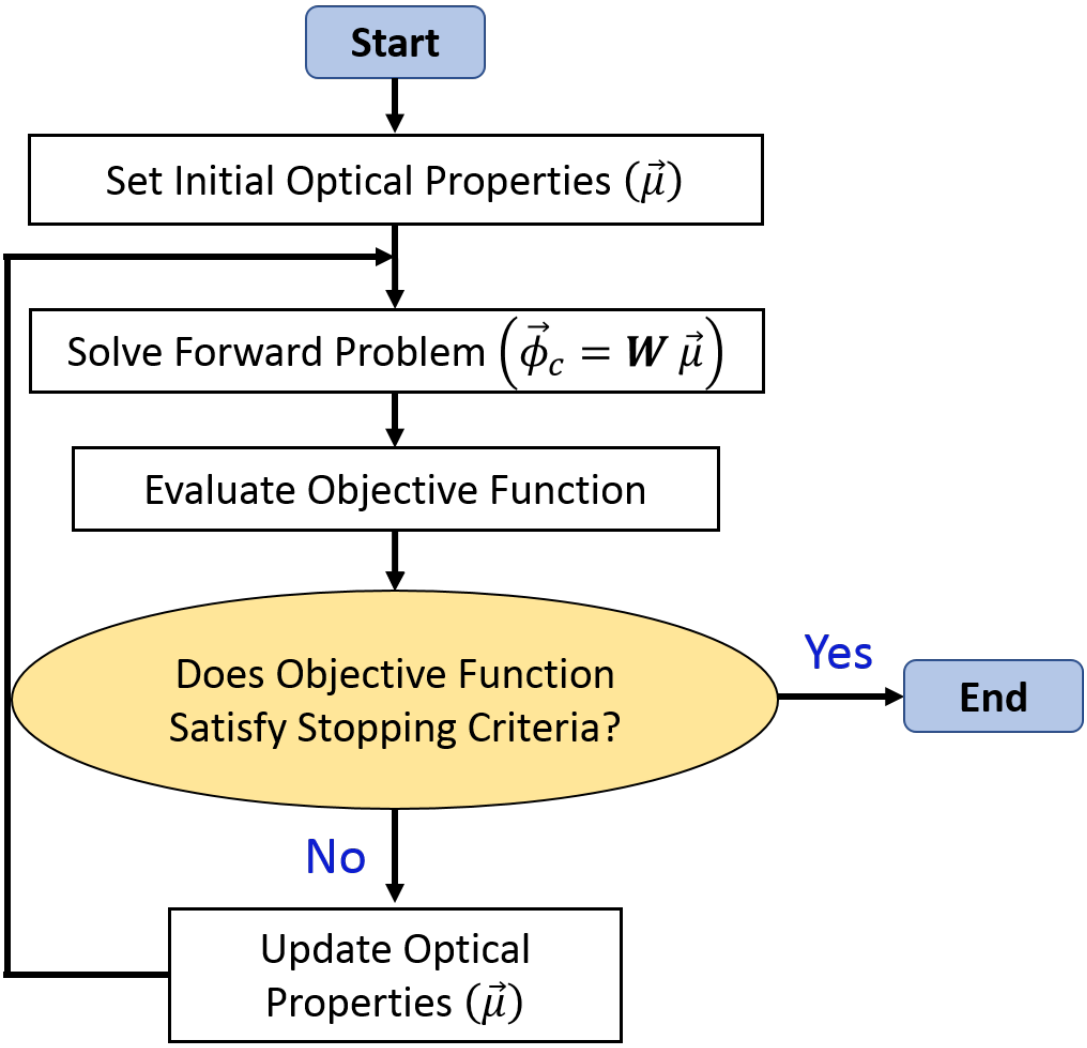

Figure 2.10: Flow Chart for Non-Linear Iterative DOT Algorithm. The non-linear iterative Diffuse Optical Tomography (DOT) algorithm for reconstructing heterogeneous optical properties across a three-dimensional medium from the measured fluence rate $\vec{\phi}_m$ is comprised of the following steps: 1) Initialization. First, set an initial optical property distribution $\vec{\mu}$. 2) Forward Problem. Next, solve the forward problem using the initial optical property vector $\vec{\mu}$ and the appropriate weight matrix **W**. This will produce a calculated fluence rate vector $\vec{\phi}_c$. 3) Objective Function Evaluation (Section 2.6.4). The objective function for the algorithm is now evaluated. This function will usually be comprised of a χ^2 term comparing the measured and calculated fluence rates, $\vec{\phi}_m$ and $\vec{\phi}_c$, and a regularization term that compensates for the ill-posedness of the matrix equation (Section 2.6.5). The goal is to minimize this objective function and, in doing so, find the appropriate optical property vector $\vec{\mu}$. If the objective function meets some stopping criteria, the algorithm ends. Otherwise, the algorithm proceeds to the next step. 4) Optical Property Update (Section 2.6.6). If the objective function does not meet the stopping criteria, $\vec{\mu}$ must be updated to make $\vec{\phi}_c$ closer to $\vec{\phi}_m$. 5) Iterate. The new optical property vector $\vec{\mu}$ is used to solve the forward problem, and the algorithm continues iterating.

The χ^2 term typically takes the form [245]

$$\chi^2 = \sum \left[\frac{\left(\vec{\phi}_c - \vec{\phi}_m \right)^2}{\vec{\sigma}^2} \right] \tag{2.140}$$

$$= \sum \left[\frac{\left(\mathbf{W}\vec{\mu} - \vec{\phi}_m \right)^2}{\vec{\sigma}^2} \right]. \tag{2.141}$$

Here, the summation is performed over all source-detector pair measurements, $\vec{\sigma}$ is a weight vector that represents the uncertainty, or standard deviation, of each source-detector pair measurement, and element-wise division is performed between the calculated-measured fluence rate difference and $\vec{\sigma}$. The weight vector is often chosen to be uniform [84; 14]; however, it can also be determined via experimental error and used to emphasize source-detector pairs with high signal-to-noise or de-emphasize noisier measurements [25] (see Section 7.2.4).

Given the definition of $\vec{\phi}$ in terms of ϕ_{sc} (Equation 2.129) and the definition of ϕ_{sc} in the perturbative framework, the $\vec{\phi}_c - \vec{\phi}_m$ term can be written as

$$\vec{\phi}_c - \vec{\phi}_m = \ln\left(\frac{U^c}{U_o^c}\right) - \ln\left(\frac{U^m}{U_o^m}\right) \tag{2.142}$$

$$= \ln\left(\frac{U^c U_o^m}{U_o^c U^m}\right) \tag{2.143}$$

$$= \left[\ln\left(\frac{A^c}{A_o^c}\right) - \ln\left(\frac{A^m}{A_o^m}\right)\right] + \imath\left[(\theta^c - \theta_o^c) - (\theta^m - \theta_o^m)\right]. \tag{2.144}$$

Thus, the χ^2 term can be written in terms of the differences between the log-amplitudes and phases of the heterogeneous and homogeneous fluence rates. If, in the experimental DOT procedure, a measurement of a homogeneous reference is made, a difference reconstruction between the tissue and reference phantom can be explicitly performed [14; 227]. To complete the objective function, a regularization term must now be added.

2.6.5 DOT Regularization Techniques

The inverse DOT problem is usually ill-posed. For a full three-dimensional reconstruction, the system of equations is under-determined because the number of reconstructed voxels is much greater than the number of source-detector pairs. The system can also be over-determined in the case of a hard-prior spatial constraint (see Section 2.6.7), which limits the reconstruction to a few homogeneous regions. Under-determined systems of equations typically suffer from non-unique solutions. Regularization ameliorates this issue by penalizing undesirable solutions, *e.g.*, optical properties far from typical tissue values or non-physical, rapidly fluctuating distributions, and thus

constraining the problem [246; 161]. Although the potential presence of local minima in the iterative algorithm precludes a definitively unique solution, regularization significantly reduces the possible solution space. There are a wide variety of regularization techniques used in DOT reconstruction [14; 84; 227]; this research uses three such techniques: Zeroth-Order Tikhonov (TK0), First-Order Tikhonov (TK1), and total variation (TV).

The simplest regularization technique is Zeroth-Order Tikhonov, which seeks to minimize the difference between the reconstructed optical properties $\vec{\mu}$ and some initial estimate or *a priori* known value of the optical property distribution $\vec{\mu}_o$.

$$R_{TK0} = \|\mathbf{I}\left(\vec{\mu} - \vec{\mu}_o\right)\|^2 \tag{2.145}$$

$$= \sum_{n=1}^{2N} \left[\mu_n - \mu_n^o\right]^2, \tag{2.146}$$

where $\mathbf{I}$ is the identity matrix, $\vec{\mu}_o$ is the initial optical property distribution, $\|\cdot\|^2$ represents the l^2-norm of the vector, and N is the number of voxels. Here, the sum goes from $n = 1$ to $2N$ because two optical properties are reconstructed for each voxel. This technique prevents reconstructed absorption and scattering coefficients in a given voxel that are unrealistically different from the initial estimates in that voxel [246].

The First-Order Tikhonov regularization parameter enforces a smoothness condition, seeking to minimize the gradient of the optical property distribution [77; 227]. This is accomplished via the same framework as Zeroth-Order Tikhonov regularization but with a different linear operator matrix $\mathbf{L}_1$, such that

$$R_{TK1} = \|\mathbf{L}_1\left(\vec{\mu} - \vec{\mu}_o\right)\|^2 \tag{2.147}$$

$$= \sum_{i=1}^{2N} \left[\sum_{j=1}^{2N} L_{i,j}\left(\mu_j - \mu_j^o\right)\right]^2. \tag{2.148}$$

Here $\mathbf{L}_1$ is the discrete first derivative matrix operator of size $2N \times 2N$, given by

$$L_{i,j} = \begin{cases} n_i & \text{if } i = j \\ -1 & \text{if } j \text{ is a neighbor of } i \\ 0 & \text{otherwise,} \end{cases} \tag{2.149}$$

where n_i is the number of neighbors surrounding the i^{th} voxel. The First-Order Tikhonov regularization term is thus dependent on the difference between the optical properties of a given voxel and the optical properties of its neighbors. This quantity is proportional to the gradient of the optical property distribution. If the initial optical property estimate is homogeneous, the First-Order

Tikhonov regularization term reduces to

$$R_{TK1} = \sum_{i=1}^{2N} \left[\sum_{j=1}^{2N} L_{i,j}\, \mu_j \right]^2 \tag{2.150}$$

because the gradient across the entire initial distribution is 0.

The total variation regularization scheme is similar to the First-Order Tikhonov method in that it minimizes the optical property distribution gradient; however, instead of using the l^2-norm, total variation regularization utilizes the l^1-norm [26], such that

$$R_{TV} = \|\mathbf{L}_1 \left(\vec{\mu} - \vec{\mu}_o\right)\|_1 \tag{2.151}$$

$$= \sqrt{\sum_{i=1}^{2N} \left[\sum_{j=1}^{2N} L_{i,j} \left(\mu_j - \mu_j^o\right) \right]^2 + T^2} - T, \tag{2.152}$$

where $\|\cdot\|_1$ is the l^1 norm of the vector and T is a small threshold parameter [227; 25], which allows for minimization in the regularization term despite any potential non-differentiability of the optical properties [205]. Total variation has an advantage over First-Order Tikhonov for tissues with sudden changes in optical properties. First-Order Tikhonov regularization tends to smooth all regions, whereas total variation retains sharper edge features [205; 26; 25], which can be important for contrast localization. As with First-Order Tikhonov regularization, total variation also reduces to a simpler form if the initial optical properties are homogeneous:

$$R_{TV} = \sqrt{\sum_{i=1}^{2N} \left[\sum_{j=1}^{2N} L_{i,j}\, \mu_j \right]^2 + T^2} - T. \tag{2.153}$$

Regardless of which type of regularization is used, the hyperparameter τ_R must be chosen to balance the regularization term with the χ^2 minimization of the difference between calculated and measured fluence rate. If the τ_R is too low, the reconstructed solution will be largely un-regularized and subject to excessive high-frequency noise. A τ_R value that's too high will result in an artificially homogeneous and/or smooth distribution that doesn't accurately reflect the tissue (see Figure 2.11). In statistical parlance, a low tau value produces a high variance and results in overfitting while a high tau value produces a large bias and is an example of underfitting [257].

The most common method for choosing the optimal τ_R value in optical tomography is L-curve selection [133; 134]. This method requires reconstructions to be performed for a series of τ_R values ranging from the underfit to the overfit regimes. The values of the χ^2 part of the objective function at the final iteration, hereafter referred to as the likelihood term [227], are then plotted against the log-values of R at the same iteration, known as the prior term [227], with each point representing

a different τ_R value. The point of maximum curvature on this plot will be the point at which both the likelihood and prior terms are nearly minimized, providing the optimal τ_R value. Figure 2.11 contains an L-curve and characteristic phantom images at different τ_R values.

Additionally, it is not necessary for the regularization hyperparameter to be a constant; instead of a constant τ_R, the parameter can be a vector $\vec{\tau_R}$ of length $2N$ with a separate value for each combination of voxel and reconstructed optical property. For instance, DOT is known to be susceptible to artifacts near tissue boundaries due to the breakdown of the assumptions inherent in the diffusion equation. Thus, a spatially-variant regularization parameter, with higher values for voxels near the tissue boundaries, can reduce image noise without significantly impairing the optical contrast elsewhere in the tissue [212; 72]. Alternatively, different values of τ_R, or even different types of regularization, can be used for individual optical properties. For example, some DOT instruments and reconstruction algorithms may inherently reconstruct the reduced scattering coefficient μ_s' with higher contrast and better resolution than the absorption coefficient μ_a. In that case, it may be beneficial to use a First-Order Tikhonov algorithm and higher τ_R value for the diffusion coefficient terms while employing Total Variation and a lower τ_R for the absorption coefficient terms. This technique proved beneficial in our reconstruction work with a high spatial density frequency domain DOT instrument [25] (see Section 7.2.4). A final use of spatially-varying regularization is so-called soft-prior reconstruction, in which *a priori* knowledge of the tissue structure is used to assign varying regularization parameters to voxels based on their proximity to the boundaries between tissue regions [84]. This will be discussed in more detail in Section 2.6.7.

Once the objective function Ψ, including the χ^2 term and the regularization term, is evaluated, it is tested against some stopping criterion, usually an acceptable value for the current iteration Ψ_i or a minimum difference between successive iterations $\Psi_i - \Psi_{i-1}$. If the objective function satisfies one of these criteria, the reconstruction algorithm ends. Note that the reconstruction can also be terminated after a set number of iterations for practical purposes. If the objective function does not satisfy the stopping criteria, the optical property vector $\vec{\mu}$ must be updated to minimize difference between the calculated and measured fluence rates.

2.6.6 DOT Optical Property Update Methods

There are several methods that can be used to update the optical property solution vector in order to force the calculated fluence rate to converge to the measured fluence rate. The underlying concept for all of these methods is the minimization of the objective function via a gradient with respect to $\vec{\mu}$. As with any optimization problem, a function will be minimized when its gradient approaches 0 [103]. The three methods used for reconstructions here are the Gauss-Newton algorithm, the

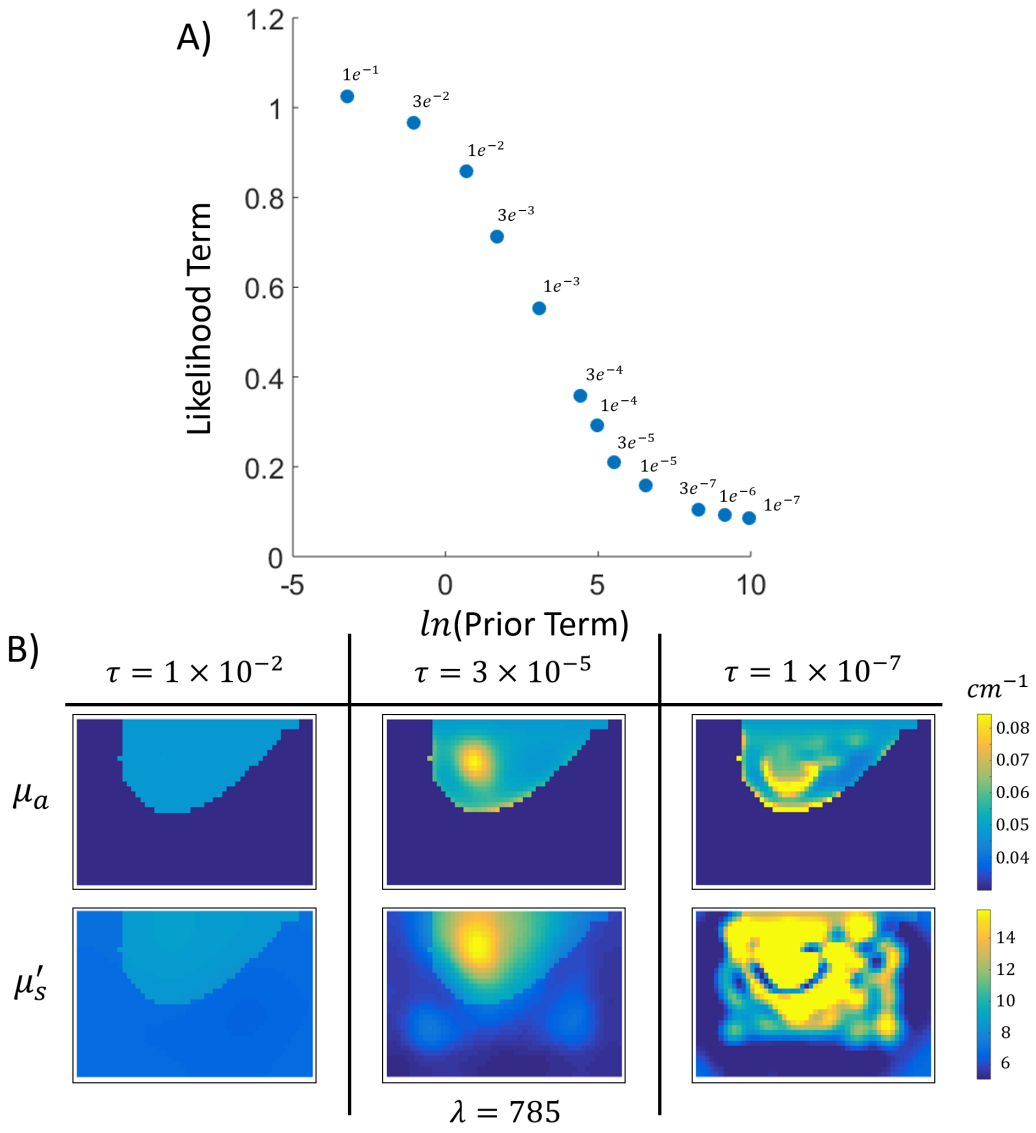

Figure 2.11: L Curve Selection and the Effect of the Regularization Hyperparameter. A series of reconstructions with different τ_R hyperparameters were performed for human subject breast cancer data from a Frequency Domain DOT instrument using the conjugate gradient method (see Section 2.6.6) and a split First-Order Tikhonov and Total Variation regularization scheme (see Section 7.2.4). A) L-Curve analysis was performed and the likelihood term was plotted against the natural logarithm of the prior term for a series of τ_R values (represented by the numbers on the plot). The optimal τ_R is then chosen to be the point that maximizes the curvature at the L-bend, which optimally minimizes both the likelihood and prior terms. For this reconstruction, $\tau_R = 3 \times 10^{-5}$ was the best fit. B) Reconstructions of μ_a and μ_s' at $\lambda = 785\,nm$ are shown for high, optimal, and low values of τ_R. Note that when τ_R is too high, the image is artificially smooth and does not provide contrast between tumor and normal tissue. When τ_R is too low, high-frequency noise dominates the reconstruction, obscuring the contrast.

Conjugate Gradient algorithm, and the Levenberg-Marquadt algorithm. These methods can be used for any of the previously discussed regularization techniques (Section 2.6.5), but, for simplicity, the update algorithms will be demonstrated using Zeroth-Order Tikhonov regularization.

Gauss-Newton Method

The Gauss-Newton method has been extensively defined and employed for DOT [15; 229; 84]. The first step is to set the derivative of the objective function Ψ (Equation 2.139 using Zeroth-Order Tikhonov regularization) equal to 0 with respect to the optical property vector $\vec{\mu}$ such that

$$\nabla\Psi = 2\sum\left[\mathbf{J}^{\top}\left(\vec{\phi}_c - \vec{\phi}_m\right) + \tau_R\mathbf{I}\left(\vec{\mu} - \vec{\mu}_o\right)\right] = 0, \tag{2.154}$$

where τ_R is the regularization hyperparameter, $\mathbf{I}$ is the identity matrix, $\vec{\mu}$ is the current optical property distribution, $\vec{\mu}_o$ is the initial optical property distribution, and $\mathbf{J}^T$ is the transpose of the Jacobian matrix $\mathbf{J}$, defined as

$$\mathbf{J} = \frac{\partial\vec{\phi}_c}{\partial\vec{\mu}} \tag{2.155}$$

$$= \begin{bmatrix} \frac{\partial\phi_c^1}{\partial\mu_a^1} & \cdots & \frac{\partial\phi_c^1}{\partial\mu_a^N} & \frac{\partial\phi_c^1}{\partial D^1} & \cdots & \frac{\partial\phi_c^1}{\partial D^N} \\ \frac{\partial\phi_c^2}{\partial\mu_a^1} & \cdots & \frac{\partial\phi_c^2}{\partial\mu_a^N} & \frac{\partial\phi_c^2}{\partial D^1} & \cdots & \frac{\partial\phi_c^2}{\partial D^N} \\ \vdots & & \vdots & \vdots & & \vdots \\ \frac{\partial\phi_c^M}{\partial\mu_a^1} & \cdots & \frac{\partial\phi_c^M}{\partial\mu_a^N} & \frac{\partial\phi_c^M}{\partial D^1} & \cdots & \frac{\partial\phi_c^M}{\partial D^N} \end{bmatrix}. \tag{2.156}$$

Here, ϕ_c^i is the calculated flunce for the i^{th} measurement, μ_a^j and D^j are the absorption and diffusion coefficients for the j^{th} voxel, N is the number of voxels, and M is the number of measurements. For difference reconstructions in the frequency domain, ϕ_c can be written in terms of differences in log-amplitude and phase as described in Equation 2.137; therefore, the difference in the log-amplitude is simply the real part of ϕ_c, and the phase difference is the imaginary part of ϕ_c. The amplitude

and phase for each measurement can then be regarded as independent parameters, such that

$$\vec{\phi} \rightarrow \begin{bmatrix} \ln\left(\frac{A^1}{A_o^1}\right) \\ \vdots \\ \ln\left(\frac{A^M}{A_o^M}\right) \\ \left(\theta^1 - \theta_o^1\right) \\ \vdots \\ \left(\theta^M - \theta_o^M\right) \end{bmatrix} = \begin{bmatrix} \Delta A^1 \\ \vdots \\ \Delta A^M \\ \Delta\theta^1 \\ \vdots \\ \Delta\theta^M \end{bmatrix}. \tag{2.157}$$

In this commonly used framework, the Jacobian becomes

$$\mathbf{J} = \begin{bmatrix} \frac{\partial \Delta A^1}{\partial \mu_a^1} & \cdots & \frac{\partial \Delta A^1}{\partial \mu_a^N} & \frac{\partial \Delta A^1}{\partial D^1} & \cdots & \frac{\partial \Delta A^1}{\partial D^N} \\ \vdots & & \vdots & \vdots & & \vdots \\ \frac{\partial \Delta A^M}{\partial \mu_a^1} & \cdots & \frac{\partial \Delta A^M}{\partial \mu_a^N} & \frac{\partial \Delta A^M}{\partial D^1} & \cdots & \frac{\partial \Delta A^M}{\partial D^N} \\ \frac{\partial \Delta\theta^1}{\partial \mu_a^1} & \cdots & \frac{\partial \Delta\theta^1}{\partial \mu_a^N} & \frac{\partial \Delta\theta^1}{\partial D^1} & \cdots & \frac{\partial \Delta\theta^1}{\partial D^N} \\ \vdots & & \vdots & \vdots & & \vdots \\ \frac{\partial \Delta\theta^M}{\partial \mu_a^1} & \cdots & \frac{\partial \Delta\theta^M}{\partial \mu_a^N} & \frac{\partial \Delta\theta^M}{\partial D^1} & \cdots & \frac{\partial \Delta\theta^M}{\partial D^N} \end{bmatrix}. \tag{2.158}$$

For either form of the Jacobian, the update to the optical properties is calculated using the linear term of a Taylor series expansion for the difference between $\vec{\phi}_c$ in successive iterations, allowing $\vec{\phi}_c$ at iteration $i+1$ to be expressed as

$$\vec{\phi}_c(i+1) = \vec{\phi}_c(i) + \mathbf{J}\delta\vec{\mu}, \tag{2.159}$$

where $\vec{\phi}_c(i)$ is the forward solution at the i^{th} iteration, $\vec{\phi}_c(i+1)$ is the forward solution at the $(i+1)^{th}$ iteration, and $\delta\vec{\mu}$ is the difference between optical properties in these two iterations $(\vec{\mu}(i+1) - \vec{\mu}(i))$. If this Taylor expansion is substituted into the summand in Equation 2.154, and it is set to 0 to minimize the objective function,

$$\mathbf{J}^\top\left(\vec{\phi}_c(i) - \vec{\phi}_m\right) + \tau_R\mathbf{I}\left(\vec{\mu}(i) - \vec{\mu}_o\right) + \mathbf{J}^\top\mathbf{J}\delta\vec{\mu} + \tau_R\mathbf{I}\delta\vec{\mu} = 0, \tag{2.160}$$

$$\mathbf{J}^\top\left(\vec{\phi}_c - \vec{\phi}_m\right) + \tau_R\mathbf{I}\left(\vec{\mu} - \vec{\mu}_o\right) = \left(\mathbf{J}^\top\mathbf{J} + \tau_R\mathbf{I}\right)\delta\vec{\mu}. \tag{2.161}$$

The optical property update to minimize the objective function is then calculated as

$$\delta\vec{\mu} = \left(\mathbf{J}^\top\mathbf{J} + \tau_R\mathbf{I}\right)^{-1}\left[\mathbf{J}^\top\left(\vec{\phi}_c - \vec{\phi}_m\right) + \tau_R\left(\vec{\mu} - \vec{\mu}_o\right)\right]. \tag{2.162}$$

Here the $\left(\mathbf{J}^\top\mathbf{J} + \tau_R\mathbf{I}\right)^{-1}$ term is a regularized pseudo-inverse of the Jacobian matrix known as the Hessian and is calculable with a variety of techniques [229]. Gauss-Newton optimization is thus dependent on a second derivative of the objective function.

The Gauss-Newton algorithm is relatively straight forward to implement but is computationally intensive and not guaranteed to converge. It is also highly dependent on the chosen initial optical properties [16].

Conjugate Gradient Method

The Conjugate Gradient algorithm is a steepest descent method dependent on the first derivative of the objective function Ψ. It incurs a lower computational cost than the Gauss-Newton method; however, it may require more iterations to converge and can sometimes act as a low-pass filter that minimizes spatial heterogeneity in the reconstruction [16; 77].

For the first iteration, a residual vector $\vec{r}_o$, calculated based on the gradient of the objective function at the first iteration Ψ_o with respect to the initial optical properties $\vec{\mu}_o$, is defined as

$$\vec{r}_o = -\left(\vec{\nabla}\Psi_o\right) \circ \vec{\mu}_o, \tag{2.163}$$

where $\circ$ indicates element-wise multiplication. For this iteration only, the search direction vector $\vec{d}_o$ is set to be equal to $\vec{r}_o$ $\left(\vec{d}_o = \vec{r}_o\right)$. The new optical property vector will then be

$$\vec{\mu}_1 = \vec{\mu}_o + \alpha_o\,\vec{d}_o, \tag{2.164}$$

where α_o is a step size constant. Here, α_o is calculated via a line search method along the search direction vector $\vec{d}_o$ which seeks the optimal step size for minimizing the objective function Ψ_1 [16; 227].

Successive iterations then calculate a new $\vec{r}_i$ where

$$\vec{r}_i = -\left(\vec{\nabla}\Psi_i\right) \circ \vec{\mu}_i \tag{2.165}$$

for the i^{th} iteration. However, instead of setting $\vec{d}_i = \vec{r}_i$,

$$\vec{d}_i = \vec{r}_i + \beta_i\,\vec{d}_{i-1}, \tag{2.166}$$

where β_i is a constant that weights the contribution of the current iteration gradient versus the previous search direction. In the reconstructions presented here, β_i was calculated using the Polak-Ribiére method [214; 16]. This method specifies a β_i of the form

$$\beta_i \equiv \frac{\vec{r}_i^{\top}\vec{r}_i - \vec{r}_i^{\top}\vec{r}_{i-1}}{\vec{r}_{i-1}^{\top}\vec{r}_{i-1}}. \tag{2.167}$$

However, to ensure convergence, β_i is set to 0 if the above definition produces a negative value. The next optical property solution vector is then set in the same manner as the first iteration, so

$$\vec{\mu}_{i+1} = \vec{\mu}_i = \alpha_i \, \vec{d}_i. \tag{2.168}$$

Here, α_i is again set via a line search minimization, and the algorithm will continue iterating until the objective function satisfies the stopping criteria.

Levenberg-Marquadt Method

The Levenberg-Marquadt algorithm is a variation of the Gauss-Newton method that modifies the regularization hyperparameter such that the optical property update is defined as [167; 84]

$$\delta\vec{\mu} = \left(\mathbf{J}^\top\mathbf{J} + \gamma\,\tau_R\mathbf{I}\right)^{-1}\left[\mathbf{J}^\top\left(\vec{\phi}_c - \vec{\phi}_m\right) + \tau_R\left(\vec{\mu} - \vec{\mu}_o\right)\right]. \tag{2.169}$$

The constant γ modifies the hyperparameter τ_R to control the level of regularization for a given iteration. A larger γ leads to a highly regularized update which is dominated by the non-Hessian term in Equation 2.169. This term is dependent on the gradient of the Ψ and thus more closely resembles the conjugate gradient method. A very small γ results in an update dominated by the Gauss-Newton-like Hessian term. A typical strategy, and the one implemented for all Levenberg-Marquadt reconstructions here, is for γ to decrease monotonically across successive iterations [260; 84; 23]. This large early regularization inhibits divergence of the reconstruction due to the aberrant search directions that can be caused by highly inaccurate initial optical properties. Less regularization at later iterations allows the reconstruction to converge once the search direction is more certain. As such, the Levenberg-Marquadt algorithm reduces some of the dependence on initial optical properties that plagues the Gauss-Newton method [167; 260].

2.6.7 *A Priori* Spatial Information

Relative to gold-standard structural imaging techniques like x-ray or MRI, Diffuse Optical Tomography has limited spatial resolution due to the large effective wavelength of the diffuse photon density waves used in the image reconstruction [195; 32; 98]. For most DOT instruments the best resolution ranges from approximately 2 to 10 mm [67; 159; 72]; the exact value of the resolution is highly dependent on the number, location, and field of view of the sources and detectors, the data quality, and the optical property contrast of the imaged inhomogeneity [32]. This relative lack of resolution can impair localization of high contrast regions, such as tumors, and the quantitative accuracy of the optical property reconstruction. One method of overcoming these issues is combining DOT with a clinically standard structural imaging modality, such as x-ray CT [169; 270; 111; 183; 280], MRI [193; 46; 142; 271; 52; 105], or ultrasound [274; 140; 275; 277]. A large majority of multi-modality

DOT instruments perform both imaging techniques simultaneously; however, it is also possible, via a co-registration algorithm, to use non-concurrent structural images with DOT reconstructions [20].

These multi-modality measurements serve three primary purposes:

1. Validation - A structural image taken simultaneously can help validate the ability of DOT to localize the optical contrast of a region of interest.

2. Constraint - The structural image can be used as an input to the DOT reconstruction, more accurately locating different regions and thus improving the quantitative optical property reconstruction.

3. Synthesis - Information from the clinical modality, such as water density or blood perfusion from MRI, can be combined with optical parameters, like tissue oxygen saturation, to create a new biomarker unavailable to either technique alone.

Validation can be performed by reconstructing the optical contrast entirely independently of the structural image and then comparing the location of the region of interest in each modality. This type of validation has been done for DOT of breast tumors with both MRI and x-ray CT [193; 52; 111] and for functional brain mapping DOT with comparison to BOLD fMRI [157; 104].

Constraining the reconstruction requires that the *a priori* spatial information obtained from the structural imaging modality serves as input to the DOT algorithm. The most common input is a segmented mask of the structural image, separating the imaging volume into distinct regions. For example, for a multi-modal DOT-MRI breast imager, the tissue could be divided into adipose (fatty), fibroglandular, and tumor regions. The reconstruction can then be constrained via these region designations in several ways. The simplest method is to simply set different initial optical properties for each region. This technique is most useful if the segmented image is divided into tissue and non-tissue regions, *e.g.*, breast tissue and a surrounding lipid emulsion bath, because it preserves the boundary location between the regions without biasing the tissue reconstruction [25]. This strategy is less effective when comparing two tissue regions, *e.g.*, tumor and healthy, because the optical contrast between the two regions will be biased by the initial conditions.

The most common use of spatial information with DOT is as a so-called hard prior. A hard prior uses the segmented image to define distinct spatial regions and then forces the reconstructed optical properties to be homogeneous within each region. This reduces the number of parameters that must be reconstructed and thus reduces the length of the optical property vector $\vec{\mu}$. Instead of reconstructing properties for many small voxels, the DOT algorithm only needs to reconstruct

a single value of each optical property for each region. For DOT instruments with many source-detector pairs, this transforms the inverse problem from an under-determined system of equations to an over-determined one. Hard-prior constraint has been shown to improve quantitative contrast between tumor and normal regions [47; 178; 117]; however, this technique is very sensitive to inaccuracy in the location of the defined regions [41; 88]. Therefore accurate segmentation and spatial co-registration between modalities is imperative.

Another implementation of the segmented image is as a soft boundary prior, in which the regularization hyperparameter τ_R is lower near region boundaries than in the region interior. This enforces a smoothing condition within a given region while allowing for significant updates at the boundaries where there is more potential for a physiological non-linearity. Soft-prior regularization has been shown to improve optical contrast relative to unconstrained DOT [145; 130; 260; 25] but is generally not as effective in this regard as hard-prior constraints [211; 259]. It also does not reduce parameter space for the inverse problem since all voxels are still reconstructed. Soft-prior regularization does have the advantage of being less critically dependent on accurate segmentation, though.

Finally, information from other modalities can be synthesized with DOT-measured water, lipid, or hemoglobin concentrations to potentially highlight new physiological processes. For example, glucose metabolism information from FDG-PET could be combined with DOT-measured tissue oxygenation to explore the relative levels of different metabolic processes [122]. Alternatively, gadolinium-uptake DCE-MRI techniques can measure tumor blood perfusion which, combined with oxygen saturation, could directly probe oxygen metabolism [52].

2.7 Finite Element Method

The DOT reconstruction methods presented so far have relied upon two primary assumptions: 1) a small perturbation from homogeneous optical property distributions and 2) a regular geometry for which an analytical Green's function solution can be calculated. The Finite Element Method (FEM) [279] is a numerical technique that helps to overcome these limitations and has been used extensively in diffuse optics [17; 228; 15; 204; 84; 227]. This method is premised on subdividing the imaging domain Ω, which contains a boundary referred to as $\partial\Omega$ into a series of discrete regions, similar to the voxels discussed earlier. These elements can take a variety of shapes but tetrahedral and cubic elements are the most common [14]. The vertices of the elements are referred to as nodes, and these nodes ($\sim 10^5$) and elements comprise the finite element mesh over which the reconstruction is performed. The nodes also serve as a basis set for discretizing the fluence rate.

The total fluence rate in the frequency-domain, here referred to by convention as Φ^h, can be written as

$$\Phi^h(\vec{r}) = \sum_{i=1}^{V} \Phi_i u_i(\vec{r}). \tag{2.170}$$

Here, $u_i(\vec{r})$ is simply a δ-function at the position of the i^{th} node, Φ_i is the fluence rate at the i^{th} node, and V is the total number of nodes. In this formulation, the vector $\vec{\Phi}$, which is the vector of all V values of Φ_i, obeys a diffusion equation of the form

$$[\mathbf{K} + \mathbf{C} + \imath\omega\,\mathbf{M} + \mathbf{A}]\,\vec{\Phi} = \vec{Q}, \tag{2.171}$$

where $\vec{Q}$ is a vector of length V of the source power at each node. In most applications, where the source positions lie on the tissue boundary, $\vec{Q}$ will only be non-zero for boundary nodes. $\mathbf{K}$, $\mathbf{C}$, $\mathbf{M}$, and $\mathbf{A}$ are all matrices of size $V \times V$ whose terms in the i^{th} row and j^{th} column are defined as follows [17; 228]:

$$K_{ij} = \int_\Omega = D(\vec{r}) \left(\vec{\nabla} u_j(\vec{r})\right) \cdot \vec{\nabla} u_i(\vec{r})\, d\Omega, \tag{2.172}$$

$$C_{ij} = \int_\Omega v\mu_a u_j(\vec{r}) u_i(\vec{r})\, d\Omega, \tag{2.173}$$

$$M_{ij} = \int_\Omega u_j(\vec{r}) u_i(\vec{r})\, d\Omega, \tag{2.174}$$

$$A_{ij} = \frac{1}{2}\frac{1 - R_{eff}}{1 + R_{eff}} \int_{\partial\Omega} u_j(\vec{r}) u_i(\vec{r})\, d(\partial\Omega). \tag{2.175}$$

Each of these terms clearly resembles part of the diffusion equation. $\mathbf{K}$ is the term containing the spatial derivatives and diffusion coefficients, $\mathbf{C}$ is the absorption term, $\mathbf{M}$ is the frequency-domain implementation of the time-derivative, and $\mathbf{A}$, which is integrated only over the surface nodes, is the discretized partial-flux boundary condition. Note that R_{eff} is the same value defined in Equation 2.97. Since $u_j(\vec{r})$ and $u_i(\vec{r})$ form an orthogonal basis set of δ-functions at each node, these integrals will only be non-zero when the i^{th} and j^{th} nodes in the integral are both vertices of the same element. Thus, all four matrices are extremely sparse. As with the analytic diffusion equation, this frequency-domain equation can easily be converted to continuous wave or time-domain.

This matrix diffusion equation can be solved using the techniques discussed previously, but now, analytic Green's function solutions for different geometries are not required. The infinite homogeneous geometry Green's function can be used for interior nodes, and the same Green's function plus the partial flux boundary condition can be used for boundary nodes. The full fluence

rate will thus be a numeric approximation of the true fluence rate which becomes more accurate for denser meshes with more nodes. The actual measurements can then be thought of as the photon flux normal to the boundary in the elements that contain the detector positions, which is calculated by integrating the fluence rate over the describing nodes of the element and using the partial flux boundary condition (see Equation 2.100).

2.8 Tissue Spectroscopy and Scattering Model

2.8.1 Tissue Spectroscopy

The analytical strategies discussed to this point have focused on modelling the photon fluence rate in order to determine the absorption (μ_a) and reduced scattering (μ_s') coefficients of tissue. While these properties have demonstrated potential clinical utility [255; 56], the concentration of chromophores that absorb light in the near-infrared wavelength range can provide particularly useful physiological information. The four primary absorbers in diffuse optics are oxygenated hemoglobin (HbO_2), deoxygenated hemoglobin (HHb), water (H_2O), and lipid. The absorption coefficient for a particular wavelength can be written as a summation of the absorption due to these tissue chromophores, such that

$$\mu_a(\lambda) = \mu_a^o(\lambda) + \sum_i \varepsilon_i(\lambda)\, C_i, \tag{2.176}$$

where ε_i $[M^{-1}cm^{-1}]$ is the extinction coefficient for the i^{th} chromophore, C_i $[\mu M]$ is the concentration of the i^{th} chromophore, and μ_a^o is a background absorption coefficient. The extinction coefficients ε are generally known for the chromophores of interest [215] (see Figure 2.12). If diffuse optical measurements are made at multiple wavelengths, *i.e.*, multi-spectrally, Equation 2.176 becomes a system of equations that can be solved for the chromophore concentrations. Given the nature of systems of equations, the number of chromophore concentrations that can be distinguished is dependent on the number of unique wavelengths used. For example, two wavelengths, if properly chosen, can be enough to determine the concentrations of HbO_2 and HHb; the ideal pair of wavelengths is one between 660 and 760 nm and another at 830 nm [34; 261]. However, given the experimental uncertainties inherent in the measurements, quantification is often improved by including more wavelengths than unknown fitted parameters.

For many applications, fitting for the four previously mentioned chromophores obviates the need to include a background absorption coefficient μ_a^o in the fitting algorithm. However, there are other chromophores that significantly contribute to absorption in certain tissues, such as myoglobin in muscle [66; 64] or collagen in the breast [243; 272]. If the concentration of these or other

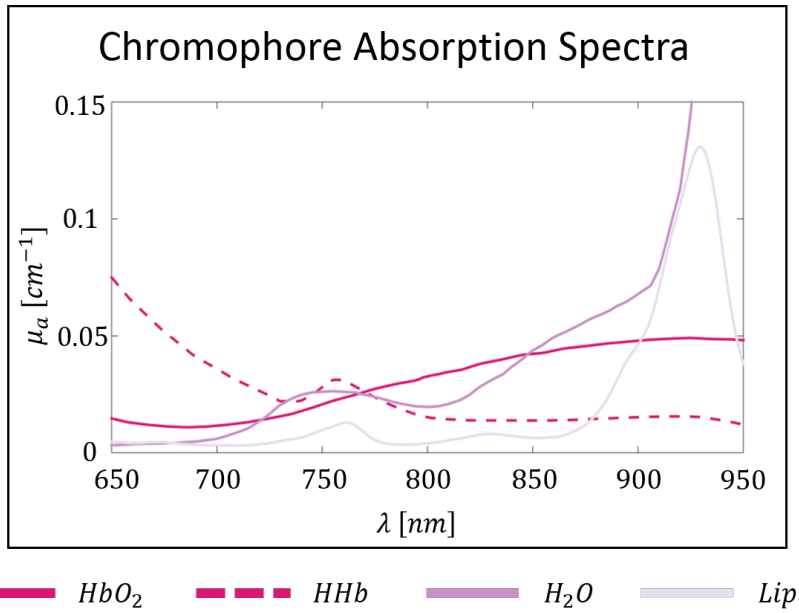

Figure 2.12: Chromophore Absorption Spectra in the Physiological Window. The absorption coefficients due to four different tissue chromophores, oxy-hemoglobin HbO_2, deoxy-hemoglobin HHb, water, and lipid, for typical chromophore concentrations are plotted [215; 148]. This wavelength range represents the so-called physiological window where tissue absorption is low enough to allow depth penetration of greater than several centimeters. The known extinction coefficients for these chromophores can be used in concert with the reconstructed μ_a value to determine chromophore concentrations.

chromophores are not determined through multi-spectral fitting, the absorption due to them can be subsumed into the background absorption coefficient μ_a^o. The most common multi-spectral measurements in diffuse optics calculate only the HbO_2 and HHb concentrations, which allows for the determination of the total hemoglobin concentration ($Hb_T = HbO_2 + HHb$) and the tissue oxygen saturation ($S_tO_2 = HbO_2/Hb_T$). The absorption due to water, lipid, and other parameters are then assumed from a population average for a given tissue [215; 148; 99]. Note that the concentrations described here are the concentrations of the given chromophores in *tissue*, not in blood. Therefore, the fitted hemoglobin concentrations, for example, will be much lower than typical hemoglobin concentrations in blood.

2.8.2 Mie Scattering Model

As with the absorption coefficient, the reduced scattering coefficient μ_s' is also wavelength dependent. In tissue, there are many particles, including proteins, organelles, and cells, with sizes on the

order of near-infrared wavelengths ($\sim 50\,nm$ to $10\mu\,m$), and therefore, near-infrared light undergoes Mie-type scattering with a weak wavelength dependence and a bias towards forward scattering [184; 186], as opposed to the Rayleigh scattering that would occur for smaller particles [137]. Thus, the reduced scattering coefficient can be expressed as

$$\mu_s'(\lambda) = A\left(\frac{\lambda}{\lambda_o}\right)^{-b}, \tag{2.177}$$

where λ_o is a reference wavelength, A is the scattering amplitude, and b is the scattering power. With measurements performed at multiple wavelengths, the wavelength-independent tissue parameters A and b can be determined. In practice, b is often assumed based on a population- or phantom-derived average [148] while a fit for A is performed.

2.8.3 Multi-spectral Fitting

In practice, there are two methods of determining the chromophore concentrations and tissue scattering parameters:

1. Perform separate fits of the Green's function solutions for μ_a and μ_s' at each measured wavelength. Then, optimize the chromophore concentrations and scattering parameters using Equations 2.176 and 2.177.

2. Perform a multi-spectral fit, wherein the fluence rates at all measured wavelengths are fit simultaneously. In this method, the models for μ_a and μ_s' in Equations 2.176 and 2.177 are built into the Green's function or DOT solutions [79; 78; 240; 25], and the chromophore concentrations C_i and tissue scattering parameters A and b are fit directly.

Multi-spectral reconstructions using the known chromophore extinction coefficients and Mie scattering model have been shown to produce more robust calculations of tissue parameters [79; 240; 102] because utilizing data from every wavelength better constrains the fitting algorithm [78]. For multi-spectral DOT, every reconstruction step discussed previously remains the same except the fit parameters are now the wavelength-independent chromophore concentrations, *e.g.*, HHb and HbO_2, and scattering properties in each voxel. The measurement vector $\vec{\phi}$ must then include the amplitude and phase data for all source-detector pairs and all measured wavelengths. Thus, a multi-spectral reconstruction is also more computationally intensive than a single-wavelength reconstruction but generally requires less computation than multiple, separate single-wavelength reconstructions.

2.9 Diffuse Correlation Spectroscopy

DOS and DOT generally measure static tissue properties, such as μ_a, μ_s', and the concentrations of oxy- and deoxy-hemoglobin, water, and lipid. Diffusive near-infrared light can also measure dynamic properties, though. Specifically, a technique called Diffuse Correlation Spectroscopy (DCS) can be used to measure the motion of the red blood cells that scatter light in tissue, providing a biomarker of blood flow.

2.9.1 Dynamic Light Scattering - Single Scattering Event

In the limit where light is introduced to a medium, undergoes a single scattering event, and is then collected by a detector, a mathematical description of dynamic light scattering is relatively simple. If a detector measures light at two time points, separated by a time offset τ, there will be an interference, or speckle, pattern [35] caused by photon propagation path-length changes. A normalized temporal auto-correlation function at these two time points for the electric field $\vec{E}$ of the light can be defined as [28; 74; 48; 98]

$$g_1(\tau) \equiv \frac{\left\langle \vec{E}^*(t) \cdot \vec{E}(t+\tau) \right\rangle}{\left\langle \left| \vec{E}(t) \right|^2 \right\rangle} = e^{\imath 2\pi f \tau} \, e^{-q^2 \left\langle \Delta r^2(\tau) \right\rangle / 6}. \tag{2.178}$$

Here, $\vec{E}^*$ is the complex conjugate of $\vec{E}$, the brackets represent a time average for experimental collection, f is the frequency of the light, and q is the magnitude of the difference between the input and output wave vectors k. This auto-correlation function will decay as a function of how far the scattering particles move from their original positions over the time delay τ. This motion can be characterized as an ensemble average of the mean-square displacement $\left\langle \Delta r^2(\tau) \right\rangle$ [48]. In most experimental setups, the detector measures intensity I rather than the electric field. Thus, only the normalized intensity auto-correlation function g_2 can be measured. Here, g_2 is defined as

$$g_2(\tau) \equiv \frac{\langle I(t)\, I(t+\tau) \rangle}{\langle I(t) \rangle^2}, \tag{2.179}$$

where the intensity $I(t) \equiv \left| \vec{E}(t) \right|^2$. In order to extract the electric field auto-correlation function g_1 from the intensity auto-correlation function g_2, the Siegert relation [162], defined as follows, can be used:

$$g_2(\tau) = 1 + \beta \, |g_1(\tau)|^2 . \tag{2.180}$$

Here, β is a constant that is a measure of the magnitude of the speckle intensity relative to the average intensity and is dependent on the system instrumentation [126; 22]. In an ideal setup,

$\beta = 1$ for completely polarized light and $\beta = 0.5$ for completely unpolarized light [33; 22]. If β is too close to 0, then there is not enough detectable contrast due to the intensity fluctuations to perform a significant measurement.

2.9.2 Dynamic Light Scattering - Multiple Scattering Events

Because tissue is highly scattering, the single scattering framework must be extended to the multiple scattering domain in order to derive physiological parameters from this correlation analysis. One method of analyzing this scenario, called Diffusing Wave Spectroscopy (DWS), has been developed extensively for light scattering in colloids [209; 172; 268]. DWS relies on the measurement of the change in phase for different photon random-walk paths after a delay time τ [98]. An alternative analysis scheme developed a transport model for the temporal auto-correlation function [6; 93] that is analogous to the RTE (see Equation 2.1). This correlation transport equation describes the transport of the direction-dependent un-normalized electric field auto-correlation function $G_1^\top$, which is defined as

$$G_1^\top(\vec{r}, \hat{\Omega}, \tau) = \left\langle \vec{E}^*(\vec{r}, \hat{\Omega}, t) \cdot \vec{E}(\vec{r}, \hat{\Omega}, t+\tau) \right\rangle. \tag{2.181}$$

The transport relation is then

$$\vec{\nabla} G_1^\top(\vec{r}, \hat{\Omega}, \tau)\hat{\Omega} = \\ -\mu_t(\vec{r}) G_1^\top(\vec{r}, \hat{\Omega}, \tau) + Q(\vec{r}, \hat{\Omega}) + \mu_s \int_{4\pi} G_1^\top(\vec{r}, \hat{\Omega}', \tau)\, g_1^s(\hat{\Omega}, \hat{\Omega}', \tau)\, f(\hat{\Omega}, \hat{\Omega}')\, d\Omega'. \tag{2.182}$$

Here, g_1^s is the normalized electric field auto-correlation function for a single scattering event (see Equation 2.178), and all other quantities are defined as in the radiative transport equation (Equation 2.1). In comparing the two transport equations, it is apparent that $G_1^\top$ is analogous to the direction-dependent radiance L. Therefore, if the appropriate assumptions are made and the P_1 approximation (see Section 2.2) is applied, a diffusion equation can be derived for a direction-independent un-normalized field auto-correlation function G_1 [33; 32], which is analogous to the fluence rate and defined as

$$G_1(\vec{r}, \tau) \equiv \int_{4\pi} G_1^\top(\vec{r}, \hat{\Omega}, \tau)\, d\Omega = \left\langle \vec{E}^*(\vec{r}, t) \cdot \vec{E}(\vec{r}, t+\tau) \right\rangle. \tag{2.183}$$

The correlation diffusion equation then takes the form

$$\vec{\nabla} \cdot \left[D(\vec{r}) \vec{\nabla} G_1(\vec{r}, \tau) \right] - \left[v\, \mu_a(\vec{r}) + \frac{\alpha}{3} v \mu_s' \kappa_o^2 \left\langle \Delta r^2(\tau) \right\rangle \right] G_1(\vec{r}, \tau) = -v\, S(\vec{r}), \tag{2.184}$$

where α is the fraction of scattering events that involve moving scatterers, $\kappa_o = 2\pi/\lambda$ is the wavenumber for the light, and $\left\langle \Delta r^2(\tau) \right\rangle$ is the mean-square displacement of the moving scatterers

defined in Section 2.9.1. All other parameters are defined in the same way as the fluence rate diffusion equation. It is clear, then, that Equation 2.184 has an identical form to the CW fluence rate diffusion equation except for a modification to the absorption coefficient term that contains the dynamic information. Because of this, solutions for G_1 will obey the same boundary conditions and have the same Green's function solutions as Φ. The only modification will be that, instead of the quantity k, as defined in Equation 2.72, the decay constant will be K, defined as

$$K = \sqrt{\frac{v\left[\mu_a + \frac{\alpha\,\mu_s'\,k_o^2\left\langle\Delta r^2(\tau)\right\rangle}{3}\right]}{D}}, \tag{2.185}$$

and the infinite homogeneous medium solution will be

$$G_1(\vec{r},\tau) = \frac{v}{4\pi D}e^{-Kr}. \tag{2.186}$$

As with the single scattering case, instruments will generally measure the light intensity and use hardware [32] or software [252] correlation to calculate the auto-correlation function G_2, defined as

$$G_2(\vec{r},\tau) = \langle I(\vec{r},t)I(\vec{r},t+\tau)\rangle\,. \tag{2.187}$$

Thus, the Siegert equation (Equation 2.180) must again be applied. For multiple scattering, this relation is only valid if almost all of the photons undergo at least one scattering event caused by a moving scatterer [98]. Because of the extremely high scattering coefficient and preponderance of moving scatterers, this condition is typically met in tissue. A schematic of the effect of moving scatterers on measured intensity and the intensity auto-correlation function can be found in Figure 2.13.

2.9.3 Physiological Meaning of Blood Flow Index

As with diffuse optical spectroscopy, the correlation diffusion equation can be solved for the effective optical properties of the medium and fit to values of G_2 measured at a range of delay times τ. In this case, the optical properties are the diffusion coefficient D and the effective absorption coefficient that is dependent on the real absorption coefficient μ_a, the reduced scattering coefficient μ_s', and the term $\alpha\left\langle\Delta r^2(\tau)\right\rangle$. As mentioned previously, α is the fraction of scattering events that involve moving scatterers. Because the primary dynamic scatterers are red blood cells, this fraction α is proportional to the tissue blood volume fraction, *i.e.* $\frac{V_{Blood}}{V_{Tissue}}$ [32; 22]. The mean-square displacement $\left\langle\Delta r^2(\tau)\right\rangle$ is dependent on the motion of the red blood cells. In DCS, Brownian motion appears to be the best model for the motion of the red blood cells [97; 101; 98; 37]. Red blood cells traveling through narrow capillaries will experience significant shear-induced diffusive

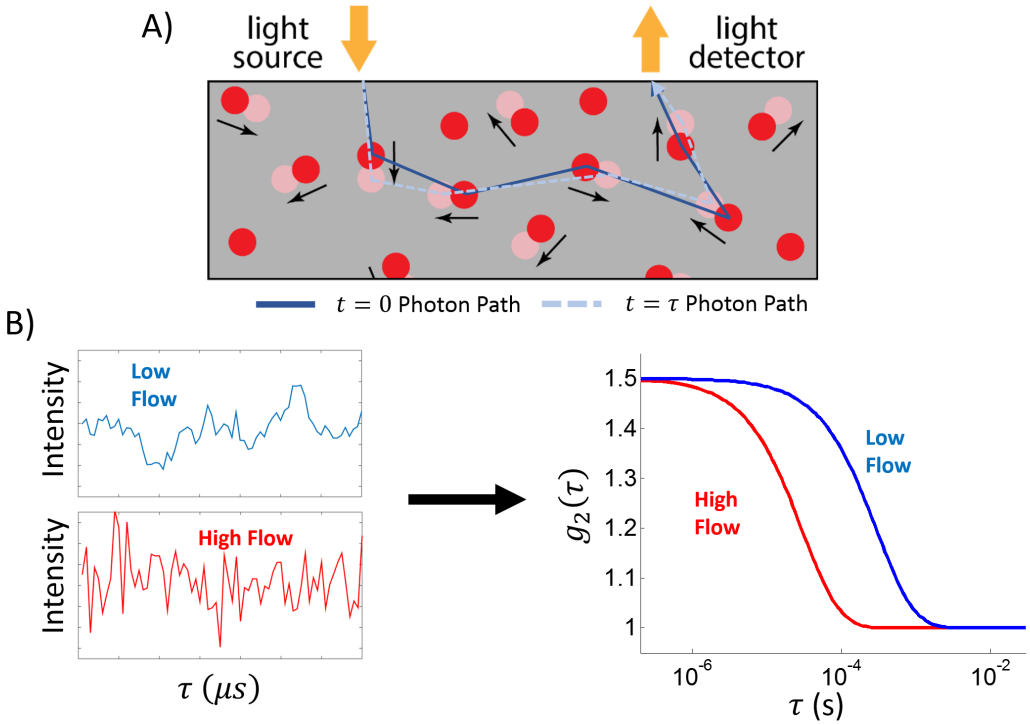

Figure 2.13: Effect of Moving Scatterers on Intensity Auto-Correlation. Diffuse Correlation Spectroscopy (DCS) utilizes an intensity auto-correlation function to measure the motion of red blood cells and thus provides an index of blood flow. A) If tissue scatterers, like red blood cells, are moving, light measured at times offset by a time delay τ will follow different paths. This path-length difference will lead to an interference, or speckle, effect that can be measured with an auto-correlation function. If the red blood cells are moving faster, the mean-square distance $\langle \Delta r^2(\tau) \rangle$ traversed by the cells will be larger, and thus the path light travels at time $t = \tau$ will be less correlated with the path the light traveled at time $t = 0$. B) Faster blood flow will lead to more significant intensity fluctuations than slow blood flow. This, in turn, leads to a more rapid decay of the intensity auto-correlation function g_2 for fast blood flow than for slow flow. This figure is adapted from a similar figure in the PhD Thesis of Wesley B. Baker [22].

motion in addition to the laminar forward flow [37]. Since DCS is primarily sensitive to blood flow in the microvasculature, it makes sense that a diffusive model best fits the data [98]. In this case, the mean-square displacement can be related to a Brownian diffusion coefficient D_B, such that

$$\langle \Delta r^2(\tau) \rangle = 6 D_B \tau. \tag{2.188}$$

In practice, it is difficult to simultaneously fit for the absorption, reduced scattering, α, and $\langle \Delta r^2(\tau) \rangle$. Doing so requires many source-detector pairs or an extension to Time-Domain DCS, which both require more expensive and complex instrumentation [242; 199]. Thus, μ_a and μ_s' are

generally treated as inputs, either calculated via DOS or assumed from population-average values, while $\alpha \left\langle \Delta r^2(\tau) \right\rangle$ is calculated from the fitting algorithm. Accurately measured optical properties significantly reduce the errors in the fit for αD_B and cross-talk between optical and flow properties [147; 114; 264; 76]. There is no simple method for individually calculating α and D_B using DCS; therefore, the combined quantity is calculated and designated as the a blood flow index BFI where

$$BFI = \alpha D_B. \tag{2.189}$$

This blood flow index is dependent on both the blood volume fraction and the red blood cell diffusion dynamics and has units of $cm^2 s^{-1}$. Thus, BFI is not measured in the traditional blood flow units used clinically, often $\frac{mL\,Blood/minute}{100\,mL\,of\,Tissue}$, and the blood volume fraction α can potentially confound the true flow measurement of BFI. However, this BFI has been validated in humans using several gold-standard flow-measuring techniques [182], including transcranial Doppler ultrasound [50], xenon contrast-enhanced computed tomography [158], and phase-encoded velocity mapping MRI [51; 151]. It appears, therefore, that BFI is proportional to the true blood flow. Though it is unnecessary for many applications, including the one discussed in Chapter 4, BFI can also be calibrated to absolute blood flow units using DOS techniques [91; 170].

2.9.4 DCS Instrumentation

The instrumentation used for DCS is similar to that required to perform DOS. This enables reasonably seamless integration of the two technologies to measure static and hemodynamic tissue properties simultaneously [69; 96; 97; 273; 158; 76]. However, there are several specific experimental considerations for DCS that are not applicable to DOS. For example, DCS requires a long-coherence length laser, generally with a coherence length greater than $5\,m$. Loss of coherence at the source can confound the ability of an instrument to resolve the broadening of the power spectrum due to the motion of red blood cells [32; 97; 22]. Single-mode, or potentially few-mode, optical fibers are also required for detection to prevent modal noise [97; 126; 22]. These single-mode fibers have much lower signal, though, than the multi-mode fibers used for DOS. Thus, DCS requires very high sensitivity avalanche photodiodes (APDs), often utilizes parallel detection, and can still suffer from a lack of signal at long source-detector separations [98; 22]. This signal consideration is more of an issue for highly absorbing tissue, *e.g.* brain and muscle, than it is for the DCS measurements in breast tissue discussed in Chapter 4.

2.10 Statistical Techniques

In addition to the standard analysis necessary to perform DOS, DOT, and DCS, the development of novel biomarkers requires statistical analysis of the reconstructed optical properties and physiological parameters for correlation with clinical diagnoses and outcomes. In the context of the work presented here, these statistical techniques fall into three categories:

1. **Z-Score Normalization**. Tissue optical properties and hemodynamic parameters display significant inter- and intra-subject heterogeneity. Thus, choosing the proper normalization technique, *e.g.*, for tumor properties with respect to normal tissue, is of paramount importance. The method demonstrated to provide the most value in the analysis presented here is z-score normalization, in which a healthy tissue mean value for a given parameter is subtracted from the tumor value and this difference is divided by the standard deviation of the normal tissue measurements. Section 2.10.1 contains a full description of this method and its statistical benefits.

2. **Logistic Regression**. Two common applications of diffuse-optically measured parameters in breast cancer are diagnosis, *e.g.*, distinguishing malignant tissue from benign tissue, and prognosis, *e.g.*, predicting responders versus non-responders to chemotherapy. These are both classification learning problems, which are addressed here using logistic regression, a technique discussed in detail in Section 2.10.2.

3. **Regression Model Evaluation**. The final step in developing useful biomarkers is to evaluate the the quality of the models that are produced. This quality is typically determined by two factors: discriminatory ability and calibration. Here, the discriminatory ability, *i.e.*, the model's ability to differentiate between the positive and negative groups, is determined by receiver operating characteristic analysis (Section 2.10.3) and the calibration, *i.e.*, the degree to which predicted probabilities correspond to actual probabilities, is characterized with Hosmer-Lemeshow analysis (Section 2.10.4).

2.10.1 Z-Score Normalization

The simplest DOS metric would be an un-normalized value of one of the -measured parameters, *e.g.*, S_tO_2. Another common metric is tissue-to-normal ratio-normalized data $S_tO_{2_{T/N}}$, wherein a measured S_tO_2 value is divided by the average S_tO_2 of a known normal tissue region. This $S_tO_{2_{T/N}}$ quantity improves upon the un-normalized S_tO_2 by accounting for the inter-subject variability in the systemic levels of DOS-measured physiological parameters (see Example 1 in Figure 2.14). However,

healthy breast tissue also exhibits significant intra-subject heterogeneity in these quantities [99; 230; 56]. This variation is not accounted for in the tumor-to-normal ratio normalization technique. Thus, $StO2_{T/N}$ provides no indication of whether a value is within the expected range of the normal tissue $StO2$ due to heterogeneity or whether the value is significantly different from the healthy tissue. To resolve this issue, the normalization technique needs to account for both the mean and the standard deviation of the normal tissue $StO2$ (see Example 2 in Figure 2.14). A z-score normalization scheme has been previously developed for this purpose with respect to differentiating malignant and healthy tissue [56; 55] (see Chapter 5).

Briefly, the natural logarithm of each data point is first taken because the log-data for each parameter was empirically determined to be more normally distributed, *i.e.*, Gaussian, across healthy tissue than the raw data [56]. Gaussian distributions, which are well-characterized by a mean and standard deviation, enable the use of z-scores, which are a measure of how many standard deviations away from the mean a given data point is [257]. These z-scores can provide a quantitative measure of how likely it is that a data point belongs to a given distribution; in this case, the z-scores measure whether a tumor physiological parameter is significantly different from the same quantity in healthy tissue.

To transform raw tumor data into z-score data, the mean and standard deviation of a normal (healthy) region of tissue is used as in Equation 3.1

$$Z_j = \frac{\ln X_j - \langle \ln X_{j_{Norm}} \rangle}{\sigma \left[\ln X_{j_{Norm}} \right]}. \tag{2.190}$$

Here, X_j is the un-normalized j^{th} measured parameter in the tumor region, $X_{j_{Norm}}$ is the un-normalized j^{th} measured parameter in a normal (healthy) region of either the tumor-bearing breast or the contralateral breast,$\langle \ln X_{j_{Norm}} \rangle$ represents the mean over all points in the normal (healthy) region, and $\sigma \left[\ln X_{j_{Norm}} \right]$ represents the standard deviation over all points in the normal (healthy) region. Z_j is then the tumor region z-score relative to the healthy tissue for the j^{th} parameter.

Thus, every tumor data point is measured in units of standard deviations from the mean of a given parameter in healthy tissue. In addition to transforming all parameters to be approximately the same magnitude, this method better accounts for the inter-subject systemic variations by finding the difference of each parameter from the mean value of the normal (healthy) tissue. It also more fully accounts for intra-subject variation in healthy tissue by normalizing with the healthy tissue standard deviation. Finally, this techniques transforms the normal tissue measurements such that they more closely obey a normal Gaussian distribution, which improves statistical robustness [206; 136; 141]. A concrete example of the benefit of this statistical transformation scheme is

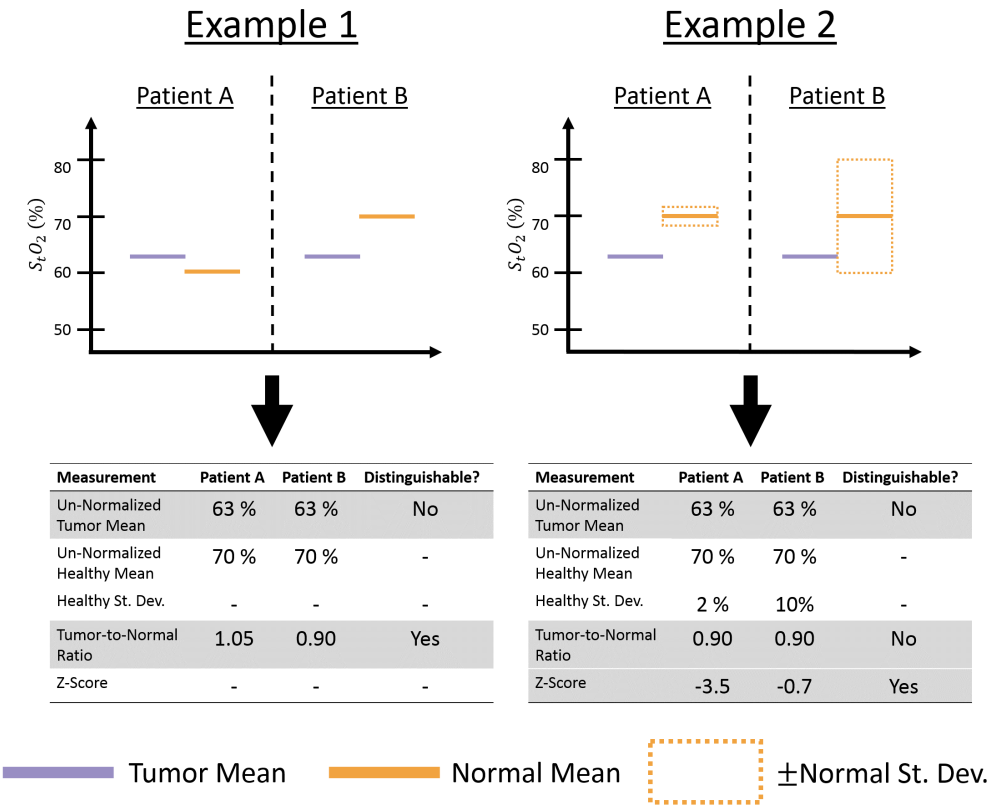

Measurement	Patient A	Patient B	Distinguishable?
Un-Normalized Tumor Mean	63 %	63 %	No
Un-Normalized Healthy Mean	70 %	70 %	-
Healthy St. Dev.	-	-	-
Tumor-to-Normal Ratio	1.05	0.90	Yes
Z-Score	-	-	-

Measurement	Patient A	Patient B	Distinguishable?
Un-Normalized Tumor Mean	63 %	63 %	No
Un-Normalized Healthy Mean	70 %	70 %	-
Healthy St. Dev.	2 %	10%	-
Tumor-to-Normal Ratio	0.90	0.90	No
Z-Score	-3.5	-0.7	Yes

Figure 2.14: Normalization to Account for Inter- and Intra-Subject Heterogeneity. Example 1 - Here, Patient A and Patient B are indistinguishable if only the un-normalized S_tO_2 tumor values are considered. However, if tumor-to-normal ratio normalization is performed by dividing the mean tumor tissue value by the mean normal tissue value, it appears that Patient A's tumor is hyperoxic relative to the normal tissue, while Patient B's tumor is hypoxic. Thus, Tumor-to-Normal normalization was able to account for systemic inter-subject variation. Example 2 - Here, Patient A and Patient B are indistinguishable with either un-normalized or tumor-to-normal data. However, if the normal tissue standard deviation is included, it is clear that Patient B has much more heterogeneous normal tissue. Accounting for this variation, via a z-score, enables a more accurate measure of whether each tumor oxygen saturation falls within the expected range of the normal tissue. Thus, the z-score normalization can account for both inter- and intra-subject heterogeneity.

shown in Figure 2.15 for Early time-point tissue oxygen saturation in the ACRIN-6691 multi-site trial subject cohort (see Chapter 3).

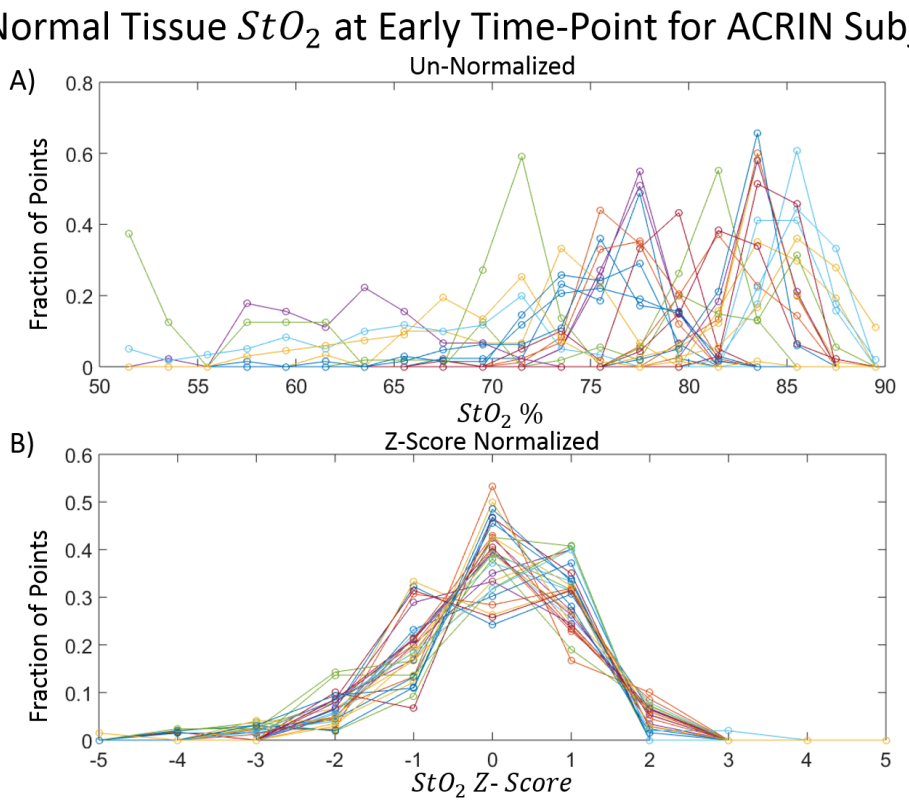

Figure 2.15: Histograms of the Early Normal Tissue S_tO_2. A) Fractional histograms of the un-normalized S_tO_2 of the normal tissue on the tumor-bearing breast at the Early time-point for each subject. Each line represents a different subject. B) Fractional histograms of the z-score normalized log-transformed S_tO_2 data of the normal tissue on the tumor-bearing breast at the Early time-point for each subject. Each line represents a different subject. Note that with the z-score normalization, the distributions for all subjects have the same means and approximately Gaussian distributions; this effect is consistent across all measured parameters and time-points. Features that obey Gaussian distributions typically produce more statistically robust models.

2.10.2 Binomial Logistic Regression

Logistic regression is one of the most common machine learning techniques for classification. This research utilizes binomial logistic regression, *i.e.*, regression against a dichotomous qualitative variable. Here, the two classifications are either malignant and healthy tissue, for Chapter 5, or complete responder or non-complete responder to chemotherapy, for Chapter 3. Full derivations of the logistic regression algorithm can be found in [257; 136; 141].

Binomial logistic regression is always performed over a set of independent variables which are typically different observed parameters for each subject in the dataset. Here the independent

variables will be represented by $\vec{Z}^i$, where

$$\vec{Z}^i = \left[Z_1, Z_2, \ldots, Z_{N_j}\right]^i. \tag{2.191}$$

Thus Z_j^i is the the j^{th} measured parameter (out of N_j parameters) for the i^{th} subject (out of N_i subjects) in the dataset. The i^{th} subject is also classified by a binary response variable Y^i, which can take only two values, 0 or 1.

Now a probability for achieving a certain state Y for a given set of observed parameters $\vec{Z}$ must be defined. Unsurprisingly, in this case, this probability is defined using a logistic function, which has the advantage of transforming any real number from $-\infty$ to ∞ onto the range 0 to 1, a necessary condition for probability. The probability of the i^{th} subject being a member of the set $Y = 1$, given the measured parameters $\vec{Z}^i$ for the i^{th} subject, is defined as

$$\mathcal{P}^i = Prob\left(Y^i = 1|\vec{Z}^i\right) \equiv \frac{\exp\left(\beta_o + \sum_{j=1}^{N_j} \beta_j \cdot Z_j^i\right)}{1 + \exp\left(\beta_o + \sum_{j=1}^{N_j} \beta_j \cdot Z_j^i\right)} = \frac{1}{1 + \exp\left(-\beta_o - \sum_{j=1}^{N_j} \beta_j \cdot Z_j^i\right)}. \tag{2.192}$$

Here, $\vec{\beta} = \left[\beta_o, \beta_1, \ldots, \beta_{N_j}\right]$ is a weight vector for each measured parameter with an intercept term β_o.

The logit, or log-odds function is then defined as

$$logit\left(\mathcal{P}^i\right) \equiv \ln\left(\frac{\mathcal{P}^i}{1 - \mathcal{P}^i}\right). \tag{2.193}$$

Thus, the log-odds is defined as the natural logarithm of the ratio of the probability of being in the positive $Y = 1$ state to the probability of being in the negative $Y = 0$ state. Substituting Equation 2.192 into the definition of the logit function results in

$$logit(\mathcal{P}^i) = \beta_o + \sum_{j=1}^{N_j} \beta_j \cdot Z_j^i. \tag{2.194}$$

This log-odds definition is called the malignancy parameter $\mathcal{M}$ in Chapter 5 and the response parameter $\mathcal{R}$ in Chapter 3.

Unlike linear regression, minimization using a least-squares method is not applicable to logistic regression because the dependent variables are classifications rather than numeric values. Thus, a term known as the likelihood L is defined such that

$$L = \prod_{i=1}^{N_i} \left(\mathcal{P}^i\right)^{Y^i} \left(1 - \mathcal{P}^i\right)^{1-Y^i}, \tag{2.195}$$

where N_i is the number of subjects, Y^i is the actual classification state for the i^{th} subject, and $\mathcal{P}^i$ is the probability that the i^{th} subject is in the $Y = 1$ state. The likelihood L is larger if subjects

in the $Y = 1$ state have probabilities close to 1 while subjects in the $Y = 0$ state have probabilities close to 0. Given the definition of $\mathcal{P}^i$ from Equation 2.192, the likelihood for a given weight vector $\vec{\beta}$ can be written as

$$L\left(\vec{\beta}\right) = \prod_{i=1}^{N_i} \frac{\exp\left(Y^i\left(\beta_o + \sum_{j=1}^{N_j} \beta_j \cdot Z_j^i\right)\right)}{1 + \exp\left(\beta_o + \sum_{j=1}^{N_j} \beta_j \cdot Z_j^i\right)}. \tag{2.196}$$

The goal of the logistic regression algorithm is to maximize this likelihood parameter L by optimizing $\vec{\beta}$. By inspection, it is clear that when $Y^i = 0$, the term inside the product is maximized as the log-odds term goes to $-\infty$. Conversely, if $Y^i = 1$, the term inside the product is maximized as the log-odds term goes to $+\infty$. Thus, an optimal weight vector $\vec{\beta}$ will produce highly negative log-odds for subjects with $Y = 0$ and highly positive values for subjects with $Y = 1$. This is consistent with the logistic definition of $\mathcal{P}$, the probability of being in state $Y = 1$. A highly positive log-odds leads to $\mathcal{P} \to 1$, and a highly negative log-odds leads to $\mathcal{P} \to 0$. A log-odds of 0 corresponds to $\mathcal{P} = 0.5$. In practice, the optimal weight vector $\vec{\beta}$ to maximize the likelihood is usually determined using some sort of Newtonian update algorithm (see Section 2.6.6) [3].

2.10.3 Receiver Operating Characteristic (ROC) Analysis

Receiver operating characteristic (ROC) analysis is a common method for assessing the discriminatory ability of a classification model, *i.e.*, a model that produces a probability metric for membership in a given class. For this research, the two classifications types are: malignant versus healthy tissue or malignant versus benign lesions (Chapter 5), and complete responder versus non-complete responder to chemotherapy (Chapter 3). The example below will describe the ROC method in terms of the malignant versus healthy tissue classification probability $\mathcal{P}_M$; however, this discussion is readily transferable to the responder versus non-responder model with probability $\mathcal{P}_R$.

ROC analysis is predicated on setting some cutoff value $\mathcal{P}_{M_c}$ for the probability of malignancy metric $\mathcal{P}_M$, such that any data point with probability of malignancy above the cutoff is predicted to be positive, *i.e.*, malignant tissue; analagously, any point below the cutoff is predicted to be negative, *i.e.*, normal tissue. Thus all of the points in the test dataset can be divided into four categories:

1. True Positives: actually malignant and predicted to be malignant due to a $\mathcal{P}_M > \mathcal{P}_{M_c}$
2. True Negatives: actually healthy and predicted to be healthy due to a $\mathcal{P}_M < \mathcal{P}_{M_c}$
3. False Positives: actually healthy but predicted to be malignant due to a $\mathcal{P}_M > \mathcal{P}_{M_c}$

4. False Negatives: actually malignant but predicted to be healthy due to a $\mathcal{P}_M < \mathcal{P}_{M_c}$.

Figure 2.16A contains a graphical representation of these classifications. In that example, there are 15 true positives, 16 true negatives, 5 false positives, and 4 false negatives.

Given these four categories, four different measures of accuracy can also be obtained:

1. True Positive Rate: fraction of actually malignant tissues predicted to be malignant. This is also known as the sensitivity.

$$TPR = Sensitivity \equiv \frac{\#\,True\,Positives}{\#\,True\,Positives\,+\,\#\,False\,Negatives} \tag{2.197}$$

2. False Positive Rate: fraction of actually healthy tissues predicted to be malignant. The quantity $(1 - False\,Positive\,Rate)$ is also known as the specificity

$$FPR = 1 - Specificity \equiv \frac{\#\,False\,Positives}{\#\,True\,Negatives\,+\,\#\,False\,Positives} \tag{2.198}$$

3. Positive Predictive Value: fraction predicted to be malignant that are actually malignant

$$PPV \equiv \frac{\#\,True\,Positives}{\#\,True\,Positives\,+\,\#\,False\,Positives} \tag{2.199}$$

4. Negative Predictive Value: fraction predicted to be healthy that are actually healthy

$$NPV \equiv \frac{\#\,True\,Negatives}{\#\,True\,Negatives\,+\,\#\,False\,Negatives} \tag{2.200}$$

These quantities are also described graphically in Figure 2.17, in which a cutoff of $\mathcal{P}_{M_c} = 0.5$ was chosen. In this example, $TPR\,(Sensitivity) = \frac{15}{15+4} = 0.789$, $FPR = \frac{5}{16+5} = 0.238$ ($Specificity = 0.762$), $PPV = \frac{15}{15+5} = 0.75$, and $NPV = \frac{16}{16+4} = 0.8$.

Varying the cutoff value $\mathcal{P}_{M_c}$ alters the number of data points in each of the four groups (see Figure 2.16B-C). For example, increasing $\mathcal{P}_{M_c}$ leads to a lower true positive rate and a lower false positive rate. Conversely, decreasing $\mathcal{P}_{M_c}$ results in both a higher true positive rate and higher false positive rate. Thus, for practical use, it is necessary to optimize $\mathcal{P}_{M_c}$ to balance these competing effects. One common method is to find the value of $\mathcal{P}_{M_c}$ that maximizes the sum of the sensitivity and specificity [115]. For a quality prediction model, this results in a high true positive rate and a low false positive rate. The overall predictive accuracy for a given cutoff can then be defined as

$$Accuracy \equiv \frac{\#\,True\,Pos\,+\,\#\,True\,Neg}{\#\,True\,Pos\,+\,\#\,True\,Neg\,+\,\#\,False\,Pos\,+\,\#\,False\,Neg}. \tag{2.201}$$

For the data shown in Figure 2.17, the overall classification accuracy is 70 %. Figures 2.16 and 2.18 demonstrate how each of these accuracy parameters changes for the model dataset in Figure

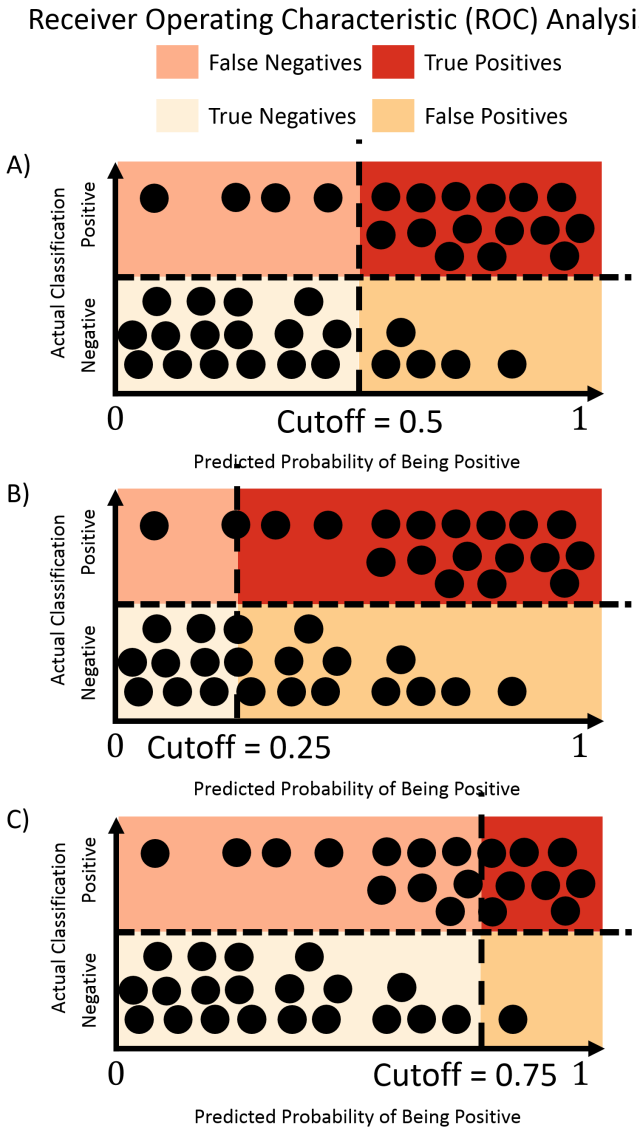

Figure 2.16: Receiver Operating Characteristic (ROC) Analysis. An example dataset is graphed such that the y-axis represents the true binomial classification, either positive or negative, of every data point, and the x-axis is the predicted probability of a data point being positive. A cutoff value for the probability $\mathcal{P}_{M_c}$ can be chosen, above which all data points are predicted to be positive, and below which all data points are predicted to be negative. This results in four possible classifications for each data point: 1) True Positives: actually positive and predicted to be positive, 2) True Negatives: actually negative and predicted to be negative, 3) False Positives: actually negative but predicted to be positive, and 4) False Negatives: actually positive but predicted to be negative. Note that the number of data points in each of these groups is determined by the cutoff value $\mathcal{P}_{M_c}$ that is chosen. A) displays a cutoff of $\mathcal{P}_{M_c} = 0.5$, B) shows a cutoff of $\mathcal{P}_{M_c} = 0.25$, and C) has a cutoff of $\mathcal{P}_{M_c} = 0.75$. Higher $\mathcal{P}_{M_c}$ cutoffs lead to more true negatives and false negatives while lower $\mathcal{P}_{M_c}$ values lead to more true positives and false positives.

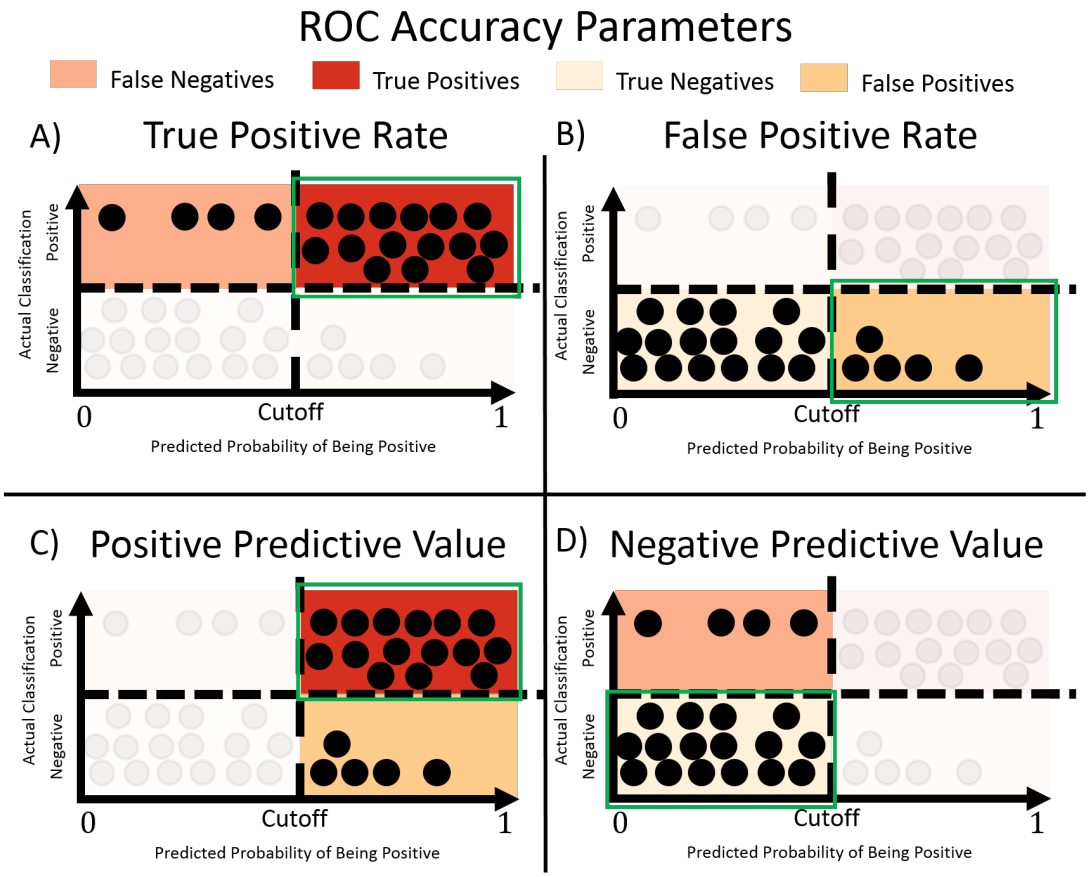

Figure 2.17: ROC Accuracy Parameters. The four most commonly used accuracy parameters for ROC analysis are displayed graphically. Each accuracy parameter can generally be thought of as the fraction of two ROC classification groups, *e.g.*, false positive and false negative, or false positive and true positive, that fall into a single one of those classification groups. Thus, for each parameter in this figure, the denominator of this fraction is the sum of data points across the two highlighted, colorful regions, and the numerator is the number of data points in the region encased by the green rectangle. Four parameters are shown: A) True Positive Rate (TPR): number of true positives divided by all actual positives, B) False Positive Rate (FPR): number of false positives divided by all actual negatives, C) Positive Predictive Value (PPV): number of true positives divided by all predicted positives, and D) Negative Predictive Value (NPV): number of true negatives divided by all predicted negatives.

2.16 given different $\mathcal{P}_{M_c}$ values. In general, higher $\mathcal{P}_{M_c}$ cutoffs lead to improvement in specificity and positive predictive value while lower $\mathcal{P}_{M_c}$ values provide better sensitivity and negative predictive value.

A more holistic measure of the discriminatory ability of a prediction model is the so-called area under the ROC curve (AUC). The ROC curve is created by plotting the true positive rate vs the false positive rate for a range of cutoff values from 0 to 1. When $\mathcal{P}_{M_c} = 0$, all data points will be

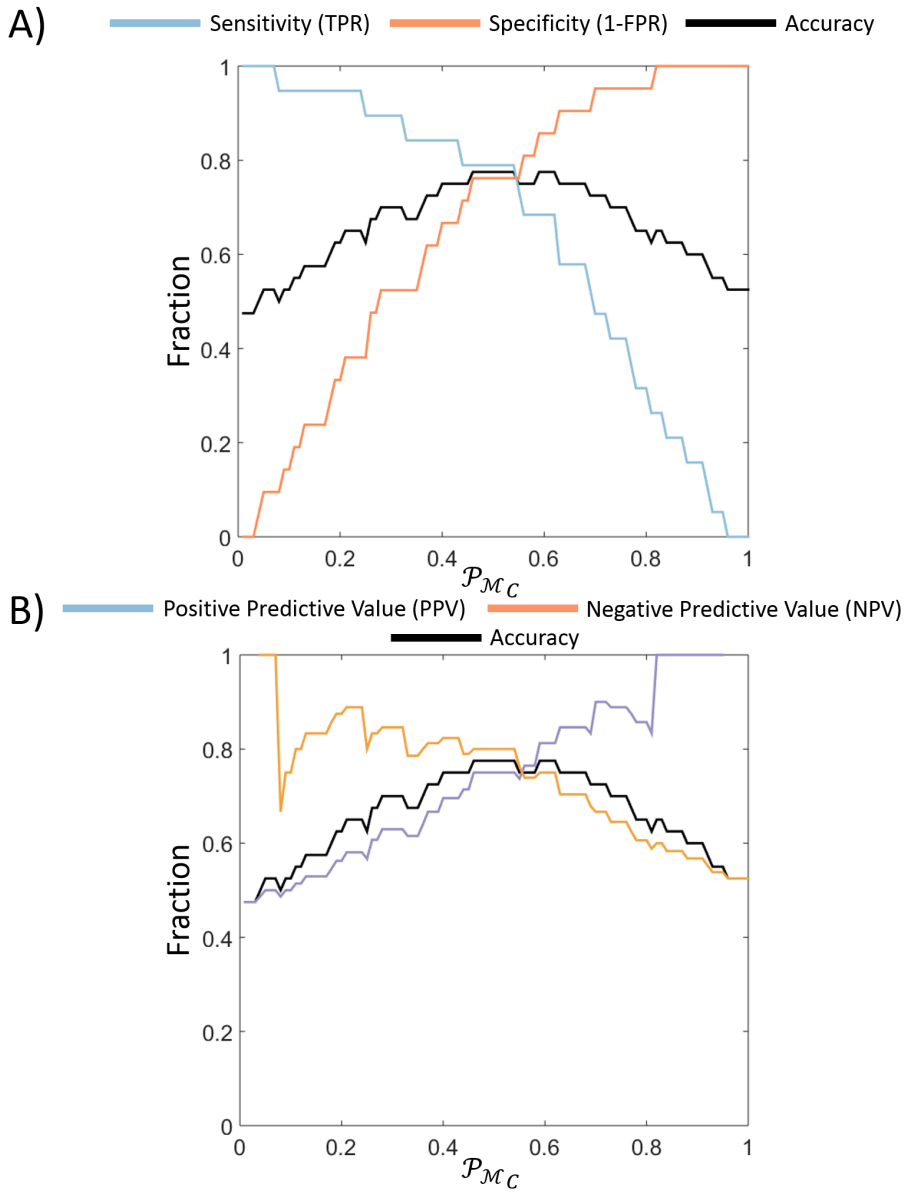

Figure 2.18: Example ROC Accuracy Parameters versus Probability Cutoff. The example data here comes from the schematic ROC analysis example in Figure 2.16. A) Plot of the overall accuracy, sensitivity (TPR), and specificity ($1-FPR$). Note that higher $\mathcal{P}_{M_c}$ cutoff values lead to lower sensitivity and higher specificity while lower $\mathcal{P}_{M_c}$ cutoffs provide higher sensitivity and lower specificity. The overall accuracy is maximized by an intermediate $\mathcal{P}_{M_c}$ value. B) Plot of the overall accuracy, positive predictive value (PPV), and negative predictive value (NPV). Note that higher $\mathcal{P}_{M_c}$ cutoffs produce better positive predictive values and worse negative predictive values. Lower $\mathcal{P}_{M_c}$ cutoffs yield worse positive predictive values and better negative predictive values.

classified as positive. Thus, the true positive rate will be 1, but the false positive rate will also be 1. Similarly, when $\mathcal{P}_{M_c} = 1$, all data points will be classified as negative. Therefore the true and false positive rates will both be zero. A perfect discriminator would have a true positive rate of 1 and a false positive rate of 0 for all cutoff values. In this scenario, the area under the plotted ROC curve would be 1. For good, but imperfect, predictors, the true positive rate rapidly increases as $\mathcal{P}_{M_c}$ decreases while the false positive rate increases slowly. This results in an area under the curve value where $0.5 < AUC < 1$, with better predictors having AUC values closer to 1. A model that randomly classifies data points as either positive or negative produces an $AUC = 0.5$; thus, AUC must be greater than 0.5 for a model to be said to have predictive value. Figure 2.19 contains an example ROC curve using the model data from Figure 2.16. In that case, the AUC is 0.82, indicating good predictive value.

2.10.4 Hosmer-Lemeshow Analysis

The calibration of a prediction model is a goodness-of-fit measure of the degree to which model-predicted probabilities of being in a particular state accurately reflect the observed data [189; 206; 141]. If a dataset contains a significant number of subjects with identical data features, and thus identical predicted probabilities, a standard Pearson χ^2 goodness-of-fit test can be performed [257; 141]. For breast cancer, this could occur if the features in question were qualitative classifers, *e.g.*, menopausal state or tumor grade. However, for studies in which no two subjects are likely to have identical features, *e.g.*, the continuous, quantitative metrics produced by DOS, Hosmer-Lemeshow analysis is a common method for assessing this calibration [141].

Once the model-predicted probabilities have been produced for each subject, in this case, via logistic regression, Hosmer-Lemeshow analysis begins by sorting all subjects by predicted probability from smallest to largest. The sorted subjects are then divided by quantile, typically into ten groups. Within each group, the numbers of subjects observed to be in the positive and negative states, O_+ and O_-, respectively, are counted, and the average model-predicted probability of being in the positive state P_+ is calculated (see Figure 2.20). The expected number of subjects in the positive and negative states for each group can then be calculated via

$$E_+ = N \cdot P_+, \tag{2.202}$$

$$E_- = N \cdot (1 - P_+), \tag{2.203}$$

where N is the number of subjects in a given group. The Hosmer-Lemeshow statistic H can then

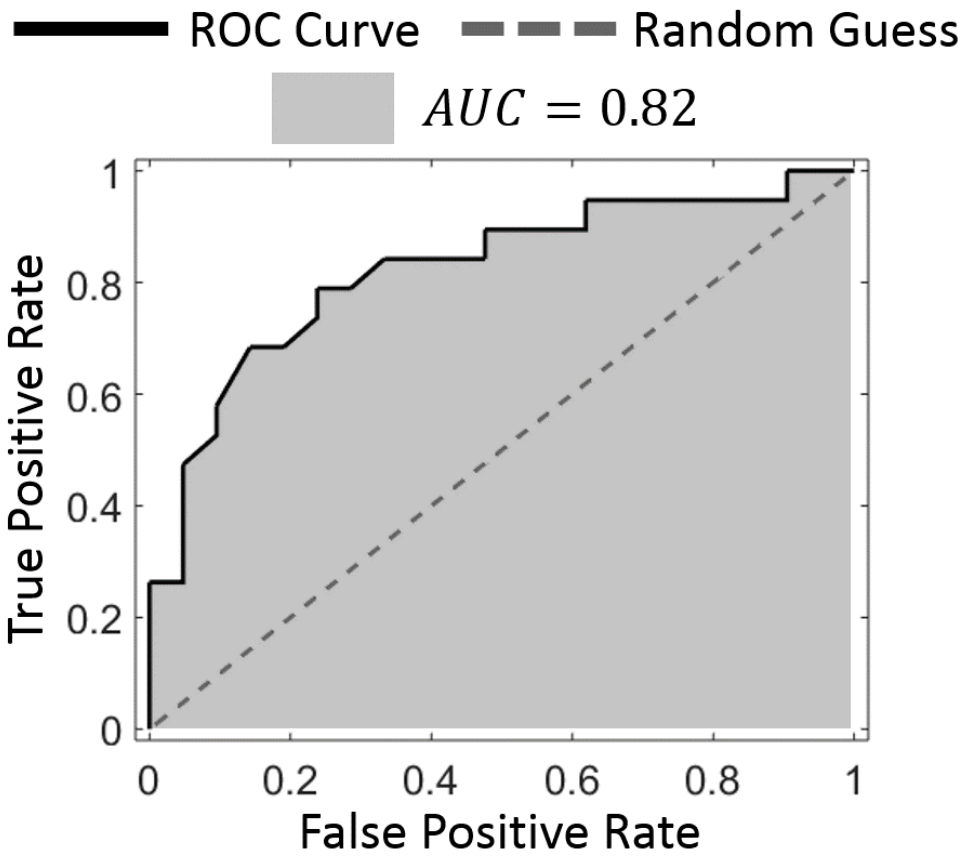

Figure 2.19: ROC Area Under the Curve (AUC). ROC curves plot the true positive rate vs the false positive rate for a given prediction model across a range of probability cutoffs $\mathcal{P}_{M_c}$ from 0 to 1. The area under this curve then serves as a measure of the model's overall discriminatory ability, with $AUC = 1$ indicating a perfect model and $AUC = 0.5$ indicating a random guess and thus a model with no predictive value. The ROC curve displayed here comes from the example dataset from Figure 2.16 and produces an $AUC = 0.82$, indicating good predictive value.

be calculated with [141]

$$H = \sum_{q=1}^{N_q} \left[\frac{\left(O_{+q} - E_{+q}\right)^2}{E_{+q}} + \frac{\left(O_{-q} - E_{-q}\right)^2}{E_{-q}} \right]. \tag{2.204}$$

Here, q is the index for a specific quantile group, and N_q is the number of groups into which the subjects are divided. This H metric, which has the form of a χ^2 value, provides a measure of the offset between the expected and observed number of subjects in each state and each group. H can then be used to determine a p-value with a χ^2 distribution with $N_q - 2$ degrees of freedom. In

this case, the null hypothesis is that there is no significant difference between the observed and expected values across all groups. Thus, if the null hypothesis is accepted ($p > 0.05$), the model is well-calibrated; a rejected null hypothesis ($p < 0.05$) is a sign of a poorly calibrated model. A common visualization for the degree of calibration is a plot of actual, *i.e.*, observed, versus expected, *i.e.*, model-derived, probabilities for each group (see Figure 2.20).

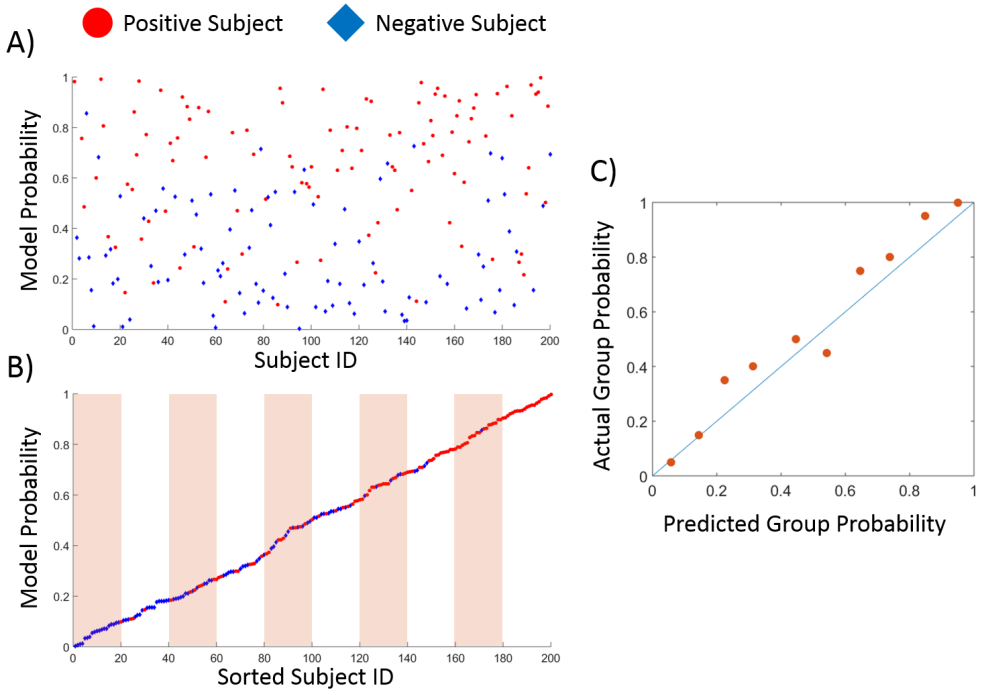

Figure 2.20: Hosmer-Lemeshow Analysis Schematic. Consider a dataset consisting of 200 subjects in either a positive or negative state. Each subject has a model-developed probability of being in the positive state. A) Plot of model-predicted probability versus an arbitrary subject ID. Positive subjects are plotted as red circles while negative subjects are plotted as blue diamonds. B) The first step in Hosmer-Lemeshow analysis is to sort the subjects in ascending order of model probability, and divide them into 10 groups, indicated by the alternating shaded regions on the plot. C) The actual (observed) and expected (model) number of subjects in the positive and negative states can be calculated for each group to perform Hosmer-Lemeshow analysis. The actual probability can then be plotted against the expected probability for each group as a visual representation of the model's calibration.

Chapter 3

Diffuse Optical Prediction of Response to Neoadjuvant Chemotherapy

3.1 Introduction

The most common treatment paradigm for breast cancer is adjuvant chemotherapy, in which the primary tumor is removed first, and chemotherapy is then given to eliminate any residual malignancy [62]. Neoadjuvant chemotherapy (NAC) is another treatment method for breast cancer in which chemotherapy is given to a patient prior to surgical resection of a tumor. NAC is widely used for locally advanced breast cancer (see Figure 1.2), typically permits increased conservation of healthy breast tissue during tumor resection, and limits the need for axillary lymph node treatment or surgery [235]. The most prevalent marker of neoadjuvant chemotherapy efficacy is pathologic complete response (pCR) to NAC, defined as no residual invasive carcinoma, which has been correlated with improved survival compared to incomplete response [217; 108]. However, this pathological assessment occurs after the completion of chemotherapy when the resected tissue is analyzed, and thus, pCR offers no intra-therapy information. The ability to predict response to NAC at an earlier time-point during chemotherapy, by contrast, could enable physicians to dynamically optimize the treatment regimen, thereby avoiding unnecessary therapy doses, reducing tissue damage, and improving patient outcomes.

In current clinical practice, physical exams and radiologic imaging are used intermittently to

monitor NAC response. Unfortunately, these methods are inadequate predictors of pCR [116; 138; 251]. Magnetic resonance imaging (MRI) provides better correlation with pathology than mammography or ultrasound [265]. In general, functional monitoring techniques offer significantly improved correlation with response at an earlier time-point relative to structural imaging modalities. Magnetic resonance spectroscopy (MRS) [181], contrast-enhanced MRI [144], and fluorodeoxyglucose positron emission tomography (FDG-PET) [173; 180; 143], for example, have predictive value with respect to pCR, but MRI, MRS, and PET all have practical constraints which limit the frequency of monitoring in clinical care. All three modalities require the use of injected contrast agents and are expensive and difficult to obtain insurance coverage for. PET has the added disadvantage of exposing the subject to ionizing radiation. Thus, while these modalities have demonstrated ability to predict which subjects will achieve pCR [7; 200; 180; 200; 160], they are not well-suited to the type of repeated, longitudinal monitoring that may be necessary over a therapy regimen that spans several months. Conversely, diffuse optical monitoring is ideally positioned for this application. Repeated measurements across months are more feasible due to the lower cost, non-invasive nature, and lack of ionizing radiation in diffuse optical instruments, and diffuse optics measures the type of functional parameters that tend to be better correlated with response to chemotherapy. Indeed, several studies have employed diffuse optics to explore functional changes in tumors during NAC and have correlated these changes with response to therapy [248; 70; 59; 154; 236; 61; 220; 109; 250; 55; 249; 76; 223; 8].

The study discussed here develops and employs a novel analytical technique to the previously reported multi-center ACRIN-6691 trial overseen by the American College of Radiology Imaging Network (ACRIN) [249]. This trial prospectively tested the ability of diffuse optical spectroscopic imaging (DOSI), discussed in more detail in Section 3.2.2, to discriminate, by the Midpoint of therapy, subjects who achieved pCR from those who did not achieve pCR. Specifically, the primary aim of ACRIN-6691 was to evaluate whether a change in a particular DOSI endpoint, the tissue optical index (TOI) (see Section 3.2.2), could be used to predict pCR by the midpoint of NAC, approximately 2-3 months after the first infusion [249]. In that initial study, significant reductions in tumor-to-normal (T/N) TOI ratios were seen for pCR subjects. A 40 % or greater change in this parameter at the midpoint, combined with Baseline tumor S_tO_2 greater than median value (77 %), was shown to be a promising predictor of pCR ($AUC = 0.83$; $95\,\% CI : 0.63 - 1$) (see Section 2.10.3 for a full explanation of AUC) [249]. The presented study explores the ACRIN-6691 secondary aim of predicting pCR much earlier in the $3 - 6$ month NAC cycle by examining DOSI response parameters within 10 days of therapy initiation. To address this goal, a logistic regression algorithm [141] was retrospectively developed and applied to correlate DOSI-measured parameters

of malignant breast lesions to subjects' post-therapy pathologic response status. The hypothesis is that identification and optimization of this new DOSI index could predict pCR to NAC at an early time-point in the course of therapy, providing significant potential for clinical utility.

3.2 Subjects and Methods

3.2.1 Trial Design and Subjects

Data for this study were collected during the ACRIN-6691 multi-site trial using a diffuse optical spectroscopic imaging (DOSI) instrument developed at the University of California, Irvine [30; 166] and deployed at seven institutions: University of California, Irvine; University of California, San Francisco; University of Pennsylvania; Boston University; Dartmouth Hitchcock Medical Center; Massachusetts General Hospital; and MD Anderson Cancer Center [249]. Subjects provided written informed consent, and the HIPAA-compliant protocol and informed consent were approved by the American College of Radiology Imaging Network Institutional Review Board, the NCI Cancer Therapy Evaluation Program (CTEP), and each site's Institutional Review Board. All 60 enrolled subjects were females between the ages of 28 and 67 with biopsy-confirmed invasive ductal carcinomas and/or invasive lobular carcinomas of at least $2\,cm$ in length along the greatest dimension. For each subject, the chemotherapy regimen was determined by the subject's physician. Chemotherapy type was not controlled in this study, except that regimens were required to include at least one cytotoxic chemotherapeutic agent. .

Pathologic complete response (pCR) to therapy was defined here as no residual invasive primary carcinoma without regard to residual lymph node disease. Some definitions of pCR require there to be no residual disease in any lymph nodes; however, since DOSI is sensitive only to the primary tumor, the lymph node condition was not enforced for this analysis. Pathologic response status was determined for each subject by post-surgery pathology reports. Subjects that achieved partial response were not distinguished from non-responders due to statistical considerations with respect to the sample size and the previously reported correlation between complete response and improved survival [217; 108]. Table 3.1 contains demographic information, as well as tumor histology, immunohistochemistry, and chemotherapy regimens for complete and non-complete responders.

A number of enrolled subjects were excluded from the final data set. Of these, three subjects withdrew from the study. An additional 13 subjects were not included in the imaging analysis because of the following DOSI scan issues: mandatory Baseline DOSI was not performed ($n = 1$), baseline DOSI was non-evaluable ($n = 8$), mandatory mid-therapy DOSI was not performed ($n = 3$), or too few normal region points were available ($n = 1$). A DOSI scan was considered

non-evaluable in the case of unrealistic physiological values or incorrect instrument configuration. This decision was made on blinded, de-identified data using instrument calibration and raw data QC reports [249]. One subject was excluded due to unavailable pathology information, and ten additional subjects were excluded because the measurement of the contralateral breast was not performed. A flow chart for this exclusion process can be found in Figure 3.1.

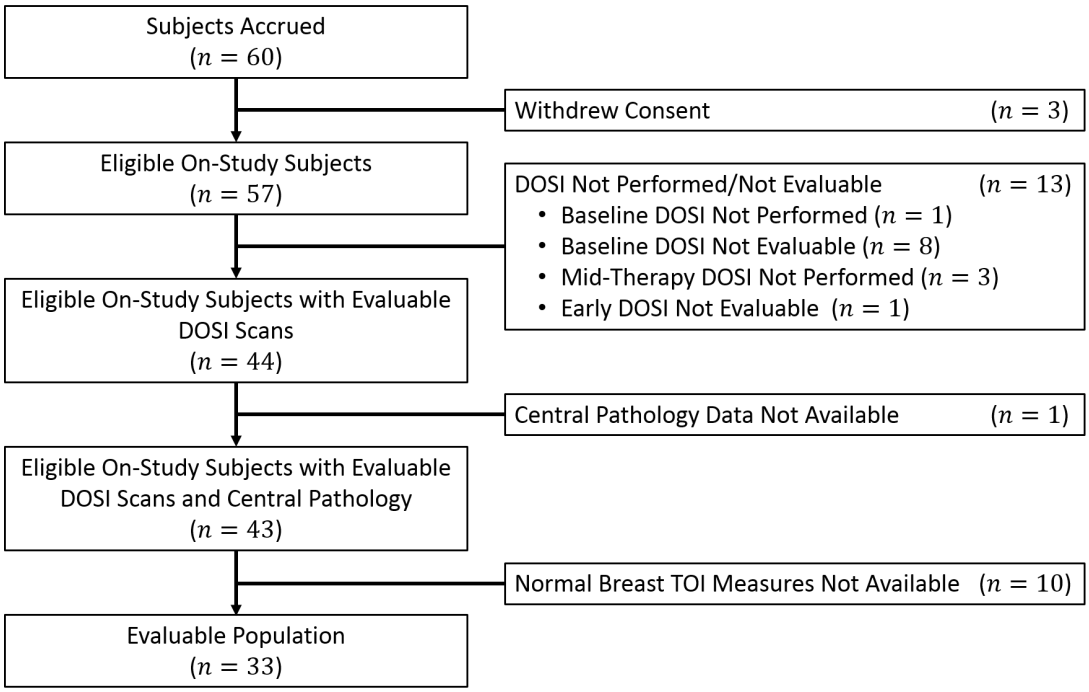

Figure 3.1: Enrollment to Analysis Population Flowchart. Although 60 subjects were enrolled in the original ACRIN 6691 trial, only 33 participants fulfilled all of the criteria to be included in the final evaluable population. Of the subjects excluded, 3 withdrew consent, 13 had DOSI measurements that weren't performed or were non-evaluable, 1 did not have the required pathology information, and 10 did not receive a normal breast measurement. This evaluable population was chosen to be identical to the that used in the ACRIN 6691 trial [249], except for the exclusion of a single additional subject whose Early time-point measurement was not evaluable for the purposes of the z-score normalization algorithm.

Subjects were measured with the DOSI system at four time-points throughout the course of their neoadjuvant chemotherapy regimens (see Figure 3.2). The first measurement (Baseline) occurred prior to the first dose of chemotherapy. The second measurement, which is referred to as the Early measurement time-point, was performed between 5 and 10 days after the first chemotherapy treatment. The third measurement (Midpoint) occurred in the middle of the therapy regimen, and a Final measurement was made after the completion of therapy but prior to tumor resection.

	Responders ($n = 15$)	Non-Responders ($n = 18$)
Age, Years		
Mean ± St. Dev. (Range)	$49.0 \pm 11.6\,(30 - 67)$	$49.4 \pm 10.9\,(28 - 66)$
Menopausal Status, n (%)		
Pre-	5 (33 %)	9 (50 %)
Peri-	1 (7 %)	2 (11 %)
Post-	9 (60 %)	7 (39 %)
Maximum Tumor Size, cm		
Mean ± St. Dev. (Range)	$37.9 \pm 22.8\,(12 - 95)$	$37.5 \pm 18.1\,(11 - 75)$
Histological Status, n (%)		
IDC	9 (60 %)	12 (67 %)
ILC	0 (0 %)	1 (6 %)
IDC + DCIS	4 (27 %)	5 (28 %)
IDC + ILC	1 (7 %)	0 (0 %)
Unknown	1 (7 %)	0 (0 %)
ER Status, n (%)		
Positive	5 (33 %)	16 (89 %)
Negative	8 (53 %)	2 (11 %)
Unknown	2 (13 %)	0 (0 %)
PR Status, n (%)		
Positive	5 (33 %)	11 (61 %)
Negative	8 (53 %)	7 (39 %)
Unknown	2 (13 %)	0 (0 %)
Her2 Status, n (%)		
1	5 (33 %)	4 (22 %)
2	1 (7 %)	9 (50 %)
3	5 (33 %)	1 (6 %)
Unknown	4 (27 %)	4 (22 %)
Molecular Subtype, n (%)		
Her2 Positive	3 (20 %)	1 (6 %)
HR Positive	0 (0 %)	2 (11 %)
Luminal A	0 (0 , %)	3 (17 %)
Luminal B	6 (40 %)	11 (61 %)
Triple Negative	4 (27 %)	1 (6 %)
Unknown	2 (13 %)	0 (0 %)

Table 3.1: Physiological Tumor Properties by Response Status. Demographic, histological, and immunohistochemical data is provided for all subjects in the ACRIN 6691 trial and divided into complete responder (pCR) ($n = 15$) and non-complete responder (non-pCR) ($n = 18$) groups. For histological information, IDC refers to invasive ductal carcinoma, ILC refers to invasive lobular carcinoma, and DCIS is ductal carcinoma *in-situ*. ER, PR, and Her2 represent estrogen receptor, progesterone receptor, and human epidermal growth factor receptor status, respectively.

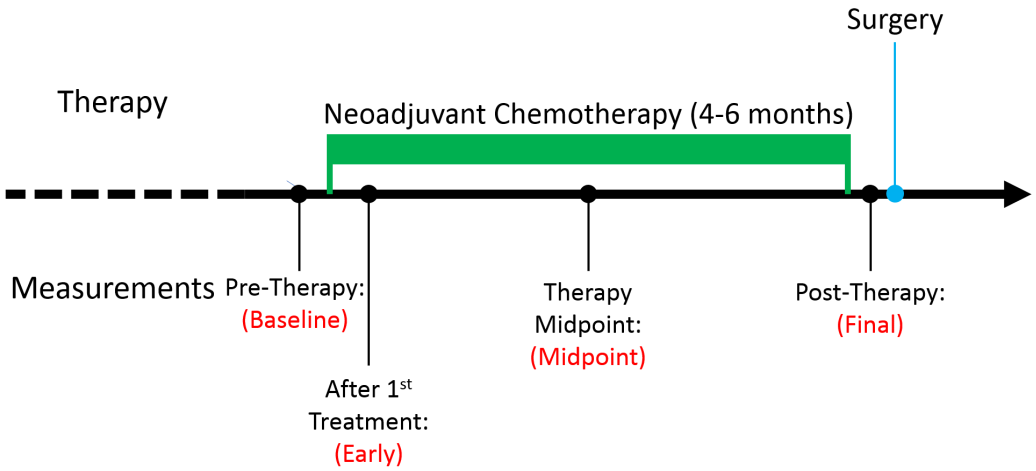

Figure 3.2: Timeline of DOSI Monitoring during Neoadjuvant Chemotherapy. Each enrolled subject underwent neoadjuvant chemotherapy for a period of 4 to 6 months. DOSI measurements were made at four time-points throughout the course of therapy: 1) Baseline – prior to the administration of therapy. 2) Early – 5 to 10 days after the first dose of therapy. 3) Midpoint – the midpoint of the therapy regimen. 4) Final – at least 7 days after the final dose of therapy and prior to tumor resection. Note, some subjects are missing data at one or more of the non-Baseline time-points, and the measurements at the Final time-point were not used for the probability of response analysis due to their limited predictive utility.

3.2.2 Optical Imaging Methods

All diffuse optical measurements were made with the diffuse optical spectroscopic imaging system developed and built at the University of California, Irvine [30; 166]. This is a hybrid DOS instrument that combines multi-spectral frequency-domain and broadband imaging to measure absolute μ_a, μ_s', and the tissue concentrations of oxygenated hemoglobin (HbO_2), deoxygenated hemoglobin (HHb), water, and lipid. The combination of these chromophores permits calculation of tissue total hemoglobin concentration (Hb_T) and tissue oxygen saturation (S_tO_2). Another optical parameter, known as the tissue optical index (TOI), defined as $TOI = \frac{HHb \cdot H_2O}{Lipid}$, is also calculated. TOI was derived empirically to maximize contrast between tumor and normal tissue [60].

For data presented herein, DOSI utilizes a single source-detector separation: $2.2\,cm$ for phantom measurements and $2.8\,cm$ for tissue measurements. At this single separation, frequency domain measurements are made using laser diodes at six wavelengths (660, 680, 785, 810, 830, and $850\,nm$) that are fiber coupled to an imaging hand-piece that, in turn, is put into contact with the tissue (see Figure 3.3). This hand-piece contains an avalanche photodiode (APD) for detection of the frequency domain signals. To compensate for the lack of multiple source-detector positions, each laser diode is

modulated at 251 to 601 distinct frequencies ranging from $50\,MHz$ to $600\,MHz$. Three frequency sweeps are performed and averaged for each wavelength, and the absorption coefficient μ_a and μ_s' are fit using a Levenberg-Marquadt algorithm for the amplitude and phase data at each frequency (see Section 2.6.6). A Mie-scattering framework is assumed for the scatterers, and thus a scattering amplitude A and scattering power b are fit using all 6 wavelengths (see Section 2.8.2).

Figure 3.3: DOSI Instrumentation and Hand-piece. This figure comes from [166]. A) DOSI Opto-Electronics Rack. This instrument cart contains the white-light source, laser diodes, spectrometer, frequency analyzer, and instrument control computer for the DOSI system. Several systems similar to this collected all of the DOSI data in Chapters 3, 4, and 5. Note that the instrument is portable and can be wheeled to the patient's bedside. B) DOSI Hand-piece and Calibration Phantom. The DOSI hand-piece contains an APD for frequency-domain detection and optical fibers coupled to the optical components on the instrument rack. A calibration phantom, placed inside a case for easy alignment with the hand-piece, is also shown. C) DOSI Hand-piece and Reflectance Standard. The DOSI hand-piece is shown in contact with the broadband reflectance standard. Note that the fiber-coupling apparatus can easily be moved to three different positions, using the silver spring-loaded hand screws seen here, to provide multiple source-detector separations.

Broadband spectroscopy is performed using a continuous-wave white-light source and diffraction-grating spectrometer with a range of 650 to $1000\,nm$, both of which are also fiber-coupled to the

tissue via the hand-piece. The best-fit A and b parameters from the frequency-domain scattering fit are then used to correct the CW reflectance spectroscopy for the tissue scattering. Additionally, the absolute absorption coefficients at the 6 frequency-domain wavelengths are used to quantitatively scale the broadband CW absorption spectrum. Finally, the DOSI instrument is calibrated using two standardized phantoms, for the frequency-domain system, and a reflectance standard, for the broadband system, before and after every measurement (see Figure 3.3). Thus, DOSI provides absolute μ_a and μ_s' values across the entire 650 to 1000 nm range.

This hybrid modality provides improved quantification of chromophore concentration relative to DOS techniques that use several individual wavelengths because of the increased spectroscopic information across the full biological window. This scheme is particularly beneficial for calculating the lipid and water concentrations because light with wavelength greater than 900 nm is more sensitive to these chromophores, and the spectrometer can easily measure the absorption spectrum at these longer wavelengths. Frequency-domain-only instruments often struggle to measure at wavelengths greater than 900 nm because the required detectors, either PMTs or APDs, typically have very poor sensitivity over this range [247]. Full descriptions of this DOSI instrumentation and analysis technique have been published [30; 166].

During each subject's Baseline measurement, a grid of $\sim 50-240$ points that encompassed both the palpated tumor region and the surrounding normal tissue was measured on the lesion-bearing breast using the DOSI handpiece. A mirrored grid of points was measured on the contralateral breast. These measurement grids were recorded using a hand-marked transparency film that was produced for each subject in order to guide DOSI handpiece placement to the same grid points during the three subsequent measurement time-points (see Figure 3.2). This practice ensured that each measurement point was probing the same tissue region during each longitudinal measurement. Each point measurement lasted approximately 2 to 5 seconds. Since the data analysis is performed independently at each point using a semi-infinite homogeneous model (see Section 2.5.4), this grid will produce separate μ_a and μ_s' values for each wavelength and each grid point. These independent measurements can then be smoothed into a two-dimensional topographic image. Figure 3.4 contains a schematic of the DOSI measurement across these spatial grids and a sample image.

3.2.3 Statistical and Analytic Methods

The primary aim of this study was to train a logistic regression algorithm to discriminate between responders and non-responders based on DOSI-measured parameters. The tumor region for each subject was determined using the Tissue Optical Index (TOI). This TOI parameter has been empirically shown to differentiate malignant tissue from normal tissue in the breast [60] and will

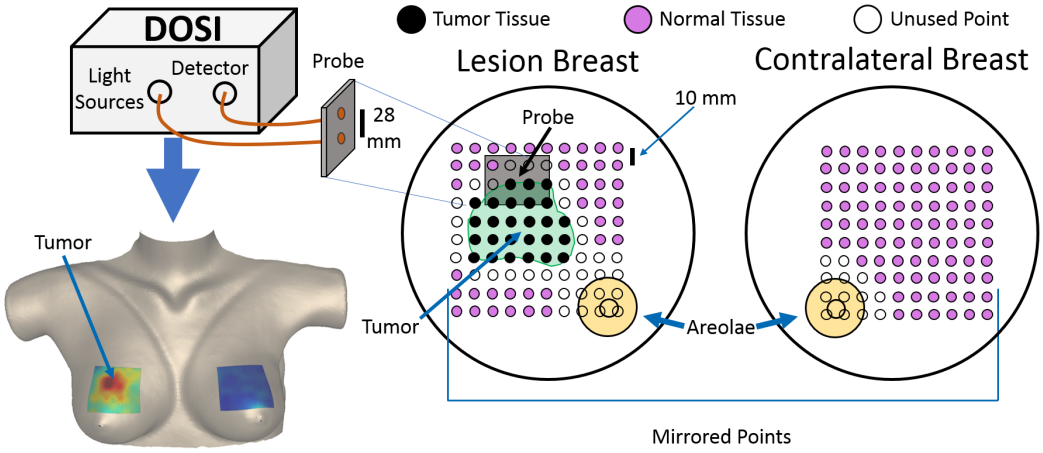

Figure 3.4: Schematic of DOSI Measurement and Region Definition. Top Left: DOSI instrument and probe. Bottom left: A sample DOSI image projected onto a model breast. Right: A grid of points, over a surface area ranging from $7\,cm \times 7\,cm$ to $15\,cm \times 16\,cm$, were measured on the lesion-bearing breast. This grid was chosen to encompass both the tumor and a portion of the surrounding healthy tissue. The grid of points was marked using a transparency, which was then used to mirror the grid for measurements on the contralateral breast. The transparency was also used to ensure consistent measurement locations across all time-points. The tumor region was chosen to be all contiguous points with magnitude greater than half of the maximum Tissue Optical Index (TOI) measurement. The tumor breast normal region was defined as all points outside the tumor region and areola, excluding a $1\,cm$ margin around both the tumor and areola. The contralateral breast normal region was defined as all measured points, excluding the areola and a $1\,cm$ margin around the areola.

again be demonstrated to have significant discriminatory value in Chapter 5. Here, the full-width-at-half-maximum contour around the point of maximum TOI in the Baseline measurement of the lesion-bearing breast was designated as the edge of the tumor region. This region remained constant throughout all longitudinal measurements for a given subject. The normal region on the lesion-bearing breast was defined as all points outside the tumor region excluding the areola and $1\,cm$ margins around the areola and tumor region (see Figure 3.4). These margins were not included in the normal region to limit signal contamination from the tumor region due to the partial volume effect and limited spatial resolution of diffuse optics [195; 163]. The normal region on the contralateral breast was chosen to be all points excluding the areola and a $1\,cm$ margin around the areola. The areola was excluded in both normal regions due to its abundance of highly scattering fibroglandular tissue and higher blood volume, which is not representative of typical non-areolar breast tissue and has been shown to contaminate healthy breast tissue measurements [230; 164].

In practice, significant inter- and intra-subject variation in optically measured physiological parameters of healthy breast tissue can arise [230; 56], and these systemic variations can bias the

logistic regression. Moreover, the optically measured tissue parameters are not normally distributed (see Figure 2.15). To remedy these issues, a z-score normalization method was developed.

Z-Score Normalization

The simplest DOSI prediction metric would be an un-normalized value of one of the DOSI-measured parameters, *e.g.*, S_tO_2, with a cutoff between S_tO_2 values for subjects that achieved pCR and subjects that did not. Another common metric employs tissue-to-normal ratio-normalized data $S_tO_{2_{T/N}}$, wherein a measured S_tO_2 value is divided by the average S_tO_2 of a known normal tissue region. This $S_tO_{2_{T/N}}$ quantity improves upon the un-normalized S_tO_2 by accounting for the inter-subject variability in the systemic levels of DOSI-measured physiological parameters. However, healthy breast tissue also exhibits significant intra-subject heterogeneity in these quantities [99; 230; 56]. This variation is not accounted for in the tumor-to-normal ratio normalization technique. Thus, $S_tO_{2_{T/N}}$ provides no indication of whether a value is within the expected range of the normal tissue S_tO_2 due to heterogeneity or whether the value is significantly different from the healthy tissue. To resolve this issue, the normalization technique needs to account for both the mean and the standard deviation of the normal tissue S_tO_2. A z-score normalization scheme has been previously developed for this purpose with respect to differentiating malignant and healthy tissue [56; 55] and is described in Section 2.10.1.

Briefly, the natural logarithm of each data point is first taken. Then the mean and standard deviation of a normal (healthy) region of tissue is used to transform raw tumor data into z-score data as in Equation 3.1

$$Z_j = \frac{\ln X_j - \langle \ln X_{j_{Norm}} \rangle}{\sigma \left[\ln X_{j_{Norm}} \right]}. \tag{3.1}$$

Here, X_j is the un-normalized j^{th} measured parameter in the tumor region, $X_{j_{Norm}}$ is the un-normalized j^{th} measured parameter in the normal (healthy) region of the tumor-bearing breast or contralateral breast, $\langle \ln X_{j_{Norm}} \rangle$ represents the mean over all points in the normal (healthy) region, and $\sigma \left[\ln X_{j_{Norm}} \right]$ represents the standard deviation over all points in the normal (healthy) region. Z_j is then the tumor region z-score relative to the healthy tissue for the j^{th} parameter. Each Z_j parameter was averaged over all spatial points in the tumor region for a given subject and time-point. As a result, the logistic regression algorithms can utilize a single tumor quantity for each subject, for each time-point, and for each measured parameter. In contrast to Chapter 5, here, only tumor parameters will be used in the regression model because this algorithm is not looking to differentiate malignant tissue from benign tissue but rather, to correlate tumor properties to a subject's pathologic response status.

Thus, every predictor data point used in the regression model is measured in units of standard deviations from the mean of a given parameter in healthy tissue. In addition to transforming all parameters to be approximately the same magnitude, this method better accounts for the inter-subject systemic variations by finding the difference of each parameter from the mean value of the normal (healthy) tissue. It also more fully accounts for intra-subject variation in healthy tissue by normalizing with the healthy tissue standard deviation. Finally, this techniques transforms the normal tissue measurements such that they more closely obey a normal Gaussian distribution, which improves statistical robustness [206; 136; 141]. A concrete example of the benefit of this statistical transformation scheme is shown in Figure 2.15 for Early time-point tissue oxygen saturation in the ACRIN-6691 subject cohort. In the present study, z-score normalization schemes that defined the normal region as either the healthy breast (excluding the areola) or all tissue on the lesion breast outside a certain margin of the tumor region (excluding the areola) were explored. See Figure 3.4 for a graphical representation of these different normalization regions.

Logistic Regression

These tumor Z_j values can then be used to run a logistic regression algorithm [141], which produces a model that optimally classifies each subject as either pathologic complete responders (pCR) or pathologic non-complete responders (non-pCR) based on the chosen parameter Z_j. In the logistic regression framework, the response parameter for a given model, which is fit to maximize the likelihood estimation, as discussed in Section 2.10.2, is defined as

$$\mathcal{R}^i = \beta_o + \sum_{j=1}^{N_j} \beta_j \cdot Z_j^i. \tag{3.2}$$

Here $\mathcal{R}^i$ is the given model's log-odds of response for the i^{th} subject, β_o is the intercept term of the fitted weight vector, β_j is the weighting term for the j^{th} measured parameter used in the model, Z_j^i is the z-score for the j^{th} measured parameter of the i^{th} subject, and N_j is the number of parameters used in a particular model. The full weight vector $\vec{\beta}$ is then

$$\vec{\beta} = \left[\beta_o, \beta_1, \ldots \beta_{N_j}\right]. \tag{3.3}$$

The $\vec{\beta}$ weight vector is fit using MATLAB's native logistic regression function, *mnrfit* [3]. The response parameter $\mathcal{R}$ can then be transformed into a probability of response parameter $\mathcal{P}_\mathcal{R}$ using a logistic function,

$$\mathcal{P}_\mathcal{R} = \frac{1}{1 + e^{-\mathcal{R}}}. \tag{3.4}$$

The parameter $\mathcal{P}_{\mathcal{R}}$ represents the probability that a subject will achieve pCR. It has a range from 0 to 1, and it can readily be used to predict each subject's status as either a pathologic complete responder, or non-complete responder, depending on threshold levels.

Because the usable dataset in this study is small ($n = 33$ subjects), a leave-one-out validation protocol [136] was employed to test the regression model. Thus, a series of logistic regression models were created for each parameter set, and each of these models leaves one of the subjects out of the training dataset (see Figure 3.5). The weight vector created by each of these models, $\vec{\beta}^i$, is the weight vector created when the i^{th} subject is left-out; it is then used to produce a probability of response prediction for the i^{th} subject $\mathcal{P}^i_{\mathcal{R}}$, which is independent of the $\vec{\beta}^i$ model. This well-known approach provides the most robust and least biased validation given the study's sample size, which precludes the use of a significantly large independent test set [136].

The quality of the predictions with respect to the actual response status is determined via receiver operating characteristic (ROC) analysis [132; 257; 115]. The primary metric for the discriminatory ability of a prediction model in ROC analysis is the area under the curve (AUC). Models with excellent predictive ability will have AUC values that are close to 1, but models with no predictive ability, *i.e.*, a random guess, will have $AUC = 0.5$. A full description of ROC analysis, the area under the curve, and other accuracy parameters can be found in Section 2.10.3.

Here, the AUC and its 95 % confidence interval for the resultant prediction models were empirically determined using DeLong's method [86]. The ROC analysis is performed using each of the individual leave-one-out models, and the reported weight vector $\left\langle \vec{\beta} \right\rangle$ will be the median $\vec{\beta}$ from the series of models created for each parameter set, with the interquartile range of these models reported as uncertainty. Figure 3.5 contains a flow-chart that summarizes the full analysis scheme performed here. Additionally, the degree to which the models are properly calibrated, *i.e.*, how well the predicted probabilities correspond to the true probabilities, is determined via Hosmer-Lemeshow analysis (see Section 2.10.4) [141]. These Hosmer-Lemeshow plots will be displayed for some prediction models.

Models based on all combinations of one, two, and three parameters from the Baseline, Early, and Midpoint time-points were tested. Models with more than three parameters were not tested to avoid over-fitting. Data from the Final time-point was not used because the focus of this work is early prediction of response. Thus, the Final time-point parameters offer little additional clinical utility.

Other normalization methods were also tested for comparison to z-score normalization. These comparisons included tumor-to-normal ratio normalization without information about the normal tissue heterogeneity, as well as raw tumor physiological values without normalization. The Z-score

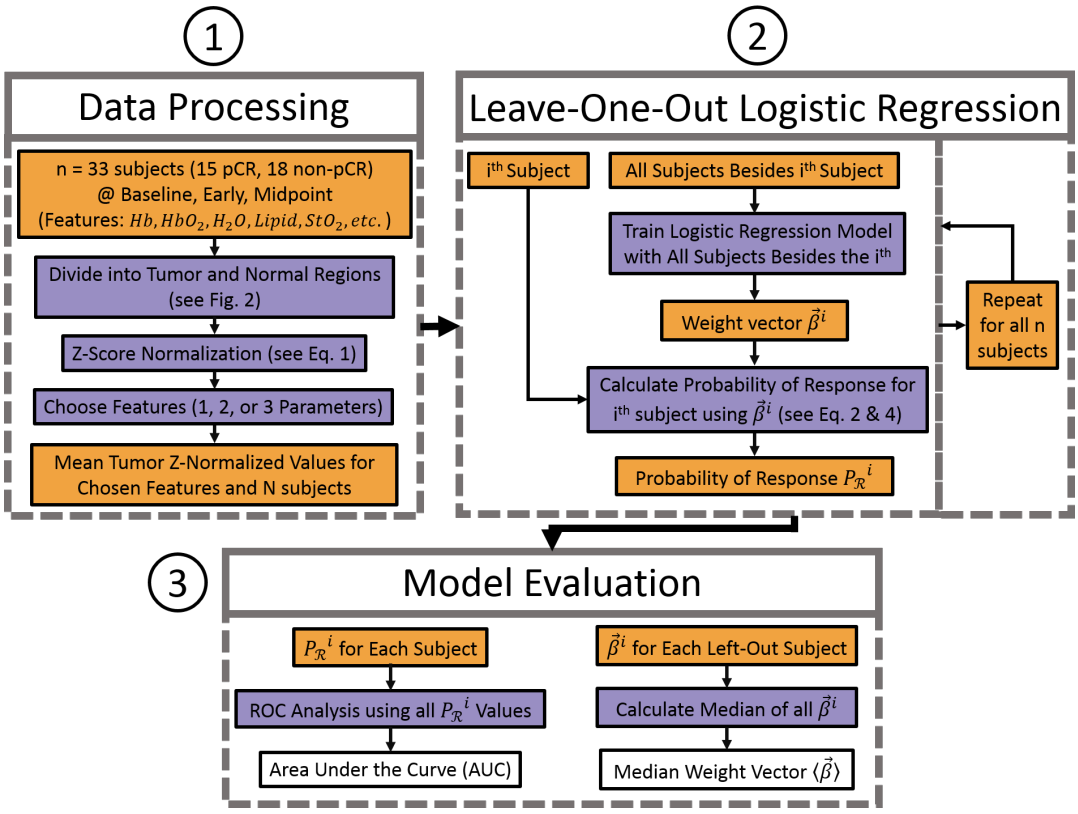

Figure 3.5: DOSI Regression Data Analysis Flow Chart. For all sections, orange boxes indicate input or intermediate data, purple boxes are analytical actions performed, and white boxes are the final outputs of the algorithm. 1) Data Processing – Measured quantities at all spatial points and all n subjects across the first three time-points are first divided into tumor and normal (healthy) regions (see Figure 3.4). All tumor points are then z-score normalized to their respective normal (healthy) regions (see Equation 3.1), and the mean is taken for a given subject and time-point. Finally, one, two, or three parameters are chosen from among the combinations of measured quantities and time-points as model inputs. 2) Leave-One-Out Logistic Regression – A set of n logistic regression algorithms are performed, each of which leaves out a single subject from the training data and produces a $\vec{\beta}^i$ weight vector. Each $\vec{\beta}^i$ is then used to calculate the probability of response for the subject left out of the given training set (see Equations 3.2 and 3.4). 3) Model Evaluation – ROC analysis is performed using the calculated $\mathcal{P}_R^i$ values to determine the area under the curve (AUC), and a median weight vector $\langle\vec{\beta}\rangle$ is calculated from the n resulting $\vec{\beta}^i$ vectors.

normalization algorithm itself was performed using two different methods: one which classified the tumor-bearing breast normal tissue as the "normal" region and one that classified the contralateral breast as the "normal" region. Finally, for data at the Early and Midpoint time-points, both the temporally absolute z-scores and the change in the z-score parameters from Baseline to the given time-point were tested as features in logistic regression models.

3.3 Results

The final data set for this study was derived from $n = 33$ subjects who had complete, evaluable data sets at the Baseline and Midpoint time-points. For models that used measured parameters from the Early time-point, slightly fewer subjects were used ($n = 29$) due to missing data at this time-point. All subjects had biopsy-confirmed invasive carcinomas and underwent a neoadjuvant chemotherapy regimen determined by their physicians (see Table 3.1) [249].

For the logistic regression algorithm, z-score normalization to the healthy tissue on the lesion breast, as opposed to normalization to the contralateral breast, produced more predictive models. Recall that z-score data was derived for multiple data types (HbO_2, HHb, Hb_T, S_tO_2, H_2O, $Lipid$) at multiple time points (Baseline, Early, Midpoint); a summary of all the data is available in Table 3.2. Regression models were produced for all combinations of one, two, and three parameters from all three time-points. Higher-order models, e.g. four-parameter, were not considered in order to avoid overfitting of the data.

The single best regression model used only the Early time-point tissue oxygen saturation (eS_tO_2). The weight vector for this model was $\langle\vec{\beta}\rangle = [\beta_o = 0.79 \pm 0.09, \beta_{eS_tO_2} = 2.29 \pm 0.04]$. This finding suggests that, at the Early time-point, tumors that are not hypoxic relative to the surrounding normal tissue, or tumors that are only slightly hypoxic and within the normal region's confidence interval, are more likely to be pathologic complete responders to neoadjuvant chemotherapy. By contrast, subjects whose tumors were significantly hypoxic relative to the normal tissue were likely to be non-responders (see Figure 3.6 for a summary of this model in traditional, clinical units). When ROC analysis was performed, this model produced an $AUC = 0.92$ with a 95 % confidence interval of $AUC = 0.82 - 1$ (see Figure 3.7). Additionally, the small uncertainties of the $\langle\vec{\beta}\rangle$ components, relative to the median, indicate that the fitted $\langle\vec{\beta}\rangle$ did not vary significantly across the leave-one-out validation protocol. The eS_tO_2 model is also well-calibrated, as demonstrated by a Hosmer-Lemeshow p-value of 0.79 and the calibration plot in Figure 3.8. Also, although many models could be produced that had comparable predictive ability using eS_tO_2 in combination with one or two other measured parameters, none of these models actually improved upon the $AUC = 0.92$ produced by eS_tO_2 alone.

This eS_tO_2 model was produced using the absolute z-score value, *i.e.*, not the change between the Baseline and Early values, and with normalization to the normal tissue on the tumor-bearing breast. Models that used the temporal change in the S_tO_2 z-score ($AUC = 0.63$) and the normal tissue on the contralateral breast ($AUC = 0.67$) were also produced but were not as predictive as the best model. For comparison, prediction models that used more common normalization

	Baseline Median Z-Score (IQR)	
	pCR	non-pCR
HbO_2	1.5 (1.1, 1.8)	1.0 (0.4, 1.9)
HHb	2.2 (1.5, 2.7)	1.9 (1.5, 4.0)
Hb_T	1.8 (1.5, 2.4)	1.4 (0.8, 2.2)
S_tO_2	−0.2 (−0.8, 0.1)	−1.8 (−2.3, −0.8)
H_2O	2.1 (1.5, 2.8)	1.8 (1.2, 3.1)
$Lipid$	−1.8 (−2.9, −1.4)	−1.4 (−2.5, −0.1)
TOI	3.0 (1.7, 3.8)	2.4 (1.6, 4.1)

	Early Median Z-Score (IQR)	
	pCR	non-pCR
HbO_2	1.4 (0.8, 1.7)	0.6 (0.1, 1.1)
HHb	1.5 (1.0, 1.9)	1.7 (1.2, 3.4)
Hb_T	1.4 (0.8, 1.8)	0.9 (0.5, 1.3)
S_tO_2	0.4 (−0.3, 0.5)	−1.2 (−1.7, −0.4)
H_2O	1.5 (1.3, 2.3)	1.2 (0.8, 3.2)
$Lipid$	−1.0 (−1.8, −0.6)	−0.9 (−2.2, −0.1)
TOI	1.7 (1.2, 2.4)	1.5 (1.2, 4.0)

	Midpoint Median Z-Score (IQR)	
	pCR	non-pCR
HbO_2	0.6 (0.4, 1.1)	0.5 (0.2, 1.3)
HHb	1.2 (0.9, 1.6)	1.4 (0.9, 3.0)
Hb_T	1.0 (0.7, 1.4)	0.9 (0.5, 1.6)
S_tO_2	−0.4 (−1.0, 0.2)	−0.9 (−1.8, −0.6)
H_2O	0.9 (0.4, 2.0)	1.3 (0.9, 2.3)
$Lipid$	−0.7 (−1.1, −0.1)	−0.9 (−1.6, −0.6)
TOI	1.5 (0.9, 2.0)	1.5 (1.2, 3.2)

Table 3.2: Median Z-score values with interquartile ranges (IQR) for each measured parameter and time-point, separated by pathologic complete response (pCR) status. Note the clear separation between the complete and non-complete responders in the S_tO_2 at the Early time-point. This is the source of the prediction from the best regression model (see Figure 3.7).

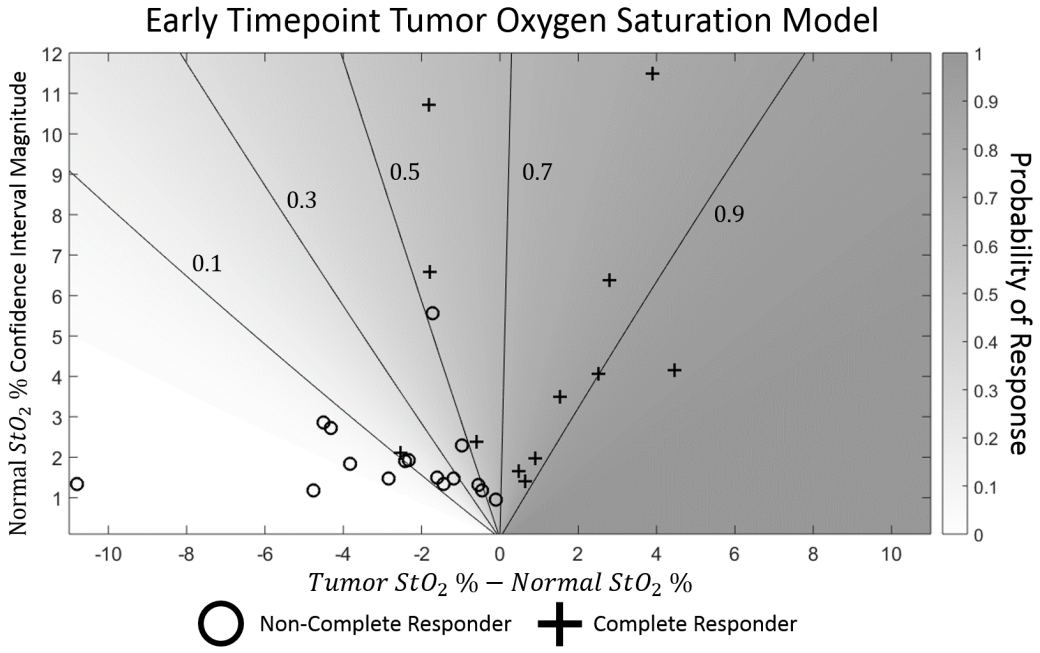

Figure 3.6: Tumor and Normal Early S_tO_2 vs Probability of Response. This graph illustrates the probability of response predicted by the regression model using only Early time-point S_tO_2 (see Figure 3.7). Contour lines of constant probability are also included. The probability of response (shading) is plotted versus the difference between the absolute tumor region percent oxygen saturation and the absolute normal region percent oxygen saturation (horizontal axis) and the size of the confidence interval for the absolute normal region oxygen saturation, corresponding to one standard deviation in the log-transformed data (vertical axis). Note, the oxygen saturation in this figure is not log-transformed or z-score normalized, and the confidence intervals for these absolute percent oxygen saturation measurements are calculated using the standard deviation of the log-transformed data. Each cross represents a subject that was a pathologic complete responder while each circle indicates a non-responding subject. All subjects that had tumor regions with absolute oxygen saturations that were higher than their normal regions achieved pCR. Subjects whose tumor regions were only slightly hypoxic relative to their normal regions were more likely to achieve pCR if the subjects' normal regions had larger confidence intervals. The observations indicate that a subject is likely to be a pathologic complete responder if the oxygen saturation of the tumor region is either higher than that of the normal region or well within the normal region's confidence interval. Subject whose tumors were significantly hypoxic relative to the normal tissue were likely to be non-responders.

schemes, *i.e.*, either no normalization or simple tumor-to-normal ratio normalization, were also produced to explore the added value of z-score normalization. These models were also significantly less predictive of response than z-score normalization with AUC values of 0.80 for tumor-to-normal ratio normalization and 0.75 for un-normalized tumor data.

The one-parameter model that used only Baseline tissue oxygen saturation (bS_tO_2) also produced a predictive model, albeit with lower accuracy than the eS_tO_2 model. The weight vector for

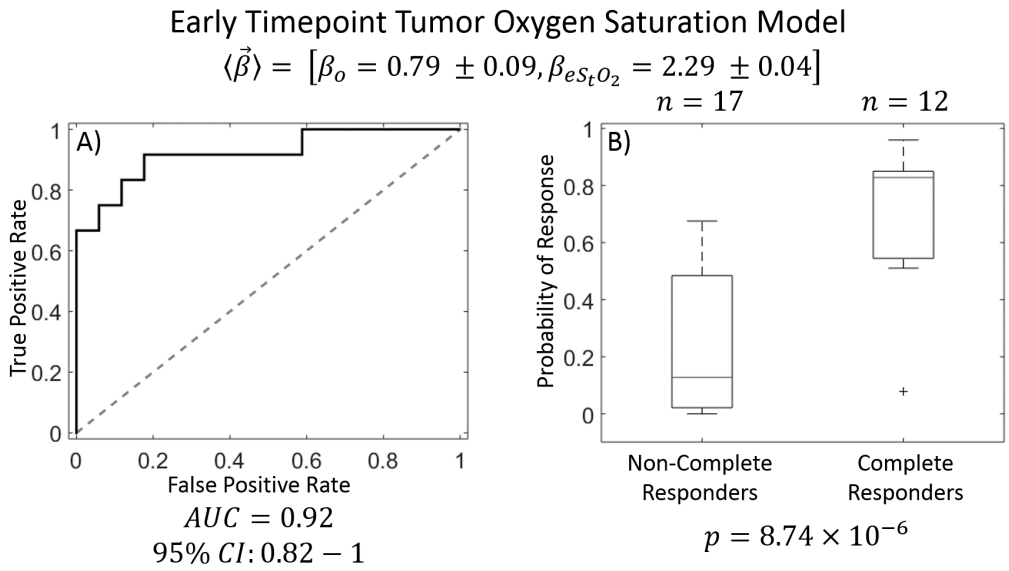

Figure 3.7: Early Time-point Oxygen Saturation Prediction Model. The model providing the best predictions used the Early time-point tissue oxygen saturation (eS_tO_2). The median weight vector $\langle\vec{\beta}\rangle = [\beta_o = 0.79 \pm 0.09,\ \beta_{eS_tO_2} = 2.29 \pm 0.04]$ indicates that tumors that are not hypoxic relative to the normal tissue on the tumor breast are more likely to be pathologic complete responders to chemotherapy. A) ROC Analysis of eS_tO_2 Model. This model produced an $AUC = 0.92\,(95\%\,CI: 0.82 - 1)$, indicating excellent predictive value. B) Boxplots of Probability of Response. The probability of response boxplots, divided into subjects that achieved pCR ($n = 12$) and subjects that did not achieve pCR ($n = 17$), indicate clear separation between the two groups using this model ($p = 8.74 \times 10^{-6}$ using a two-sample student's t-test). The hinges of the boxplots represent the first and third quartiles of the data, the whiskers represent the range of measurements within a distance 1.5× the interquartile range, and the cross represents an outlier. Note that there is no overlap between the interquartile ranges of the probabilities of response of the complete and non-complete responders.

this model was $\langle\vec{\beta}\rangle = [\beta_o = 1.05 \pm 0.09,\ \beta_{bS_tO_2} = 1.24 \pm 0.06]$, and the AUC was $0.79\,(95\,\%\,CI: 0.64 - 0.94)$ (see Figure 3.9). Importantly, this model demonstrates a similar physiological relationship: relative tumor hypoxia is a predictor of non-complete response. Thus, although it is less predictive than the Early time-point S_tO_2 model, a Baseline tissue oxygen saturation model may still be of clinical utility due to its earlier prediction time-point. A biomarker based on bS_tO_2 could be produced before a patient had to undergo a single chemotherapy treatment.

The best model that exclusively used Baseline data, *i.e*, a model that would enable pre-treatment prediction, was a two-parameter model that provided an $AUC = 0.83$ with a 95 % confidence interval of $AUC = 0.70 - 0.97$. This two-parameter model incorporated the Baseline oxygen saturation (bS_tO_2) and water concentration (bH_2O), and the median weight vector was $\langle\vec{\beta}\rangle = [\beta_o =$

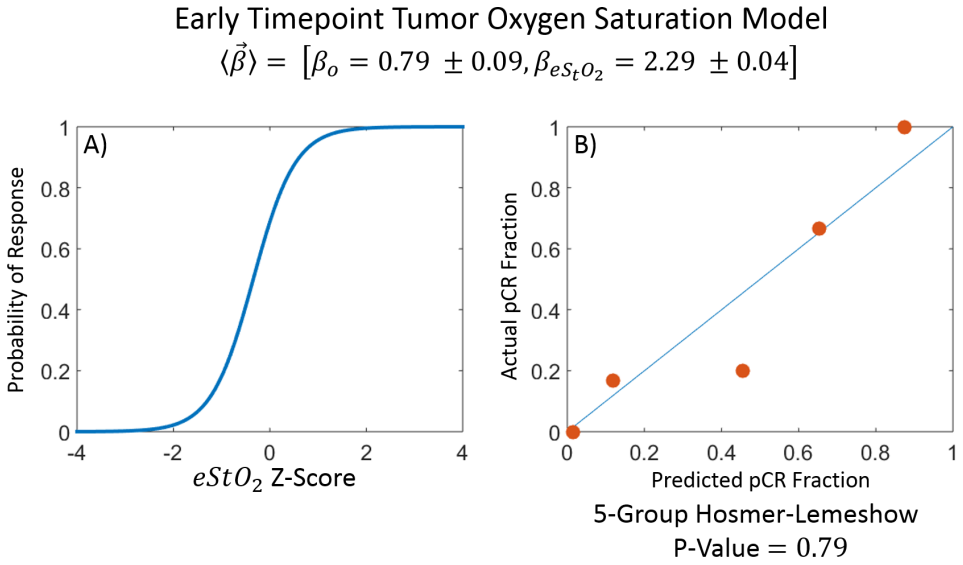

Figure 3.8: Early Time-Point Oxygen Saturation Logistic Function and Calibration A) Logistic function plot displaying the relationship between the predicted probability of response and the eS_tO_2 z-score, which represents how many standard deviations the tumor S_tO_2 is from the mean normal tissue S_tO_2. For example, a z-score of -1.3 produces a $\mathcal{P}_R = 0.1$, a z-score of -0.35 produces a $\mathcal{P}_R = 0.5$, and a z-score of 0.61 produces a $\mathcal{P}_R = 0.9$. B) Five-group Hosmer-Lemeshow calibration plot comparing the actual fraction of subjects in a group that achieved pCR versus the predicted fraction of subjects in that group that should achieve pCR based on their individual $\mathcal{P}_R$ values. See Section 2.10.4 for more information. Note that $p = 0.79$ indicates a good correspondence between actual and predicted pCR fractions.

0.14 ± 0.09, $\beta_{bS_tO_2} = 1.69 \pm 0.06$, $\beta_{bH_2O} = 0.65 \pm 0.03$] (see Figure 3.10). Again, the uncertainties in the $\langle\vec{\beta}\rangle$ components for H_2O and S_tO_2 are small, signifying a consistent fitted model across the leave-one-out validation procedure. Since $\beta_{bS_tO_2} > \beta_{bH_2O}$, the model indicates that the oxygen saturation is a more significant predictor of pCR than water concentration at the Baseline time-point. As with the Early time-point model, subjects with hypoxic tumors were less likely to achieve pCR.

As previously mentioned, many models were produced that did not include either the Baseline or Early time-point (S_tO_2), and some of these models were predictive ($AUC = 075 - 0.80$). However, all of the other models that were definitively predictive, when accounting for the 95 % confidence interval, incorporated at least one parameter from the Midpoint measurement. Thus, these models could only enable predictions ~ 2 months after the Baseline and Early S_tO_2 models.

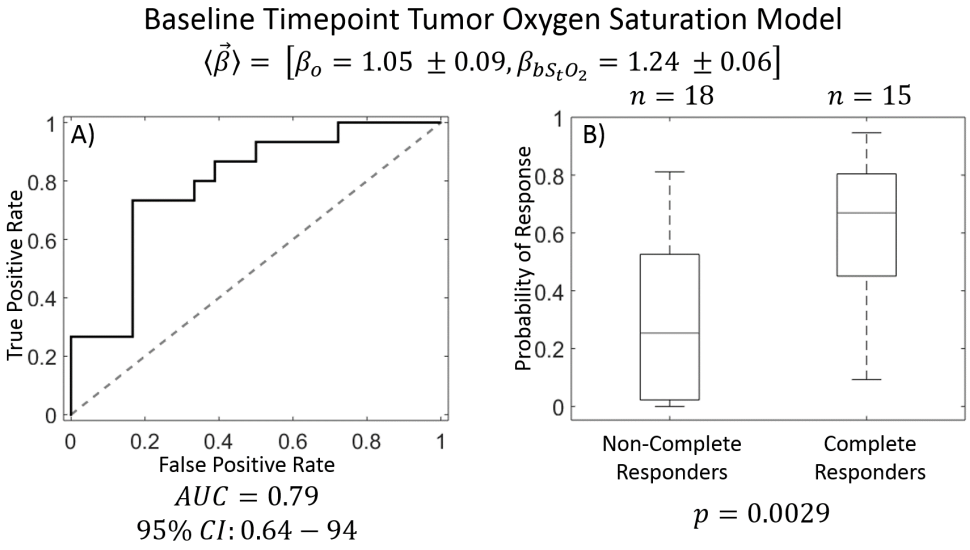

Figure 3.9: Baseline Time-point Oxygen Saturation Prediction Model. The model using only the Baseline time-point tissue oxygen saturation (bS_tO_2) produced a median weight vector $\langle\vec{\beta}\rangle = [\beta_o = 1.05 \pm 0.09,\ \beta_{bS_tO_2} = 1.24 \pm 0.06]$. This finding indicates that tumors that are not hypoxic relative to the normal tissue on the tumor breast are more likely to be pathologic complete responders to chemotherapy. A) ROC Analysis of bS_tO_2 Model. This model produced an $AUC = 0.79\,(95\%\,CI: 0.64 - 0.94)$, indicating predictive value, though considerably less than the AUC obtained with the eS_tO_2 model (Figure 3.7). B) Boxplots of Probability of Response. The probability of response boxplots, divided into subjects that achieved pCR (n=15) and subjects that did not achieve pCR (n=18), indicate fairly good separation between the two groups using this model ($p = 0.0029$ using a two-sample student's t-test). The hinges of the boxplots represent the first and third quartiles of the data, and the whiskers represent the range of measurements within a distance 1.5× the interquartile range.

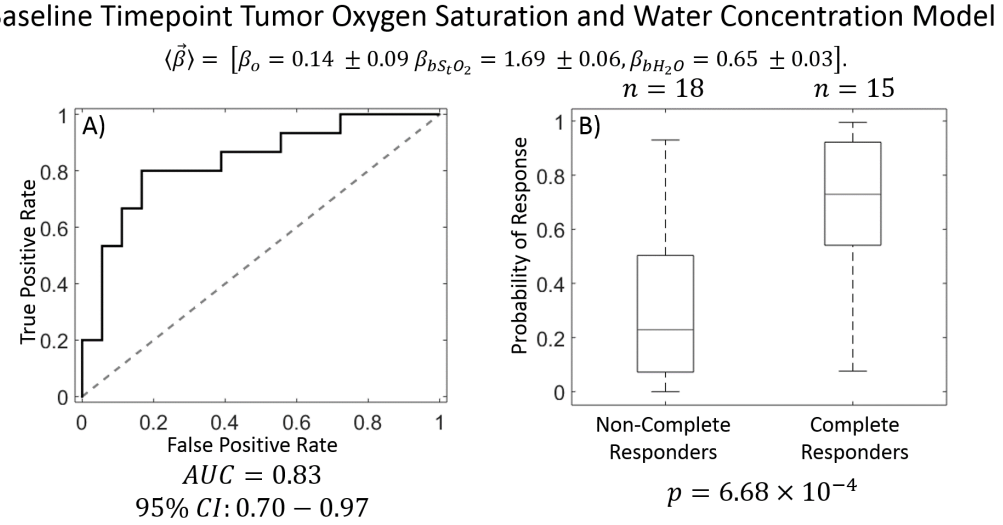

Figure 3.10: Baseline Time-point Oxygen Saturation and Water Prediction Model. The model using the Baseline time-point tissue oxygen saturation (bS_tO_2) and the Baseline water concentration (bH_2O) produced a median weight vector $\langle\vec{\beta}\rangle = [\beta_o = 1.05 \pm 0.09,\ \beta_{bS_tO_2} = 1.24 \pm 0.06,\ \beta_{bH_2O} = 0.65 \pm 0.03]$. This model indicates that tumors that are not hypoxic relative to the normal tissue on the tumor breast are more likely to be pathologic complete responders to chemotherapy and that Baseline oxygen saturation is more predictive than Baseline water concentration ($\beta_{bS_tO_2} > \beta_{bH_2O}$). A) ROC Analysis of $bS_tO_2 - bH_2O$ Model. This model produced an $AUC = 0.83\,(95\%\,CI: 0.70 - 0.97)$, indicating predictive value, though considerably less than the AUC obtained with the eS_tO_2 model (Figure 3.7). B) Boxplots of Probability of Response. The probability of response boxplots, divided into subjects that achieved pCR (n=15) and subjects that did not achieve pCR (n=18), indicate good separation between the two groups ($p = 6.68 \times 10^{-4}$ using a two-sample student's t-test). The hinges of the boxplots represent first and third quartiles of the data, and the whiskers represent the range of measurements within a distance 1.5× the interquartile range. Note that there is no overlap between the interquartile ranges of the probabilities of response of the complete and non-complete responders.

3.4 Discussion

By application of a logistic regression model using z-score normalized DOSI measurements, a robust predictor of response ($AUC = 0.92$; $95\,\%\,CI : 0.82 - 1$) can be derived within the first 10 days after a subject's initial chemotherapy dose. Using an optimally chosen cutoff value of $\mathcal{P}_R = 0.50$, which maximizes the sum of the sensitivity and specificity, this model provided an overall classification accuracy of 86 % (25 of 29 subjects), including a positive predictive value of 79 % for subjects predicted to achieve pCR (11 of 14), and a negative predictive value of 93 % for subjects predicted to not achieve pCR (14 of 15). These positive and negative predictive values are dependent on the chosen cutoff point (see Figure 3.11). Thus, for example, the positive predictive value could be optimized by using a higher $\mathcal{P}_R$ cutoff value.

Additionally, the Baseline S_tO_2 z-score can be used to create a predictive model ($AUC = 0.79$; $95\,\%\,CI : 0.64 - 0.94$), where higher S_tO_2 is once again correlated with pathologic complete response. This model is not as predictive as the Early time-point S_tO_2 model, with overall accuracy of 79 % (26 of 33), positive predictive value of 79 % (11 of 14), and negative predictive value of 79 % (15 of 19) at an optimal cutoff of $\mathcal{P}_R = 0.57$. Though the AUC value and prediction accuracy are lower for this model compared to the Early time-point S_tO_2 model, prediction of response prior to the initiation of therapy offers additional clinical utility because it provides a potential determination of future response at a time-point that could prevent a patient from receiving any unnecessary doses of chemotherapy. With this goal in mind, a two-parameter model, which also relies only on Baseline data, using the Baseline S_tO_2 and water concentration ($AUC = 0.83$; $95\,\%\,CI : 0.70 - 0.97$) was produced. This model provides an overall accuracy of 82 % (27 of 33), a positive predictive value of 80 % (12 of 15), and a negative predictive value of 83 % (15 of 18) at a probability cutoff of $\mathcal{P}_R = 0.53$. Thus, this two-parameter model represents an improvement over the bS_tO_2 model, but does not perform as well as the eS_tO_2 model.

Prediction of response at these early therapy time-points was a secondary aim of the ACRIN 6691 trial [249] and could, with further validation, enable clinicians to modify the patient's therapeutic plan after a single dose of chemotherapy. This ability holds potential to improve patient outcomes and prevent unnecessary side effects from ineffective treatments. The predictive ability of these models is comparable to, or slightly better than, early prediction models developed with other modalities, such as MRI [7; 200], FDG-PET [180; 200; 160], and biomarker analysis [125; 19; 95]. Some of these studies produced predictions prior to or within the first 10 days of treatment initiation [19; 95; 125; 160] while other approaches relied on imaging that occurred either after 6 weeks of NAC [7], at the midpoint of therapy [180], or after the completion of NAC [200]. The potential

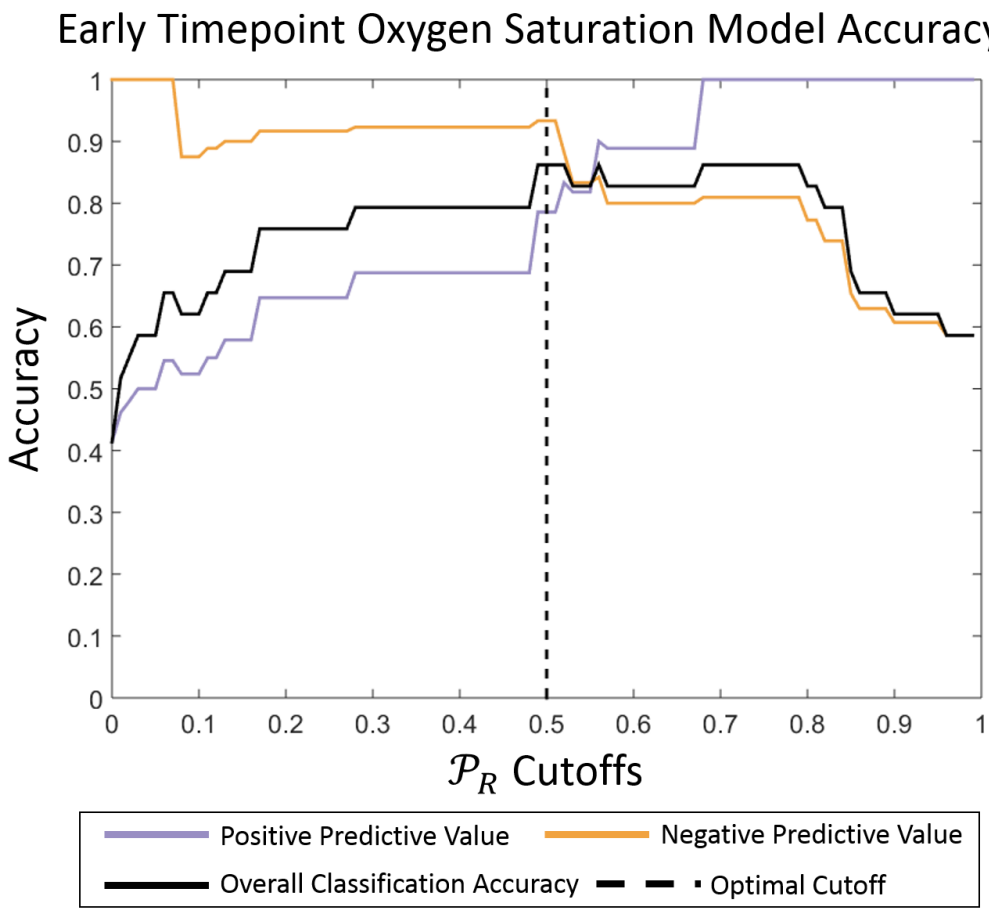

Figure 3.11: Early Time-Point Oxygen Saturation Model Accuracy. The eS_tO_2 model produces probability of response values $\mathcal{P}_{\mathcal{R}}$ for each subject. In order to predict whether individual subjects will achieve pCR, a cutoff value for $\mathcal{P}_{\mathcal{R}}$ must be chosen. In this plot, the purple line represents the positive predictive value, *i.e*, the percentage of subjects predicted to achieve pCR who are accurately classified, as a function of $\mathcal{P}_{\mathcal{R}}$ cutoff. The orange line is the negative predictive value, *i.e*, the percentage of subjects predicted to not achieve pCR that are accurately classified. The black line is the overall classification accuracy, and the dotted black line is the optimal cutoff value chosen by maximizing the sum of the sensitivity and specificity. See Section 2.10.3 for more information about these quantities.

advantage of this logistic regression DOSI model is premised on its unique combination of accurate prediction at an early time-point in therapy and the portability, low cost, and lack of ionizing radiation inherent in diffuse optical imaging techniques.

3.4.1 Physiological Meaning

All three of the best models indicated that low S_tO_2 at the Early or Baseline time-points relative to the surrounding normal tissue was predictive of non-response to chemotherapy. Physiologically, this hypoxia could be a sign of tumors that are not well-perfused in the early stages of treatment. Thus, the supply of oxygen is not sufficient to meet the metabolic demands of the tumor, leading to a hypoxic environment. This lack of perfusion could also inhibit efficient delivery of chemotherapy, preventing the subject from achieving pCR [90; 139; 150]. Tumors in oxygen-rich environments are also typically more responsive to therapy than hypoxic tumors, which often exhibit resistance to treatment independent of the perfusion level [139; 150]. These physiological mechanisms could explain the correlation between oxygen saturation and response at both the Baseline and Early time-points. The Early time-point S_tO_2 correlation could also be related to the actual tumor response to therapy. The lack of hypoxia in complete responders could indicate a decreased oxygen demand due to suppression of tumor metabolism by the chemotherapy, an indication that therapy is quickly working to destroy the tumor [94]. Alternatively, the improved correlation at the Early time-point could be due to the measurement of tumors that have undergone vascular renormalization, wherein the initial destruction of inefficient blood vessels via therapy reduces the interstitial pressure, allowing for increased perfusion [150]. Section 4.4 contains a more complete discussion of this phenomenon. These oxygen saturation models are also consistent with previous diffuse optical studies, which have observed correlation between pathologic complete response and optically-measured tissue oxygen saturation prior to the start of therapy [250] and after the first dose [220].

The two-parameter Baseline model also correlates high tumor water content relative to the normal tissue with probability of achieving pCR. The Baseline water weight factor β_{bH_2O} is significantly less than the Baseline oxygen saturation weight $\beta_{bS_tO_2}$ in this model, indicating that the water concentration is less predictive of pCR than S_tO_2. Given the relatively small sample size, it is unclear if including the Baseline water concentration with the Baseline S_tO_2 actually improves the model, or if the apparent improvement is due to statistical noise. Higher water concentration could correlate with likelihood to achieve pCR because water concentration is likely correlated with blood volume; therefore, higher water concentration could indicate a more well-perfused tumor [198], which would tend to achieve better therapy response [139; 150].

Lastly, Early time-point optical measurements may be a more reliable predictor of response than Midpoint measurements due to the mechanism of chemotherapeutic effects. The Early time-point measurements typically occur before significant anatomic changes in tumor size arise. This feature

enables the DOSI measurement to sample known tumor tissue more easily; at the Midpoint of therapy, by contrast, the tumor size has decreased and signal contamination between the malignant and healthy tissue can occur due to the partial volume effect, limiting the ability of DOSI to determine tumor physiological parameters accurately. This inability to distinguish tumor and normal tissue properties at the Midpoint is of particular concern with the z-score normalization algorithm that relies on accurate measurement of both regions.

3.4.2 Comparison to Other Normalization Techniques

Previous diffuse optical studies of response to breast cancer neoadjuvant chemotherapy have typically used the contralateral breast for normalization, have not utilized z-score normalization, and/or have correlated temporal changes in measured physiological parameters with response to treatment [248; 70; 59; 154; 236; 61; 220; 109; 250; 55; 223; 8]. These alternative approaches were explored in the current study to determine the optimal normalization method for prediction.

First, z-score normalization was implemented to place all parameters on the same magnitude scale, which mitigates systemic physiological differences among the subject population and accounts for the systemic effects of chemotherapy. For comparison, models were created that used fully un-normalized data and Tumor-to-Normal ratio normalization, *i.e.*, an average value of a tumor parameter divided by the average of the same parameter in the normal tissue. As with the z-score normalized data, the logistic regression algorithm was run to produce probabilities of response. With Tumor-to-Normal ratio normalization, a one-parameter model with Early time-point S_tO_2 produced an $AUC = 0.80$, the Baseline S_tO_2 model resulted in an $AUC = 0.69$, and the two-parameter model with Baseline time-point S_tO_2 and H_2O produced an $AUC = 0.67$. The AUC values for the same models but with no normalization were even lower ($AUC = 0.75$, $AUC = 0.64$, and $AUC = 0.67$, respectively). The advantage of un-normalized or Tumor-to-Normal data is that it can be acquired with fewer spatial data points. However, these mean values do not account for the inherent heterogeneity of the normal breast tissue. For example, without some knowledge of the normal tissue heterogeneity, such as a standard deviation across many spatial points, there is little context to indicate whether a given Tumor-to-Normal parameter value represents a significant contrast between the tumor and normal tissue or simply a random variation that could be expected to be found in the normal tissue itself. This limitation, along with the statistical issues inherent in regressing over features with large magnitude variations and features with non-Gaussian distributions, could explain the improved correlation generated by z-score normalized data [206; 136; 141].

Many diffuse optical chemotherapy monitoring studies also utilize temporal normalization, whereby the change in parameters from Baseline are correlated with response to treatment [248;

59; 154; 236; 61; 220; 109; 55]. Z-score regression models with this temporally normalized data were also tested. However, even the most predictive of the models derived in this analysis that used the change in any DOSI physiological parameter between the Baseline and Early time-points only produced an $AUC = 0.63$. The best temporal change model between the Baseline and Mid-point produced an $AUC = 0.74$, which, although more predictive than the models at the Early time-point, has the disadvantage of providing predictions approximately two months later in the chemotherapy cycle. The temporal change models of S_tO_2, in particular, could be limited by the large inter-subject dispersion of the Baseline oxygen saturation; this large dispersion prevents the change in S_tO_2 between the Baseline and Early time-points alone from accurately reflecting the oxygenation state of the tumor relative to the normal region. By contrast, the eS_tO_2 model presented here does not depend on the Baseline S_tO_2 and, as such, is not affected by inter-subject Baseline variation. In other words, the set of subjects whose tumors exhibit high Early time-point S_tO_2 z-scores encompasses both those subjects whose Baseline S_tO_2 was high and subjects whose Baseline S_tO_2 experienced a large increase after the first dose of therapy. Models that rely on the change in S_tO_2 between the Baseline and Early time-points may not accurately reflect the normoxic or hyperoxic states of tumors that began with high S_tO_2 and experienced a limited change.

Finally, z-score normalization to the contralateral breast tissue, rather than the normal tissue on the tumor-bearing breast, was tested. This is a common method of normalization in the diffuse optical community due to the fear of tumor tissue signal contamination in the tumor-bearing breast normal tissue caused by the partial volume effect. If the contralateral breast was used for z-score normalization with the primary models discussed here, the one-parameter Early S_tO_2 model produced an $AUC = 0.67$, the one-parameter Baseline S_tO_2 model produced and $AUC = 0.68$, and the two-parameter model with Baseline S_tO_2 and H_2O produced an $AUC = 0.64$. Thus, z-score normalization to normal tissue on the tumor-bearing breast appears to enable better predictions of response to therapy than use of the contralateral breast data. This could be a result of systemic differences in oxygen saturation between the ipsilateral and contralateral breast. Thus, comparison of the tumor oxygen saturation to the contralateral oxygen saturation may not be an accurate representation of the relative level of tumor hypoxia. The comparatively better quality of the tumor breast z-score normalized models suggests that measurement of the contralateral breast is less important for early prediction of response to therapy than previously thought, which confirms other work done with the DOSI instrument [163]. If this is true, then a new imaging paradigm could eliminate the need for contralateral measurement and reduce imaging time by half. This advance could enable easier clinical adoption of the DOSI system.

3.4.3 Limitations and Future Directions

The primary limitations of this study are the relatively small number of subjects and the highly variable chemotherapy regimens across the subject population. Additionally, the initial study had a fairly high dropout rate (see Figure 3.1) [249], introducing a potential bias into the statistical analysis. Finally, although the initial ACRIN 6691 trial was a prospective study, this z-score parameter imaging metric was retrospectively optimized using a standard leave-one-out protocol. The leave-one-out technique limits overfitting and enhances the generalizability of the prediction metric [136]; it has been used extensively in the cancer imaging community [152; 7; 250; 185; 153]. However, a fully prospective validation with an independent cohort of subjects will be necessary to test this biomarker prior to clinical adoption.

Per the first limitation noted above, application of this model to a prospective study with a larger subject population is a natural course of action. A new multi-site trial has already been initiated for this purpose. Importantly, because the DOSI instrumentation has been shown to provide consistent performance over time, across multiple instruments, and across multiple measurement sites [166], the weight vectors derived for these S_tO_2 models (see Figures 3.7, 3.9, and 3.10) could be used with z-score normalized measurements in future DOSI studies to calculate a probability of response, i.e., without creating a new logistic regression model for each population. In this case, the future study would serve as a direct, independent test set for the results obtained by the current model. Additionally, a new logistic regression could also be run on this larger data set to derive an improved prediction model based on a larger training set. If a future study were performed on a significantly different patient population, e.g., patients with tumors in non-breast tissue, then deriving a new weight vector via logistic regression would likely be beneficial.

Besides providing evidence to further corroborate the results of this pilot investigation, the larger subject population may enable stratification of the subject population by tumor subtype and/or chemotherapy regimen. The current results are reported for a diverse patient population with various tumor molecular subtypes (see Table 3.1), as well as an assortment of chemotherapy regimens [249]. Tumor subtypes may have different levels of tissue oxygen saturation and may respond to chemotherapy differently [221; 107; 108]. The physiological mechanisms of chemotherapy regimens also vary [62]. Thus, especially for parameters at the Early time-point, response prediction might be improved by creating individual models for different classes of chemotherapy and/or different tumor subtypes or by incorporating hormone biomarkers into the prediction models. Also, measurement of independent hypoxia biomarkers, such as carbonic anhydrase IX [2] or O-15 water

PET [173], and assays for vascular density, such as CD31 staining [2], may enable better understanding of the mechanism responsible for the correlation between tissue oxygen saturation and response. The simplest method for investigating this is to combine this DOSI model with DCS measurements, as is done in Chapter 4. This blood flow information could help to disentangle the roles of perfusion and metabolism in the oxygen saturation measurement. Exploration of these questions should be possible in a larger study.

3.5 Conclusion

Logistic regression models of z-score normalized physiological parameters measured by diffuse optical spectroscopic imaging (DOSI) were found to predict pathologic complete response (pCR) to neoadjuvant chemotherapy. The best model successfully predicted pCR ($AUC = 0.92$; $95\,\%\,CI : 0.82 - 1$) using tumor and normal tissue oxygen saturation measured within the first 10 days after the initial dose of therapy based on data from the ACRIN 6691 multi-site clinical trial [249]. This model suggests that if tumors are hypoxic relative to the surrounding normal tissue, then they are less likely to achieve pCR. Models that incorporate the pre-therapy (Baseline) oxygen saturation were also predictive and demonstrated a similar correlation between physiology and response to chemotherapy. These early predictions of therapeutic efficacy are based on quantitative DOSI measurements of tumor and normal tissue functional parameters, which have been shown to be more predictive of response to therapy than structural changes in tumor size [173; 181; 180; 144; 143]. The DOSI-measured models produced here had similar or improved predictive power at a comparable or earlier time-point to gold-standard functional imaging modalities [180; 7; 200; 160] in addition to the inherent logistical benefits of DOSI, such as low imaging costs, portable instruments, and lack of ionizing radiation. The z-score normalization of the tumor physiological data also yielded improved prediction models compared to tumor-to-normal ratio or un-normalized data, indicating the importance of incorporating the heterogeneity of breast tissue into diffuse optical analysis. Prospective validation with a fully independent population is still needed to confirm these promising results, and a study is underway for this purpose across many of the same sites that participated in the ACRIN-6691 trial. With this validation set, DOSI and logistic regression methods could be used early in the course of neoadjuvant chemotherapy to optimize treatment regimens for individual patients, potentially improving outcomes and sparing patients the unnecessary side effects associated with ineffective treatments.

Chapter 4

Combined DOS and DCS Monitoring of Breast Tumors during Neoadjuvant Chemotherapy

4.1 Introduction

Chapter 3 introduced neoadjuvant chemotherapy (NAC) in clinical breast cancer treatment, discussed limitations of current treatment monitoring modalities, and introduced a diffuse optical method for predicting pathologic complete response (pCR) to chemotherapy. This technique utilized a z-score normalization technique and logistic regression, based on parameters measured with diffuse optical spectroscopic imaging (DOSI).

However, all of the DOSI-measured parameters are steady-state measures. That is, while DOSI provides a measure of blood volume, via the total hemoglobin concentration (Hb_T), and oxygenation, via the tissue oxygen saturation (S_tO_2), it does not directly probe blood flow. In previous NAC monitoring studies, other imaging modalities that have predictive value with respect to pCR, such as magnetic resonance spectroscopy (MRS) [181], contrast-enhanced MRI [144], and positron emission tomography (PET) [173; 180], suggest that metabolism and/or blood flow are correlated with treatment response. Unfortunately, MRI, MRS, and PET all suffer from logistical limitations which limit their viability for serial monitoring of therapy progression in patients undergoing

chemotherapy, including high-cost, use of exogenous contrast agents, and ionizing radiation in the case of PET. Thus, a concurrent diffuse optical measurement of blood flow should provide useful information for predicting treatment response without the inherent practical limitations of MRI and PET. Fortunately, diffuse correlation spectroscopy (DCS), a technique introduced in Section 2.9, offers such a measurement of blood flow.

Recall, from Section 2.9, that DCS utilizes the temporal fluctuations of detected light intensity to probe microvasculature blood flow in deep tissue [32; 98]. The blood flow index (BFI) [cm^2/s] measured by DCS has been validated in humans against numerous gold-standard techniques [182], including transcranial Doppler ultrasound [50], phase-encoded velocity mapping MRI [51; 151], and xenon-enhanced computed tomography [158]. DCS has also been used to characterize hemodynamic properties of normal and malignant human breast tissue [273; 100; 269; 53; 73], to investigate blood flow in the early stages of NAC [273], and to longitudinally explore chemotherapy regimens in a murine model [216].

The present study utilized both DCS and DOSI; their combined use provides several benefits. First, absolute μ_a and μ_s' values derived by DOSI constrain DCS blood flow fittings and thus reduce cross-talk between changes in optical and blood flow parameters [147; 114; 76; 264]. Additionally, the combination of S_tO_2, measured by DOSI, with BFI, measured by DCS, permits investigation of oxygen metabolism in malignant tissue. Oxygen metabolism is a comparatively new biomarker for chemotherapy response that could enable direct comparison of optical diagnostics to other imaging modalities such as FDG-PET.

This study utilized four patients enrolled in the previously discussed ACRIN-6691 clinical trial [249]. They were monitored longitudinally using both DCS and DOSI throughout their NAC regimens. The blood flow data in tumor and healthy breast tissue was analyzed to ascertain potential hemodynamic differences between responders and non-responders. Previous studies have used combinations of DCS and DOS instrumentation to monitor breast tumors [100; 273; 73; 264] and to monitor head and neck tumors [241; 147], but the present work is the first investigation to use DCS to measure blood flow throughout the course of NAC in humans with breast cancer, and it is the first to correlate DCS hemodynamic properties with pCR and treatment in humans [76].

These pilot measurements suggest that DCS-derived blood flow parameters are correlated with pCR. Importantly, this blood flow information could enable more reliable prediction of lesion response or elucidation of the mechanism by which tumors respond or don't respond (see Section 3.4.1), enabling physicians to individually optimize treatment regimens, avoid unnecessary therapy doses, reduce tissue damage, and improve patient outcomes.

	Subject 1	Subject 2	Subject 3	Subject 4
NAC Response	pCR	non-pCR	pCR	non-pCR
Age, Years	65	56	32	39
Menopausal Status	Post-	Peri-	Pre-	Pre-
Max. Tumor Size	3.2 *cm*	6.2 *cm*	6.5 *cm*	2.1 *cm*
Histological Status	IDC	IDC	IDC+DCIS	IDC
ER Status	Negative	Positive	Positive	Negative
PR Status	Negative	Positive	Positive	Negative
Her2 Status	Negative	Negative	Positive	Negative
Molecular Subtype	Triple Neg.	Luminal B	Her2 Positive	Triple Neg.
NAC Regimen	Doxorubicin Cyclophos.	Taxol Carboplatin Tamoxifen	Taxol Carboplatin Herceptin	Doxorubicin Cyclophos.

Table 4.1: DOSI/DCS Study Tumor Properties by Response Status. Demographic, histological, immunohistochemical, and chemotherapy regimen data is provided for all four subjects from the ACRIN 6691 trial used in this pilot study. The NAC response status is either pCR for pathologic complete responders or non-pCR for non-complete responders. For histological information, IDC refers to invasive ductal carcinoma, and DCIS is ductal carcinoma *in-situ*. ER, PR, and Her2 represent estrogen receptor, progesterone receptor, and human epidermal growth factor receptor status, respectively. The neoadjuvant chemotherapy (NAC) regimens given here are the treatments initially received by the subject; some subjects underwent a change in regimen after the Midpoint of therapy. Finally, Triple Neg. refers to the triple negative molecular subtype, and Cylcophos. refers to the chemotherapy drug cyclophosphamide.

4.2 Subjects and Methods

4.2.1 Study Design and Subjects

For this study, four breast cancer patients who were enrolled in the ACRIN-6691 DOSI trial [249] and imaged at the University of Pennsylvania were also measured with a DCS system developed at the University of Pennsylvania. The subjects were females between the ages of 31 and 65 with biopsy-confirmed invasive carcinomas of at least 2 *cm* in diameter along the largest axis. These subjects underwent an NAC regimen prior to surgery. All four subjects received either Doxorubicin/Cyclophosphamide, Taxol, or a combination of both within the course of NAC treatment. In addition, hormone receptor positive subjects were given hormone therapy. The chemotherapy regimen was determined by each subject's physician and was not controlled for in this study. Here, pathologic complete response (pCR) was defined in the same manner as Chapter 3, *i.e*, no residual invasive carcinoma, as determined by post-surgery pathology reports, without regard to residual lymph node disease. Table 4.1 contains relevant physiological information for these subjects.

Each subject was imaged at the four prescribed time-points throughout the course of treatment

from the ACRIN-6691 trial (see Figure 3.2). The first (Baseline) measurement occurred prior to the subject's first chemotherapy treatment. The second measurement, referred to as the Early measurement, was performed between 5 and 10 days after the first chemotherapy treatment. This time period was chosen in order to avoid the so-called oxyhemoglobin flare that has been found to occur immediately after chemotherapy treatment [273; 220]. A third measurement was made at the midpoint of the therapy regimen (Midpoint), and a final measurement (Final) was made at the conclusion of the regimen, prior to surgical intervention.

4.2.2 Optical Imaging Methods

The custom-built DCS instrumentation used in this study is described in full elsewhere [97]. Briefly, light from a continuous wave, long-coherence length ($> 5m$), $785\,nm$ laser (DL785-100-3O, CrystaLaser, Reno, Nevada) with a maximum power of $100\,mW$, attenuated to within ANSI power limits and coupled to a multi-mode fiber ($200\,\mu m$ core/$0.22NA$, $4\,m$ in length, OZ Optics, Ontario, Canada), illuminated the breast tissue. A single-mode detection fiber ($5\,\mu m$ mode field diameter/$0.13\,NA$, $4\,m$ in length, OZ Optics, Ontario, Canada) couples diffusive light emerging from the tissue to a single photon counting avalanche photodiode (SPCM-AQ4C, Excelitas, Quebec, Canada) operating in photon counting mode. The source and detector probe was placed on the tissue with minimal pressure to prevent significant pressure-induced changes in blood flow [53]. The photodiode's collected light intensity at time t ($I(t)$) was sent to a multiple-τ hardware correlator (Flex02OEM4ch, Correlator.com, New Jersey) for computation of the normalized intensity autocorrelation function in real time, *i.e.*, computation of $g_2(\tau) \equiv \langle I(t)I(t+\tau)\rangle/\langle I(t)\rangle^2$. Here, the angular brackets $\langle\rangle$ represent time-averages over an interval of 2.5 s. A semi-infinite homogeneous tissue model is employed to derive a DCS blood flow index (BFI) from the temporal decay of $g_2(\tau)$. Section 2.9 contains a more complete description of the theory underlying DCS. Multi-layer models for DCS fitting have also been explored to reduce the signal contamination from blood flow in the superficial skin/skull layer of the head [149; 231; 22]. However, in this study, the superficial (skin) layer was very thin in comparison to the source-detector separation, and breast tissue is less susceptible to layer-dependence than cerebral measurements which must traverse the skull. Moreover, the study did not incorporate multiple source-detector separations nor *a priori* anatomical knowledge of the superficial layer thickness. Therefore, the simple semi-infinite model was both the best fit for breast anatomy and did not require unverified assumptions.

Formally, the normalized autocorrelation function of the electric field (E(t)), *i.e.*, $g_1(\tau) \equiv \langle \mathbf{E}^*(t)\cdot\mathbf{E}(t+\tau)\rangle/\langle I(t)\rangle$ (Equation 2.178), is obtained from the measured normalized intensity autocorrelation function (Equation 2.179) via the Siegert relation (Equation 2.180) [162]. $g_1(\tau)$

is in turn modeled by the semi-infinite homogeneous medium solution to the correlation diffusion equation (Equation 2.184), which depends on the underlying tissue blood flow index (BFI), μ_a, and μ_s' [33; 38]. The semi-infinite correlation diffusion solution is fit to $g_1(\tau)$ using a nonlinear minimization algorithm [3], and an estimate of BFI is obtained from the fit [38; 98].

The same DOSI instrument that was described in Section 3.2.2 was used in the present study. It combines multi-spectral frequency-domain and broadband imaging to measure absolute μ_a, μ_s', and the tissue concentrations of oxygenated hemoglobin (HbO_2), deoxygenated hemoglobin (HHb), water, and lipid. The combination of these chromophores permits calculation of tissue total hemoglobin concentration (Hb_T) and tissue oxygen saturation (S_tO_2). Full descriptions of this instrument and imaging technique have been published [30; 166].

As with the rest of the subjects in the ACRIN-6691 trial, a grid of approximately 10×10 points with 10 mm spacing between adjacent points was marked on the subject's skin during the Baseline measurement. The location of this grid was chosen to encompass the entire extent of the lesion and to include the surrounding healthy tissue. The location of and extent of the lesion was derived from an ultrasound image. The measurement grid was then recorded using a transparency, so that its location could be accurately replicated during future measurements. A mirrored grid of points was also marked on the contralateral breast. DOSI data was recorded at each of the points on both grids, thereby providing images of the underlying tissue optical properties and chromophore concentrations, as well as absolute optical properties at each point.

DCS data was collected along a single line of points (~ 10 points) on each grid. This line was chosen to traverse both lesion and non-lesion tissue on the tumor-bearing breast and was mirrored to the same locations on the contralateral breast (see Figure 4.1). Spatial points were categorized as either tumor measurements, which were those spatial points measuring the ultrasound-defined tumor region at the Baseline measurement, ipsilateral normal tissue measurements, which were the points away from the tumor region on the tumor-bearing breast, and contralateral normal measurements, *i.e.*, all points on the contralateral breast.

4.2.3 Statistical and Analytic Methods

The first application of the co-located DOSI and DCS measurement is to utilize the absolute DOSI-measured μ_a and μ_s' at each point as inputs in the fitting algorithm for the DCS BFI. The DCS BFI was also calculated using a single set of assumed μ_a and μ_s' values that most closely fit our DOSI-measured optical property data. The error in the BFI between these two methods was then calculated as a function of the μ_a and μ_s' errors in order to determine the effect of inaccurate optical properties on the BFI calculation.

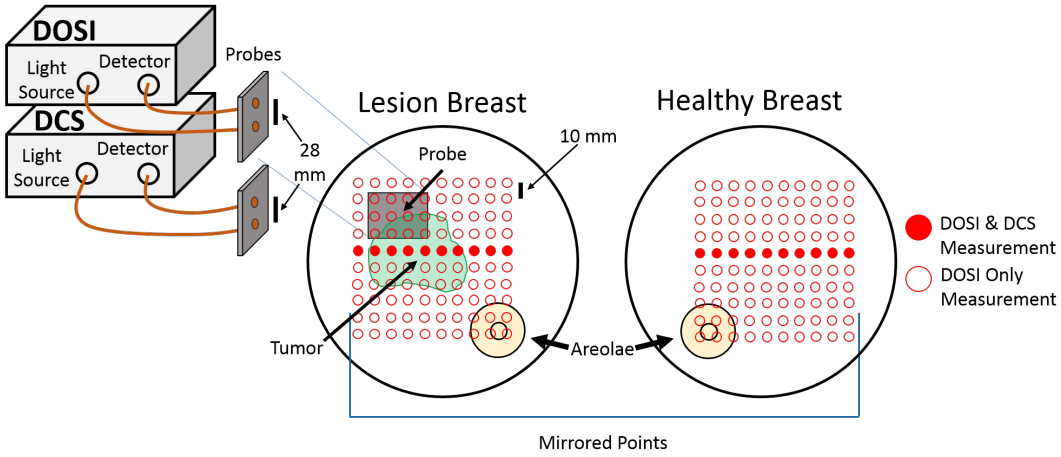

Figure 4.1: Schematic of the DOSI and DCS measurements. Left: DCS and DOSI instruments and probes. Right: A grid of approximately 10×10 DOSI measurements were made on each of the subject's breasts. The location of the grid was chosen to encompass the entire lesion, in addition to surrounding normal tissue, and was then recorded on a transparency along with physiological landmarks such as moles, freckles, and the areolae. This transparency allowed for a mirrored grid of points to be measured on the contralateral (healthy) breast. DCS measurements were made at a single line of ~ 10 grid points that completely traversed the lesion and the ~ 10 corresponding points on the contralateral breast.

Measurements of absolute BFI, tumor-to-normal ratio BFI, *i.e.*, the BFI_T in the tumor region divided by the corresponding BFI_N on the contralateral breast, and Baseline-normalized BFI, *i.e.*, the BFI in the tumor region at a given time-point divided by the BFI at the same spatial point during that subject's Baseline measurement $BFI_{T,B}$, were then calculated across all four time-points (see Figure 3.2). Qualitative initial correlations between these hemodynamic parameters and the subjects' pathologic response statuses were than explored.

Finally, as previously noted, the combination of DCS blood flow measurements (BFI) with DOSI tissue oxygen saturation (S_tO_2) measurements permits investigation of oxygen metabolism. A steady-state compartment model and the Fick principle [118] can be used to calculate a so-called mammary metabolic rate of oxygen consumption $MMRO_2$ [273; 54]. Briefly, the $MMRO_2$ in a tissue compartment is proportional to the blood flow to the compartment multiplied by the difference in oxygen concentration between the arterial and venous compartments (see Figure 4.2). Thus, $MMRO_2$ can thus be written as

$$MMRO_2 \propto BFI \cdot (S_aO_2 - S_vO_2)\,, \tag{4.1}$$

where BFI is the DCS blood flow index, S_aO_2 is the arterial oxygen saturation, and S_vO_2 is the venous compartment oxygen saturation. Note that a proportionality constant κ is needed here

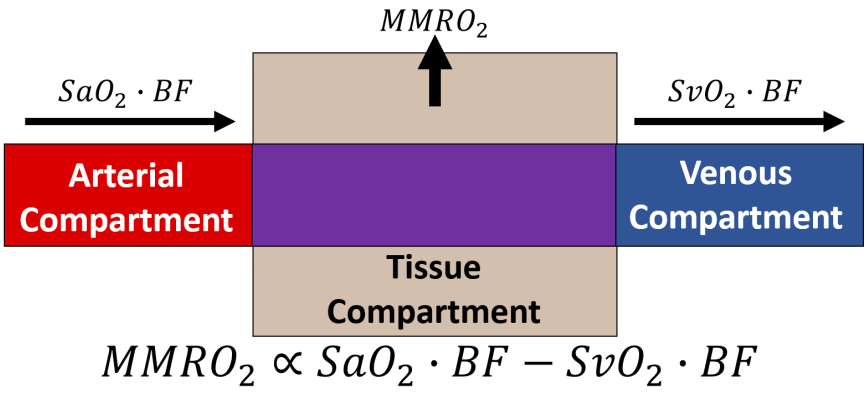

Figure 4.2: Schematic of Steady-State $MMRO_2$ Compartment Model. In steady-state, the mammary metabolic rate of oxygen consumption $MMRO_2$ in the tissue compartment can be modeled as being proportional to the blood flow BFI times the difference in arterial and venous oxygen saturations, S_aO_2 and S_vO_2, respectively. This model is based on the Fick principle [118] and has been previously utilized in breast tissue [273; 54]. Note, the inability to determine the exact proportionality constant for this relationship necessitates the use of relative measurements of $MMRO_2$.

to calculate absolute $MMRO_2$ because the BFI must be calibrated to absolute clinical blood flow units (see Section 2.9.3). While this equation offers a useful relation, DOS actually measures the tissue oxygen saturation S_tO_2 which is sensitive to the oxygen saturation averaged across the microvasculature. Thus the the measured S_tO_2 should be modeled as a weighted average of the arterial and venous oxygen saturations, *i.e.*,

$$S_tO_2 = (1-\gamma)\, S_aO_2 + \gamma\, S_vO_2. \tag{4.2}$$

Here, γ is a weighting factor indicating the fraction of S_tO_2 that is dependent on S_vO_2. In practice, γ represents

$$\gamma \equiv \frac{HHb_v/Hb_{T_v}}{HHb/Hb_T} \tag{4.3}$$

Thus, γ depends on the ratio of deoxyhemoglobin to total hemoglobin concentration in the venous vascular compartment (*i.e.*, $HHb_v/Hb_{T,v}$) relative to the ratio of deoxyhemoglobin to total hemoglobin in all tissue (*e.g.*, as determined by DOSI tissue measurements). The aforementioned proportionality coefficient between BFI and absolute blood flow, *i.e.*, κ, can also be subsumed into this constant. In both this data set and in past studies [273; 54], γ is unknown because it is not readily feasible to separate the venous compartment contribution to the optical signal from that of the arterial and capillary contributions, and because the DCS-measured BFI $[cm^2/s]$ has not been calibrated to obtain κ. Therefore, instead of estimating absolute $MMRO_2$, the present work focuses on the relative tumor-normal (T/N) oxygen metabolism ratio, $rMMRO_{2_{(T/N)}}$, and

temporal changes in tumor oxygen metabolism relative to the Baseline time-point (see Figure 3.2), $rMMRO_{2_B}$. The first step is to simplify Equation 4.1 by substituting for S_vO_2 using Equation 4.2, resulting in

$$MMRO_2 = \frac{1}{\gamma}\left(S_aO_2 - S_tO_2\right) \cdot BFI. \tag{4.4}$$

Then, it can be assumed that $S_aO_2 \approx 1$ since the hemoglobin in arterial blood is almost fully oxygenated. This simplifies the equation further to

$$MMRO_2 = \frac{1}{\gamma}\left(1 - S_tO_2\right) \cdot BFI. \tag{4.5}$$

Thus, other than the proportionality constant γ, the calculation of $MMRO_2$ can be accomplished using two quantities, S_tO_2 and BFI, measured by DOSI and DCS, respectively. Assumption of a constant γ permits relative measurements of $MMRO_2$ to normalize away the γ factor and provide useful measurements of $rMMRO_2$. For example, the relative tumor-normal oxygen metabolism ratio is the oxygen metabolism of a point over the tumor divided by the oxygen metabolism at the corresponding position on the contralateral breast. It is calculated via

$$rMMRO_{2_{(T/N)}} \approx \left(\frac{1 - S_tO_{2_T}}{1 - S_tO_{2_N}}\right)\left(\frac{BFI_T}{BFI_N}\right). \tag{4.6}$$

Here, $S_tO_{2_T}$ and BFI_T represent S_tO_2 and BFI measurements made at a spatial location within the tumor region (see Figure 4.1) at the time point of interest during NAC treatment (see Figure 3.2), and $S_tO_{2_N}$ and BFI_N are derived from S_tO_2 and BFI measurements made at the corresponding spatial location on the contralateral breast. Equation 4.6 assumes that γ in Equation 4.5 is the same for both breasts.

Similarly, temporal relative changes in tumor oxygen metabolism are calculated via

$$rMMRO_{2_B} \approx \left(\frac{1 - S_tO_{2_T}}{1 - S_tO_{2_{T,B}}}\right)\left(\frac{BFI_T}{BFI_{T,B}}\right), \tag{4.7}$$

where $S_tO_{2_T}$ and BFI_T are defined as in Equation 4.6 and $S_tO_{2_{T,B}}$ and $BFI_{T,B}$ explicitly denote $S_tO_{2_T}$ and BFI_T for the Baseline time-point (see Figure 3.2). Equation 4.7 assumes that γ in Equation 4.5 remains constant for all measurement time-points during NAC treatment.

While this approach is a sensible first approximation, the assumption of constant γ is not verified, and its verification would require research into the microcirculation of malignant and healthy tissue that is beyond the scope of this study. See Section 4.4 for more discussion of this complication.

4.3 Results

4.3.1 Blood Flow Measurements

All four of the measured subjects were diagnosed with biopsy-confirmed invasive ductal carcinomas. Two of the four subjects achieved pCR as determined by the post-surgery pathology report. One of the complete responders was pre-menopausal and one was post-menopausal. Similarly, one of the non-pCR subjects was pre-menopausal while the other was peri-menopausal. Across the four subjects, 36 total spatial points were measured on the subjects' lesion-bearing breasts, and 40 total spatial points were measured on the subjects' contralateral breasts ($\sim$ 10 spatial points per subject per breast) for each of the four longitudinal time points. Of the 36 total spatial points on the ipsilateral breast, 22 points were directly above the ultrasound-confirmed location of the lesion. Notably, these four subjects all exhibited the expected Early time-point S_tO_2 from the prediction model in Chapter 3 for their respective response statuses.

The data were divided into contralateral (healthy) and lesion-bearing breast data for each subject, and then grouped based on response to chemotherapy (pCR and non-pCR). The points on the lesion breast were further divided into points directly over the tumor and points in the nominally normal tissue surrounding the tumor. The blood flow at the non-tumor points on the lesion-bearing breast tended to resemble the blood flow in the healthy breast and thus will not be shown in the figures. For the responder group (pCR), 11 spatial points were measured in the tumor region (5 on one subject, 6 on the other subject), and 19 spatial points were measured on the healthy breast (9 on one subject, 10 on the other subject) across the two subjects. The non-responder group (non-pCR) had 11 spatial points in the tumor region (6 on one subject, 5 on the other subject), and 21 spatial points on the healthy breast (10 on one subject, 11 on the other subject). Note, due to the small sample size of our data set, herein potentially interesting distinctions that are suggested by the data are explored, but no claim of statistically significant differences between the responders and non-responders can be made.

Figure 4.3 shows the DCS BFI measurements at each of the four longitudinal time points for both healthy breast and tumor tissue. Notice first that the BFI is lower in responders compared to non-responders. This distinction exists at all four temporal points, but the distinction becomes more pronounced at the Midpoint and Final time points of the chemotherapy regimen, at which time, the difference between the responders' and non-responders' tumor blood flow is apparent despite clear intra-subject spatial heterogeneity in blood flow. At these points the responders' tumor BFI begins to resemble the BFI in the responders' healthy breast tissue while the non-responders' tumor

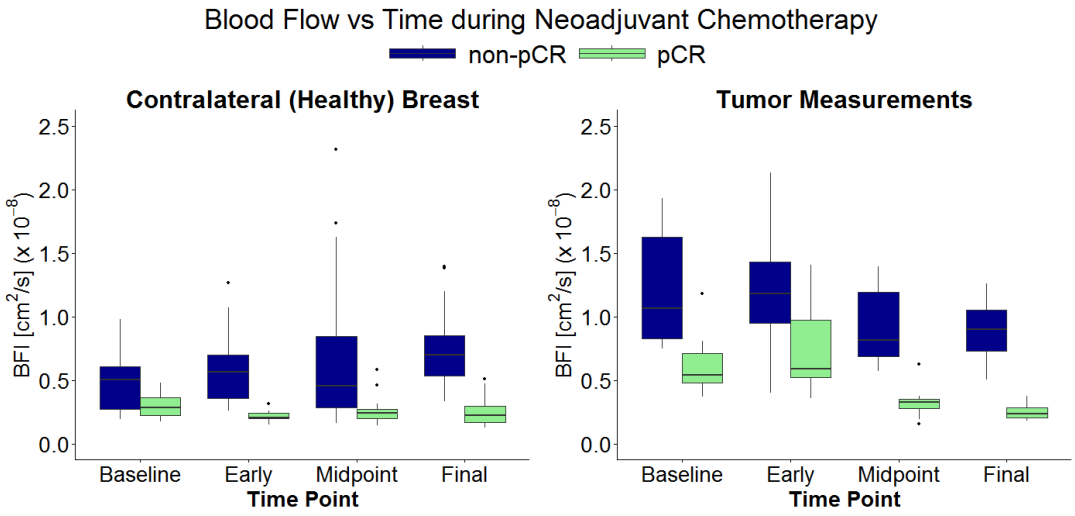

Figure 4.3: Absolute Blood Flow Measurements for NAC Responders vs Non-Responders. Boxplots of the DCS blood flow index (BFI) $[cm^2/s]$ measurements made in healthy tissue (left panel) and tumor tissue (right panel) at each measurement time-point during the NAC treatment (see Figure 3.2). The two boxplots for each measurement time-point correspond to the measurements in subjects with pathologic complete response (pCR) ($n = 19$ points in healthy tissue and $n = 11$ points in tumor tissue) and with non-pathologic complete response (non-pCR) ($n = 21$ points in healthy tissue and $n = 11$ points in tumor tissue). In both healthy and tumor tissue, the absolute BFI is lower for responders than for non-responders. Furthermore, the separation between responders and non-responders is larger at the Midpoint and Final measurements. At these points, the tumor BFI for responders is approaching that of the responders' normal tissue, potentially indicating the efficacy of chemotherapy. The hinges of the boxplots are the first and third quartiles of the data. The whiskers indicate the farthest measurements within $1.5x$ the interquartile range. Outliers beyond $1.5x$ the interquartile range are plotted as crosses.

BFI remains elevated relative to the non-responders' normal tissue. Furthermore, the potential for differentiation can be seen in both the tumor-bearing and healthy breasts, indicating that the response, or lack of response, to chemotherapy may be a systemic effect.

BFI in the lesion-bearing breast was also normalized to BFI in the contralateral breast. This relative tumor-to-normal (T/N) blood flow index ($rBFI_{(T/N)}$) is analogous to the T/N ratios of S_tO_2 and Hb_T concentration, among other markers explored in the ACRIN-6691 study [249]. The $rBFI_{(T/N)}$ at each time point for both responders and non-responders is shown in Figure 4.4. Interestingly, at the Midpoint measurement, the responders' $rBFI_{(T/N)}$ approaches 1 (mean $rBFI_{(T/N)} = 1.34$ across the responders' 11 measured spatial points) while the non-responders' tumor blood flow remains elevated relative to normal tissue (mean $rBFI_{(T/N)} = 2.65$ across the non-responders' 11 measured spatial points). Additionally, differences between responders and non-responders can be seen in the fractional change of average $rBFI_{(T/N)}$ between the Baseline and Early measurements (pCR $= +70.9\,\%$, non-pCR $= -42.5\,\%$) and between the Early and

Midpoint measurements (pCR = $-63.6\,\%$, non-pCR = $+3.5\,\%$). Thus, though there is not a sufficiently large sample size to draw definitive conclusions, these observations represent promising and physiologically suggestive results that strongly indicate further investigation is warranted.

4.3.2 Benefit of Absolute Optical Properties

The data also demonstrate the benefit of including the DOSI measurements of absolute μ_a and μ_s' as inputs in the DCS fitting algorithm for calculating BFI. Without the DOSI measurement, optical properties must be assumed based on literature values. This assumption can be problematic due to the relatively large observed inter- and intra-subject heterogeneity of breast tissue optical properties (see Figure 4.5) [230; 56]. To characterize this effect, the BFI values calculated using DOSI-measured optical properties were compared to $BFI_{assumed}$ values calculated using constant (assumed) optical properties. Here the assumed optical properties that provided the best overall agreement between $BFI_{assumed}$ and BFI, $\mu_a = 0.0045\ mm^{-1}$ and $\mu_s' = 0.85\ mm^{-1}$, were chosen. Figure 4.6 demonstrates the extent to which deviations between assumed and measured optical properties affect the calculated BFI.

For example, a percent error of $50\,\%$ in μ_a produces an $\sim 20\,\%$ change in BFI, while a percent error of $25\,\%$ in μ_s' produces a $25 - 45\,\%$ change in BFI, which is consistent with the errors due to optical property offsets seen in a previous study [147]. These variations are within typical intra-subject optical property ranges, as evidenced by Figure 4.5, particularly in the lesion-bearing breast. Additionally, using assumed optical properties, approximately $75\,\%$ of the measured BFI values are at least $10\,\%$ away from their true value, and approximately $51\,\%$ of the measured BFI values are at least 20% away from their true value (see Figure 4.6-Inset).

The effects of optical property errors on the relative BFI parameters (*i.e.*, $rBFI_{(T/N)}$) is less severe but still significant, especially for scattering errors. In Figure 4.4, each blood flow index boxplot for non-responders, which represents $rBFI_{(T/N)}$ at a given longitudinal time point, has a $35\,\%$ larger normalized standard deviation (on average) when assumed optical properties are used instead of DOSI-measured properties. We observe no significant difference in the normalized standard deviation for the responders in this data set because the responders' measured optical properties are, on average, less heterogeneous than the non-responders', and the responders' μ_s' values, which have a larger effect on the BFI calculation than μ_a (see Figure 4.6), are clustered around the assumed μ_s' value (see Figure 4.5). The observed heterogeneity in optical properties suggest that in future studies, subject-specific measurement of optical properties is important, and therefore the combination of DOSI and DCS will likely be necessary for maximizing the utility of DCS blood flow as an early marker of NAC treatment efficacy.

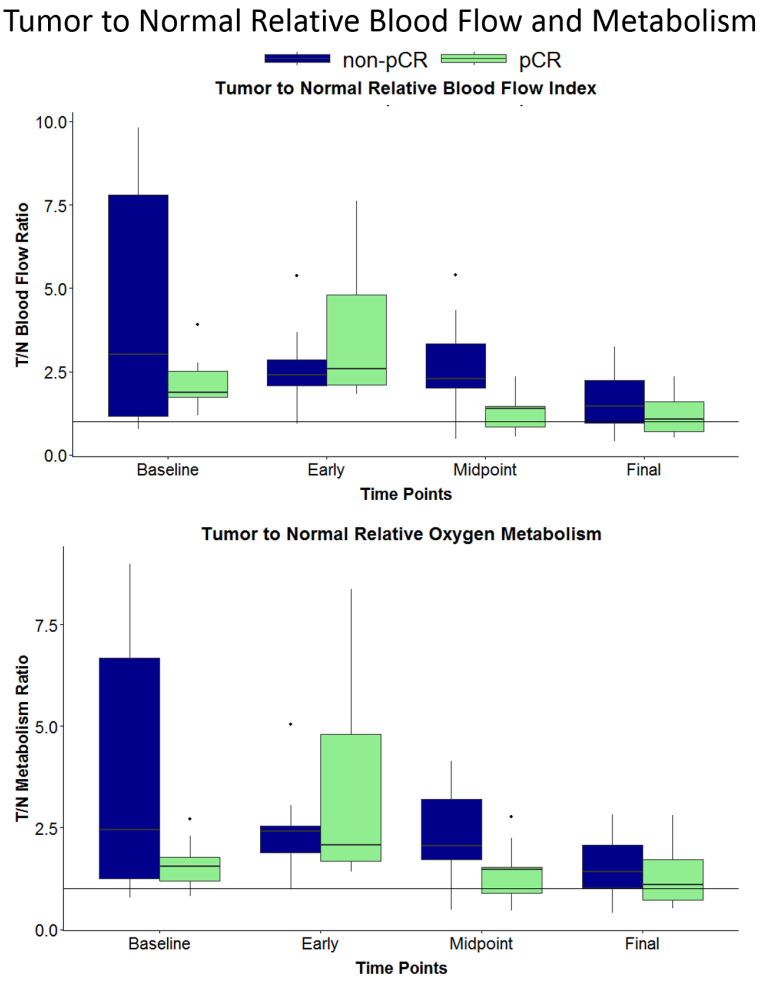

Figure 4.4: Tumor to Normal Blood Flow and Oxygen Metabolism Measurements. Top: Box plots of blood flow in the tumor tissue normalized to the flow in the contralateral (healthy) breast ($rBFI_{(T/N)}$) at each time point separated into responders (pCR) and non-responders (non-pCR). The responder group experiences an increase in $rBFI_{(T/N)}$ between the Baseline and Early measurements, followed by a steep decline in $rBFI_{(T/N)}$ between the Early and Midpoint measurements. The non-responder group experiences a slight decrease in $rBFI_{(T/N)}$ between the Baseline and Early measurements but no change between the Early and Midpoint measurements. At the Midpoint measurement, the responder group has a mean $rBFI_{(T/N)}$ of 1.34 ($n = 11$ spatial points) while the non-responder group has a mean $rBFI_{(T/N)}$ of 2.65 ($n = 11$ spatial points). This indicates that the responders' blood flow in the lesion is approaching normal levels by the midpoint of therapy while the non-responders' is still elevated. Bottom: Box plots of oxygen metabolism in the tumor tissue normalized to the oxygen metabolism in the contralateral (healthy) breast ($rMMRO2_{(T/N)}$). Note that $rMMRO2_{(T/N)}$ follows a similar trend to the $rBFI_{(T/N)}$ for responders and non-responders due to the relatively small difference in S_tO_2 between tumor and normal tissue. The hinges of all boxplots are the first and third quartiles of the data. The whiskers indicate the farthest measurements within $1.5x$ the interquartile range. Outliers beyond $1.5x$ the interquartile range are plotted as crosses.

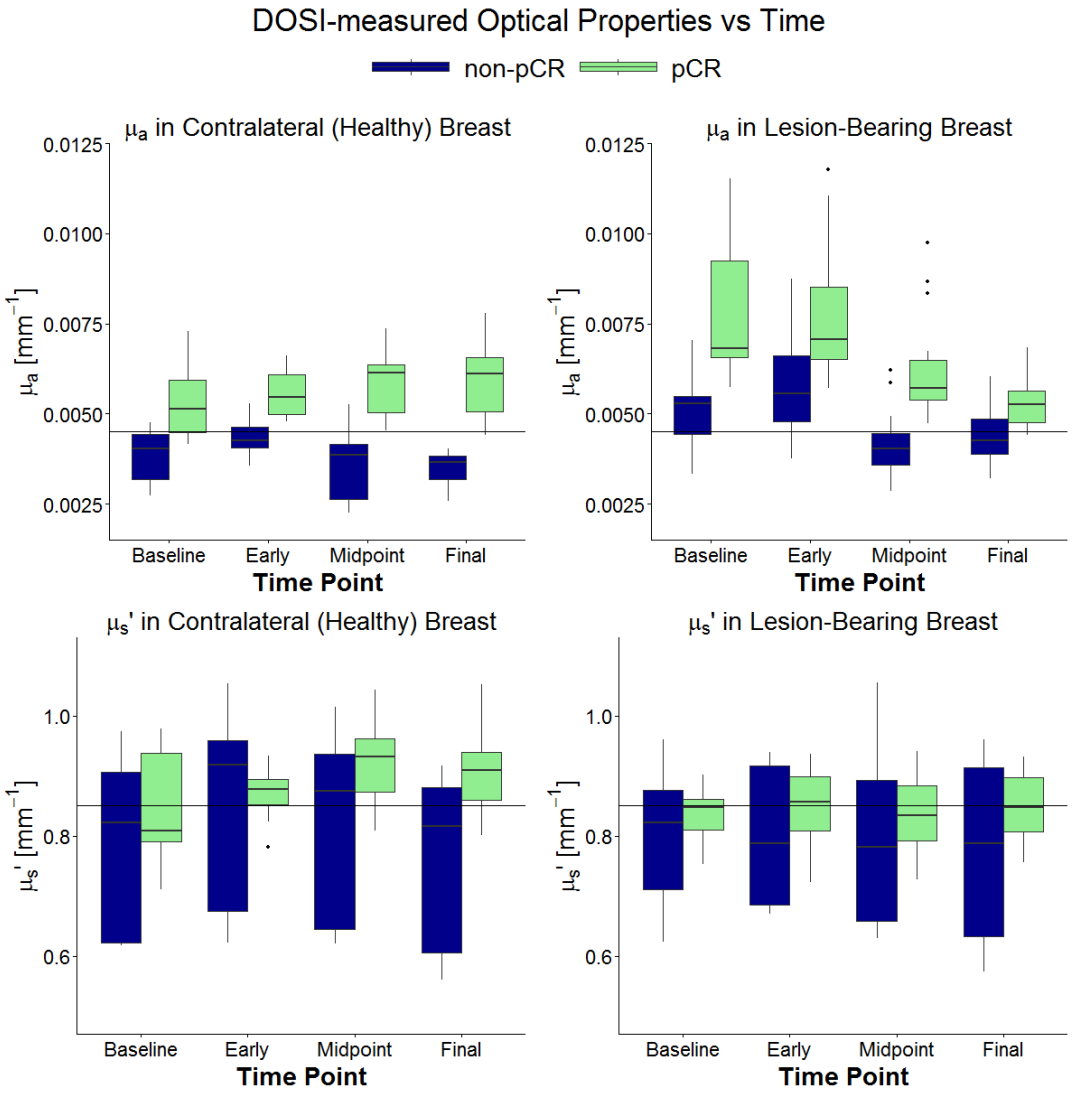

Figure 4.5: DOSI-Measured Optical Properties in Breast Tissue. Boxplots of μ_a and μ_s' at $\lambda = 785\,nm$ in both breasts are plotted for responders and non-responders across all four time points. The responders' data set consists of 15 spatial points measured on the lesion-bearing breasts and 19 spatial points measured on the healthy breasts. The non-responders' data set consists of 21 spatial points on the lesion-bearing breasts and 21 spatial points on the healthy breasts. The horizontal lines on each graph indicate the assumed optical properties ($\mu_a = 0.0045\ mm^{-1}$; $\mu_s' = 0.85\ mm^{-1}$) used as inputs to the DCS fits for calculation of BFI when the DCS analysis is performed without DOSI data. Note that the responders and non-responders exhibit similar heterogeneity and offset from the assumed values in the μ_a plots. However, the optical properties of the responders are more homogeneous and clustered around the assumed value for the μ_s' plots. This observation explains why the non-responders have a relatively large increase in normalized standard deviation of $rBFI_{(T/N)}$ ($\sim 35\,\%$) when assumed optical properties are used while the standard deviation for the responders' data is virtually unchanged. The hinges of the boxplots are the first and third quartiles of the data. The whiskers indicate the farthest measurements within $1.5x$ the interquartile range. Outliers beyond $1.5x$ the interquartile range are plotted as crosses.

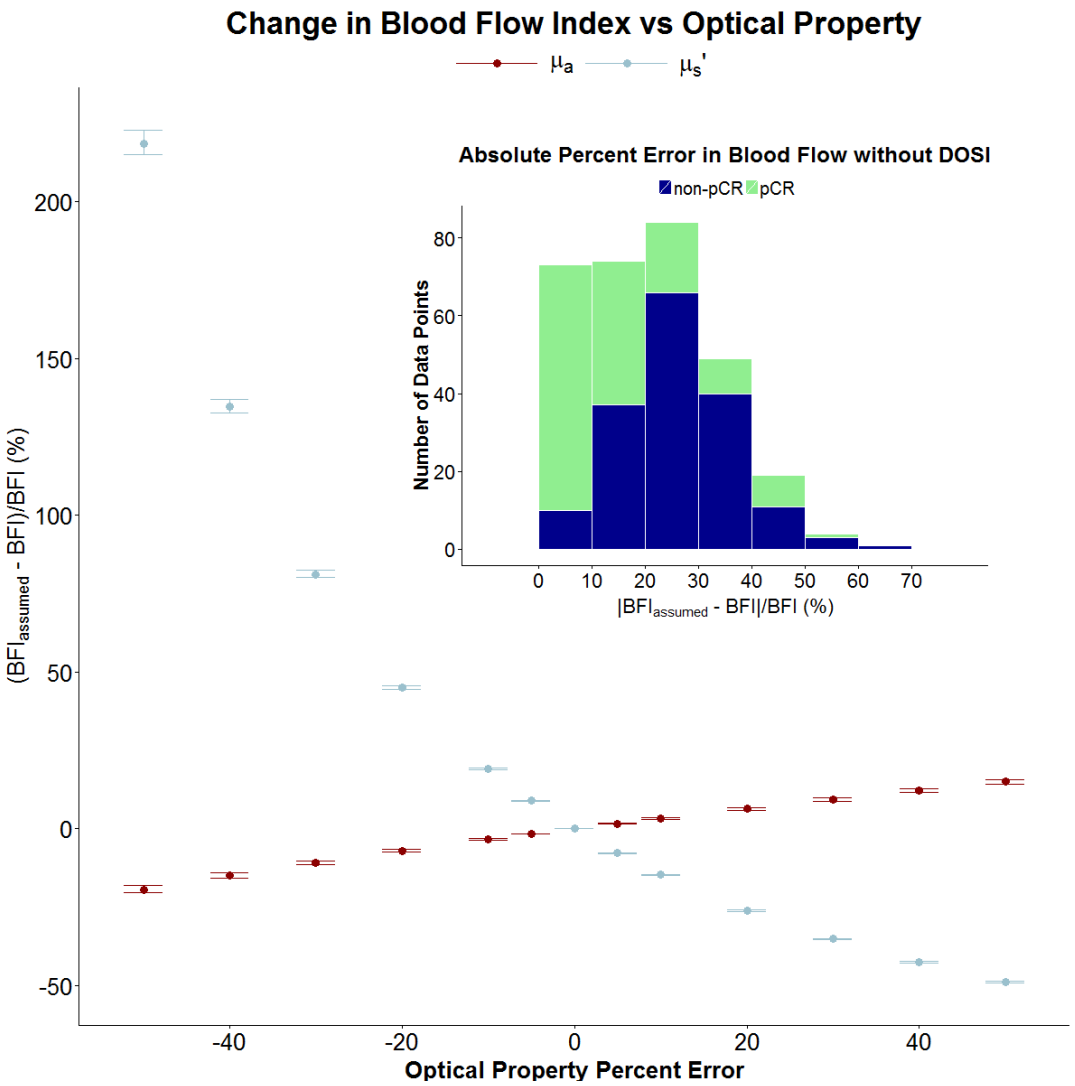

Figure 4.6: Effect of Tissue Optical Property Errors on BFI Calculation. Main: Percent error in the calculated absolute BFI (*i.e.*, $100 \times (BFI_{assumed} - BFI)/BFI$) plotted against the percent error in the assumed μ_a relative to the DOSI-measured value (red curve) and against the percent error in the assumed μ_s' relative to the DOSI-measured value (blue curve). Note that the values on the vertical axis are plotted as mean ± SD for the data points at each value of the optical property percent error. Clearly, μ_s' errors have a larger effect on the calculated BFI than μ_a errors. Inset: Histogram of the error in BFI measurements when using assumed μ_a and μ_s' vs DOSI-measured μ_a and μ_s' across all subjects and time points. Approximately 75 % of all points have an error of greater than 10 %, 51 % of all points have an error of greater than 20 %, and 22 % of all points have an error of greater than 30 %. Also note that the responders generally have less error in the BFI measurements with assumed optical properties than non-responders; this effect is due to a smaller error in the assumed μ_s' for the responders (see Figure 4.5).

4.3.3 Oxygen Metabolism Calculation

Finally, the combination of S_tO_2 measurements from the DOSI data and BFI measurements with DCS allows for the calculation the T/N ratio of oxygen metabolism, $rMMRO_{2_{(T/N)}}$ (Equation 4.6). The $rMMRO_{2_{(T/N)}}$ measured here closely tracks $rBFI_{(T/N)}$ because of the relatively small difference in S_tO_2 between tumor and normal tissue (see Figure 4.4). To further explore the utility of the oxygen metabolism measurement, the Baseline-normalized blood flow index $rBFI_B$, oxygen saturation $rStO_{2_B}$, and oxygen metabolism $rMMRO_{2_B}$ (Equation 4.7) were calculated. Figure 4.7 provides a case study comparing these three quantities for a single subject, along with potential physiological explanations for the findings, which are discussed in Section 4.4.

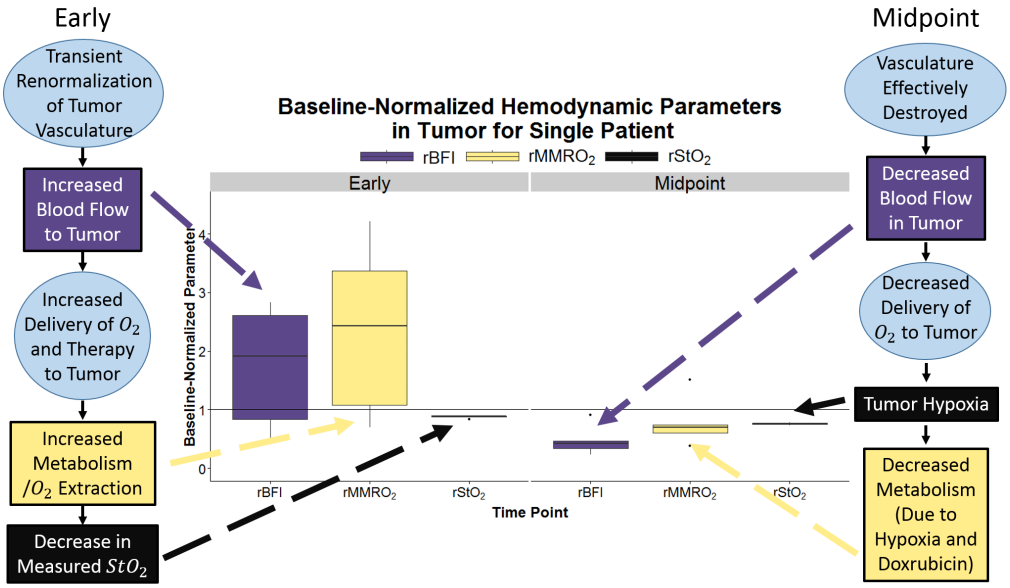

Figure 4.7: Baseline-Normalized Hemodynamic Parameters during A/C Therapy in a Single Subject. Each measured point is normalized to the corresponding spatial point in the Baseline measurement. The flow charts indicate the expected physiological mechanism of the chemotherapy at the given time points. At the Early time point, transient re-normalization of the vasculature leads to increases in both $rBFI_B$ and $rMMRO_{2_B}$. At the Midpoint, the therapy has effectively destroyed the tumor vasculature, which, combined with the cytotoxicity of Doxorubicin, has inhibited cell metabolism, leading to decreased $rBFI_B$ and $rMMRO_{2_B}$, as well as relative tumor hypoxia, *i.e.*, decreased $rStO_{2_B}$. This case study displays the potential of oxygen metabolism measurements from combined DCS and DOSI to track the physiological mechanisms and efficacy of chemotherapy treatment.

4.4 Discussion

The results presented here represent an important step towards the use of DCS-measured blood flow (BFI) as a biomarker of NAC response. In the long term, the ability to accurately quantify BFI in multiple subjects and at different spatial locations across optically heterogeneous breasts will be an important factor in determining the utility of DCS blood flow as a predictor of a patient's response to treatment. The incorporation of absolute tissue optical properties determined by DOSI into the DCS blood flow calculation improves the accuracy of blood flow measurements by isolating the effects of actual blood flow changes from concurrent changes in optical properties.

The absolute BFI measurements and the normalized $rBFI_{(T/N)}$ offer interesting possibilities for early differentiation between responders and non-responders. For example, effective chemotherapy treatments should inhibit cell metabolism and/or angiogenesis. Thus, the tumor regions of responders should have lower blood flow levels compared to non-responders. The lower levels of absolute BFI and $rBFI_{(T/N)}$ during chemotherapy for responders found in our study are consistent with these expectations, as well as with changes found in previous blood flow studies using FDG-PET [173; 18] and with the changes in hemoglobin concentration measured in the ACRIN-6691 study [249]. It is also possible that the increase in responders' $rBFI_{(T/N)}$ between the Baseline and Early measurements (see Figure 4.4) could correspond to the oxyhemoglobin flare that has previously been observed in NAC responders [273; 220] or to particular chemotherapeutic mechanisms that will be discussed later (see Figure 4.7).

Indications of treatment efficacy at the midpoint of treatment or earlier are of particular interest because they could enable oncologists to augment or change an ineffective therapy regimen. At the Midpoint time-point in this data set, the average $rBFI_{(T/N)}$ of the responders approaches 1 while the same quantity for the non-responders remains abnormal. This observation suggests that by the treatment midpoint, blood flow in the lesion has begun to resemble that of the normal breast in responders, while the non-responders still have anomalous blood flow. Again, this finding is consistent with both intuition about the efficacy of treatment and with data from the larger ACRIN 6691 DOSI study which indicate that some hemodynamic properties of responders and non-responders are distinguishable by the midpoint of treatment [249].

The calculation of T/N oxygen metabolism, $rMMRO_{2_{(T/N)}}$, closely tracks $rBFI_{(T/N)}$ (see Figure 4.4), which is consistent with a relatively small average difference in S_tO_2 between tumor and normal tissue that is seen in this study and in previous studies [60; 72; 56]. However, investigation into $rMMRO_{2_{(T/N)}}$ is still important because the oxygen saturation of tumors is very heterogeneous and dependent on biochemical characteristics and the stage of the cancer [72]. Therefore, the tumor

S_tO_2 may vary greatly from the normal S_tO_2 for a given patient. In that case, $rBFI_{(T/N)}$ alone would not be an accurate marker of metabolism.

One important reason to measure oxygen metabolism is that there are potential physiological scenarios wherein blood flow and metabolism measurements could more accurately reflect the physiological changes in the tumor, *e.g.*, compared to measurements of blood flow alone or oxygen saturation alone. For example, in Chapter 3, the Early time-point S_tO_2 prediction model (see Figure 3.7) describes the correlation between higher relative oxygen saturation and complete response to chemotherapy. However, there are several competing hypotheses for the mechanism behind this correlation. Lower tumor metabolism in eventual complete responders, due to effective chemotherapy, could lead to higher S_tO_2 values relative to non-responders. This effect would likely be coupled to lower blood flow for responders. However, vascular re-normalization due to anti-angiogenic drugs could lead to higher S_tO_2 and higher BFI in responders than non-responders. Importantly, DCS measurements of BFI could help to elucidate these physiological processes that underlie the correlation between S_tO_2 and response. The calculation of oxygen metabolism could provide further insight to these processes.

Here, a case study of a single subject is presented to explore these potential physiological changes (see Figure 4.7). The data correspond to Baseline-normalized $rBFI_B$, $rMMRO_{2_B}$, and $rStO_{2_B}$ during the administration of a Doxorubicin/Cyclophosphamide treatment regimen. In this case, the blood flow and metabolism increase in the tumor from the Baseline to Early time point, which is consistent with blood flow increases seen immediately after the administration of this therapy combination in mouse models [216]. This initial increase in blood flow is likely due to the transient re-normalization of the tumor vasculature caused by the anti-angiogenic effects of the chemotherapy regimen [150]. Vascular re-normalization allows for increased oxygen metabolism and enables delivery of therapy to the tumor cells. At the Midpoint measurement, however, $rBFI_B$ and $rMMRO_{2_B}$ are depressed, potentially indicating an effective response to treatment in which the Doxorubicin/Cyclophosphamide combination has inhibited cell metabolism and effectively destroyed the tumor vasculature. In contrast, a chemotherapy regimen that primarily disrupts cancer cell metabolism, with little angiogenic inhibition, would likely exhibit more significant changes in measurements of $rMMRO_{2_B}$ than in measurements of $rBFI_B$ while still possibly exhibiting the same changes in $S_tO_{2_B}$. The combination of DCS and DOSI, along with the subsequent calculation of oxygen metabolism, will enable further exploration of these physiological changes, and their correlation with treatment response, in future optical studies.

The distinctions between the responders and non-responders in absolute BFI (Figure 4.3),

$rBFI_{T/N}$, and $rMMRO2_{(T/N)}$ (Figure 4.4), combined with the fact that these effects are consistent with both expectations about hemodynamics from previous studies and with the expected physiological mechanisms of chemotherapy, provide motivation to further investigate the predictions of DCS measurements during neoadjuvant chemotherapy with a larger sample size. An obvious future direction for this work is to complete a study with a larger subject population that permits more statistically significant differentiation between responders and non-responders, especially at the more clinically valuable Early and Midpoint measurements. The combination of z-score normalization and logistic regression presented in Chapter 3 could be utilized to develop prediction models incorporating BFI and S_tO_2 or BFI alone.

Over the course of this future study, several changes could also be made to the measurement protocol to collect additional useful information. First, more spatial points could be collected on each breast to enable diffuse correlation tomography (DCT) blood flow image reconstruction. In this case, DOSI measurements could also be used to spatially constrain the DCT inverse problem. This augmentation could improve blood flow index quantification in the lesion tissue, in the nominally healthy tissue of the lesion-bearing breast, and in the contralateral breast.

Finally, it appears valuable to explore techniques for determining absolute oxygen metabolism ($MMRO_2$) instead of relative oxygen metabolism ($rMMRO2_{(T/N)}$) by isolating the venous contribution to the optical signal. This pursuit is of particular interest because it is currently unknown whether γ is truly constant between tumor and normal tissues or across longitudinal measurements. Progress has been made towards using DOS to measure S_vO_2 in the brain [171]; however, it is unclear if this technique would be applicable to breast measurements. Advances along these lines would enable the DCS/DOSI combination to potentially track systemic metabolic changes in addition to the relative changes between healthy and lesion-bearing breasts.

4.5 Conclusion

The pilot study presented here [76] was the first to use diffuse correlation spectroscopy (DCS) to monitor blood flow throughout the course of neoadjuvant chemotherapy (NAC) in a human clinical trial and the first investigation into the potential correlation between DCS-measured blood flow index (BFI) and NAC response. Diffuse optical spectroscopic imaging (DOSI) was performed in conjunction with DCS, which allowed for both the constraint of the DCS fitting using absolute DOSI-measured optical properties, and for the calculation of relative oxygen metabolism. Clearly, DCS and DOSI are attractive modalities for the monitoring of response to treatment due to their

sensitivity to functional hemodynamic properties, as well as their portability, their use of non-ionizing radiation, and their relatively low cost. The results suggest the existence of an interesting correlation between pathologic complete response to NAC and both lower absolute BFI and lower relative BFI between the tumor and normal tissue at the midpoint of the chemotherapy regimen. The calculation of oxygen metabolism using the combined DOSI and DCS data also presented an interesting opportunity to more accurately explore the physiological mechanisms and efficacy of chemotherapy. DCS measures of BFI and metabolism could both have predictive value with respect to chemotherapy pCR; they could also help to elucidate the mechanisms underlying the Early time-point S_tO_2 correlation to response found in Chapter 3. These pilot results provide both clear evidence for combining DOSI and DCS in future comprehensive clinical studies and interesting pilot data for guiding these studies towards a more complete understanding of tumor hemodynamics during chemotherapy.

Chapter 5

Statistical Differentiation of Malignant and Healthy Breast Tissue

5.1 Introduction

Chapters 3 and 4 explored the role that diffuse optics could play in monitoring and predicting breast cancer patients' responses to neoadjuvant chemotherapy. This prognostic role is one of the most promising potential applications of diffuse optics in the oncologic setting. However, optically measured parameters have also shown ability to discriminate malignant from healthy tissue in the breast [240; 239; 60; 72; 253; 111; 177], and thus DOS/DOT may also have diagnostic applications.

In standard clinical practice, breast cancer diagnosis is performed in two steps. First, suspicious lesions are identified via x-ray mammography [29]. Thus, the first step requires differentiating potentially malignant tissue from the surrounding healthy tissue. Second, invasive needle-aspiration biopsies are performed to determine whether the suspicious lesion is malignant or benign [29]. Treatment plans can then be developed for malignant carcinomas while benign lesions are either surgically resected or left in place.

Diffuse optics holds potential to contribute to both phases of this diagnostic process. Although its spatial resolution is likely too low to replace x-ray mammography [195; 32; 98], DOT has demonstrated the ability to locate lesions and provide significant contrast with respect to background tissue [240; 60; 168; 218; 253; 111]. This localization ability is also very important for the

prognostic monitoring of chemotherapy response. For example, the prediction models developed in Chapter 3 rely on the tissue oxygen saturation of both the tumor and normal tissue. Thus, accurate identification of these regions is vital.

Optics could also play a role in the second phase of breast cancer diagnosis. DOT has shown great promise in its ability to distinguish malignant and benign lesions [72; 111; 177]. Thus, if properly validated, DOS/DOT could serve as a non-invasive biopsy after identification of the lesion with mammography. Even if diffuse optics does not replace invasive biopsies, it could serve as an initial test that could be performed immediately to rule out, or rule in, obvious cases. This scheme could significantly reduce the number of lesions falsely identified as malignant by mammography that needed to progress to an invasive biopsy, saving time, money, and stress.

Another, less fully explored, area concerns the potential heterogeneity in optically measured parameters among breast carcinoma molecular subtypes. These subtypes are determined by the hormone receptor (HR) statuses, *i.e.*, estrogen (ER), progesterone (PR), and human epidermal growth factor (Her2) receptor status, and the Ki-67 proteomic marker level [40; 29]. The subtypes included in this analysis are luminal A, luminal B, HR positive, Her2 positive, and triple negative. All these variations have different molecular and genetic structures and may be treated with different therapies [29]. However, to this point, there has been very little research into variations in the physiological parameters that are accessible to optics.

The dataset explored in this chapter offers a unique opportunity to investigate both the diagnostic abilities of DOS and any potential heterogeneity across tumor subtypes. This very large subject population ($n = 222$) includes patients with a variety of malignant carcinomas with different tumor subtypes and subjects with benign lesions. All subjects were measured using the same diffuse optical spectroscopic imaging (DOSI) technique discussed in Chapters 3 and 4, providing consistency across the full sample. Logistic regression models were run to differentiate malignant tissue from the surrounding normal tissue using various DOSI-measured properties. These models were then applied to a test set which contained malignant tumors, benign lesions, and normal tissue to ascertain the model's ability to perform both stages of the breast cancer diagnostic paradigm. The different normalization techniques discussed in Chapter 3 were explored. Z-score normalized models using both the deoxy-hemoglobin concentration HHb and the DOSI-derived tissue optical index TOI were able to differentiate malignant tissue from both normal tissue and benign lesions. This work thus provides an important piece of evidence for the utility of diffuse optics in the diagnostic setting.

The heterogeneity in DOSI-measured parameters across tumor subtypes was also explored. However, no prominent differences among subtypes were found for any single DOSI parameter.

This observation suggests that the single parameter models explored here, and in Chapter 3, should be universally applicable, regardless of tumor subtype. Nevertheless, more work can still be done in the future to determine if multi-parameter DOSI models might be able to provide distinct optical signatures for each subtype.

5.2 Subjects and Methods

5.2.1 Subjects

For this analysis, a database of $n = 222$ subjects imaged with diffuse optical spectroscopic imaging (DOSI) devices across seven different institutions (University of Pennsylvania; University of California, Irvine; University of California, San Francisco; Massachusetts General Hospital; Dartmouth Hitchcock Medical Center; Boston University; and MD Anderson Cancer Center) was utilized. Subjects provided written informed consent, and the HIPAA-compliant protocols and informed consent documents were approved by each site's Institutional Review Board. The 222 subjects were women between the ages of 20 and 77 with breast lesions of at least $1\,cm$ in length along the greatest dimension. Within this dataset, 181 subjects had biopsy-confirmed invasive ductal carcinoma (IDC), invasive lobular carcinoma (ILC), or both; 10 subjects had pre-malignant ductal or lobular carcinoma *in-situ* (DCIS or LCIS); and 31 subjects had a benign lesion. Table 5.1 contains demographic information, as well as tumor histology, immunohistochemistry, and molecular subtype breakdowns for the subjects with malignant and benign lesions. Note that this population includes, but is not limited to, the subjects from the ACRIN-6691 study [249] (Chapter 3).

The subjects in this study were measured across a variety of imaging studies wherein the total number of subjects was greater than 222; however, the group presented here represents the subset of subjects considered evaluable based on criteria relating to data quality and acquisition [30; 60; 249; 166]. Although some subjects were measured longitudinally, *e.g.*, throughout the course of chemotherapy (see Chapters 3 and 4), only the pre-therapy measurements are presented for analysis herein. Thus, none of the tissue has been altered by chemotherapy or any other treatment regimen.

5.2.2 Optical Imaging Methods

The DOSI instrument used in this study combines multi-spectral frequency-domain and broadband diffuse optical spectroscopy to measure tissue concentrations of oxygenated hemoglobin (HbO_2), deoxygenated hemoglobin (HHb), water (H_2O), and lipid, as well as the tissue scattering amplitude (A) and power (b), as defined by a simplified Mie scattering model (see Section 2.8) [184].

	Malignant ($n = 181$)	Benign ($n = 31$)
Age, Years		
Mean ± St. Dev. (Range)	$50.2 \pm 11.8\,(26 - 77)$	$40.5 \pm 11.9\,(20 - 69)$
Menopausal Status, n (%)		
Pre-	86 (48 %)	25 (81 %)
Peri-	11 (6 %)	1 (3 %)
Post-	84 (46 %)	5 (16 %)
Maximum Tumor Size, cm		
Mean ± St. Dev. (Range)	$34.6 \pm 21.7\,(10 - 120)$	$19.5 \pm 7.8\,(10 - 39)$
Histological Status, n (%)		
IDC	133 (73 %)	–
ILC	9 (5 %)	–
IDC + DCIS	28 (15 %)	–
ILC + LCIS	2 (1 %)	–
IDC + ILC	5 (3 %)	–
Other Malignant	4 (2 %)	–
Fibroadenoma	–	20 (65 %)
Cyst	–	5 (16 %)
Other Benign	–	6 (19 %)
ER Status, n (%)		
Positive	129 (71 %)	–
Negative	49 (27 %)	–
Unknown	3 (2 %)	–
PR Status, n (%)		
Positive	115 (64 %)	–
Negative	63 (35 %)	–
Unknown	3 (2 %)	–
Her2 Status, n (%)		
Positive	50 (28 %)	–
Negative	121 (67 %)	–
Equivocal	2 (1 %)	–
Unknown	8 (4 %)	–
Molecular Subtype, n (%)		
Her2 Positive	16 (9 %)	–
HR Positive	12 (7 %)	–
Luminal A	36 (20 %)	–
Luminal B	82 (45 %)	–
Triple Negative	27 (15 %)	–
Unknown	8 (4 %)	–

Table 5.1: Physiological Malignant and Benign Lesion Properties. Demographic, histological, and immunohistochemical data is provided for all subjects in the differential diagnosis dataset and divided into malignant ($n = 181$) and benign ($n = 31$) lesion groups. Note that data for the $n = 10$ pre-malignant subjects is not included here because these subjects were excluded from the analysis. For histological information, IDC refers to invasive ductal carcinoma, ILC refers to invasive lobular carcinoma, DCIS is ductal carcinoma *in-situ*, and LCIS is lobular carcinoma *in-situ*. ER, PR, and Her2 represent estrogen receptor, progesterone receptor, and human epidermal growth factor receptor status, respectively.

The combination of these measured parameters permits calculation of total tissue hemoglobin concentration ($Hb_T = HbO_2 + HHb$), tissue oxygen saturation ($S_tO_2 = HbO_2/Hb_T$) and the tissue reduced scattering coefficient (μ_s'). A more complete description of the DOSI method and instrument [30] can be found in Section 3.2.2. The ACRIN-6691 multi-center trial also demonstrated the consistency and quality of multiple individual DOSI instruments across two years and all seven measurement sites [166].

DOSI measurements were made at a grid of distinct points on the tumor-bearing breast. This grid was chosen to encompass the entire tumor and surrounding normal tissue; it ranged in size from $7\,cm \times 7\,cm$ to $15\,cm \times 16\,cm$ with an average size of approximately $10\,cm \times 10\,cm$. The tumor location was generally determined via an ultrasound and/or palpation. A mirrored grid of points was then measured on the contralateral breast. The two measurement grids enabled the definition of three distinct regions. The first region is the tumor tissue, which, for this dataset, was defined as an area of the known dimensions and orientation of the tumor, as measured by ultrasound, centered about the point of maximum TOI. Thus, though TOI was used to center the lesion location, the definition of its extent was independent of any optical parameters. The second region is the normal tissue on the healthy breast, which was defined as a set of points as far away from the tumor region as possible on the measurement grid, excluding the areola. This approach helps to prevent any signal contamination in the normal region due to the partial volume effect. The areola was excluded from this region because of its high blood flow and scattering, which is more similar to tumor tissue than normal tissue. Finally, the contralateral breast tissue, *i.e.*, the third region, was defined as the entire grid on the contralateral breast outside the areolar region. Figure 5.1 contains a schematic of these DOSI grid measurements and a sample image.

5.2.3 Statistical and Analytic Methods

Since TOI has been empirically shown to distinguish malignant tissue from healthy tissue in a single subject [60], there is significant interest in determining the ability of TOI to distinguish between malignant lesions, benign lesions, and healthy tissue across a subject population. The goal of the analysis performed here was to establish diagnostic metrics using TOI, or other DOSI-measured parameters, and apply those metrics to multiple tissue types.

As discussed in Section 2.10.1, the simplest diagnostic metric would be an un-normalized value of a DOSI-measured parameter, *e.g.*, TOI, with a cutoff between TOI values that are considered normal and those that are consistent with malignant tissue. To this end, tumor-to-normal ratios of TOI ($TOI_{(T/N)}$) improve upon the un-normalized TOI by accounting for inter-subject variability in the systemic levels of DOSI-measured physiological parameters. However, because healthy breast

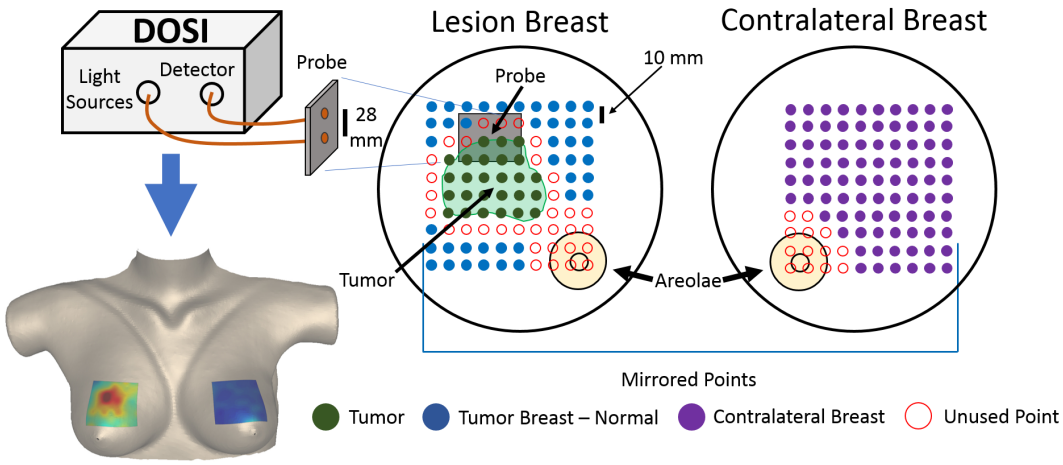

Figure 5.1: Schematic of DOSI Measurement and Region Definition for Differential Diagnosis. Bottom left: A sample DOSI image projected onto a three-dimensional breast surface. Top Left: DOSI instrument and probe. Right: A grid of points, over a surface area ranging from $7\,cm \times 7\,cm$ to $15\,cm \times 16\,cm$, was measured on the lesion-bearing breast. This grid was chosen to encompass both the tumor and a portion of the surrounding healthy tissue. The grid of points was marked using a transparency, which was then used to mirror the grid for measurements on the contralateral breast. The tumor region was chosen to be a region with an area equal to the known tumor size, as measured with ultrasound, centered about the point of maximum Tissue Optical Index (TOI). The tumor breast normal region was defined as the set of points farthest away from the tumor region, excluding the areola. The contralateral breast normal region was defined as all measured points, excluding the areola.

tissue also exhibits significant intra-subject heterogeneity in these quantities [99; 230; 56], a metric that takes into account the normal tissue heterogeneity might be expected to be more robust and provide the most complete information. With this goal in mind, a z-score normalization scheme [56; 55], which transforms the logarithm of a DOSI-measured parameter on the tumor-bearing breast to a z-score relative to the mean and standard deviation of the same parameter on the contralateral breast can be used. This z-score parameter is defined as

$$Z_j = \frac{\ln X_j - \langle \ln X_{j_{Cont}} \rangle}{\sigma\left[\ln X_{j_{Cont}}\right]}. \tag{5.1}$$

Here, X_j is an un-normalized j^{th} measured parameter from a single spatial location on the tumor-bearing breast, $X_{j_{Cont}}$ is the un-normalized j^{th} measured parameter at a spatial point on the contralateral breast, and $\langle \ln X_{j_{Cont}} \rangle$ and $\sigma\left[\ln X_{j_{Cont}}\right]$ represent the mean and standard deviation, respectively, over all points on the contralateral breast. Z_j is thus the z-score for a given spatial measurement on the tumor-bearing breast relative to the healthy contralateral breast tissue for the j^{th} parameter. The Z_j parameters are then separately averaged over all spatial points in the

tumor region and normal region on the tumor-bearing breast, resulting in an average tumor Z_j and an average normal Z_j for each subject. This z-score normalization also happens to transform the values of the data points to obey an approximately Gaussian distribution centered about $Z_j = 0$; this feature improves the robustness of statistical algorithms, like logistic regression, that use these data points. Figure 2.15 provides an example of this distribution transformation.

Logistic Regression

The resultant tumor and normal Z_j values can be used to run a logistic regression algorithm [141], which produces a model that optimally classifies each data point as either malignant or healthy based on the chosen parameter Z_j. A full description of the logistic regression algorithm is given in Section 2.10.2. Briefly, a malignancy parameter $\mathcal{M}$ is fit to maximize the likelihood estimation, and $\mathcal{M}$ is given by

$$\mathcal{M}^i = \beta_o + \sum_{j=1}^{N_j} \beta_j \cdot Z_j^i. \tag{5.2}$$

Here, $\mathcal{M}^i$ is the given model's log-odds of malignancy for the i^{th} subject, β_o is the intercept term of the fitted weight vector, β_j is the weighting term for the j^{th} measured parameter used in the model, Z_j^i is the z-score for the j^{th} measured parameter of the i^{th} subject, and N_j is the number of parameters used in a particular model. For this analysis, $N_j = 1$, 2, or 3. The full weight vector $\vec{\beta}$ is then

$$\vec{\beta} = \left[\beta_o, \beta_1, \ldots \beta_{N_j}\right]. \tag{5.3}$$

The $\vec{\beta}$ weight vector is fit using MATLAB's native logistic regression function, *mnrfit* [3]. The malignancy parameter $\mathcal{M}$ can then be transformed into a probability of malignancy, $\mathcal{P}_\mathcal{M}$, using a logistic function,

$$\mathcal{P}_\mathcal{M} = \frac{1}{1 + e^{-\mathcal{M}}}. \tag{5.4}$$

The parameter $\mathcal{P}_\mathcal{M}$ represents the probability that a sampled tissue is malignant. It has a range from 0 to 1, and it can readily be used to predict the malignancy status of the tissue, depending on threshold levels.

Once the probability of malignancy $\mathcal{P}_\mathcal{M}$ metric has been determined, it must be tested to analyze its discriminatory ability for malignant and non-malignant tissue. This is achieved by applying the weight vector $\vec{\beta}$ to all tumor and normal regions across the subjects in the test set, *i.e.*, subjects

who were explicitly left out of the training set, and then calculating $\mathcal{P}_{\mathcal{M}}$ for these test data subjects. Importantly, this approach provides a validation of the fitted model that is not biased towards the sample on which the training was performed [257]. The quality of the predictions, *i.e.*, how well the predictions correspond to the actual tissue type, is determined via receiver operating characteristic (ROC) analysis [132; 257; 115]. ROC analysis is discussed more fully in Section 2.10.3. For this particular ROC analysis, the AUC is calculated using DeLong's method for the AUC and its 95 % confidence interval [86]. In addition to discriminatory ability, all models were also tested for their calibration, *i.e.*, the degree to which the predicted probabilities of malignancy correspond to the actual rate of malignancy in the data. This analysis was performed using the Hosmer-Lemeshow method, [141], a goodness-of-fit metric which sub-divides the subject population by model-predicted probability of malignancy and compares the expected and actual probabilities within each group. A more complete description of this technique is given in Section 2.10.4.

Training and Test Sets

For this dataset, the probability of malignancy model was trained using only the tumor and normal tissue for subjects with biopsy-confirmed invasive carcinomas. Thus, the $n = 31$ subjects with benign lesions and the $n = 10$ subjects with only carcinomas *in-situ* were not used to train the model. This choice of training set provides maximum contrast between known healthy and malignant tissues. Additionally, only subjects that had contralateral breast measurements could be used for the z-score normalization algorithm; therefore, only $n = 158$ of the $n = 181$ subjects with malignant lesions were utilized. Because the remaining subjects with malignant lesions still comprised a large dataset, a subset of these subjects were set aside to serve as an independent test set for the trained model. In this case, 60 % of the subjects ($n = 95$) were used to train the model, and 40 % ($n = 63$) were set aside for independent validation. In addition, the fitted model was applied to the lesion and healthy tissues for the $n = 31$ subjects that had benign masses. This additional application thus provides information about whether benign lesions can be distinguished from malignant tumors using the same metric that differentiates malignant lesions from surrounding healthy tissue. Figure 5.2 contains a flow chart detailing the sub-division of the full dataset.

Finally, the variation in performance of the malignancy prediction models across different tumor characteristics, *e.g*, molecular subtype, was explored.

For comparison, models using completely un-normalized DOSI-measured parameters and tumor-to-normal ratio normalized parameters were also tested.

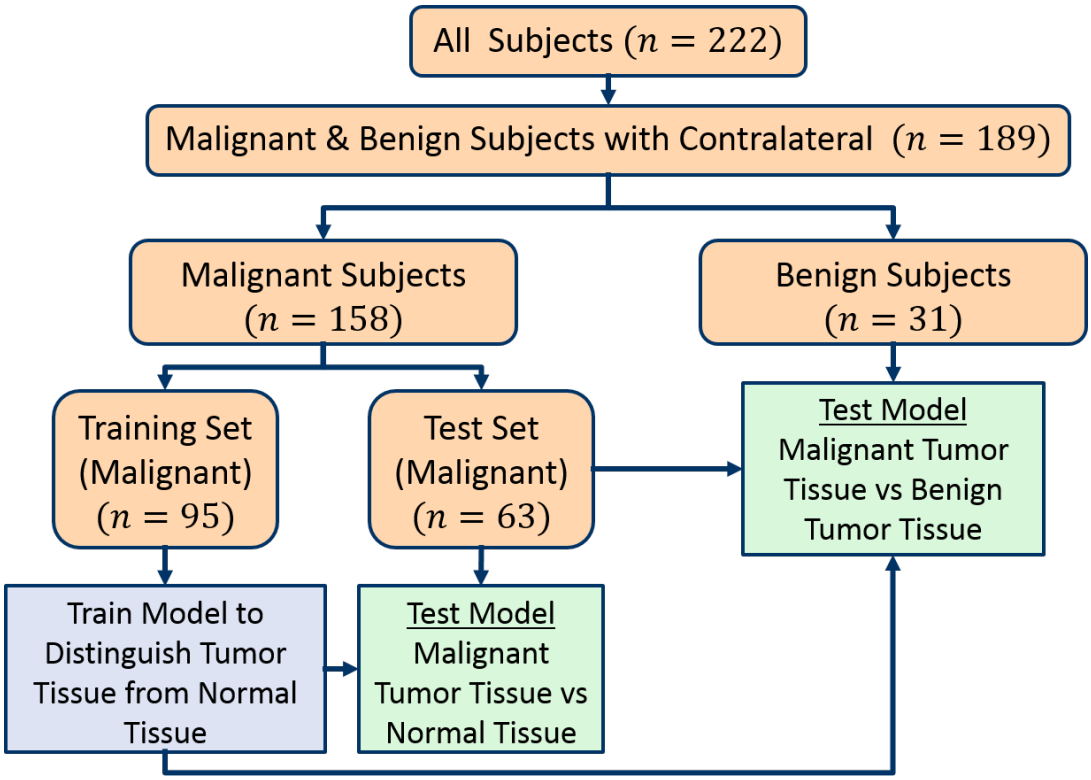

Figure 5.2: Flow Chart of Subject Population Division for Differential Diagnosis. The full dataset contains $n = 222$ subjects. $N = 10$ were excluded because their lesions were pre-malignant, rather than malignant or benign, and $n = 23$ were excluded because they did not undergo contralateral breast measurements. Of the remaining 189 subjects, 158 had biopsy-confirmed malignant tumors, and 31 had benign lesions. The subjects with malignant lesions were further subdivided into an $n = 95$ subject training set and an $n = 63$ subject test set. The training set was used to train logistic regression models to distinguish between malignant and normal tissue using various DOSI-measured parameters. These models were then applied to the tumor and healthy tissues in the test set to validate the models' abilities to differentiate malignant lesions from surrounding normal tissue. The same models were then applied to the $n = 63$ malignant tumors in the test set and the $n = 31$ benign lesions to determine their abilities to categorize lesions as malignant or benign.

5.3 Results

Logistic regression models to differentiate malignant tissue from the surrounding normal tissue were run for every combination of one, two, and three DOSI-measured parameters in the specified test set. Each model was also run using z-score normalization, tumor-to-normal ratio normalization, and no normalization. These models were then applied to both the malignant tumors and healthy tissue in the test set and to the lesion tissues of subjects with benign tumors. The model can be evaluated by two performance metrics: 1) Ability to distinguish between malignant tumors and

healthy tissue, which it was trained to do, and 2) Ability to distinguish malignant tumors from benign lesions.

Regardless of normalization technique, the tissue optical index TOI and deoxy-hemoglobin concentration HHb proved to be the best parameters for predicting malignancy. For models using these two parameters, however, normalization had a significant effect on diagnostic ability. All models indicated that higher values of HHb or TOI were predictive of malignancy. This effect can be seen in the values of the β weight vectors in Figures 5.3-5.8. The HbO_2, Hb_T, H_2O, and lipid concentrations were also predictive of malignancy; however, none of these parameters performed as well as HHb or TOI and thus, are not presented here.

The un-normalized HHb model (see Figure 5.3) produced an $AUC = 0.85$ and a 95 % confidence interval of 0.78 to 0.92 for discriminating malignant from normal tissue, indicating good diagnostic ability. However, this model's ability to distinguish malignant from benign lesions was more marginal with an $AUC = 0.75\,(95\,\%\,CI:\ 0.62$ to $0.88)$. The un-normalized TOI model (see Figure 5.4) produced worse diagnoses than the corresponding HHb models with a malignant versus normal $AUC = 0.80\,(95\,\%\,CI:\ 0.72$ to $0.88)$ and a malignant versus benign $AUC = 0.54\,(95\,\%\,CI:\ 0.41$ to $0.67)$. Thus, un-normalized TOI was somewhat able to discriminate between malignant tissue and healthy tissue, but it was unable to distinguish malignant lesions from benign lesions.

Tumor-to-normal ratio normalization improved both the malignant versus normal discrimination $AUC = 0.89\,(95\,\%\,CI:\ 0.84$ to $0.95)$ and the malignant versus benign discrimination $AUC = 0.86\,(95\,\%\,CI:\ 0.79$ to $0.94)$ for the TOI model (see Figure 5.6). However, the tumor-to-normal HHb model (malignant versus normal $AUC = 0.91\,(95\,\%\,CI:\ 0.85$ to $0.96)$; malignant versus benign discrimination $AUC = 0.71\,(95\,\%\,CI:\ 0.59$ to $0.83)$ - see Figure 5.5) did not offer significant improvement over the un-normalized model.

Finally, when z-score normalization was used, both HHb and TOI provided very good diagnostic models, for malignant versus normal and malignant versus benign. The z-score HHb model had $AUC = 0.90\,(95\,\%\,CI:\ 0.85$ to $0.95)$ for malignant versus normal tissue and $AUC = 0.85\,(95\,\%\,CI:$ 0.77 to 0.93) for malignant versus benign lesions (Figure 5.7). The z-score TOI model had $AUC = 0.88\,(95\,\%\,CI:\ 0.82$ to $0.94)$ for malignant versus normal tissue and $AUC = 0.85\,(95\,\%\,CI:\ 0.77$ to $0.93)$ for malignant versus benign lesions (Figure 5.8).

Since HHb or TOI were used in all models presented here, it was desirable to explore any potential variation in these parameters across different molecular subtypes. For the subtypes investigated here, namely luminal A, luminal B, hormone receptor positive, Her2 positive, and triple negative (see Table 5.1), no significant differences were seen in HHb or TOI across subtype regardless of normalization technique (see Figure 5.9). This observation provides evidence that the diagnostic

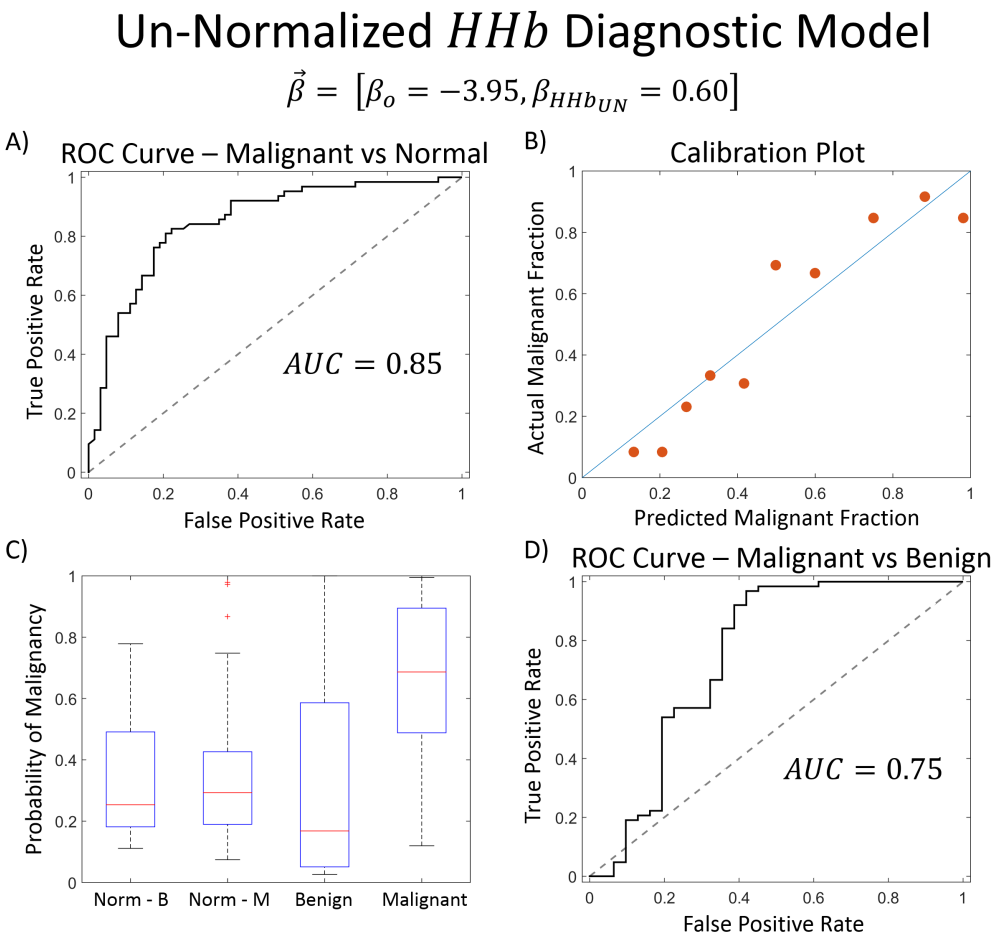

Figure 5.3: Un-Normalized Deoxy-Hemoglobin Diagnostic Model. A) ROC curve for discrimination between malignant lesions and normal tissue. B) Ten-group Hosmer-Lemeshow calibration plot (see Section 2.10.4) comparing the actual fraction of tissue regions in the group that were malignant versus the predicted fraction of tissue regions in that group that should be malignant based on their individual probability of malignancy $\mathcal{P}_{\mathcal{M}}$ values. A well-calibrated model will have points that approximately lie along the identity line. C) Boxplots of $\mathcal{P}_{\mathcal{M}}$ divided into four groups: 1) Norm - B: normal tissue for subjects with benign lesions 2) Norm - M: normal tissue for subjects with malignant tumors 3) Benign: benign lesions 4) Malignant: malignant tumors. The hinges of the boxplots represent the first and third quartiles of the data, the whiskers represent the range of measurements within a distance 1.5× the interquartile range, and the crosses represent outliers. D) ROC curve for discrimination between malignant lesions and benign lesions. This model provides good diagnostic ability for malignant versus normal tissue but more marginal discrimination between malignant and benign lesions. Note that the β weight vector for the model is given at the top of the figure.

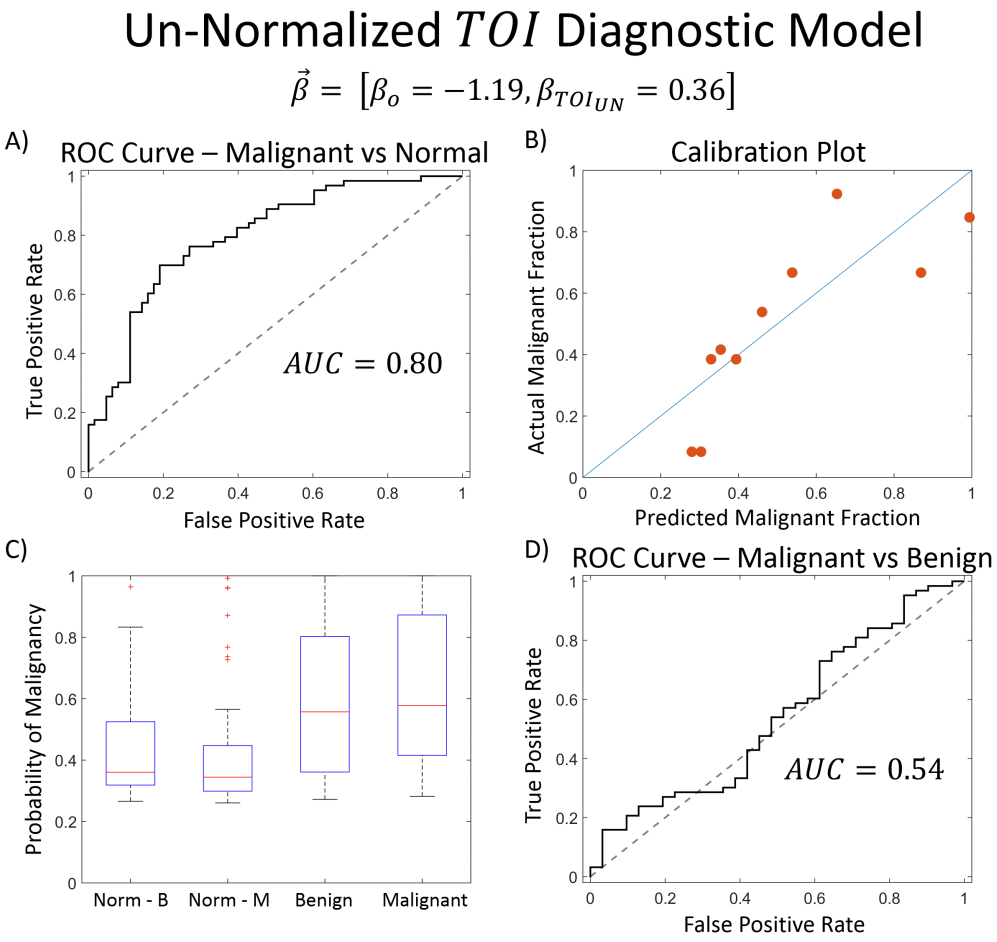

Figure 5.4: Un-Normalized Tissue Optical Index Diagnostic Model. A) ROC curve for discrimination between malignant lesions and normal tissue. B) Ten-group Hosmer-Lemeshow calibration plot (see Section 2.10.4) comparing the actual fraction of tissue regions in the group that were malignant versus the predicted fraction of tissue regions in that group that should be malignant based on their individual probability of malignancy $\mathcal{P}_{\mathcal{M}}$ values. A well-calibrated model will have points that approximately lie along the identity line. C) Boxplots of $\mathcal{P}_{\mathcal{M}}$ divided into four groups: 1) Norm - B: normal tissue for subjects with benign lesions 2) Norm - M: normal tissue for subjects with malignant tumors 3) Benign: benign lesions 4) Malignant: malignant tumors. The hinges of the boxplots represent the first and third quartiles of the data, the whiskers represent the range of measurements within a distance 1.5× the interquartile range, and the crosses represent outliers. D) ROC curve for discrimination between malignant lesions and benign lesions. This model provides average diagnostic ability for malignant versus normal tissue but no significant discrimination between malignant and benign lesions. Note also in the boxplots that there are no $\mathcal{P}_{\mathcal{M}} < 0.25$. This could be a sign that the model is not properly calibrated. Note that the β weight vector for the model is given at the top of the figure.

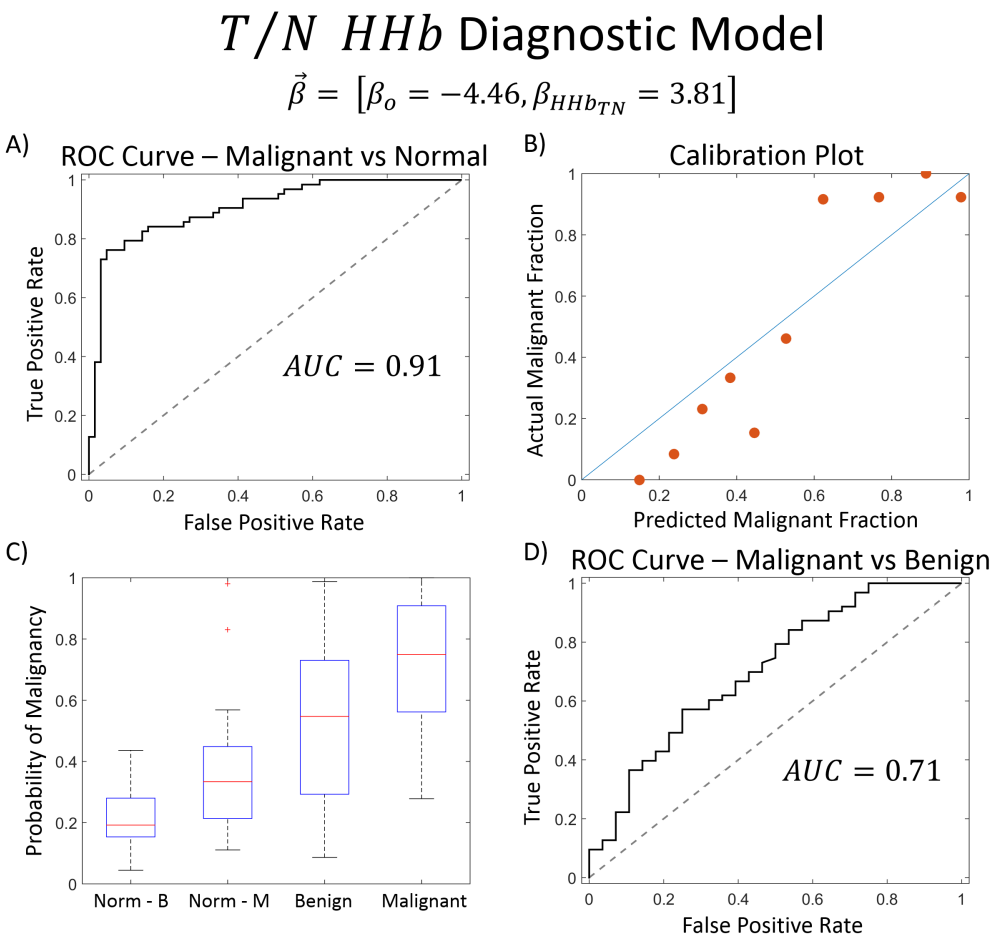

Figure 5.5: Tumor-to-Normal Deoxy-Hemoglobin Diagnostic Model. A) ROC curve for discrimination between malignant lesions and normal tissue. B) Ten-group Hosmer-Lemeshow calibration plot (see Section 2.10.4) comparing the actual fraction of tissue regions in the group that were malignant versus the predicted fraction of tissue regions in that group that should be malignant based on their individual probability of malignancy $\mathcal{P}_{\mathcal{M}}$ values. A well-calibrated model will have points that approximately lie along the identity line. C) Boxplots of $\mathcal{P}_{\mathcal{M}}$ divided into four groups: 1) Norm - B: normal tissue for subjects with benign lesions 2) Norm - M: normal tissue for subjects with malignant tumors 3) Benign: benign lesions 4) Malignant: malignant tumors. The hinges of the boxplots represent the first and third quartiles of the data, the whiskers represent the range of measurements within a distance 1.5× the interquartile range, and the crosses represent outliers. D) ROC curve for discrimination between malignant lesions and benign lesions. This model provides excellent diagnostic ability for malignant versus normal tissue but significantly worse discrimination between malignant and benign lesions due to the large variation in $HHb_{(T/N)}$ for benign masses. Note that the β weight vector for the model is given at the top of the figure.

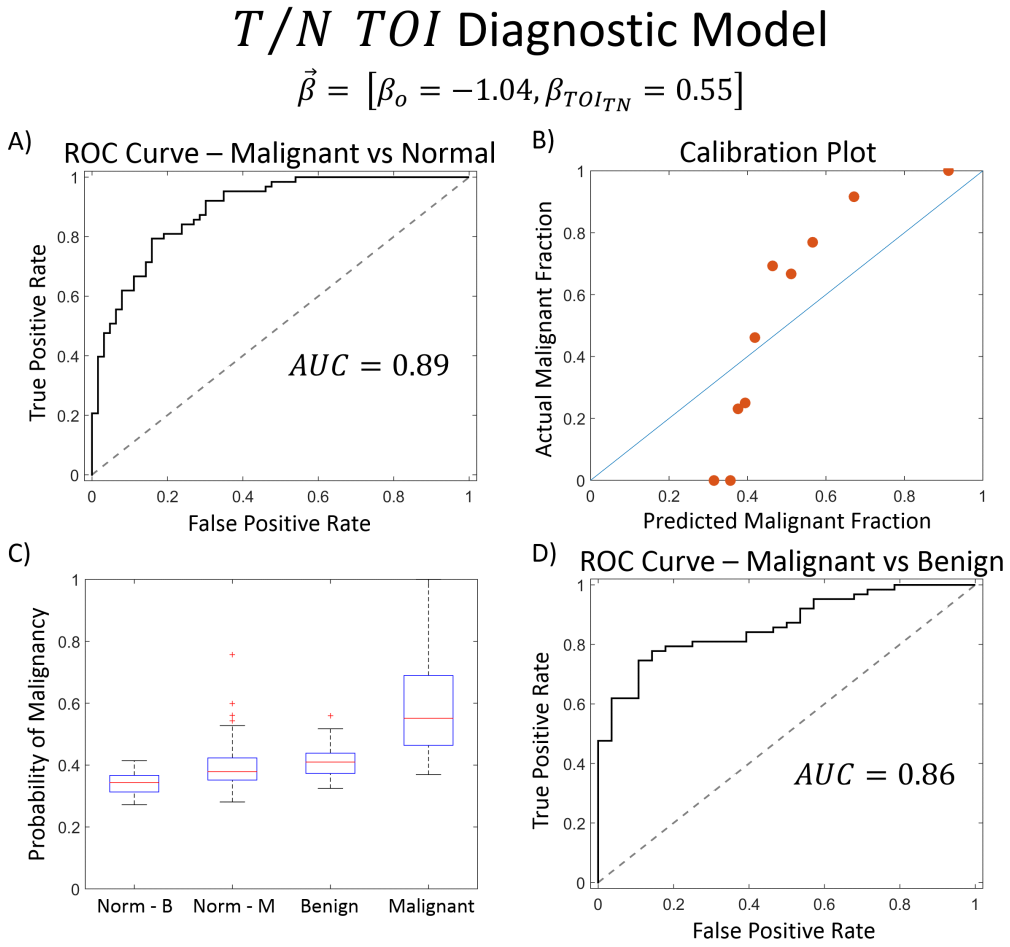

Figure 5.6: Tumor-to-Normal Tissue Optical Index Diagnostic Model. A) ROC curve for discrimination between malignant lesions and normal tissue. B) Ten-group Hosmer-Lemeshow calibration plot (see Section 2.10.4) comparing the actual fraction of tissue regions in the group that were malignant versus the predicted fraction of tissue regions in that group that should be malignant based on their individual probability of malignancy $\mathcal{P}_{\mathcal{M}}$ values. A well-calibrated model will have points that approximately lie along the identity line. C) Boxplots of $\mathcal{P}_{\mathcal{M}}$ divided into four groups: 1) Norm - B: normal tissue for subjects with benign lesions 2) Norm - M: normal tissue for subjects with malignant tumors 3) Benign: benign lesions 4) Malignant: malignant tumors. The hinges of the boxplots represent the first and third quartiles of the data, the whiskers represent the range of measurements within a distance 1.5× the interquartile range, and the crosses represent outliers. D) ROC curve for discrimination between malignant lesions and benign lesions. This model provides good diagnostic ability for both malignant versus normal tissue and malignant versus benign lesions. However, the model does not seem to be very well calibrated, as evidenced by the Hosmer-Lemeshow plot that is significantly different from unity and the lack of tissues with $\mathcal{P}_{\mathcal{M}} < 0.28$. Note that the β weight vector for the model is given at the top of the figure.

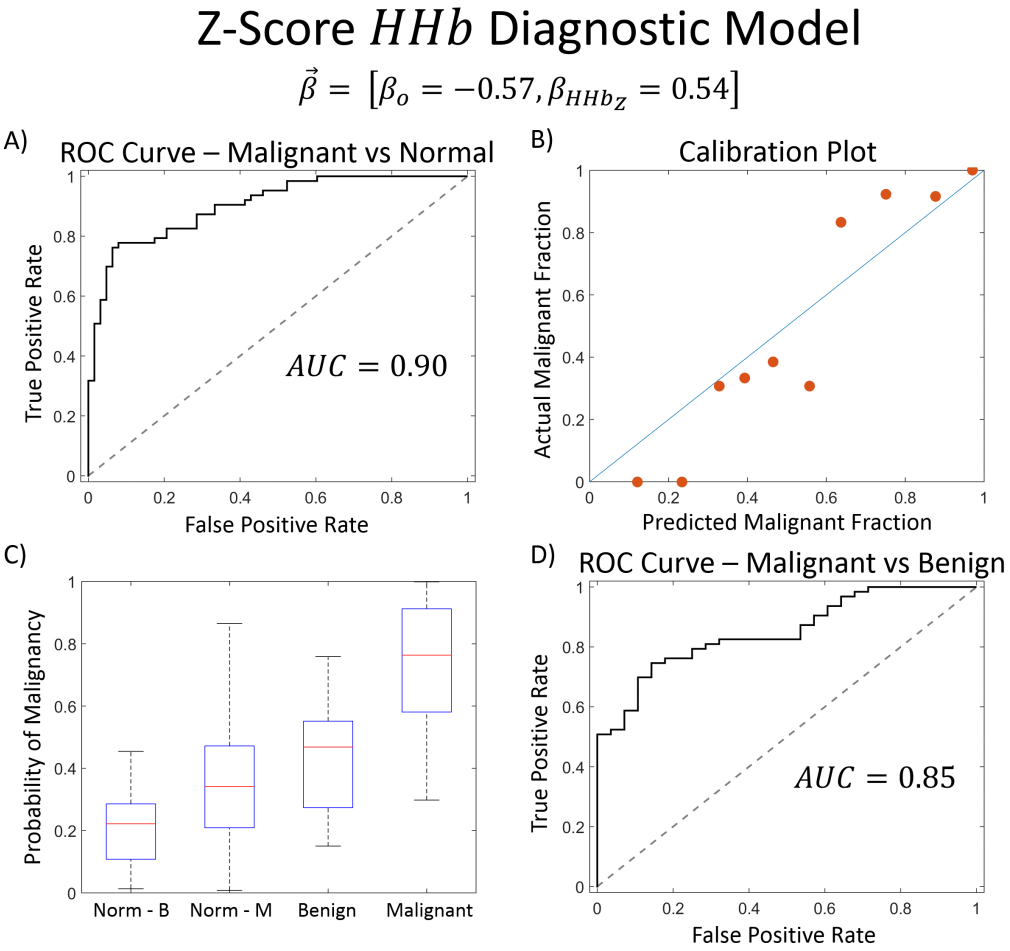

Figure 5.7: Z-Score Normalized Deoxy-Hemoglobin Diagnostic Model. A) ROC curve for discrimination between malignant lesions and normal tissue. B) Ten-group Hosmer-Lemeshow calibration plot (see Section 2.10.4) comparing the actual fraction of tissue regions in the group that were malignant versus the predicted fraction of tissue regions in that group that should be malignant based on their individual probability of malignancy $\mathcal{P}_{\mathcal{M}}$ values. A well-calibrated model will have points that approximately lie along the identity line. C) Boxplots of $\mathcal{P}_{\mathcal{M}}$ divided into four groups: 1) Norm - B: normal tissue for subjects with benign lesions 2) Norm - M: normal tissue for subjects with malignant tumors 3) Benign: benign lesions 4) Malignant: malignant tumors. The hinges of the boxplots represent the first and third quartiles of the data, the whiskers represent the range of measurements within a distance 1.5× the interquartile range, and the crosses represent outliers. D) ROC curve for discrimination between malignant lesions and benign lesions. This model provides very good diagnostic ability for both malignant versus normal tissue and malignant versus benign lesions. The separation between these three tissue types can be seen in the $\mathcal{P}_{\mathcal{M}}$ boxplots where all three groups are distinguishable. Note that the β weight vector for the model is given at the top of the figure.

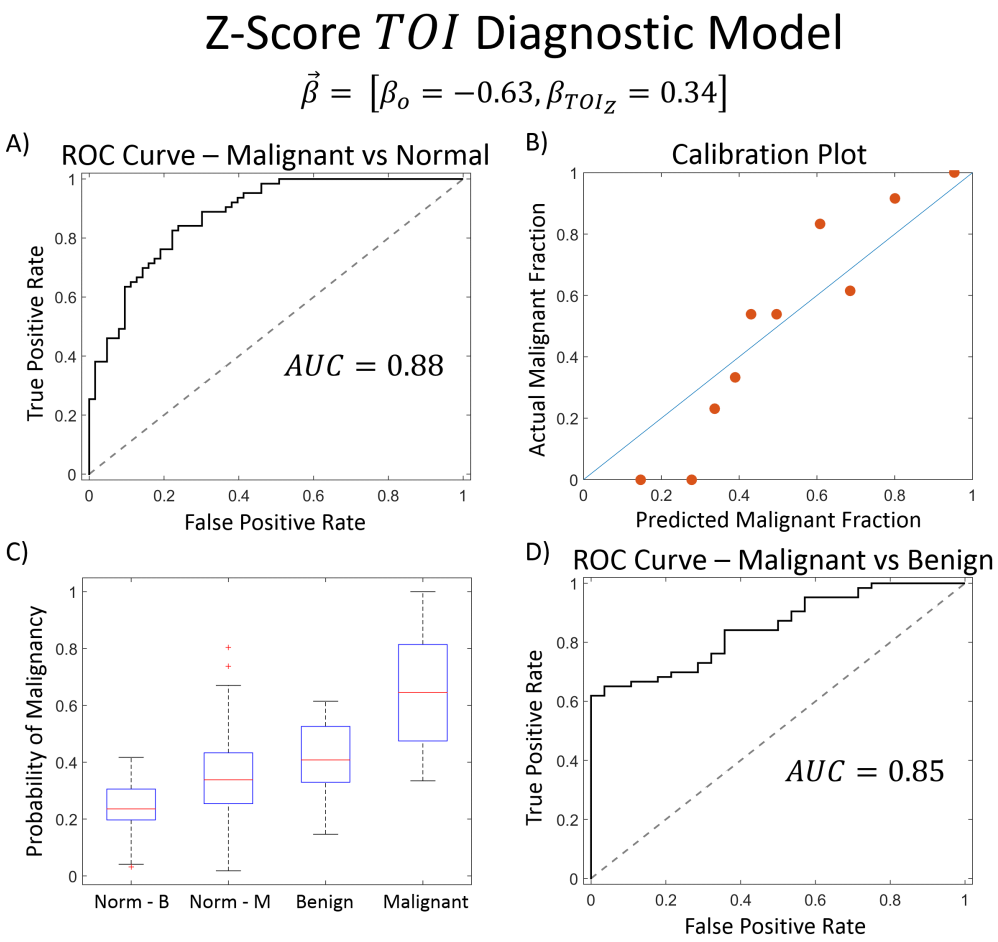

Figure 5.8: Z-Score Normalized Tissue Optical Index Diagnostic Model. A) ROC curve for discrimination between malignant lesions and normal tissue. B) Ten-group Hosmer-Lemeshow calibration plot (see Section 2.10.4) comparing the actual fraction of tissue regions in the group that were malignant versus the predicted fraction of tissue regions in that group that should be malignant based on their individual probability of malignancy $\mathcal{P}_{\mathcal{M}}$ values. A well-calibrated model will have points that approximately lie along the identity line. C) Boxplots of $\mathcal{P}_{\mathcal{M}}$ divided into four groups: 1) Norm - B: normal tissue for subjects with benign lesions 2) Norm - M: normal tissue for subjects with malignant tumors 3) Benign: benign lesions 4) Malignant: malignant tumors. The hinges of the boxplots represent the first and third quartiles of the data, the whiskers represent the range of measurements within a distance 1.5× the interquartile range, and the crosses represent outliers. D) ROC curve for discrimination between malignant lesions and benign lesions. This model provides very good diagnostic ability for both malignant versus normal tissue and malignant versus benign lesions. The separation between these three tissue types can be seen in the $\mathcal{P}_{\mathcal{M}}$ boxplots where all three groups are distinguishable. This model is also very well-calibrated, as seen in the Hosmer-Lemeshow plot and in the boxplots where $\mathcal{P}_{\mathcal{M}}$ spans the range from 0 to 1. Note that the β weight vector for the model is given at the top of the figure.

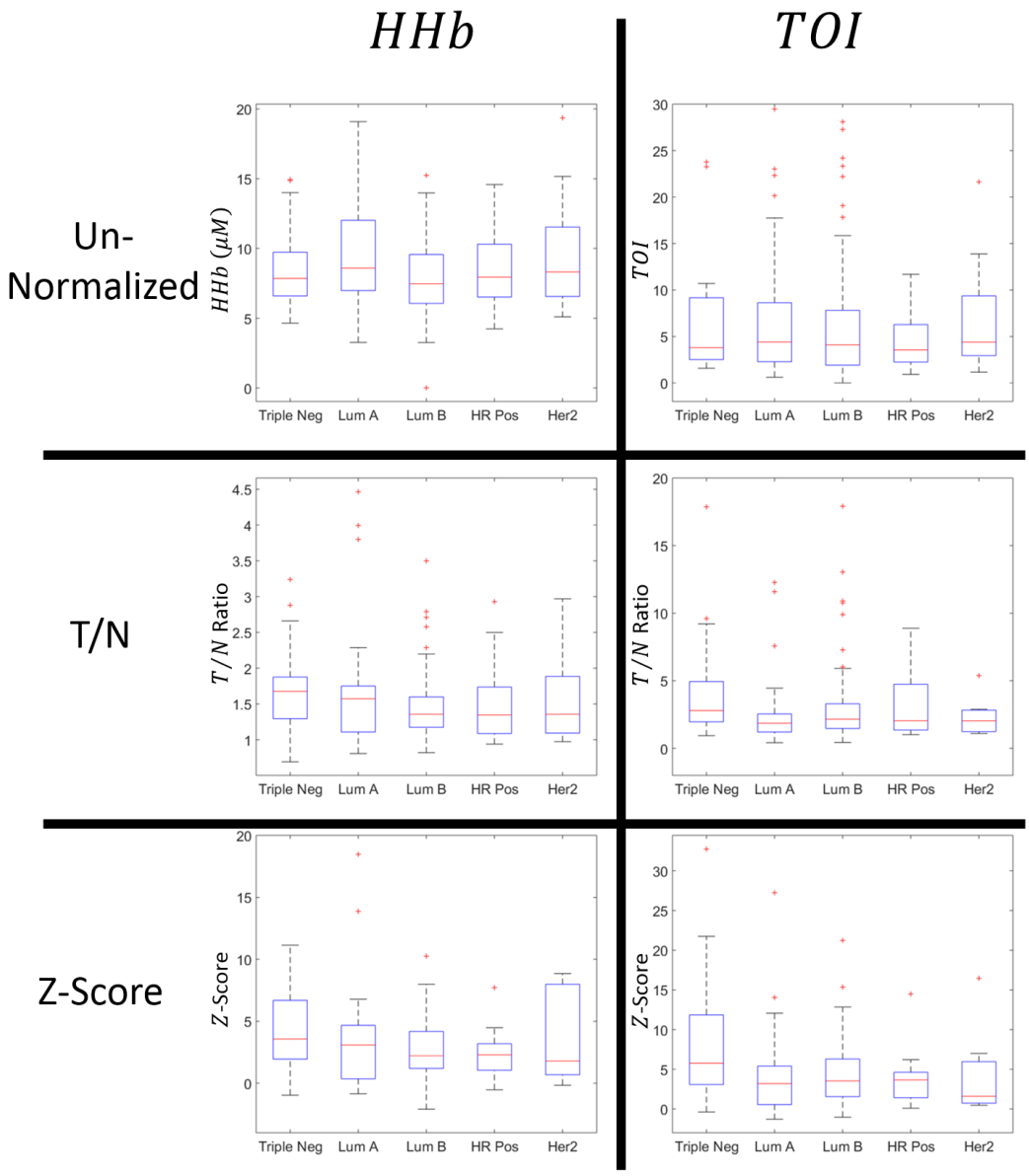

Figure 5.9: HHb and TOI by Normalization Technique and Molecular Subtype. Boxplots are shown for un-normalized, tumor-to-normal, and z-score normalized values of deoxy-hemoglobin (HHb) and tissue optical index (TOI). Each boxplot is divided into tumors of five molecular cancer subtpyes: triple negative (Triple Neg), luminal A (Lum A), luminal B (Lum B), hormone receptor positive (HR Pos), and human epidermal growth factor positive (Her2). Notice that there is no significant difference between the subtypes for any of these parameters. This indicates that the diagnostic models presented in this section, which rely on HHb or TOI, should not vary significantly in performance for different molecular subtypes.

models presented in this section should not significantly vary in performance for different molecular subtypes.

5.4 Discussion

The primary goal of this study was to determine the ability of various DOSI-measured parameters to accurately differentiate between malignant tissue and normal tissue, as well as between malignant tumors and benign lesions, in a large, heterogeneous subject population. An additional aim was to explore the effect of different data normalization techniques on these diagnostic models. The tumor and normal tissues from $n = 95$ subjects with biopsy-confirmed invasive carcinomas were used to train logistic regression models to predict malignancy using DOSI-measured parameters. Three different models were run for each parameter with three distinct normalization techniques: no normalization, tumor-to-normal ratio normalization, and z-score normalization (see Section 5.2.3). Each model was then applied to an independent test set of $n = 63$ subjects with invasive carcinomas to test the model's ability to discriminate malignant from healthy tissue. Every model could then be applied to measurements of the lesion tissue for $n = 31$ subjects with benign masses. These benign lesion measurements were then compared to the malignant lesion measurements to test the model's ability to distinguish malignant and benign masses.

This work represents the result of a robust statistical procedure, utilizing the largest known database of diffuse optically measured breast tumors, as well as a fully independent validation dataset to reduce training bias. Importantly, each prediction model created by this method can be used to both 1) localize lesions with respect to the surrounding normal tissue and 2) determine whether that lesion is malignant or benign. Thus, models like this could either be used as a non-invasive optical biopsy (see Section 1.1) or as a means of accurately identifying tumor and normal tissue to improve therapy monitoring (see Chapters 3 and 4).

The two optically-measured parameters that consistently performed the best, regardless of normalization method, were deoxy-hemoglobin concentration (HHb) and the tissue optical index ($TOI = (HHb \cdot H_2O)/Lipid$). Multi-feature regression did not significantly improve upon either of these two single-parameter models. TOI and HHb were both able to distinguish between malignant and healthy tissue (all $AUC > 0.80$) regardless of normalization technique; however, tumor-to-normal and z-score normalization did improve upon the un-normalized models. Moreover, z-score normalization significantly improved each of these parameter's ability to differentiate malignant lesions from benign lesions with an $AUC = 0.85$ for both HHb and TOI (see Figures 5.7 and 5.8). The tumor-to-normal TOI also provided clear differentiation between malignant and

benign lesions with an $AUC = 0.86$. However, this model is sub-optimal for two reasons. First, it does not appear to be very well-calibrated, especially for the lower end of the probability range. This can be seen in the Hosmer-Lemeshow plot in Figure 5.6, in which the plot of actual versus expected malignancy fractions varies significantly from the identity line. Second, TOI relies on measurement of HHb, H_2O, and $Lipid$ concentrations. This reliance is not an issue for the DOSI system, which uses broadband spectroscopy to accurately quantify all of these parameters. However, most DOS or DOT systems use two to five distinct wavelengths, and more often than not, they only reconstruct HHb and HbO_2 concentrations. Thus, if a model that relied only on HHb could produce predictions of equal quality to one that used TOI, the HHb model would be preferable because it could be more widely adopted. For the present dataset, z-score normalization is the only technique that provides acceptable prediction quality using HHb concentration.

It should also be noted that it is not particularly surprising that z-score normalization improves the diagnosis of malignant versus benign lesions much more than it does the diagnosis of malignant versus normal tissue. This is because the separation in these parameters is larger between malignant and normal tissue than it is between malignant and benign lesions. Thus, the "noise" introduced by inter- and intra-subject variations is larger relative to the malignant versus benign "signal" than the malignant versus normal "signal." The differences between the three groups can easily be seen in the boxplots in Figures 5.3 and 5.4.

The other aim of this analysis was to determine if there were meaningful differences in the DOSI-measured parameters across various tumor subtypes. In the simple analysis performed here, no significant differences among the molecular subtypes were found for either HHb or TOI (see Figure 5.9). This uniformity should ensure that the diagnostic models developed here are applicable across malignant tumors, regardless of molecular variations.

Several areas could be further explored with respect to diagnostic markers in this type of dataset. First, differentiation of malignant and benign lesions was determined using a prediction model that was trained to distinguish malignant from normal tissue, rather than benign lesions. Thus, it would be instructive to explore direct binomial logistic regression between invasive carcinomas and benign masses. If this analysis produced similar physiological correlations between HHb or TOI and malignancy, it would be further evidence of the robustness of these methods. This technique was not attempted for this dataset due to the approximate $5:1$ disparity between the number of available malignant and benign lesions. This type of discrepancy between the two training classes can significantly bias the fitting algorithm towards the larger class [136]. Additionally, the ideal role for DOSI in the diagnostic setting must be determined. Though it is unlikely to replace gold-standard invasive biopsy as a means of determining malignancy, DOSI could be used a preliminary

screening tool to prevent clearly unnecessary biopsies for obviously benign lesions. For example, if the probability of malignancy cutoff value was set to be very low, *i.e.*, relatively close to 0, a very high negative predictive value could be achieved, with which only patients with clearly benign lesions would be identified as benign. Thus, these subjects could avoid undergoing a costly, invasive biopsy that is extremely unlikely to yield a positive result. This could be of particular use for subjects with high density breasts who are prone to false positives in x-ray mammography. The ideal cutoff and prediction metric for this type of screening would require further validation.

The determination of optically measured differences across molecular subtypes could also be performed with a more complex analytic technique. For example, a machine learning algorithm could be performed with DOSI-measured parameters as features, but with tumor subtypes used as the model classes instead of malignancy status. Thus, the models would be trained to directly predict tumor subtype based on DOSI measurements. If successful, these models would determine the characteristic optical properties of each subtype, which could enable improved normalization and lesion identification. A similar procedure could also be utilized for different pathological or radiographic markers, such as breast density, hormone receptor level, or menopausal status. This differential diagnosis could both provide more knowledge about the hemodynamic, structural, and optical characteristics of tumors and help guide DOSI studies to the specific populations that could benefit most from optical imaging.

5.5 Conclusion

A dataset of $n = 222$ subjects, including those with both malignant and benign lesions, were measured using diffuse optical spectroscopic imaging (DOSI). Logistic regression models using single DOSI-measured parameters were created to distinguish malignant tissue from normal tissue on the tumor-bearing breast in a subset of the subjects with malignant carcinomas. These models were then applied to an independent set of subjects with malignant lesions, and to all subjects with benign lesions, in order to test the model's ability to discriminate both malignant tissue from normal tissue and malignant lesions from benign lesions. Different normalization techniques, including no normalization, tumor-to-normal-ratio normalization, and z-score normalization, were tested. The best models used either the deoxy-hemoglobin concentration (HHb) or the tissue optical index (TOI) parameters. Z-score normalization produced the most robust and well-calibrated models across both parameters and provided a significant improvement for HHb models. This is of particular importance because most DOS systems have fewer available wavelengths than DOSI and thus are unable to calculate the water and lipid concentrations necessary to calculate TOI.

These z-score normalized models discriminated malignant tissue from normal tissue with $AUCs$ of $0.90\,(95\,\%\,CI:0.85$ to $0.95)$ and $0.88\,(95\,\%\,CI:\ 0.82$ to $0.94)$ for HHb and TOI, respectively. The same models for HHb and TOI could accurately distinguish malignant and benign lesions with an $AUC = 0.85\,(95\,\%\,CI:\ 0.77$ to $0.93)$ for both parameters (see Figures 5.7 and 5.8), indicating that DOSI not only has the ability to distinguish malignancies from healthy tissue in a single subject, but also to differentiate between malignant and benign lesions with the same quantitative models. This positions DOSI as an attractive modality for performing preliminary, non-invasive biopsies.

An initial investigation of the heterogeneity in HHb and TOI across different tumor molecular subtypes was also performed. No significant difference in either HHb or TOI was found among these subtypes, suggesting that the HHb and TOI diagnostic parameters should perform well across all subtypes. Further work is needed to more fully characterize optically measured differences between various tumor and subject characteristics and, thus, to determine DOSI's ability to perform differential diagnosis of breast cancer patients.

Chapter 6

Development of a DOT Instrument for Simultaneous Measurement with MRI

6.1 Introduction

The diffuse optical techniques presented thus far have essentially been point measurements of homogeneous optical property distributions. The DOSI instrument collects these point measurements over a grid of spatial points, thereby deriving a two-dimensional topographic map of optical properties and chromophore concentrations; however, DOSI does not provide enough information for full tomographic image reconstruction, as discussed in Section 2.6. This more sophisticated type of three-dimensional imaging is complicated by several issues. First, DOT image reconstruction is dependent on solving an ill-posed inverse problem for the optical property distributions. Second, DOT typically has limited spatial resolution due to the diffusive nature of photon transport in tissue [195; 32; 98]. Both of these limitations can be ameliorated by incorporating information from another clinically-standard structural imaging modality into the DOT imaging protocol. As enumerated in Section 2.6.7, this additional structural information serves multiple purposes: validation of DOT's ability to localize tumors, constraint of the DOT reconstruction algorithm, and synthesis of functional DOT parameters with other quantitative parameters from MRI, PET, X-ray, or ultrasound that may provide novel physiological insight.

Fortunately, the portable nature, comparatively low cost, and lack of ionizing radiation associated with diffuse optics makes combination with standard clinical modalities simple compared to the combination of two clinical imaging modalities, such as MRI-PET or PET-CT. Several groups have successfully combined DOT with x-ray mammography [169; 270; 111; 183; 280], ultrasound [274; 140; 275; 277], or MRI [193; 46; 142; 271; 52; 105]. It is usually advantageous for these combined instruments to acquire data simultaneously. This is especially true for breast imaging because the compressibility of breast tissue makes non-concurrent co-registration difficult, requiring a sophisticated deformation algorithm and a series of assumptions [20].

The instrument presented herein was designed, built, and implemented over the last several years at the University of Pennsylvania. It is a hybrid DOT system that performs both high-spatial density continuous wave (CW) DOT and time-domain (TD) DOS measurements concurrently with clinical MRI instrumentation. This incorporation of a research DOT system into clinical MRI RF coils is a significant advance that enables improved patient throughput and the use of more sophisticated and robust MR pulse sequences than a custom-built RF coil. Furthermore, the combination of a high-density CW system with TD measurements enables both absolute quantification, via the TD system, and relatively fast, high-quality three-dimensional reconstructions, via the CW system. Additionally, this instrument contains the most source and CW detector locations (64 and 108, respectively) of any DOT-MRI system yet reported. This will improve the fidelity of images for comparison to and synthesis with MRI. Finally, this combined instrument system provides two new venues for exploring the combination of the static tissue properties from DOS with blood flow or perfusion information. First, this platform also contains 20 source and 20 detector positions for DCS measurements. This density of optode positions could enable not only point DCS measurements, but also potentially diffuse correlation tomography (DCT), which would provide three-dimensional images of the blood flow index (BFI). Second, the combination of the DOT system with a clinical coil enables the use of fast DCE-MRI measurements, such as KWIC, that provide metrics of tumor perfusion and permeability [237; 238; 92].

At this stage, the joint DOT-MRI instrument has been fully implemented in the clinic at the Hospital of the University of Pennsylvania. Healthy volunteers have been measured to test the patient interface and data acquisition algorithms, and multi-modality phantoms have been constructed and imaged to test the data analysis and image reconstruction procedures. In time, this instrument should provide improved quantification of tumor optical and hemodynamic properties, which could serve as a well-validated reference for studies seeking to distinguish malignant from healthy tissue (Chapter 5) or attempting to predict and understand chemotherapy response (Chapters 3 and 4).

6.2 Instrument Design

A new platform for combined diffuse optical and magnetic resonance imaging was developed at the University of Pennsylvania. The initial stages of this instrument's construction have been previously reported [52], but the system has since been completed as a part of this thesis. This instrument integrates both time domain (TD) and continuous wave (CW) diffuse optical imaging systems for simultaneous DOT with either 1.5T or 3T MRI. Adjustable optical modules permit optimized optode positioning for each subject and enable opto-electronic compatibility with future 7T MRI platforms. This system provides the largest in-magnet, *i.e.*, concurrently measured with MRI, DOT spatial data sets yet reported. Figure 6.1 displays a schematic of the optical and electronic instrumentation in the system, and Figure 6.2 displays the opto-electronic instrument rack.

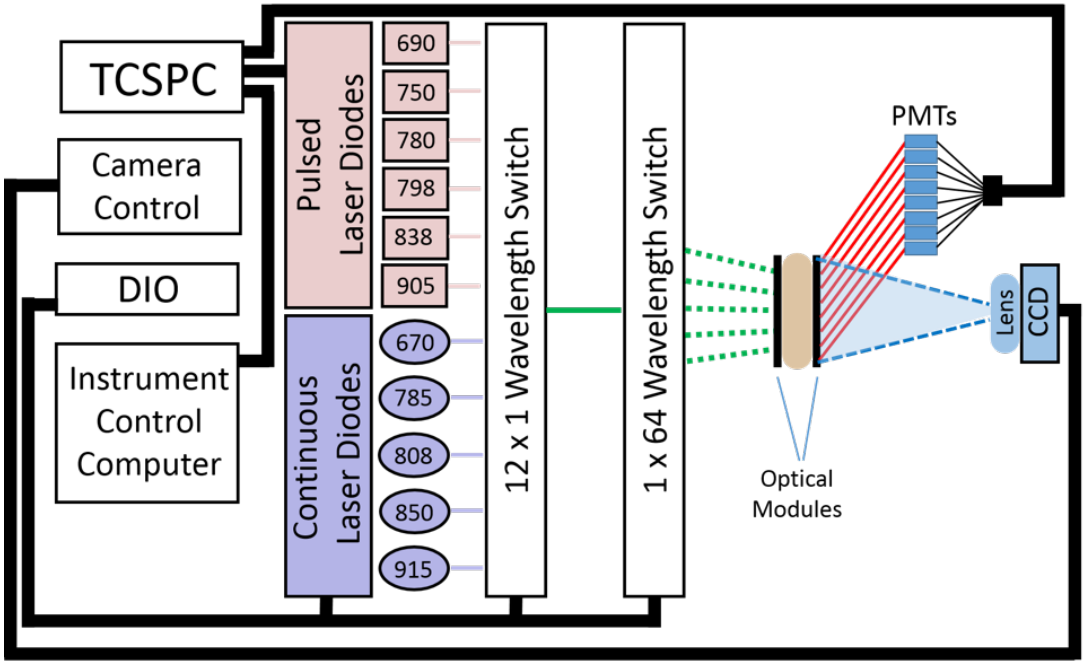

Figure 6.1: Schematic of DOT-MRI Instrument Optics and Electronics. This hybrid CW and TD DOT-MRI system employs 6 pulsed laser sources (690 nm, 750 nm, 780 nm, 798 nm, 838 nm, 905 nm) for TD measurement of absolute bulk optical properties and 5 continuous wave laser sources (670 nm, 785 nm, 808 nm, 850 nm, 915 nm) for producing three-dimensional reconstructions of relative optical properties. The sources are coupled to optical imaging modules via a 12×1 wavelength switch and an effective 1×64 source position switch. CW detection is performed via detection fibers mounted on a plate and imaged onto a CCD, and TD detection is accomplished with PMTs and time-correlated single photon counting (TCSPC) modules. All components are controlled via the instrument computer, digital input/output channels and a National Instruments DAQ board. This figure is modified from a similar one in the PhD Thesis of David R. Busch [52].

Figure 6.2: DOT-MRI Instrument Rack. The optical and electronic components of the DOT-MRI instrument are housed within an instrument rack on pneumatic wheels for easy transport to and from the MR suite. This rack contains all laser sources, the pulsed laser diode driver, all optical switches, the CW detection fiber imaging plate and CCD, PMTs and PMT control-units for TD detection, and TCSPC control instrumentation.

6.2.1 Continuous Wave System

The CW measurements are performed using five steady-state AlGaAs lasers with wavelengths 670 nm (Sony - Tokyo, Japan), 785 nm (Frankfurt Laser Company - Friedrichsdorf, Germany), 808 nm, 850 nm, and 915 nm (Roithner LaserTechnik - Vienna, Austria). These lasers account for five of the inputs to a 12×1 optical switch (PiezoJena - Jena, Germany), the output of which is coupled to a $95:5$ optical fiber splitter (OZ Optics - Carp, ON, Canada). The 95 % output of the splitter is then fiber-coupled to an attenuator, which is coupled to a 1×2 optical switch (DiCon FiberOptics - Richmond, CA) and then further to two 1×32 optical switches (DiCon FiberOptics - Richmond, CA). For CW laser sources, the attenuator is set to maximize signal delivered to the tissue. The proximal end of the optical source fibers (62.5/125 diameter, FiberOptic Systems, Inc. - Simi Valley, CA, USA) are then coupled to each of the 64 switch outputs. These fibers are then bundled together into the fiber bundles discussed in Section 6.2.3.

CW detection is performed via 108 1-mm diameter optical fibers (FiberOptic Systems, Inc - Simi Valley, CA, USA) whose proximal ends are mounted to an imaging plate and imaged onto an Andor IKon CCD (Model No.: DW936N-#BV - Belfast, Northern Ireland, UK) (see Figure 6.3). The 5 % output from the fiber splitter coupled to the 12×1 switch is also mounted onto this imaging plate. This fiber serves as a reference channel by which fluctuations in the laser amplitude are directly measured and can thus be accounted for via normalization of the detected signal.

6.2.2 Time Domain System

The time domain system consists of six pulsed lasers sources (PicoQuant - Berlin, Germany) with wavelengths 690 nm, 750 nm, 780 nm, 798 nm, 838 nm, and 905 nm. These sources account for six more of the inputs to the 12×1 wavelength switch (PiezoJena - Jena, Germany), the output of which is then attenuated and coupled to the source position switches.

Time domain light is collected by 8 3-mm optical fibers which are each coupled to a photomultiplier tube (PMT) (H7422-50mod, Hamamatsu - Hamamatsu, Japan). This larger fiber diameter enables more photons to be collected and thus provides a vital improvement in signal-to-noise for the PMT detection system. The instrument contains sixteen distinct PMT modules, enabling the use of the PMTs with optimal sensitivity and providing back-up detectors in the event of damage. These PMTs are protected from saturation via the source-side attenuator coupled to the laser sources and with individual shutters designed to protect the detectors when not in use. The PMTs are connected to Becker & Hickl (Berlin, Germany) time-correlated single photon counting (TCSPC) modules. The single photon counting techniques are necessary to temporally resolve the

Figure 6.3: Detection Fiber Plate and CCD. CW detection fibers and the CW reference channel are mounted onto a plate which is then imaged onto a CCD. The spot on the CCD from each fiber tip can then be used as an individual detector. Note that this is a photograph of the plate in the early stages of construction [52], prior to completion of the system; the final version contains considerably more fibers.

detected signal collected by the PMTs and thus measure the point-spread functions necessary for the determination of optical properties via time-domain techniques (see Section 2.3.3).

6.2.3 Optical Modules, RF Coil, and Imaging Platform

All fibers, including the source fibers, CCD-coupled CW detection fibers, and PMT-coupled TD detection fibers are gathered together into approximately 10 m-long shielded fiber bundles. The bundles must be this long to enable optical data to be collected inside an MR suite; the instrument's electronic modules must also be kept sufficiently far away, *i.e.*, outside the restricted area of the magnetic field. The proximal end of all fibers are permanently mounted inside four custom-built optical modules made of grey PVC material with a 3D-printed plastic shielding; these materials were demonstrated to have no detectable magnetic susceptibility that could contaminate the MR signal. Each of the four module faces, which are placed in contact with the tissue, have a length of 16.4 cm, and a height of either 3 cm or 3.5 cm. This provides a sufficient coverage area of source and detector positions for most breasts. The two source modules each contain 32 source fibers. The first detector module contains 54 CW detection fibers and 5 TD detection fibers while the second detector module contains 54 CW detection fibers but only 3 TD detection fibers. The fiber optic modules also contain 20 DCS source fibers (FiberOptic Systems, Inc. - Simi Valley, CA, USA), shared across the two detector modules, and 20 single-mode DCS detector fibers (FiberOptic Systems, Inc. - Simi Valley, CA, USA), spread across the two source modules. Note that these fibers are not coupled to DCS source and detector instrumentation on the current opto-electronics rack. Instead, a separate DCS device must be used if DCS measurements are to be performed. Figure 6.4 contains photographs of the mounted fibers and the tissue interfaces of the optical modules.

These modules are mounted in a parallel-plate geometry within the windows of two clinically standard Sentinelle RF biopsy coils (INVIVO Corp. Gainesville, FL Part No.:4000044-11), with the two source modules on the medial side of the subject's breast and the two detector modules on the lateral side of the breast (see Figure 6.5). This alignment puts the source positions farther away from lateral side of the breast where a majority of breast tumors form [222], and thus limits contamination between the tumor contrast and the known imaging artifacts found near the source plane [80; 25]. In clinical use, the RF coils have open windows with plastic grids so that MRI-guided breast biopsies can be performed. If the plastic grids are removed, the coil provides an ideal window for the optical modules to couple to tissue. The biopsy coils are housed in a patient imaging platform in which the patient lies prone and the breast is inserted between the two coils for simultaneous optical and MR imaging. The compatible coils available at the Hospital of the University of Pennsylvania can be used in either 1.5T or 3T large-bore MR scanners, *e.g.*, the 1.5T

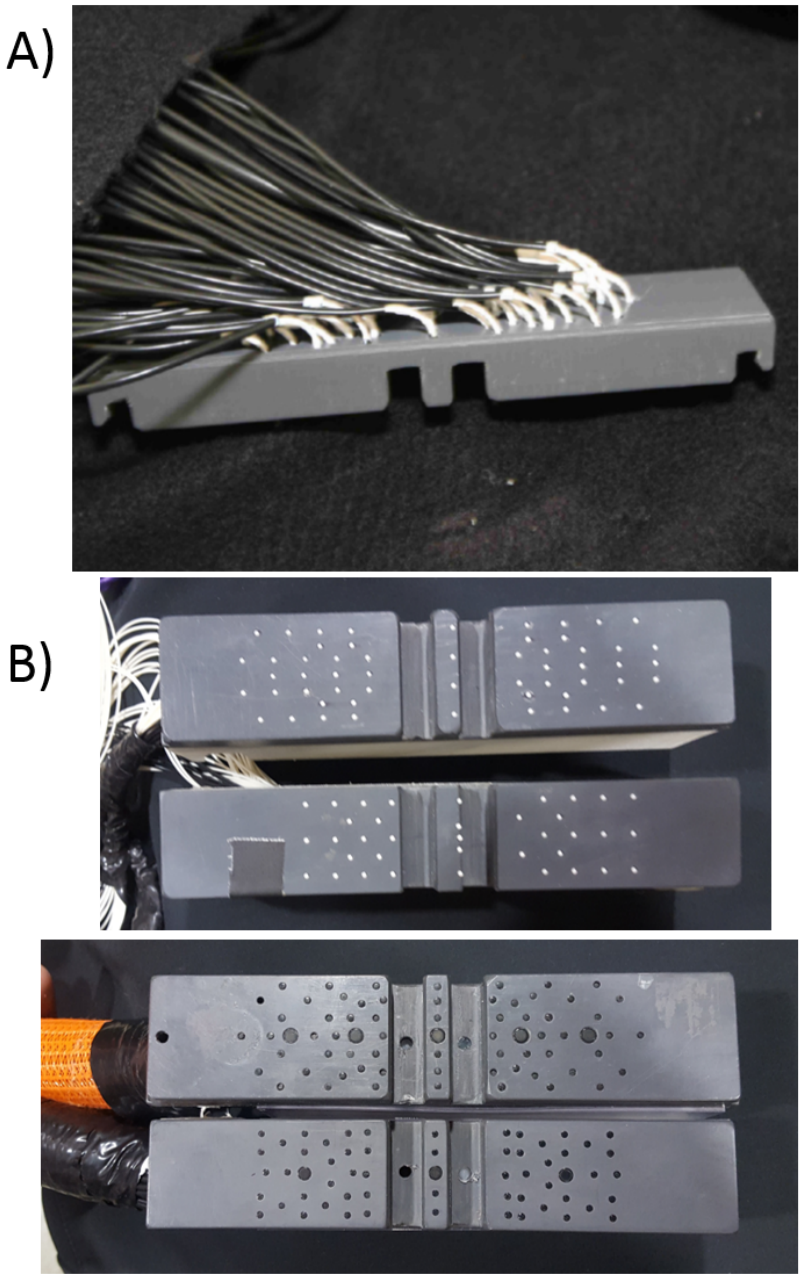

Figure 6.4: Optical Source and Detector Modules. A) Side view of source fibers mounted onto one of the source modules. Note that the exposed parts of these fibers are shielded by a 3D-printed cover when the module is in use. This photograph is from the PhD Thesis of David R. Busch [52]. B) Front view of two source modules (top) and two detector modules (bottom). On the detector modules, the large fiber tips are the 3-mm fibers coupled to PMTs, and the smaller tips are either the 1-mm fibers imaged onto the CCD or DCS source fibers. The fiber tips on the source modules are either source fibers coupled to the optical position switch or single-mode DCS detection fibers.

Siemens Espree system (Erlangen, Germany). The optical modules can also be positioned at any height within the biopsy window, enabling optimization of the source and detector positions, which allows for better coverage of the tumor region and limits the number of sources and detectors that are not directly in contact with tissue. Finally, MRI fiducial markers are mounted on the optical modules to permit co-registration of the DOT and MR imaging geometries (see Figure 6.4).

6.2.4 System Control and Stability

All of the aforementioned optical and electrical components, along with the instrument control computer, are housed in a rack-mounted instrument with pneumatic wheels for simple, safe transport of the instrument to and from the MR suite (see Figure 6.2). As previously mentioned, the $\sim 10\,m$ fiber bundles can then be passed through the MR suite waveguide, so that the optical modules can be mounted on the RF coil, while the instrument rack remains outside the high magnetic field of the MRI (see Figure 6.6). The instrument computer controls the function of all components through LabVIEW (National Instruments, Austin, TX) and Becker & Hickl (Berlin, Germany) software and is coupled to the opto-electronic components via digital input/output channels and a National Instruments DAQ board (Austin, TX, USA).

Prior to imaging, the lasers must be turned on for a thirty-minute warm-up period, after which the CW laser intensities are stable to $< 1\,\%$; the remaining power variations are normalized using the low power arm of the 95 : 5 splitter. The time domain system requires a somewhat longer period of ~ 1 hour to stabilize. This appears to be due primarily to jitter in the laser diode driver oscillator (PicoQuant, Berlin, Germany); the pulsed laser instability is also more difficult to eliminate via normalization because the detected power from the TD lasers is not high enough to quantify using the reference channel imaged by the CCD.

Light leakage at the detectors is minimized to the point that DOT images can be successfully carried out in typical clinical lighting conditions. However, the bore light in the MRI is turned off, and the subject is covered with a sheet, to minimize stray light at the patient interface.

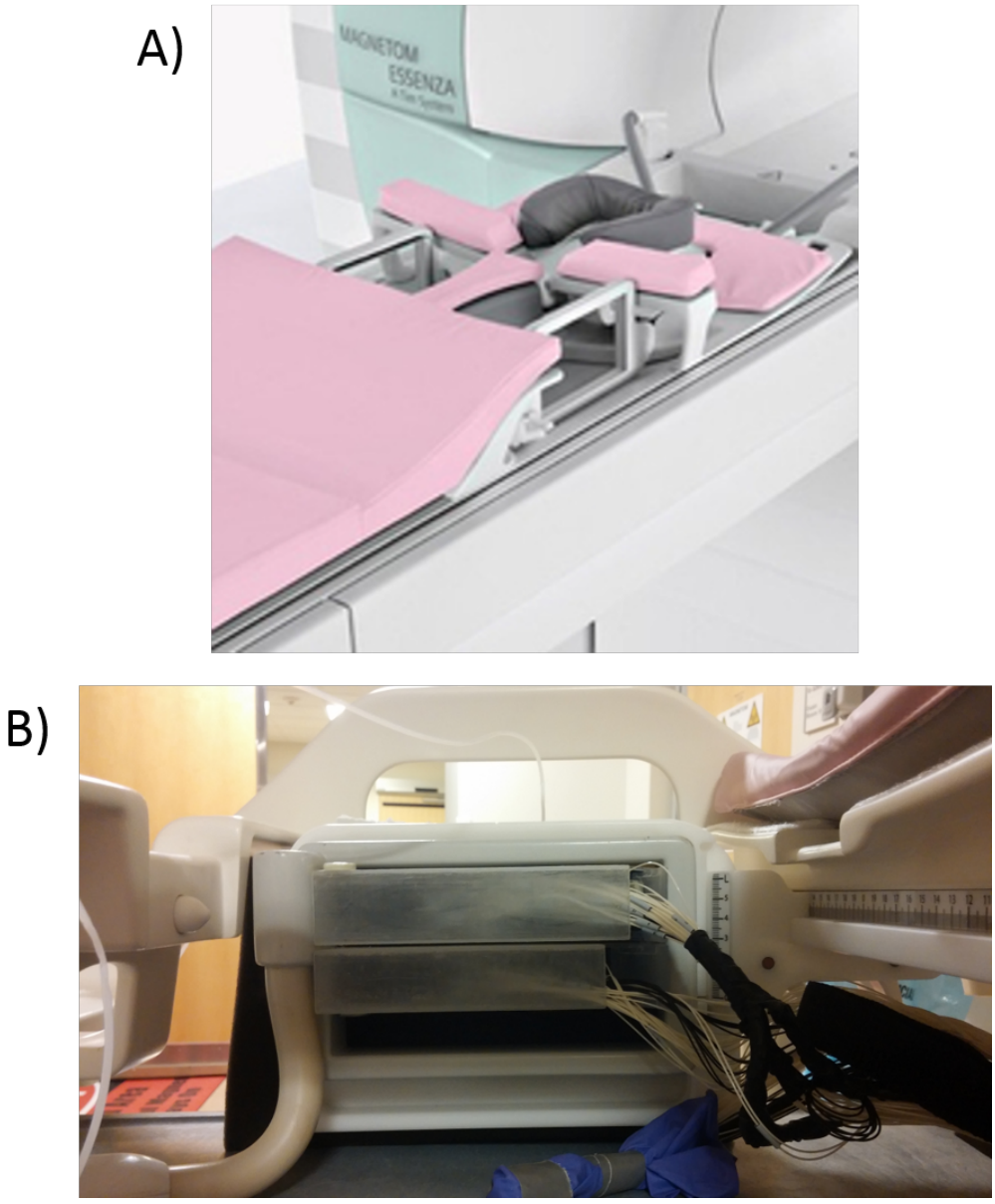

Figure 6.5: RF Coil and Optical Modules. A) Sentinelle breast biopsy RF coil photo courtesy of Siemens, Inc. Note the window in the biopsy coil that allows the optical modules to interface with tissue. B) A rear view of the DOT-MRI source modules in the breast biopsy coil. Note that the modules can be placed at any vertical position within the coil to optimize source locations. The same can also be done for the detector modules on the lateral side of the breast. A fiducial marker, which enables co-registration of the optical and MR geometries, is visible on the top left side of the top source module.

Figure 6.6: DOT-MRI System in MR Suite. When in use, the DOT instrument rack is brought to the control room of the MR suite at the Hospital of the University of Pennsylvania. The fiber bundles then pass through the waveguide and are incorporated into the clinical breast biopsy RF coil, on which the subject can lie in a prone position to be simultaneously imaged by MRI and DOT

6.3 Data Acquisition and Analysis

For this hybrid instrumentation, three imaging sequences must be performed for each subject or phantom measurement: continuous wave (CW) DOT, time domain (TD) DOS, and MRI (see Figure 6.7). Because the optical measurements do not interfere with the magnetic field, the MRI and optical sequences can be performed simultaneously; however, the CW and TD diffuse optical imaging must be performed sequentially. In addition to the target measurement, a reference phantom is imaged using the same TD and CW sequence as the target. This reference measurement enables reconstruction based on differences, which eliminates error due to source-detector coupling coefficients (see Section 2.5.7) and ensures that the small perturbation condition of the Rytov approximation (see Section 2.6.1) is met.

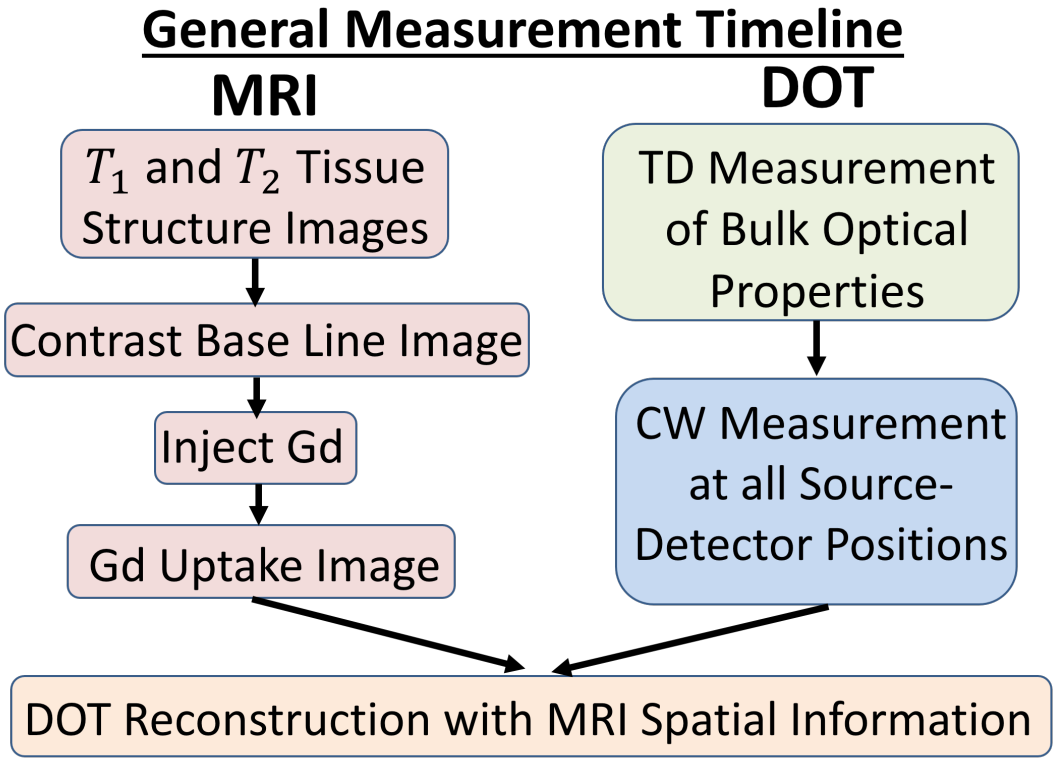

Figure 6.7: DOT-MRI Imaging Sequence Flow Chart. The DOT-MRI instrument performs the optical and MRI measurements simultaneously. Structural T1- and T2-weighted MRI measurements are made prior to the injection of a gadolinium contrast agent. After the contrast injection, another set of MR images are acquired, thereby permitting subtraction imaging that enables optimal tumor contrast. Simultaneously, optical data is acquired. First, TD measurements are made at several positions to determine absolute bulk optical properties. Then, CW measurements are made at all source and detector positions to enable full three-dimensional reconstruction.

6.3.1 MRI

The MRI pulse sequences performed with this instrument are clinically standard gadolinium-contrast (Gd-contrast) uptake sequences used for breast MR imaging. These sequences typically consist of a series of T1- and T2-weighted structural image sequences, a baseline T1-weighted sequence sensitive to the Gd-contrast agent, and then a contrast image of the same type as the baseline image after the Gd-contrast agent uptake by the tumor. These MR images provide the location and structure of the breast and a clear subtraction Gd-contrast image of the tumor. The MRI will also image the fiducial markers placed at known positions on the optical modules, which enables the co-registration of the optical and MRI coordinate systems.

6.3.2 Time Domain Measurements

The optical imaging sequence begins with a series of TD measurements. Approximately 4 of the 64 source positions are illuminated with each of the 6 available pulsed laser wavelengths. These measurements are performed sequentially for each source-wavelength combination, and all eight available PMT detector locations are active for every measurement. In practice, fewer than eight detectors will be used for each source position due to signal limitations caused by differences in source-detector separations. The PMTs, in conjunction with the TCSPC electronics (see Section 6.2.2), then record point-spread functions for each wavelength/source-detector combination. These point-spread functions are dependent on the absorption and reduced scattering coefficients of the tissue. The light pulse input to the tissue is not a true delta function due to broadening of the light pulse that occurs in the optical switches, attenuators, and fibers (see Section 2.4.5). This broadening, known as the instrument response function (IRF), is of particular concern with this DOT-MRI instrument due to the long ($\sim 10\,m$) optical fibers on both the source and detector sides. Thus, to distinguish the temporal broadening due to diffusion through tissue from the inherent broadening in the instrument, the IRF must be measured. With this system, the IRF can be found by performing TD measurements without an optically thick diffusive medium, *e.g.*, without a breast or phantom, between the source and detector planes. Care must be taken in this step to attenuate the source light to avoid saturating and/or damaging the PMTs. Once the IRF is known, it serves as an effective temporal source profile, which can be convolved with the Green's function solution for an infinite slab (see Section 2.5.5). The measured point-spread function is then fit to this solution function using a non-linear fitting algorithm, in this case, the MATLAB function *fminsearchbnd* [3], to calculate the optimal absorption and reduced scattering coefficients.

Since only a few source positions are used for the TD measurements, the fitted absorption and

reduced scattering coefficients for each source-detector pair are typically averaged with all other measurements at the same wavelength. Performing TD measurements at more source positions could enable a sort of coarse imaging of absolute optical properties; however, this benefit must be balanced by the time it adds to the patient imaging sequence, and thus, it is not feasible under most circumstances.

6.3.3 Continuous Wave Imaging

The CW imaging sequence is performed after the completion of the TD measurements. Each of the 5 CW laser wavelengths and 63 of the available 64 source positions are cycled through sequentially. One source position is usually left disconnected to provide a sham measurement for background normalization purposes. A single frame is acquired by the CCD for each source-wavelength combination. This frame will contain the outputs from the fiber tips at the imaging plate. Thus each detector fiber will be imaged over an approximate circle containing ~ 80 pixels (see Figure 6.8). The detector locations on the CCD are determined using a mask for the sum over all measured frames. The signal used for analysis of a single detector is the sum over all pixels assigned to the given detector fiber for a single camera frame. The entire sequence of source and wavelength combinations is often performed several times to guard against potential motion artifacts or other systematic instabilities. The data from these multiple passes through the entire sequence are then averaged for each wavelength-source-detector combination. In the case of a clear artifact, the data is excluded from the average.

Once this data is collected, single-wavelength or multi-spectral reconstruction is performed. The absolute bulk absorption and reduced scattering coefficients from the TD analysis are used as the initial conditions for the reconstruction. Because this high-spatial density system is CW, only the absorption coefficient, and by extension the chromophore concentrations are reconstructed, while the reduced scattering remains constant. The knowledge of absolute background absorption coefficient from the TD instrumentation transforms the relative absorption coefficients typically reconstructed in CW DOT to absolute values. It may be possible to perform multi-spectral CW reconstructions that simultaneously reconstruct oxy- and deoxy-hemoglobin concentrations as well as the scattering amplitude (A) and scattering power (b) by utilizing all 5 CW wavelengths. However, this approach is heavily dependent on the the medium obeying the Mie scattering model and accurate estimation of non-reconstructed chromophore concentrations, such as water and lipid. As such, this type of reconstruction was not employed for the initial phantom tests.

A finite difference method reconstruction is performed using TOAST++ [227]. This normalizes the source-detector coupling coefficients and provides a convenient reconstruction framework for

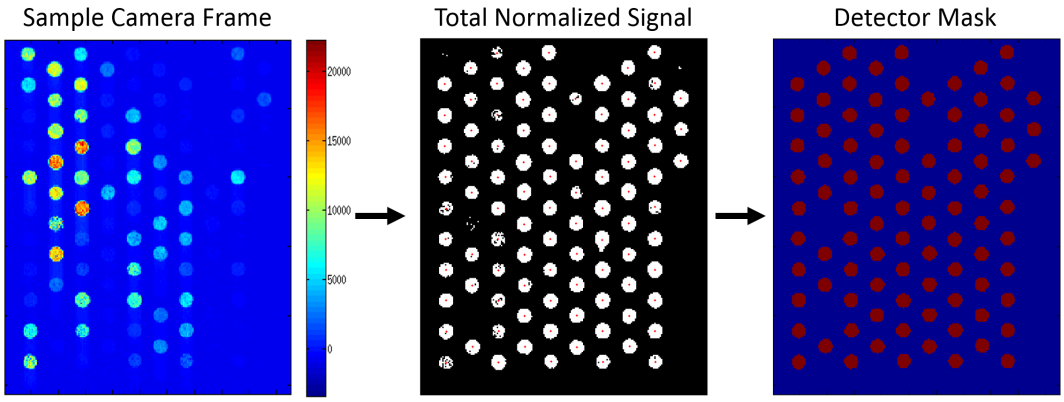

Figure 6.8: Detector Measurement Extraction from CCD. The left image shows a sample CCD frame. Each circle is a single imaged fiber tip. Note that different detectors have different signal levels due to their varying proximity to the source position and the heterogeneous absorption and scattering coefficients of the tissue. The center image is a sum over all camera frames, *i.e.*, for all wavelengths and sources, normalized by a dark image. The centroids (small red dots in center image) of each region of high signal are then found. These centroids and the average diameter of the high signal regions are used to create a mask of detector locations (right). This mask indicates which pixels belong to each individual detector. Note that this image is cropped to show only the ~ 90 detectors that were in contact with the measured phantom.

utilizing the reference phantom. For phantom measurements, single-wavelength reconstructions are performed for each wavelength while human subject data is usually reconstructed with a multi-spectral algorithm that directly determines the oxy- and deoxy-hemoglobin concentrations. Given the number of available wavelengths, water or lipid concentrations could also be reconstructed. This would likely be easier if a hard-prior constraint (see Section 6.3.4) was used, minimizing the under-determined nature of the DOT inverse problem.

6.3.4 Incorporation of MRI into DOT Reconstruction

The primary purpose of simultaneous DOT and MRI, other than the validation of the ability of DOT to localize tumors, is the use of MRI structural images as a prior constraint on the DOT reconstruction. After the co-registration of the two coordinate systems using the MR fiducial markers, the MRI must be segmented into a mask identifying distinct regions. This mask is created via signal thresholding, in which signal cutoff values between various regions are determined. It is possible to create a four-region mask, *e.g*, non-tissue, adipose, fibroglandular, and tumor; however, for this system, the MRI is generally segmented into non-tissue regions, background breast tissue, and tumor. This type of segmentation is particularly simple for contrast-enhanced MRI because the subtraction image provides distinct contrast between the tumor and the rest of the breast tissue.

Figure 6.9 contains an example of a phantom MRI and the segmented mask. Note that the regions outside the breast are not reconstructed.

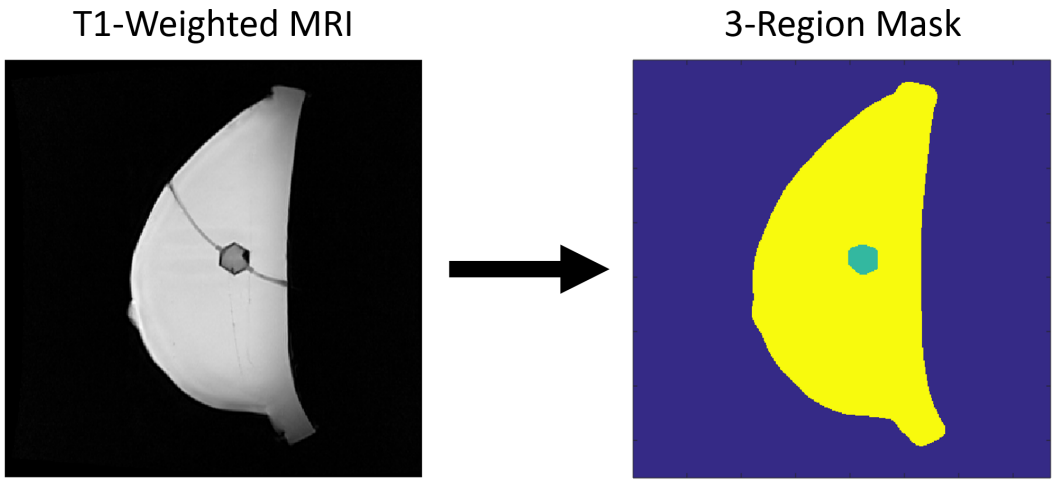

Figure 6.9: Phantom MRI and Segmented Mask. MR images are segmented using signal thresholds to define distinct regions in the tissue. Here a tissue-like, multi-modality gelatin phantom containing a liquid target (see Section 6.4.1) was imaged with a T1-weighted MR sequence. The three regions with distinct signals, *i.e*, the liquid target, the gelatin phantom, and the background region, were then segmented into a mask using signal thresholds to determine the region boundaries. The three-region mask is then ready for use as a hard- or soft-prior constraint.

Once the MRI has been segmented into distinct regions, these regions can be used to constrain the DOT reconstruction using the MRI as either a hard prior or a soft prior. Section 2.6.7 contains more information about these two types of constraints.

6.4 Phantom Image Tests

Initial tests of the imaging capability of this joint DOT-MRI system were conducted using a tissue-like phantom with both magnetic and optical absorption contrast. This phantom provided a test for the DOT acquisition sequence, data processing, and image reconstruction techniques in a controlled environment with known optical properties.

6.4.1 Phantom Construction and Characteristics

Most diffuse optics phantom experiments utilize liquid phantoms comprised of water, ink (for absorption contrast), and Intralipid (for scattering). This is not an ideal solution for experiments performed in the MR suite because liquid phantoms expose expensive MRI equipment to potential

damaging spills. Thus, a gelatin phantom was created for this purpose.

First, a mold was designed and 3D-printed using a segmented MRI to mimic the approximate shape of a breast. A porcine gelatin powder (Sigma-Aldrich, St. Louis, MO) was mixed with water, India Ink (Higgins, Leeds, MA), a 20 % Intralipid soy emulsion (Fresenius Kabi Global - Bad Homburg, Germany), and a Gd-chelate magnetic contrast agent (MultiHance - Bracco Diagnostics, Milan, Italy). Air bubbles were removed from the gelatin mixture using a vacuum pump prior to the gelatin setting to prevent non-diffusive regions from forming in the phantom. A hollow target, 16 mm in diameter with 1 mm thick Delrin walls, was suspended approximately in the center of the gelatin mold prior to the pouring of the gelatin. This target was connected to thin nylon tubing with both ends of the tubing terminating outside of the gelatin phantom (see Figure 6.10), which enabled the injection of small amounts of liquid with different magnetic and absorption properties into the target for varying levels of contrast with the background phantom.

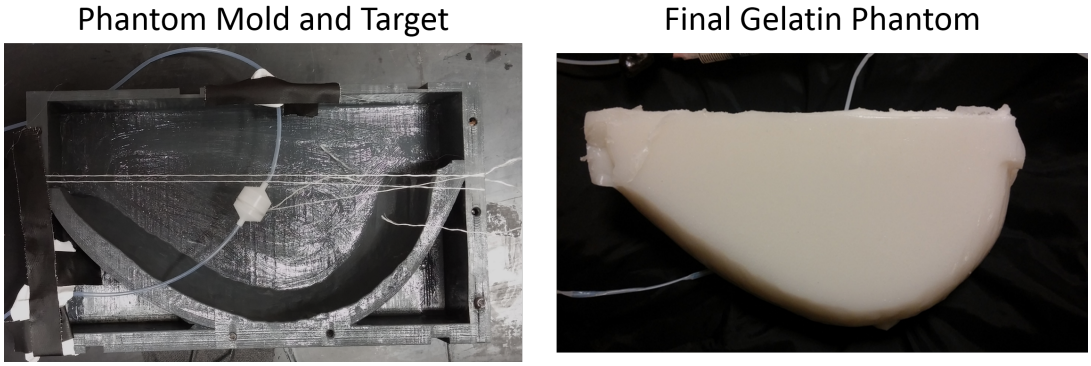

Figure 6.10: Gelatin Phantom and Mold. Left: One half of the breast-shaped gelatin phantom mold with target prior to pouring of the gelatin mixture. Note that the target is held in place by thin, white string which does not significantly change the optical properties of the phantom. Right: Final gelatin phantom. Different liquid phantom materials can be injected, via the nylon tubing, into the target within the gelatin.

In this experiment, the background gelatin, Gd ink and Intralipid solution had optical properties of $\mu_a = 0.05\,cm^{-1}$ and $\mu_s' = 8\,cm^{-1}$ at $785\,nm$. Additional India Ink was added to the target India Ink and Intralipid solution to create a 4:1 optical contrast in μ_a. The background phantom also contained $0.5\,mM$ MultiHance Gd-chelate to create an MR contrast relative to the target, which did not contain the Gd-contrast agent. A reference phantom could be created for the difference measurement by injecting a liquid phantom with the same optical and magnetic properties as the gelatin into the target.

	μ_a at 785 nm $[cm^{-1}]$		
	Avg. Background	Max. Target	Contrast
Expected	0.05	0.20	4 : 1
Time-Domain	0.053	–	–
Unconstrained	0.06	0.14	2.3 : 1
Hard-Prior	0.051	0.095	1.9 : 1
Soft-Prior	0.055	0.15	2.7 : 1

Table 6.1: DOT-MRI Reconstructed Optical Properties. Expected and reconstructed μ_a values for the unconstrained, hard-prior, and soft-prior reconstructions, as well as the bulk absolute measurement with the time-domain system, in both the background and target regions. Note that the reconstructed contrast is unlikely to ever fully reach the expected 4 : 1 value, which represents the ratio of target to background μ_a, due to the broadening of the reconstructed target (see Section 6.5). Thus, unconstrained and soft-prior reconstructions both demonstrate reasonably good contrast.

6.4.2 MR and Optical Imaging

A T1-weighted fat-suppressed gradient echo MRI pulse sequence was run to provide MR images with good contrast between the target and background phantom (see Figure 6.11A). Optical data was collected using all available wavelengths at all source positions for the CW measurement and all available wavelengths at four spatially dispersed source positions for the TD measurement (see Section 6.2 for details). Because the phantom optical properties were known precisely only at 785 nm, the single wavelength reconstruction of only the 785 nm data is presented here. Note that the absolute optical properties measured at 780 nm with the TD system were assumed to be approximately equivalent to the optical properties at 785 nm, which is a very reasonable assumption. The slight offsets between the CW and TD laser wavelengths only present an issue for single-wavelength reconstructions; multi-spectral reconstructions for both the TD and CW data would rely on wavelength-independent chromophore concentrations. Here, the fitted time domain data resulted in absolute bulk optical properties of $\mu_a = 0.053\,cm^{-1}$ and $\mu_s' = 7.6\,cm^{-1}$, which are within 6 % and 5 %, respectively, of the expected background values.

DOT images were reconstructed using the TOAST++ software suite [227]. A Gauss-Newton method for the optical property update (see Section 2.6.6) and total variation (TV) regularization (see Section 2.6.5) were used. Figure 6.11B contains an unconstrained DOT reconstruction from this data. Thus, this image was created with no *a priori* information from the MRI. Note that this reconstruction provides relatively good quantitative contrast between the target and background (see Table 6.1); however, there are also image artifacts of comparable contrast near the phantom boundary and the source and detector planes.

A priori information from the segmented MRI was used in attempt to suppress these artifacts

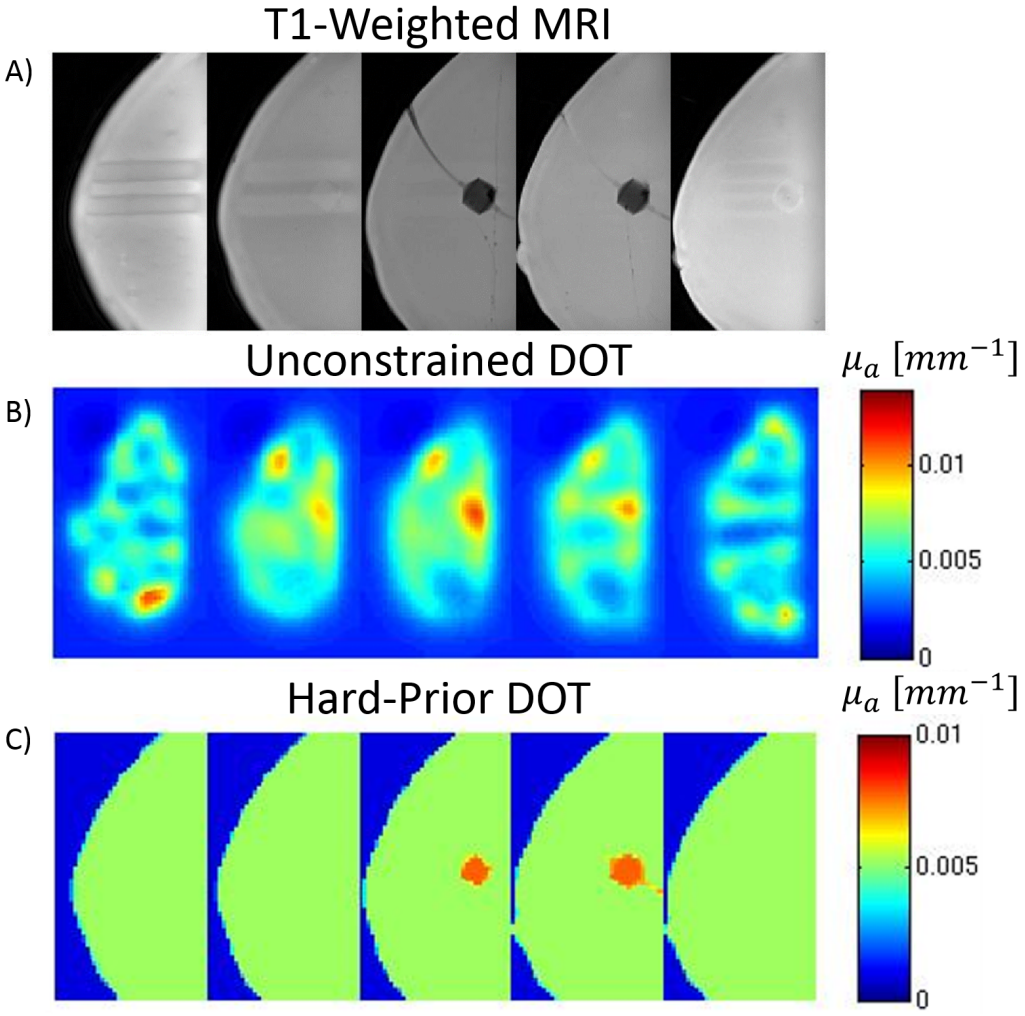

Figure 6.11: Unconstrained and Hard-Prior DOT Reconstructions. A) Sagittal slices, separated by $1\,cm$, of a T1-weighted fat-suppressed gradient echo MRI of the gelatin phantom and target. Note that the horizontal lines on the first (source-side) and last (detector-side) slices are indentations in the phantom from the optical modules. B) Sagittal slices of an unconstrained DOT reconstruction. The DOT reconstruction accurately localizes the target and provides good absorption contrast relative to the background. However, there are numerous boundary artifacts with reconstructed μ_a values similar to the target's. C) Sagittal slices of a DOT reconstruction constrained by a hard spatial prior. Although the artifacts are removed by the hard-prior constraint, the contrast here is also reduced. This is likely due to inaccuracy in the co-registration of the segmented MR image.

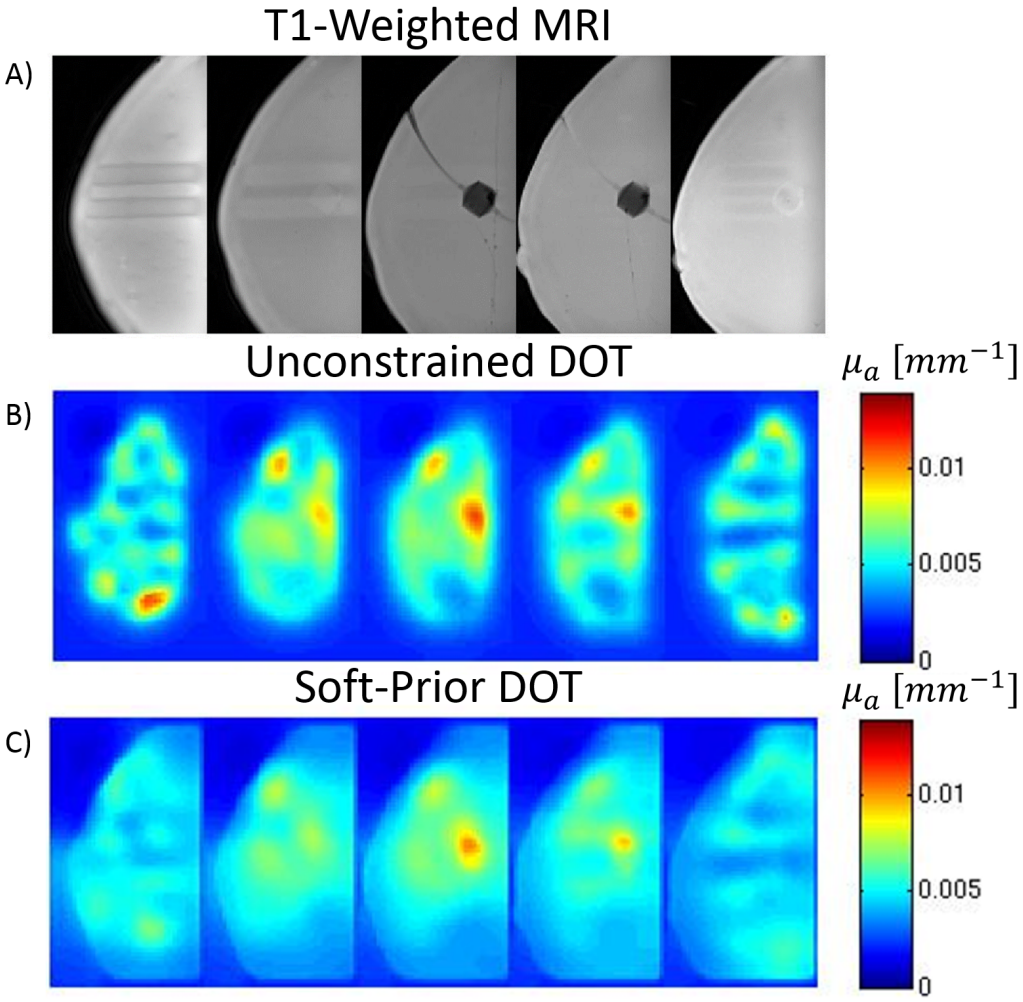

Figure 6.12: Unconstrained and Soft-Prior DOT Reconstructions. A) Sagittal slices, separated by $1\,cm$, of a T1-weighted fat-suppressed gradient echo MRI of the gelatin phantom and target. Note that the horizontal lines on the first (source-side) and last (detector-side) slices are indentations in the phantom from the optical modules. B) Sagittal slices of an unconstrained DOT reconstruction. The DOT reconstruction accurately localizes the target and provides good absorption contrast relative to the background. However, there are numerous boundary artifacts with reconstructed μ_a values similar to the target's. C) Sagittal slices of a DOT reconstruction constrained by a soft spatial prior. Note the slightly improved contrast and significantly reduced artifacts relative to the unconstrained reconstruction.

and improve contrast. A hard-prior constraint was placed on the DOT reconstruction, enforcing homogeneous optical property updates within both the target and background regions (see Figure 6.11C). Though this technique eliminates the artifacts, by definition, the contrast between the target and background is unexpectedly low. This is likely due to an inaccuracy in the coordinate system co-registration and thus imperfect spatial designations for the two regions. To overcome this flaw, soft-prior constraint was also utilized. Here, a first-order Tikhonov regularization scheme (see Section 2.6.5) was used with a regularization parameter that increased with increasing distance away background-target boundary. Figure 6.12C displays this soft-prior reconstruction. The boundary artifacts present in the unconstrained reconstruction are now gone, and the contrast between the target and background has slightly increased.

6.5 Discussion

6.5.1 DOT Reconstruction Validation

The images reconstructed from a breast-shaped, gelatin phantom in Section 6.4.2 provide a validation of the ability of the DOT-MRI platform to provide high spatial resolution, three-dimensional images of the absorption coefficient and demonstrate the utility of using MR images as spatial priors. First, the time-domain system produced accurate quantification of the average absolute absorption and reduced scattering coefficients with errors of only 6 % and 5 %, respectively. The unconstrained CW reconstruction (see Figure 6.11), which was performed with no input from the MR image, reconstructed a target with reasonably good contrast (2.3 : 1 vs an expected contrast of 4 : 1) at the appropriate location in three-dimensions. This is evidence that the high-spatial density DOT system provides quality reconstructions without *a priori* information. Note that reconstructed images are expected to have lower maximum contrast than the actual physical contrast due to the partial volume effect and spatial broadening of the target, which spreads the total contrast over a larger volume [195; 25]. Despite the quality localization, there were, however, artifacts in the absorption reconstruction near the boundaries, which would complicate the imaging of heterogeneous breast tissue.

To address these artifacts, *a priori* structural information from the MRI was used. A hard-prior reconstruction, whereby the background and target regions determined by the segmented MRI are forced to update homogeneously, unexpectedly provided worse contrast than the unconstrained reconstruction (1.9 : 1). This is likely due to inaccuracy of the co-registration of the optical and MRI coordinate systems. Hard-prior reconstructions are particularly sensitive to this offset [41; 88]. To mitigate this source of error in future measurements, more well-defined fiducial markers in precisely

measured locations have been added. The soft-prior constraint reconstruction provided the best overall image quality for this phantom, with the highest target-to-background contrast (2.7 : 1) and the elimination of the boundary artifacts found in the unconstrained reconstruction.

In future human subject imaging, all three types of reconstruction (unconstrained, hard-prior, and soft-prior) could be used. The unconstrained image is most useful for directly validating DOT as an imaging technology against gold-standard MRIs. Although the hard-prior is the most commonly used constraint, soft-prior reconstructions may be more beneficial in this study. Chapter 3 demonstrated the benefits of incorporating information about the normal tissue heterogeneity, via a standard deviation, in predicting response to chemotherapy. This information is accessible from a soft-prior reconstruction but suppressed by a hard-prior constraint. Additionally, in Chapter 3, $1\,cm$ margins around both the tumor and areola were excluded from the data to avoid contamination due to the partial volume effect. This technique is also not feasible with the hard-prior reconstruction unless more regions are defined, which would increase possible sources of error in the over-determined reconstruction.

6.5.2 Instrument Advances and Applications

The primary advances associated with the joint imaging system presented in this thesis are the high-spatial density optical information, absolute optical property quantification via the TD system, compatibility with a clinical RF coil, and the inclusion of DCS fibers for measurement of blood flow. These instrument characteristics help to address some of the most interesting applications of DOT in breast cancer.

The improved reconstruction quality over DOT-MRI systems with fewer source and detector positions, and those with only relative optical property calculation, can enhance both the localization and quantification of tumor optical and physiological properties. This could enable improved differentiation between malignant and healthy tissue (as in Chapter 5) or improved characterization of tumors for prediction of response to chemotherapy (as in Chapter 3). The spatial information provided by the MRI will also improve the identification of tumor and normal tissue regions.

The use of the clinical coil itself is of great benefit; it provides higher-quality MRI and a more comfortable patient experience than a custom-built RF coil. Patient comfort is very important, not only for the increased ability to recruit study subjects, but also because of the reduction in motion artifacts associated with a comfortable resting position. The modular design of the optical interface with the RF coil also enables optimization of the source and detector locations, individually optimizing coverage of each tumor and enabling subjects with unusually positioned tumors to be enrolled in trials.

This clinical coil also enables the use of more advanced DCE-MRI techniques, such as K-space weighted image contrast (KWIC), which relies on fast, compressed-sensing pulse sequences and imparts information about tumor perfusion [237; 238; 92]. These techniques, along with the 20 DCS source fibers and 20 DCS detector fibers, provide two methods of obtaining three-dimensional maps of blood flow with precise structural knowledge. The benefits of this are three-fold. First, the blood flow information could be used as a predictor of response to chemotherapy as in Chapter 4. Second, the flow information could be combined with tissue oxygen saturation to explore three-dimensional oxygen metabolism maps. Finally, the DCT and KWIC DCE-MRI perfusion markers could be compared to provide a more complete picture of flow in the tumor vasculature. KWIC techniques are sensitive to uptake and washout and are thus dependent on the permeability of the blood vessels whereas the DCS BFI is a more direct measure of flow. This information could be complementary, especially in untangling the effects of chemotherapy on the vasculature, as discussed in Section 3.4.1.

6.5.3 Future Improvements

During this instrument's initial testing phase, it became apparent that several minor improvements were needed. The first, which has already been completed, is the incorporation of more precise fiducial markers to improve the co-registration between the optical and MRI coordinate systems. The new fiducial makers are thin tubes, three of which are attached to each optical module in orthogonal orientations to ensure accurate localization in all three dimensions. A second instrumental shortcoming is the lack of sensitivity of the PMT detectors to the $905\,nm$ pulsed laser, which reduces the number of available TD wavelengths and inhibits the system's ability to accurately reconstruct water concentration. This limitation could be ameliorated by complementing the current PMTs with newer, custom-built PMT modules [244] that are more sensitive to infrared light. The final significant instrument deficiency was an aspect of the control software. The system is currently designed to capture frames from the CCD with a single exposure time across all wavelengths. Because the various CW lasers have different powers, and because tissue absorbs some wavelengths more than others, an optimal exposure time for one wavelength could result in saturation or low signal for another wavelength. In the current setup, this flaw can be overcome by manually changing the exposure time for each wavelength in the series; however, this is a time-consuming process which can't feasibly be done during a patient measurement. Thus, it would be beneficial to automate this procedure by incorporating an exposure-time optimization scheme. An algorithm to accomplish this goal has been designed and is currently being tested for the instrument.

6.6 Conclusion

A joint DOT-MRI platform for simultaneous clinical MRI and hybrid continuous wave (CW) and time domain (TD) optical imaging has been presented. This system has 64 source fiber positions, 108 CW detector fiber positions, and 8 TD detector positions, with 5 CW and 6 TD laser sources at wavelengths ranging from 670 nm to 915 nm. The instrument has modular optical interfaces that can be used in 1.5T or 3T clinical MR suites; these optical interfaces also contain 20 DCS source fibers and 20 single-mode DCS detector fibers for potential incorporation of diffuse correlation tomography (DCT).

The DOT reconstruction algorithm has been validated using a breast-shaped gelatin phantom with a liquid target. Unconstrained, soft-prior constrained, and hard-prior constrained images were produced, which demonstrated the ability of the system to accurately locate lesions and provide reasonable levels of target-to-background contrast. The soft-prior constrained image, in particular, provided a quality reconstruction with high contrast and limited artifacts.

This system will be used in the clinic to more accurately quantify tumor and healthy tissue for diagnosis of malignant lesions, prediction of response to neoadjuvant chemotherapy, and exploration of blood flow and oxygen metabolism in breast cancer. Thus, this system provides an excellent opportunity to improve the accuracy of diffuse optical measurements and explore the development of new multi-modal flow and oxygenation biomarkers that could illuminate tumor physiology.

Chapter 7

Optimization of DOT Reconstruction Algorithm

7.1 Introduction

As discussed in Section 2.6, diffuse optical tomography (DOT) can be performed with a wide variety of initial conditions, normalization methods, update algorithms, spatial constraints, and regularization techniques. Optimizing these procedures can improve tumor contrast and spatial localization, reduce cross-talk between reconstructed parameters, and alleviate the prevalence of image artifacts. All of these reconstruction improvements are important for the accurate measurement of tumor and normal region tissue properties that is needed for the diagnostic and prognostic imaging tests in Chapters 3, 4, and 5.

In this chapter, different reconstruction techniques are considered and compared for data collected by a spatially dense, frequency domain (FD) DOT breast cancer imaging system developed at the University of Pennsylvania [25]. Different update algorithms were tested, but a conjugate gradient scheme (see Section 2.6.6) was used for all final images. Both first-order Tikhonov (TK1) and total variation (TV) regularization techniques were explored. In addition, a range of regularization hyperparameters were examined to balance the image smoothness versus the ability to accurately update the tissue properties (Section 2.6.5). A standard-deviation weighting method for the difference data was developed and employed to weight source-detector pairs, thereby limiting the detrimental effects of noisy measurements on the reconstruction. Finally, the minimum number of source positions required to produce high quality images was investigated.

The resulting improvements in image quality due to the optimization of some of these conditions

were discussed in a previous publication that described this FD-DOT system [25]. Here, the focus of the discussion will be on development of the optimal reconstruction algorithms. Both phantom and human subject data will be presented to demonstrate the value of these algorithmic advances.

7.2 FD-DOT Instrument and Experiments

7.2.1 FD-DOT Instrument

The frequency domain (FD) DOT instrument used here has been described in detail in another publication [25]. Briefly, five laser sources ($660\,nm$, $690\,nm$, $785\,nm$, $808\,nm$, $830\,nm$) are amplitude-modulated at $70\,MHz$ by a frequency generator and coupled to a galvonometer source position switch that is fiber-coupled to an 11×19 grid of 209 source positions with $8\,mm$ separation between successive points. Several reference channels are used to normalized amplitude fluctuations and phase drift in the signal. A gain-modulated image intensifier is modulated at $70MHz + 1Hz$ to enable heterodyne detection at $1Hz$ with a CCD. An optical profilometry system utilized spatially modulated light to determine the exact breast boundary for use as a spatial prior. A schematic can be found in Figure 7.1.

In this DOT system, the patient lies prone on a biopsy table with her breast resting in an Intralipid bath. This Intralipid prevents light outside of the tissue from saturating the CCD and maximizes the usable dynamic range of the system. Subjects can be imaged in either the sagittal or axial geometries due to the two examination beds connected to the system. Figure 7.2 contains a photograph of the instrument. This DOT imaging platform is currently installed at the Hospital of the University of Pennsylvania.

During data acquisition, each source position is illuminated sequentially by light at a single wavelength. Seventeen frames are acquired by the CCD at each source position over a 2 second period. Virtual detectors are then assigned at different positions on the CCD imaging surface, similar to the detector grid in the DOT-MRI instrument in Section 6.3.3. The resulting sinusoidal profile for each detector can be fit for the amplitude and phase offset. These two parameters are then used for the frequency domain reconstruction of absolute absorption coefficient, or, in the multi-spectral framework, chromophore concentrations, and reduced scattering coefficient. Figure 7.3 contains a sample CCD image and sinusoidal profile of the diffusive wave.

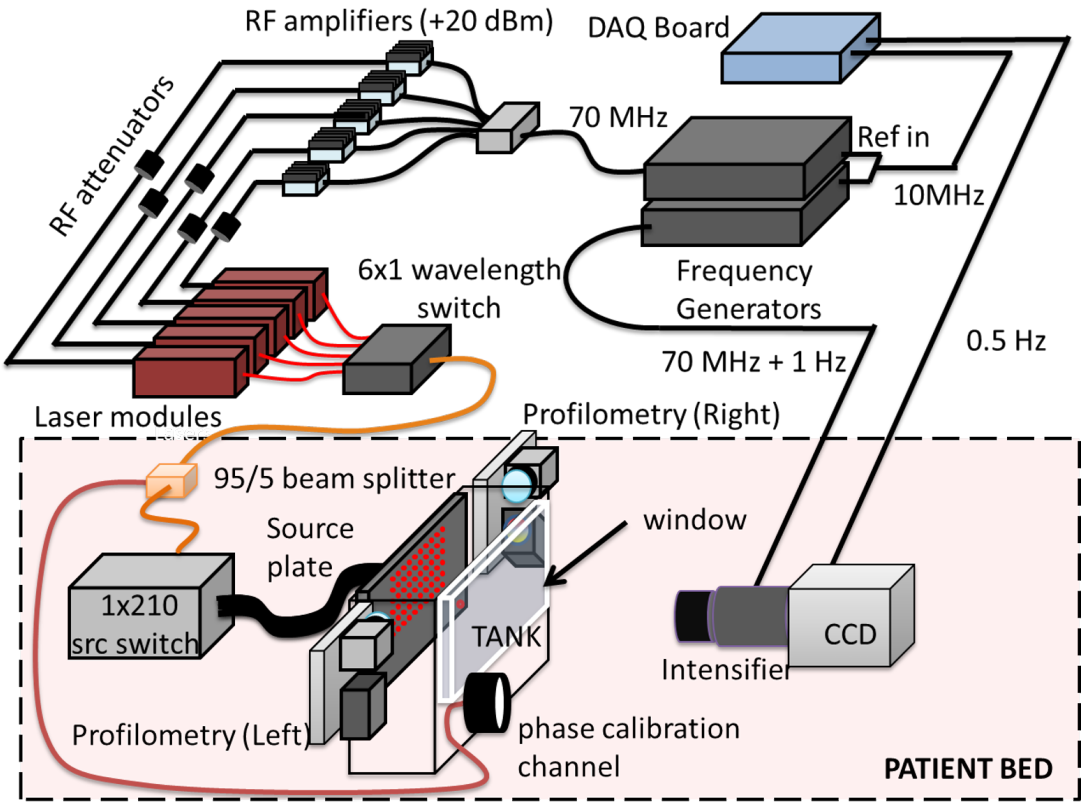

Figure 7.1: Schematic of FD-DOT Imaging System. This frequency domain DOT imaging system utilizes $70\,MHz$ modulated laser sources at five wavelengths ($660\,nm$, $690\,nm$, $785\,nm$, $808\,nm$, $830\,nm$), directed by a galvonometer optical switch to a grid of 209 source positions. Two reference channels for signal normalization are also used. Heterodyne detection is accomplished via a gain-modulated image intensifier and CCD. An optical profilometry system is also incorporated to determine the boundary between the breast tissue and the surrounding Intralipid bath. This schematic can also be found in [25].

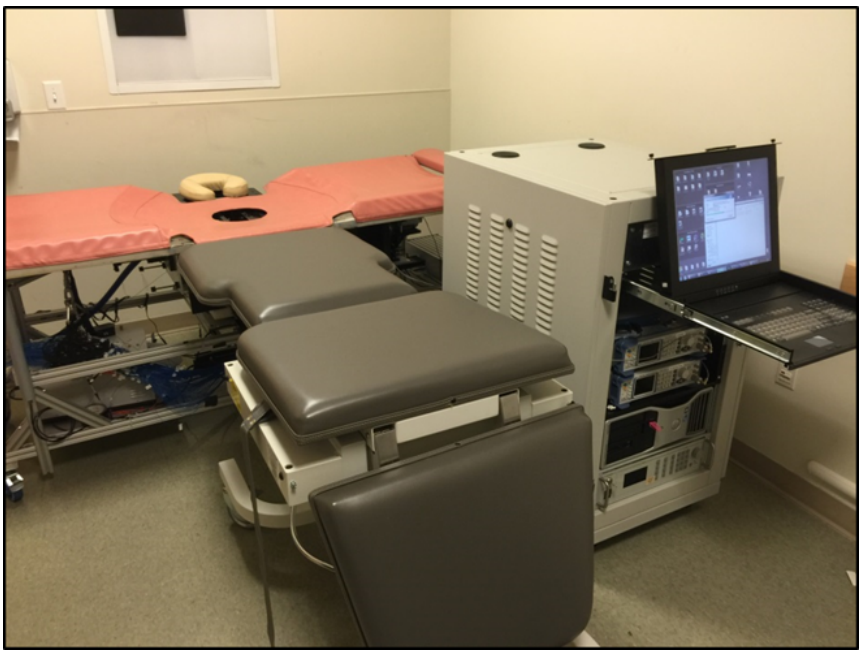

Figure 7.2: FD-DOT System in the Clinic. This instrument is installed in the clinic at the Hospital of the University of Pennsylvania. The instrument rack on the right contains the laser sources and instrument control components. The pink biopsy bed contains the imaging tank, as well as the source fibers and detection instrumentation. Axial imaging is performed with the subject lying on the pink bed. Sagittal imaging can also be performed using the grey examination bed. A similar figure appears in [25].

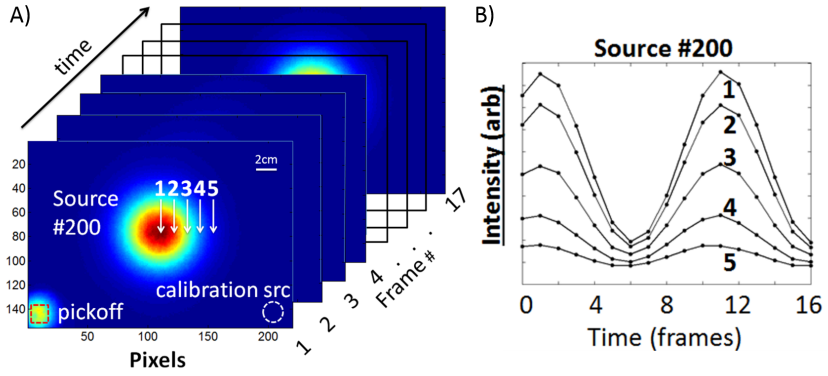

Figure 7.3: Sample Data Acquisition for FD-DOT System. A) Sample CCD images for a single source position. Note that 17 frames are taken to capture the sinusoidal oscillation of the frequency-domain signal. On this plot, five different detector positions, arbitrarily labeled $1-5$ are shown, in addition to the pickoff and calibration channel positions, which are used for data normalization. B) Intensity plot for five different detectors of varying distance from the source position. Note that the amplitudes of the sine curves decrease and the phase shifts change as the detector moves farther from the source.

7.2.2 Phantom Experiment

The phantom experiments presented here involved three targets similar to the one described in Section 6.4.1. The targets were connected to nylon tubing that could be used to easily change the contrast level in each target, and then placed in a liquid Intralipid phantom with optical properties of $\mu_a = 0.05\,cm^{-1}$ and $\mu_s' = 8\,cm^{-1}$ at a wavelength of $785\,nm$. The absorption contrast in the phantom was provided by two inks with different spectral properties: Nigrosin (Sigma-Aldrich, St. Louis, MO) and IR-806 (Sigma-Aldrich, St. Louis, MO). These inks play the roles of different tissue chromophores whose concentrations would be reconstructed in a patient measurement. One target was filled with a liquid with a 2× contrast in the scattering and no absorption contrast relative to the background. Another target was filled with either 2×, 3×, or 6× concentration of Nigrosin relative to the background, and the third target was filled with 2×, 3×, or 6× the concentration of IR-806. Figure 7.4 contains a schematic of this phantom and the absorption spectra of the two chromophores.

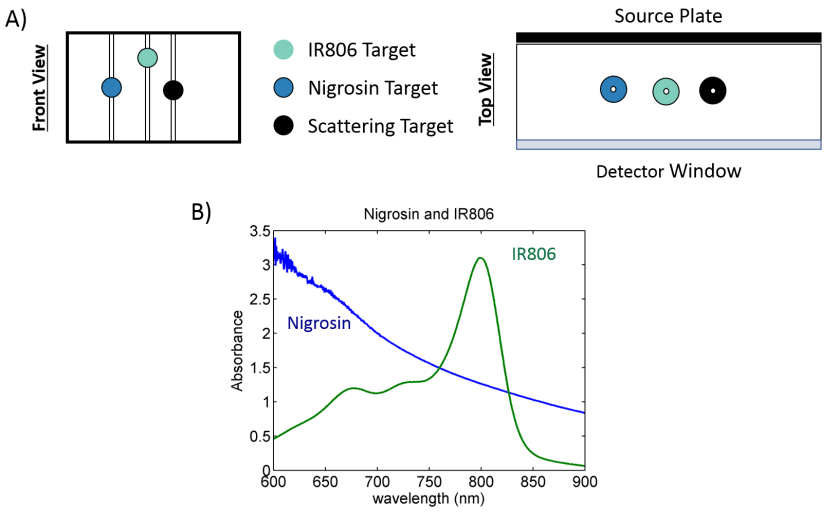

Figure 7.4: FD-DOT 3-Target Phantom Experiment Schematic. A) Schematic of the three targets: Nigrosin concentration contrast, IR-806 concentration contrast, and scattering contrast. Note that the scattering target always has a μ_s' that is 2× the background while the two ink targets can have concentration contrasts of 2×, 3×, or 6×. B) Absorption spectra of Nigrosin and IR-806 inks. Note that these two chromophores behave similarly to the oxy- and deoxy-hemoglobin extinction coefficients in this wavelength range. Thus, distinguishing between these two inks is a reliable indicator of the system's ability to quantitatively separate HbO_2 and HHb concentrations.

This phantom experiment was a useful tool for the characterization and optimization of the FD-DOT instrument, including the system's ability to differentiate absorption contrast from scattering

contrast, to differentiate two spectrally different absorption chromophores, to spatially localize the target contrast, and to do so with quantitative accuracy and limited image artifacts.

7.2.3 Human Subject Imaging

Several cancer patients have also been imaged with this FD-DOT system. All subjects were consented and enrolled under a research protocol approved by the IRB at the University of Pennsylvania. The one subject whose reconstructions are presented here was a 79 year old with a biopsy-confirmed invasive mammary carcinoma, *i.e.*, the carcinoma had both ductal and lobular features, of $1.8\,cm$ along the largest dimension. The subject was also non-concurrently imaged with a standard DCE-MRI sequence, which is used only for comparison.

7.2.4 Reconstruction Methods

All images presented here are multi-spectral, non-linear reconstructions using the TOAST++ software suite developed at University College London [227]. Although multiple parameter update procedures were tested, a conjugate gradient approach was primarily used (see Section 2.6.6).

The most significant aspect of the reconstruction optimization was the determination of the best regularization technique and regularization hyperparameter. Both first-order Tikhonov (TK1) and total variation (TV) techniques were tested (see Section 2.6.5). Because scattering and absorption features can update at different rates for different imaging systems, the scattering and chromophore concentration parameters were not necessarily constrained by the same regularization methods. Different techniques and different hyperparameters were tested across the two properties. The L-curve method was also used for optimization of the hyperparameter (see Figure 2.11).

A heterogeneous weight vector $\vec{\sigma}$ was also used in the χ^2 term of the objective function (see Equation 2.140) to account for varying levels of noise for different source-detector separations. This vector $\vec{\sigma}$ was calculated by binning all measurements by source-detector separation $|\vec{r}| = \sqrt{z^2 + \rho^2}$ into $1\,mm$ bins, calculating the standard deviation across all measurements in a given bin, and dividing this standard deviation by the mean of all measurements in that bin. Because the tissue or phantom volumes are assumed to have only a small perturbation from a homogeneous medium, all measured intensities at a given source-detector separation should be approximately the same. Thus, the normalized standard deviation of these ring-shaped bins are an approximate measurement of the experimental noise, with longer source-detector separations generally having larger normalized standard deviations. This decreases the weighting factor for large source-detector separation measurements, *i.e.*, where the source and detector positions are off-axis. Note that, for these reconstructions, no source-detector separations longer than $90\,mm$ were used due to the noise

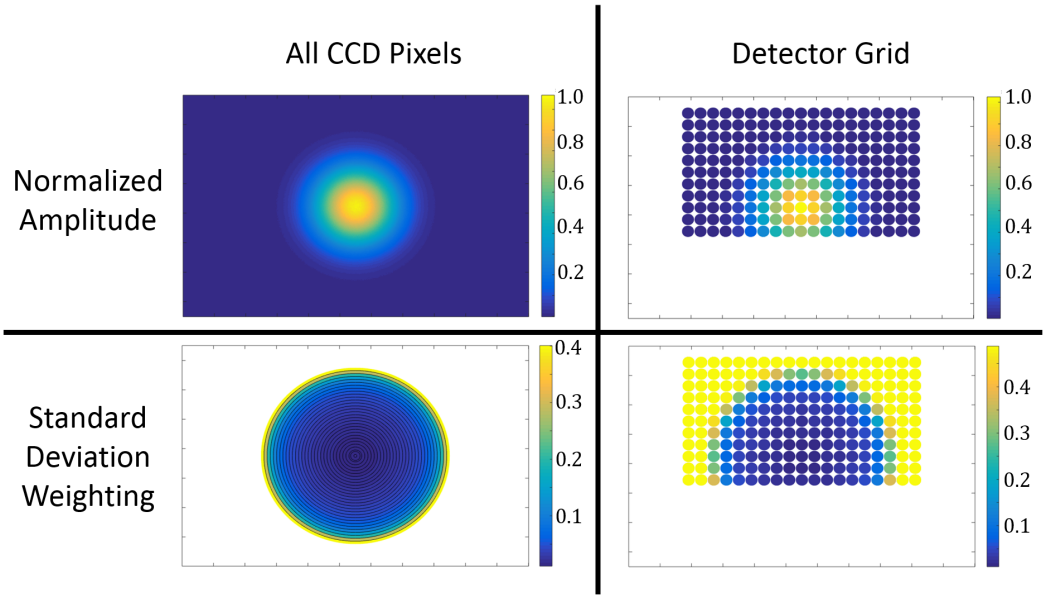

Figure 7.5: FD-DOT Detector and Standard Deviation Weighting Schematic. Top Left: Example CCD frame measuring intensity at the detector plane due to light at a single source position. Top Right: Example of assigned detector positions on CCD imaging plane. In this case, 209 detectors directly across from the source fibers are defined with the signal summed over a diameter of 8 mm. Bottom Left: Standard deviation calculation example. Because, in a homogeneous medium, the intensity decreases symmetrically with respect to the cylindrical angle φ, all measured intensities at a given position ρ relative to the source position should be constant. Thus, variation across these points can be thought of as noise. Here, 2 mm thick, ring-shaped bins along the ρ dimension are chosen, and the standard deviation is calculated for all data in each ring and divided by the mean of the data in that ring. Bottom Right: The calculated standard deviations are assigned to the given detector positions. These standard deviation values are then used to weight the χ^2 contributions for each source-detector pair (see Equation 2.140).

floor. Figure 7.5 contains an example of this standard deviation calculation for a single source position.

The final area of investigation is the number of source and detector positions used in the reconstruction. This instrument is the most spatially-dense fiber-coupled DOT instrument yet presented [25]; therefore, the marginal benefit of the additional source positions for image quality was undetermined. This effect is explored here. The number of source positions can be set by simply choosing which positions to illuminate in the data collection algorithm. The detector locations, though, can be chosen to be anywhere on the CCD imaging plane. For simplicity, the detectors identified on the CCD here are always directly across from the active source positions. Thus, if 60 source positions are used, there are also 60 detector positions.

Image reconstruction quality was assessed using a number of factors. First, the reconstructed target region was determined using a full-width-half-maximum contour around the maximum value of each reconstructed parameter. The contrast within that contour relative to the background was them summed and normalized by the expected total contrast between the target and background for the given parameter. This metric determines the degree to which the expected contrast is recovered. The total size of the reconstructed target, as determined by the number and size of the pixels within the contour, was divided by the expected target size to determine the degree to which the reconstructed target was broadened. Finally, the standard deviation of the reconstructed parameter in the background region outside the target contour, which is expected to be homogeneous, was calculated as a measure of image artifacts.

7.3 Results

7.3.1 Phantom Results - Regularization

Multi-spectral reconstructions using the five available wavelengths were performed for data taken with the FD-DOT system discussed in Section 7.2.1 at 209 source positions. L-curve optimization was used to determine the optimal τ hyperparameter for the regularization (see Figure 2.11). Here, the best regularization scheme used $\tau = 8 \times 10^{-4}$ and a total variation (TV) prior for the absorption coefficient and $\tau = 8 \times 10^{-3}$ and a first-order Tikhonov (TK1) prior for the reduced scattering coefficient (see the reconstructed image in Figure 7.6). This regularization scheme was chosen based on its ability to maximize reconstructed contrast and minimize the spatial broadening across all three targets. Table 7.1 provides a comparison of these parameters, along with the standard deviation of the background regions, which is a measure of the image artifacts and/or target cross-talk, across four different regularization methods. The "Split 1×" technique still employed TV

regularization for the absorption coefficient and TK1 regularization for the reduced scattering coefficient, but it used the same τ value for all parameters (see Figure 7.7). The other two methods used either total variation (TV 10×) or first-order Tikhonov (TK1 10×) with the $10 \times \tau$ offset between the absorption and scattering parameters (see Figures 7.8 and 7.9).

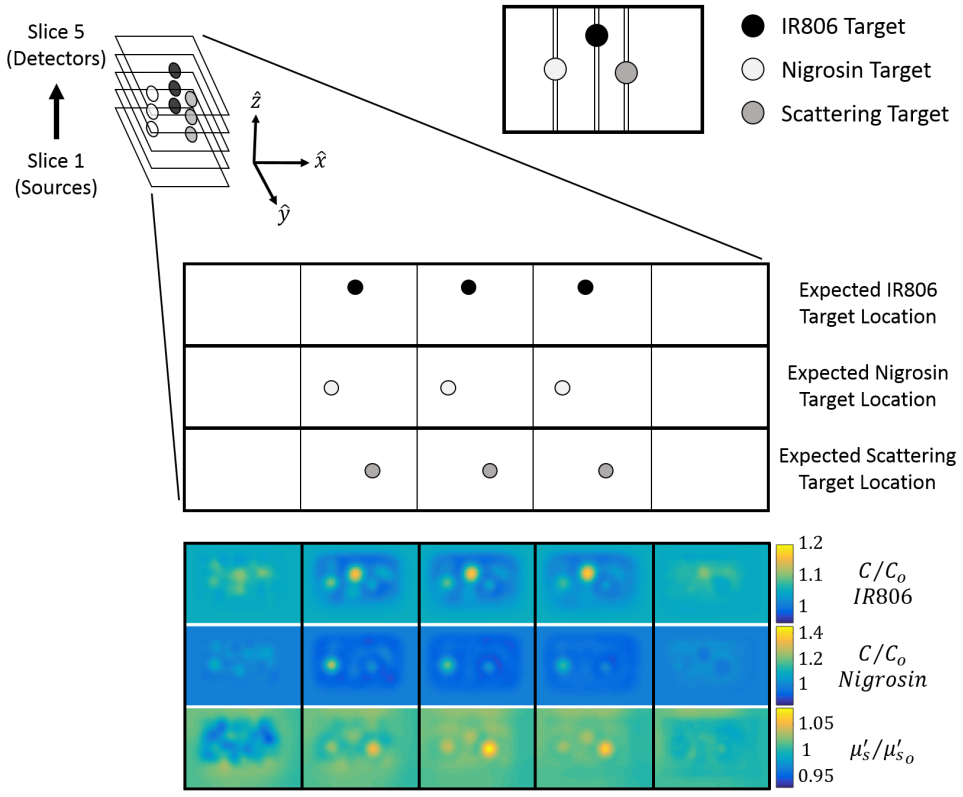

Figure 7.6: Phantom Schematic and Best Reconstructed Image. The phantom described in Figure 7.4 is used here. In these figures, each window represents a single sagittal slice of the reconstruction, and each slice is separated by 15 mm. Top: Schematic of Phantom with respect to Reconstructed Images. The top panel represents five sagittal slices of the IR806 concentration reconstruction, the middle panel is five slices of the Nigrosin reconstruction, and the bottom is the reduced scattering coefficient reconstruction. This schematic indicates the expected location of each of these targets. Bottom: Reconstructed image using the Split 10× method which was determined to be the optimal reconstruction method for this instrument. Note that C/C_o, here and in all other figures, is the reconstructed concentration C normalized by the expected background concentration C_o, and μ_{s_o}' is the expected background reduced scattering coefficient.

Once the optimal regularization method was determined, reconstructions were performed with a varying number of source positions and mirrored detector positions. Here, the series of reconstructions that were performed used $N_s = N_d = 10$, 20, 30, 40, 50, 60, 70, 80, 90, 100, 110, 120, 140,

	Split 10×	Split 1×	TV 10×	TK1 10×
IR806 Target				
Fraction of Expected Contrast	0.63	0.67	0.69	0.65
Fraction of Expected Target Size	2.94	3.21	3.19	3.71
Background Standard Deviation	0.01	0.01	0.01	0.01
Nigrosin Target				
Fraction of Expected Contrast	0.68	0.74	0.75	0.69
Fraction of Expected Target Size	4.28	5.17	4.93	6.62
Background Standard Deviation	0.02	0.02	0.02	0.02
Scattering Target				
Fraction of Expected Contrast	0.68	0.87	1.04	0.68
Fraction of Expected Target Size	1.67	1.29	1.22	1.67
Background Standard Deviation	0.01	0.03	0.05	0.01

Table 7.1: FD-DOT Phantom Regularization Comparison. Four different regularization schemes for the phantom reconstruction are shown here: 1) Split 10×: TV with $\tau = 8\times10^{-4}$ for absorption and TK1 with $\tau = 8\times10^{-3}$ for reduced scattering. 2) Split 1×: TV with $\tau = 8\times10^{-4}$ for absorption and TK1 with $\tau = 8\times10^{-4}$ for reduced scattering. 3) TV 10×: TV with $\tau = 8\times10^{-4}$ for absorption and TV with $\tau = 8\times10^{-3}$ for reduced scattering. 4) TK1 10×: TK1 with $\tau = 8\times10^{-4}$ for absorption and TK1 with $\tau = 8\times10^{-3}$ for reduced scattering. Note that the Split 10× method reconstructs approximately the same fraction of the expected contrast in all three targets. This method also minimizes the spatial broadening of all three targets, as seen by the Fraction of Expected Target Size. Most of this broadening occurs along the axis perpendicular to the source and detector planes, as expected [210; 193; 80; 25]. Finally, note that the standard deviation in the background regions, which is a measure of reconstruction artifacts, is only notably higher in the Split 1× and TV 10× scattering reconstructions. This can be seen clearly in Figures 7.7 and 7.8.

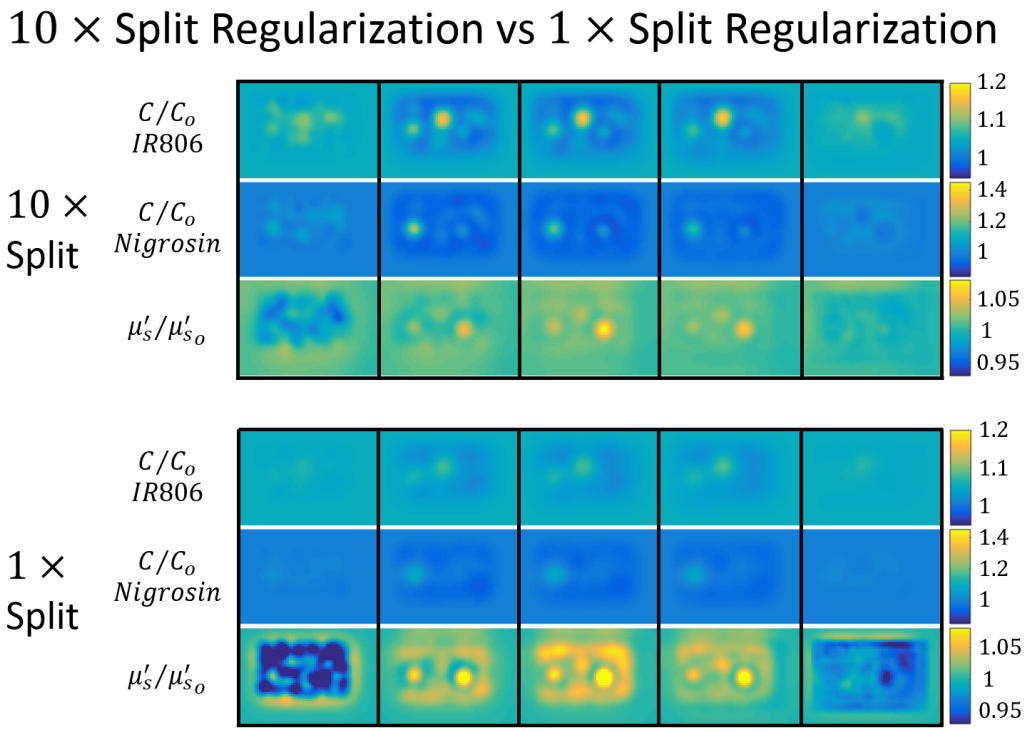

Figure 7.7: Phantom Reconstruction - Effect of Regularization Hyperparameter Offset. Top: Phantom reconstruction with Split 10× regularization algorithm. Bottom: Phantom reconstruction with Split 1× regularization algorithm. Thus, the only difference between these two reconstructions is that the reduced scattering coefficient τ is 8×10^{-3} for Split 10× and 8×10^{-4} for Split 1×. Note that Split 1× regularization leads to significant image artifacts in the scattering reconstruction and significantly reduced contrast for the chromophore absorption targets relative to the Split 10× reconstruction.

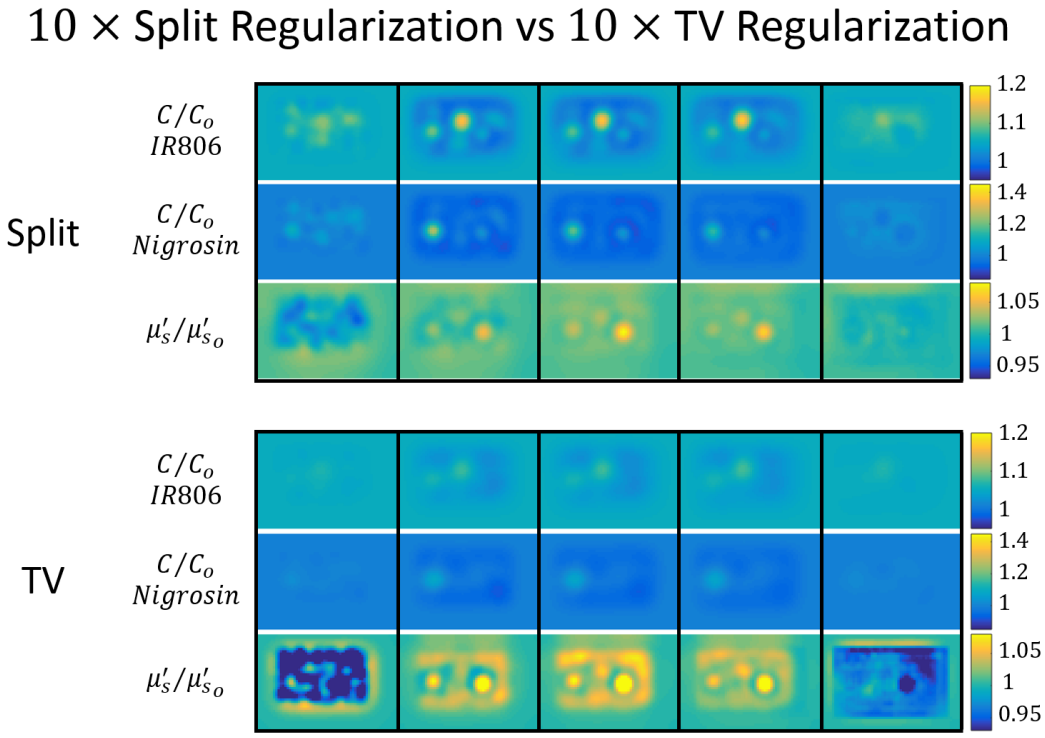

Figure 7.8: Phantom Reconstruction - Split versus Total Variation Regularization. Top: Phantom reconstruction with Split 10× regularization algorithm. Bottom: Phantom reconstruction with TV 10× regularization algorithm. Thus, the only difference between these two reconstructions is that the reduced scattering coefficient uses TK1 regularization for Split 10× and TV regularization for TV 10×. Note that TV 10× regularization leads to significant image artifacts in the scattering reconstruction and significantly reduced contrast for the chromophore absorption targets relative to the Split 10× reconstruction.

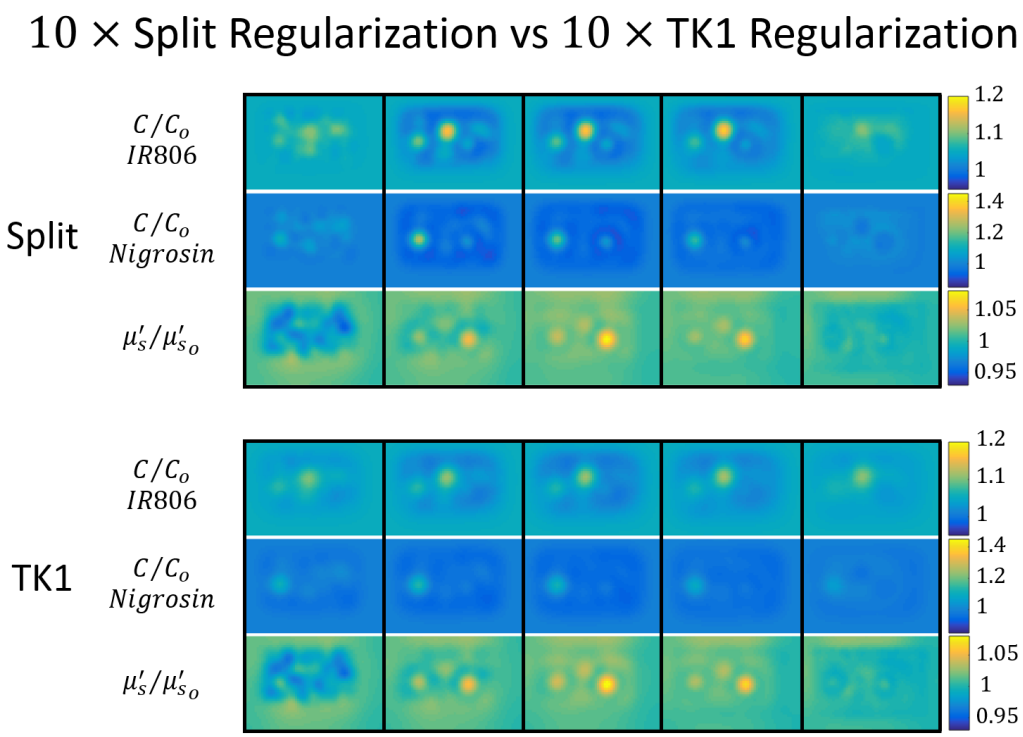

Figure 7.9: Phantom Reconstruction - Split versus First-Order Tikhonov Regularization. Top: Phantom reconstruction with Split 10× regularization algorithm. Bottom: Phantom reconstruction with TK1 10× regularization algorithm. Thus, the only difference between these two reconstructions is that the absorption coefficient uses TV regularization for Split 10× and TK1 regularization for TK1 10×. Note that the TK1 10× regularization scheme reconstructs the chromophore targets with significantly more spatial broadening than the Split 10× reconstruction (see Table 7.1).

160, 180, 200, and 209. Once $N_s > 80$, there was little improvement in either the reconstructed contrast or target size, and after $N_s > 100$, the results became consistent enough that further source positions were seemingly unnecessary (see Figure 7.10).

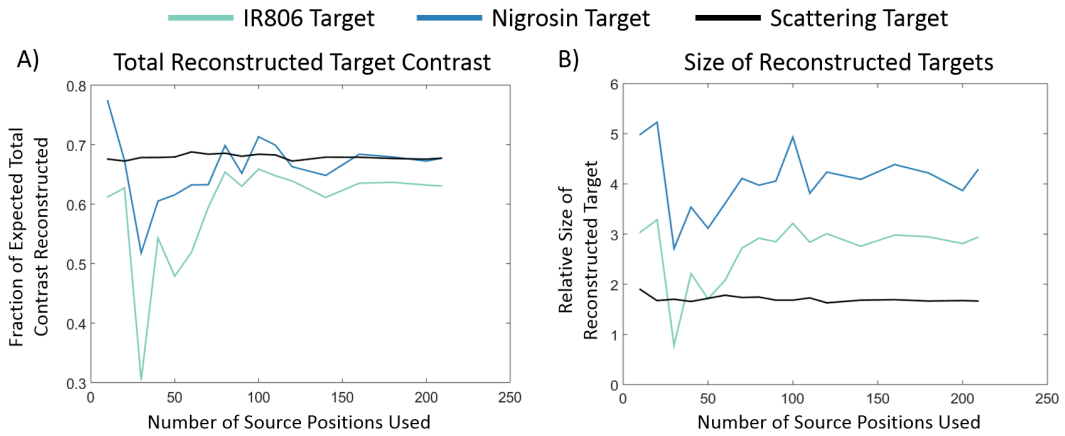

Figure 7.10: Reconstructed Contrast and Target Size versus Number of Source Positions. A) Fraction of Expected Target Contrast Reconstructed vs Number of Source Positions Used. Note that, except for $N_s = 10$ and $N_s = 20$ source positions, where the size of the reconstructed targets is very large, the reconstructed contrast increases for the chromophore targets through approximately $N_s = 80$. The scattering target is reconstructed consistently regardless of N_s. B) Size of Reconstructed Targets Relative to Actual Target Size. The reconstructed chromophore target size remains approximately constant after $N_s = 100$, and the scattering target reconstructs at the same size regardless of N_s. Note that a size of 1 would correspond to perfectly accurate reconstruction of the target size. The broadening seen here is expected [210; 193; 80] and occurs primarily along the transverse axis. The reconstructed scattering target size is significantly closer to the actual size, likely due to the increased sensitivity function for scattering with this instrument [25].

It was necessary to optimize the number and density of optode positions, as well as the regularization scheme, using phantom DOT measurements because phantoms provide more exact information about target contrast and size than human subjects. Thus, these phantom reconstructions enable an assessment of image quality that is inaccessible to human measurements. Since the instrumentation is constant and the imaging medium is very similar between phantoms and human subjects, these optimized parameters should be readily transferable to patient measurements.

7.3.2 Human Subject Results and Standard Deviation Weighting

The subject presented here is a 79-year-old female with a biopsy-confirmed invasive carcinoma of maximum size $18\,mm$ with both ductal and lobular features. As part of her routine clinical care, the subject received DCE-MR imaging prior to being measured with the FD-DOT instrument.

The patient consented to participate in this study under conditions approved by the University of Pennsylvania Institutional Review Board.

The optimal regularization scheme developed in phantom imaging, Split 10×, was used for the multi-spectral image reconstruction of the data collected from this subject. Figure 7.11 provides a subtraction MR image for comparison and contains reconstructions of the oxy- (HbO_2) and deoxy- (HHb) hemoglobin concentrations, as well the reduced scattering coefficient μ_s'. The MRI in Figure 7.11 is not a perfect comparison standard for the DOT reconstructions due to unaccounted-for differences in imaging geometry and breast compression; however, the DOT reconstruction displays significant contrast in HbO_2, HHb, and μ_s' in the approximate expected tumor location, with reasonable physiological values.

The benefits of including source-detector pair weighting based on the source-detector separation, as was discussed in Section 7.2.4, can also be seen in this example patient. Reconstructions with and without this normalization technique are included in Figure 7.11.

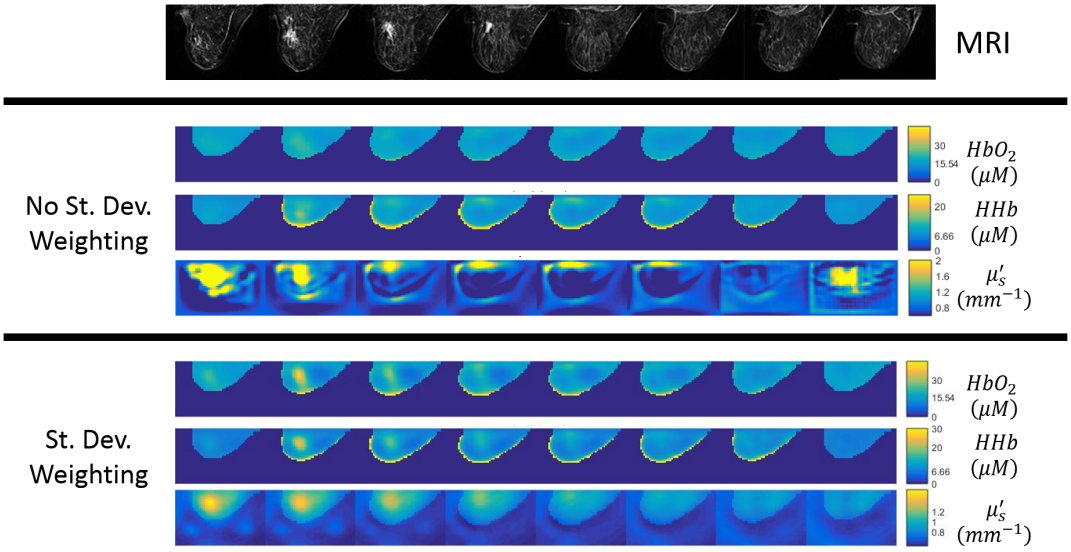

Figure 7.11: Human Subject Reconstruction - Effect of Standard Deviation Weighting. Top: Sagittal slices of a gadolinium-enhanced DCE-MRI subtraction image of an invasive mammary carcinoma. Each slice is separated by approximately 8 mm. Middle: Sagittal slices of a FD-DOT image reconstruction of HbO_2, HHb, and μ_s' without standard-deviation weighting by source-detector separation. Each slice is separated by $\sim 8.5\,mm$. Note that there are significant image artifacts in the μ_s' reconstruction and very low contrast in the HbO_2 and HHb reconstructions. Bottom: Sagittal slices of a FD-DOT image reconstruction of HbO_2, HHb, and μ_s' with standard-deviation weighting by source-detector separation. Note the significant reduction in image artifact and improved contrast in all three reconstructions. Note also that the location of the apparent tumor reconstruction in the DOT images corresponds very well to the tumor location in the DCE-MR images.

7.4 Discussion

Optimization of the DOT reconstruction parameters and techniques for this frequency-domain instrument is an important step in translating this technology from the bench-top to the clinic. Additionally, the lessons learned from the exploration of different regularization and normalization techniques, as well as the marginal benefit of including more optode positions, can be applied to future instrument construction and implementation.

First, it became apparent in the initial reconstructions of data from this FD-DOT instrument that scattering features were reconstructing with higher contrast and resolution than the absorption features, *i.e.*, chromophore concentrations. This was preventing the chromophore concentrations from updating enough to accurately reflect the known values in phantoms. To correct this, a stricter regularization needed to be enforced on the scattering parameter than the chromophore concentrations. The simplest method of doing this was to implement a τ hyperparameter for μ_s' that was 10 times greater than the optimal τ determined by the L-curve method, which was used for μ_a. When this was done with total variation regularization (TV), there was still significant noise in the μ_s' image and limited improvement in the chromophore concentration contrasts (see Figure 7.8). The $10\times$ τ contrast method implemented with first-order Tikhonov (TK1) regularization did improve both image artifacts and chromophore contrast relative to the TV $10\times$ method; however, the reconstructed chromophore targets were still significantly broadened, especially along the transverse axis (see Figure 7.9).

Thus, the "Split $10\times$" method was tried. This regularization method still used the $10\times$ offset in the τ hyperparameter, but instead of a uniform regularization scheme, Split $10\times$ regularization employed TV regularization for μ_a and TK1 regularization for μ_s'. This was expected to have the desired effect because the TV regularization allows for a sharper contrast than TK1 regularization (see Section 2.6.5), thus improving the resolution of the absorption-dependent reconstructions. The new regularization scheme did indeed produce the best images for phantom experiments, providing maximum contrast that was approximately the same across all reconstructed parameters and minimizing the spatial broadening of the reconstructed targets. Table 7.1 contains summaries of these image quality parameters (Section 7.2.4) for the various regularization schemes. This is the first use of split regularization with both different τ values and different regularization techniques for the absorption and reduced scattering coefficients in DOT [25] and could represent an important advance in tuning the DOT reconstruction algorithm to accurately quantify optical and physiological properties.

Another technique explored in these reconstructions was weighting the data from given source-detector pairs by their separation distance (see Figure 7.5 for a schematic of the algorithm). Because the amplitude of the photon fluence rate decreases approximately as e^{-r}/r, off-axis source-detector pairs can have orders of magnitude less signal than on-axis pairs. Thus, the signal-to-noise ratio decreases dramatically with respect to the source-detector separation. Weighting the contributions of long source-detector separations to the objective function less than the contributions from short source-detector separations was shown to improve image quality by decreasing artifacts and increasing contrast (see Figure 7.11). Although the effect of this weighting is only shown for the human subject imaging here, the effect was consistent throughout all phantom tests. The method proposed here is a reasonably simple technique that could easily be applied to any spatially-dense DOT system.

Finally, this FD-DOT system contains the most source positions of any fiber-based DOT imager and a full CCD detection scheme. Thus, it is able to provide very spatially-dense information. Because of the system's novelty, however, it was unknown how beneficial each marginal source would be to the reconstruction quality. This effect was explored by using different numbers N_s of the total available source positions and using detector positions at the mirrored locations to the active source positions on the detector plane. Thus, for each experiment, $N_s = N_d$. Reconstructions that used significantly fewer than the total available source positions, *i.e.*, $N_s \leq 70$, provided noticeably worse contrast and resolution. However, for N_s beyond ~ 110, the reconstruction did not meaningfully improve (see Figure 7.10). Given the $0.8\,cm$ spacing between successive source locations, if all source positions are used, each source covers an area of approximately $0.64\,cm^2$. Thus, for $N_s = 110$, the number of sources above which there is minimal image improvement, the optode density is approximately 1 source per $1.22\,cm^2$. This is a similar finding to an earlier study, which found limited improvement in resolution for optode spacing less than $\sim 1\,cm$ [81].

There is some variation in the reconstructed contrasts and target sizes between successive N_s values beyond $N_s = 110$; however, these fluctuations are likely due to which source positions are chosen and their positions relative to the stationary targets. These fluctuations are smaller for greater N_s because the coverage area changes less between successive values of N_s than it does in the small N_s regime. A similar relationship between number of sources used and image quality was seen in the patient imaging as well. This information could both guide future instrument construction, by setting an upper limit on the necessary density of optodes near ~ 1 source per $1.2\,cm^2$, and increase the speed of imaging with the current system by enabling the instrument to cycle through fewer source positions while maintaining the same image quality. Shorter imaging times could improve patient comfort, reduce motion artifacts, increase patient throughput, or enable

the use of more wavelengths for quantification of other chromophores, like the water concentration.

The advances developed here for improving image quality do have several limitations. One is that the split regularization technique is likely to be highly dependent on the individual DOT system that is used. Thus, the specific technique developed here may not be applicable to all instruments because of differences in the relative absorption and scattering sensitivity profiles. Additionally, the source-detector standard deviation weighting, while limiting noise, also reduces the information available from off-axis source-detector pairs. This narrows the aperture of the effective light cone-beam, which limits resolution along the transverse axis and leads to the spatial broadening seen here, hindering the ability of this DOT system to accurately localize tumors. Thus, a balance will need to be struck between including off-axis measurements to improve resolution and discarding measurements which are dominated by noise. Finding this optimal cutoff point is an area of ongoing research.

7.5 Conclusion

The frequency-domain DOT instrument presented here represented an important advance in high spatial-density, optical-only DOT for absolute quantification of optical and physiological properties. The optimization of the reconstruction algorithms used with this system was a vital step in its introduction to clinical use. Using both multi-chromophore phantoms and human subject imaging, multi-spectral reconstructions were performed with a variety of regularization techniques, noise-weighting schemes, and number of sources.

Initial tests indicated that this system was more sensitive to changes in scattering than in absorption. Thus, the best regularization algorithm used total variation regularization for μ_a and first-order Tikhonov regularization for μ_s'. The τ hyperparameter for μ_s' was also chosen to be $10\times$ greater than the τ used for μ_a. This split regularization scheme provided consistently high contrast and resolution across both scattering and chromophore concentration reconstructions and significantly improved images relative to previously used regularization methods (see Table 7.1).

It was also determined that not all of the available 209 source positions were necessary to achieve optimal image quality. Increasing the number of sources beyond approximately 110 did not provide any significant benefits in either contrast or resolution (see Figure 7.10). Thus, the data acquisition algorithm can be modified to cycle through only half the sources, decreasing imaging time by a factor of two. This will likely improve patient comfort, reduce motion artifacts, and increase patient throughput with the current system. It could also serve as a guide for future systems in determining the necessary density of optodes.

Finally, the noise-weighting algorithm based on source-detector separation (see Figure 7.5) clearly reduced image artifacts and increased contrast (see Figure 7.11). This final optimization, along with the other advances, enabled this FD-DOT system to provide high-contrast, high-resolution optical-only images of HbO_2, HHb, and μ_s', demonstrating the system's ability to accurately and robustly locate and characterize breast tumors.

Chapter 8

Conclusion

Diffuse optical spectroscopy (DOS) and diffuse correlation spectroscopy (DCS) are promising optical techniques for developing biomarkers of breast cancer. Both modalities provide functional information at the bedside with no ionizing radiation, thus positioning them as ideal candidates for non-invasive differentiation of malignant lesions from benign lesions and for longitudinally monitoring of treatment outcome.

This thesis has presented further development of these biomarkers for both diagnosis and prognosis of breast cancer. First, a robust prognostic biomarker which could predict pathologic complete response to neoadjuvant chemotherapy (NAC) within 10 days of treatment initiation was developed (Chapter 3). This predictive model utilized DOS-measured tumor tissue oxygen saturation (S_tO_2), z-score normalized to healthy tissue S_tO_2, and a logistic regression algorithm applied to 33 subjects from a multi-site clinical trial. Tumor hypoxia relative to the surrounding tissue was found to be predictive of non-response to therapy. This method arguably offers the most compelling evidence yet of the ability of diffuse optics to predict chemotherapy response. Then, to more fully explore tumor hemodynamics during chemotherapy, the first pilot study to longitudinally monitor breast cancer with DCS throughout the course of a NAC regimen was performed (Chapter 4). This study provided interesting preliminary correlations between blood flow and complete response to therapy; it also demonstrated how combined S_tO_2 information from DOS, blood flow information from DCS, and the resultant calculation of oxygen metabolism could help to characterize the physiological mechanisms that underlie tumor response to chemotherapy. There are still significant aspects of these biomarkers to explore in future studies. First and foremost, the initial prediction models presented in Chapter 3 need to be validated on a larger, independent subject population. This is a vital step in the translation of these biomarkers into clinical use. In the same vein, a larger

DCS neoadjuvant chemotherapy study would allow the pilot correlations found between blood flow and therapy response in Chapter 4 to be quantified and modeled using the methods developed in Chapter 3. These larger subject populations would also allow for sub-division of patients by tumor subtype, chemotherapy regimen, and other physiological parameters, which could enable different prediction models optimized for each sub-population. Additionally, the ability to significantly analyze more homogeneous sub-populations will also provide the opportunity to accurately correlate diffuse optical measurements with physiological mechanisms.

Similar statistical techniques, *i.e.*, z-score normalization and logistic regression, were used to develop diagnostic models from DOS-measured deoxy-hemoglobin concentration (HHb) and a tissue optical index (TOI) that has been previously shown to differentiate tumors from healthy tissue in a single subject. This analysis was performed with a large ($n = 222$), heterogeneous subject population and indicated that higher HHb and TOI values were predictive of malignancy (Chapter 5). Importantly, if z-score normalization was utilized, a single model could provide differentiation between tumors and the surrounding healthy tissue and between malignant lesions and benign lesions. Thus, these models hold the potential to improve optical tumor localization and to enable non-invasive, optical biopsy. In the future, different statistical techniques could be investigated to explore optically measured differences among molecular subtypes and other tumor characteristics. One such area of exploration is the use of the full absorption and scattering spectra across the entire wavelength range as features in machine learning models rather than the fitted constituent chromophore concentrations, *e.g.*, HHb, HbO_2, H_2O, $Lipid$, etc., that were used here. This could introduce more structural information, such as collagen content, into the functional prediction models. These techniques could also be used to perform differential diagnosis, in which optically measured parameters are correlated directly with tumor properties, such as subtype, breast density, and proteomic biomarkers.

In a different vein, this thesis described the development of several advances in diffuse optical tomography (DOT). The first of these advances concerned the construction, optimization, and testing of a new experimental DOT instrument designed to image subjects concurrently with clinical MRI (Chapter 6). This instrument offers spatially dense data and hybrid continuous-wave and time-domain DOT for three-dimensional image reconstruction and absolute optical property quantification. This quality optical data, combined with clinical MRI, enables validation of DOT localization, constraint of the DOT reconstruction for more accurate quantification of physiological properties, and synthesis of diffuse optical markers with advanced perfusion MRI sequences that provide markers of blood flow. This newly implemented DOT-MRI instrument requires the recruitment of a significant number of patients to fully validate the system's multi-spectral reconstruction

ability. A key aspect of these future studies could also be the synthesis of DOT images with microvasculature blood flow information from the embedded diffuse corrrelation tomography (DCT) system and tumor perfusion information from gadolinium-contrast uptake MR images. These studies could present a novel method of obtaining non-invasive images of oxygen metabolism, furthering the understanding of tumor hemodynamics

The final contribution of this thesis concerns optimization of the DOT reconstruction algorithm (Chapter 7) for a DOT-only instrument. This work includes data noise-weighting, novel regularization schemes, and the determination of optimal data spatial density. These advances clearly improved DOT tumor-to-background contrast, reduced imaging artifacts, and minimized the imaging time required to produce quality images. More investigation is needed to determine how transferable the optimization for this instrument is to other systems. The first step in this analysis can be performed with the aforementioned joint DOT-MRI system.

The advances presented in this thesis and the future directions discussed here represent the next stage in the continued translation of diffuse optics from research imaging to a clinically viable modality with important roles to play in the breast cancer diagnosis and treatment paradigm.

Appendices

Appendix A

Diffuse Optical Theory Derivations

A.1 Spherical Harmonic Representation of Φ and $\vec{J}$

A.1.1 Spherical Harmonics

The spherical harmonic series is used as a series expansion for the radiance in 2.2.4. The spherical harmonic terms $Y_{lm}(\hat{\Omega})$ are defined as [9]

$$Y_{lm}(\hat{\Omega}) = Y_{lm}(\theta, \varphi) = (-1)^m \sqrt{\frac{2l+1}{4\pi} \frac{(l-m)!}{(l+m)!}} P_{lm}(\cos\theta) e^{\imath m\varphi}, \tag{A.1}$$

where θ and φ are the angular spherical coordinates and P_{lm} is the Legendre polynomial, which is given by [9]

$$P_{lm}(x) = \frac{1}{2^l l!}(1-x^2)^{m/2} \frac{\partial^{l+m}}{\partial x^{l+m}}(x^2-1)^l. \tag{A.2}$$

Importantly, the spherical harmonic terms form an orthonormal set [9], and thus

$$\int_{4\pi} Y^*_{lm}(\hat{\Omega})\, Y_{l'm'}(\hat{\Omega})\, d\Omega = \delta_{ll'}\, \delta_{mm'}, \tag{A.3}$$

where $Y^*_{lm}(\hat{\Omega})$ is the complex conjugate of $Y_{l'm'}(\hat{\Omega})$. Therefore, if $l = l'$ and $m = m'$, the integral in Equation A.3 equals 1; otherwise, the integral equals 0. This condition allows the spherical harmonics to form a basis set for expansion, as done with the radiance L in Equation 2.26

$$L(\vec{r}, \hat{\Omega}, t, \lambda) = \sum_{l=0}^{N} \sum_{m=-l}^{l} \sqrt{\frac{2l+1}{4\pi}}\, \tilde{\phi}_{lm}(\vec{r}, t, \lambda)\, Y_{lm}(\hat{\Omega}), \tag{A.4}$$

where $\tilde{\phi}_{lm}(\vec{r}, t, \lambda)$ is the spherical harmonic coefficient, with no angular dependence, for the $Y_{lm}(\hat{\Omega})$ spherical harmonic term.

A.1.2 Spherical Harmonic Expansion of Φ

Equation A.4 and the definition of the photon fluence rate in Equation 2.15 can be used to write a spherical harmonic representation of Φ as

$$\Phi(\vec{r},t,\lambda) = \int_{4\pi} \sum_{l=0}^{N} \sum_{m=-l}^{l} \sqrt{\frac{2l+1}{4\pi}}\, \tilde{\phi}_{lm}(\vec{r},t,\lambda)\, Y_{lm}(\hat{\Omega})\, d\Omega. \tag{A.5}$$

Given that the angular dependence of the expansion is entirely contained by the Y_{lm} terms, Equation A.5 can be rewritten as

$$\Phi(\vec{r},t,\lambda) = \sum_{l=0}^{N} \sum_{m=-l}^{l} \sqrt{2l+1}\, \tilde{\phi}_{lm}(\vec{r},t,\lambda) \int_{4\pi} \sqrt{\frac{1}{4\pi}}\, Y_{lm}(\hat{\Omega})\, d\Omega. \tag{A.6}$$

Then, by substituting $l = 0$ and $m = 0$ into Equations A.1 and A.2,

$$Y_{00}(\hat{\Omega}) = Y_{00}^{*}(\hat{\Omega}) = \sqrt{\frac{1}{4\pi}}, \tag{A.7}$$

allowing Equation A.6 to become

$$\Phi(\vec{r},t,\lambda) = \sum_{l=0}^{N} \sum_{m=-l}^{l} \sqrt{2l+1}\, \tilde{\phi}_{lm}(\vec{r},t,\lambda) \int_{4\pi} Y_{00}^{*}(\hat{\Omega})\, Y_{lm}(\hat{\Omega})\, d\Omega. \tag{A.8}$$

Given the orthonormality condition in Equation A.3, the only non-zero term in the expansion of Φ will be the term where $l = 0$ and $m = 0$, which, when Equation A.8 is simplified, means that

$$\Phi(\vec{r},t,\lambda) = \tilde{\phi}_{00}(\vec{r},t,\lambda) = \sqrt{4\pi}\, \tilde{\phi}_{00}(\vec{r},t,\lambda)\, Y_{00}(\hat{\Omega}). \tag{A.9}$$

Thus, the photon fluence rate can be expressed, without any approximation, as the $l = 0$ coefficient of the spherical harmonic expansion for the radiance.

A.1.3 Spherical Harmonic Expansion of $\vec{J}$

Equation A.4 and the definition of the photon flux in Equation 2.16 can be used to write the spherical harmonic representation of $\vec{J}$ as

$$\vec{J}(\vec{r},t,\lambda) = \int_{4\pi} \left[\sum_{l=0}^{N} \sum_{m=-l}^{l} \sqrt{\frac{2l+1}{4\pi}}\, \tilde{\phi}_{lm}(\vec{r},t,\lambda)\, Y_{lm}(\hat{\Omega}) \right] \hat{\Omega}\, d\Omega. \tag{A.10}$$

Note that $\hat{\Omega}$, which is normally defined using the spherical coordinates θ and φ, can be expressed in Cartesian coordinates as [9]

$$\hat{\Omega} = \sin\theta\cos\varphi\, \hat{x} \; + \sin\theta\sin\varphi\, \hat{y} \; + \cos\theta\, \hat{z}. \tag{A.11}$$

Substituting this Cartesian representation and separating the angular components allows Equation A.10 to be rewritten as

$$\vec{J}(\vec{r},t,\lambda) = \sum_{l=0}^{N}\sum_{m=-l}^{l}\sqrt{\frac{2l+1}{4\pi}}\,\tilde{\phi}_{lm}(\vec{r},t,\lambda) \int_{4\pi} Y_{lm}(\hat{\Omega})\,\left[\sin\theta\cos\varphi\,\hat{x}\;+\sin\theta\sin\varphi\,\hat{y}\;+\cos\theta\,\hat{z}\right]\,d\Omega. \quad \text{(A.12)}$$

Now, using Equations A.1 and A.2, the three $l = 1$ terms, *i.e.*, $m = -1$, $m = 0$, and $m = 1$, are written as

$$Y_{1-1}(\hat{\Omega}) = \frac{1}{2}\sqrt{\frac{3}{2\pi}}\sin\theta\left[\cos\varphi - \imath\sin\varphi\right], \quad \text{(A.13)}$$

$$Y_{10}(\hat{\Omega}) = \sqrt{\frac{3}{4\pi}}\cos\theta, \quad \text{(A.14)}$$

$$Y_{11}(\hat{\Omega}) = -\frac{1}{2}\sqrt{\frac{3}{2\pi}}\sin\theta\left[\cos\varphi + \imath\sin\varphi\right]. \quad \text{(A.15)}$$

These equations can now be used to derive expressions for the Cartesian components of $\hat{\Omega}$, $\sin\theta\cos\varphi$, $\sin\theta\sin\varphi$, and $\cos\theta$ (see Equation A.11), in terms of the complex conjugates of the spherical harmonics. From Equation A.14,

$$\cos\theta = 2\sqrt{\frac{\pi}{3}}\,Y^{*}_{10}(\hat{\Omega}). \quad \text{(A.16)}$$

Then, via algebraic manipulation of Equations A.13 and A.15, the other two components of $\hat{\Omega}$ are

$$\sin\theta\cos\varphi = \sqrt{\frac{2\pi}{3}}\left(Y^{*}_{1-1} - Y^{*}_{11}\right), \quad \text{(A.17)}$$

$$\sin\theta\sin\varphi = -\imath\sqrt{\frac{2\pi}{3}}\left(Y^{*}_{1-1} + Y^{*}_{11}\right). \quad \text{(A.18)}$$

Substituting Equations A.16, A.17, and A.18 into Equation A.12 yields

$$\vec{J}(\vec{r},t,\lambda) = \sum_{l=0}^{N}\sum_{m=-l}^{l}\sqrt{\frac{2l+1}{4\pi}}\,\tilde{\phi}_{lm}(\vec{r},t,\lambda) \int_{4\pi}\left[\sqrt{\frac{2\pi}{3}}\left(Y^{*}_{1-1} - Y^{*}_{11}\right)\,\hat{x}\;+-\imath\sqrt{\frac{2\pi}{3}}\left(Y^{*}_{1-1} + Y^{*}_{11}\right)\,\hat{y}\;+2\sqrt{\frac{\pi}{3}}\,Y^{*}_{10}(\hat{\Omega})\,\hat{z}\right]\,Y_{lm}(\hat{\Omega})\,d\Omega. \quad \text{(A.19)}$$

The orthonormality of the spherical harmonics (Equation A.3) forces all $l \neq 1$ terms to 0, such that

$$\vec{J}(\vec{r},t,\lambda) = \frac{1}{\sqrt{2}}\left[\tilde{\phi}_{1-1}(\vec{r},t,\lambda) - \tilde{\phi}_{11}(\vec{r},t,\lambda)\right]\,\hat{x} \\ - \frac{\imath}{\sqrt{2}}\left[\tilde{\phi}_{1-1}(\vec{r},t,\lambda) + \tilde{\phi}_{11}(\vec{r},t,\lambda)\right]\,\hat{y} + \tilde{\phi}_{10}(\vec{r},t,\lambda)\,\hat{z}. \quad \text{(A.20)}$$

Then, performing a dot product with $\hat{\Omega}$ on both sides of Equation A.20, and using the Cartesian definition of $\hat{\Omega}$ results in

$$\vec{J}(\vec{r},t,\lambda)\cdot\hat{\Omega} = \frac{1}{\sqrt{2}}\left[\tilde{\phi}_{1-1}(\vec{r},t,\lambda) - \tilde{\phi}_{11}(\vec{r},t,\lambda)\right]\,\sin\theta\cos\varphi - \\ \frac{\imath}{\sqrt{2}}\left[\tilde{\phi}_{1-1}(\vec{r},t,\lambda) + \tilde{\phi}_{11}(\vec{r},t,\lambda)\right]\,\sin\theta\sin\varphi + \tilde{\phi}_{10}(\vec{r},t,\lambda)\,\cos\theta. \quad \text{(A.21)}$$

Grouping the three spherical harmonic coefficients in Equation A.21, and using the trigonometric identity $e^{\imath x} = \cos x + \imath \sin x$ [9], results in

$$\vec{J}(\vec{r},t,\lambda)\cdot\hat{\Omega} = \tilde{\phi}_{10}(\vec{r},t,\lambda)\cos\theta + \frac{1}{\sqrt{2}}\tilde{\phi}_{1-1}(\vec{r},t,\lambda)\sin\theta e^{-\imath\varphi} - \frac{1}{\sqrt{2}}\tilde{\phi}_{11}(\vec{r},t,\lambda)\sin\theta e^{\imath\varphi}. \quad \text{(A.22)}$$

Using the equations for the $l = 1$ spherical harmonics (Equations A.13, A.14, and A.15), $\vec{J}(\vec{r},t,\lambda)\cdot\hat{\Omega}$ can be written in terms of spherical harmonics as

$$\vec{J}(\vec{r},t,\lambda)\cdot\hat{\Omega} = \sqrt{\frac{4\pi}{3}}\left[\tilde{\phi}_{1-1}(\vec{r},t,\lambda)Y_{1-1}(\hat{\Omega}) + \tilde{\phi}_{10}(\vec{r},t,\lambda)Y_{10}(\hat{\Omega}) + \tilde{\phi}_{11}(\vec{r},t,\lambda)Y_{11}(\hat{\Omega})\right]. \quad \text{(A.23)}$$

Thus the dot product of the photon flux and $\hat{\Omega}$ is generally proportional to the sum of the three $l = 1$ spherical harmonic terms.

A.2 Vector Calculus Integral Identities

To further simplify the RTE in Equation 2.41, the vector identities in Equations 2.42, 2.43, and 2.44 must be used.

A.2.1 Integral of $\hat{\Omega}$

The first integral of interest is

$$\int_{4\pi} \hat{\Omega}\, d\Omega. \quad \text{(A.24)}$$

First, rewrite $\hat{\Omega}$ in Cartesian coordinates using Equation A.11 and the volume integral element using spherical coordinates, such that

$$\int_{4\pi} \hat{\Omega}\, d\Omega = \int_{\theta=0}^{\pi}\int_{\varphi=0}^{2\pi} [\sin\theta\cos\varphi\,\hat{x} + \sin\theta\sin\varphi\,\hat{y} + \cos\theta\,\hat{z}]\sin\theta\, d\theta\, d\varphi. \quad \text{(A.25)}$$

The integral over φ from 0 to 2π forces the $\hat{x}$ and $\hat{y}$ terms to 0, leaving only

$$\int_{4\pi} \hat{\Omega}\, d\Omega = 2\pi \int_{\theta=0}^{\pi} \cos\theta \sin\theta\, \hat{z}\, d\theta. \tag{A.26}$$

This integral can be solved by substitution for $\sin\theta$, which, when completed, demonstrates that

$$\int_{4\pi} \hat{\Omega}\, d\Omega = 0. \tag{A.27}$$

This is the identity given in Equation 2.42.

A.2.2 Integral of $\hat{\Omega}\left[\hat{\Omega}\cdot\vec{A}\right]$

The next integral that is required to simplify the RTE is

$$\int_{4\pi} \hat{\Omega}\left[\hat{\Omega}\cdot\vec{A}\right]\, d\Omega, \tag{A.28}$$

where $\vec{A}$ is a generic vector quantity. It is possible, without a loss of generality, to define $\vec{A}$ such that it is parallel to $\hat{z}$, which can be written mathematically as

$$\frac{\vec{A}}{|\vec{A}|} = \hat{z}. \tag{A.29}$$

Then, using the Cartesian coordinate representation of $\hat{\Omega}$ in Equation A.11, the dot product of $\hat{\Omega}$ and $\vec{A}$ can be written as

$$\hat{\Omega}\cdot\vec{A} = |\vec{A}|\cos\theta. \tag{A.30}$$

With this representation of the dot product, as well as the Cartesian coordinate definition of $\hat{\Omega}$, the integral can be rewritten as

$$\int_{4\pi} \hat{\Omega}\left[\hat{\Omega}\cdot\vec{A}\right]\, d\Omega = |\vec{A}| \int_{\theta=0}^{\pi}\int_{\varphi=0}^{2\pi} \cos\theta\,[\sin\theta\cos\varphi\,\hat{x} + \sin\theta\sin\varphi\,\hat{y} + \cos\theta\,\hat{z}]\sin\theta\, d\theta\, d\varphi. \tag{A.31}$$

Note that for the integration over φ, this integral is identical to the one in Equation A.25. Thus, the $\hat{x}$ and $\hat{y}$ terms go to 0, leaving only

$$\int_{4\pi} \hat{\Omega}\left[\hat{\Omega}\cdot\vec{A}\right]\, d\Omega = 2\pi|\vec{A}| \int_{\theta=0}^{\pi} \cos^2\theta \sin\theta\, \hat{z}\, d\theta. \tag{A.32}$$

This integral can be solved via substitution for $\cos^2\theta$, resulting in

$$\int_{4\pi} \hat{\Omega}\left[\hat{\Omega}\cdot\vec{A}\right]\, d\Omega = \frac{4\pi}{3}|\vec{A}|\hat{z}, \tag{A.33}$$

which, given the definition of $\vec{A}$ in Equation A.29, can be simplified to

$$\int_{4\pi} \hat{\Omega}\left[\hat{\Omega}\cdot\vec{A}\right]\, d\Omega = \frac{4\pi}{3}\vec{A}. \tag{A.34}$$

This is the identity given in Equation 2.43.

A.2.3 Integral of $\hat{\Omega}\left[\hat{\Omega}\cdot\vec{\nabla}\left(\vec{A}\cdot\hat{\Omega}\right)\right]$

The final integral of interest that appears in Equation 2.41 is

$$\int_{4\pi}\hat{\Omega}\left[\hat{\Omega}\cdot\vec{\nabla}\left(\vec{A}\cdot\hat{\Omega}\right)\right]\,d\Omega. \tag{A.35}$$

The first step in simplifying this integral is exploiting the vector calculus identity [39]

$$\vec{\nabla}\left(\vec{A}\cdot\vec{B}\right)=\left(\vec{A}\cdot\vec{\nabla}\right)\vec{B}+\left(\vec{B}\cdot\vec{\nabla}\right)\vec{A}+\vec{A}\times\left(\vec{\nabla}\times\vec{B}\right)+\vec{B}\times\left(\vec{\nabla}\times\vec{A}\right), \tag{A.36}$$

where $\vec{A}$ and $\vec{B}$ are generic vectors. For the integral in Equation A.35, $\vec{A}=\vec{A}$ and $\vec{B}=\hat{\Omega}$. Since $\hat{\Omega}$ is a constant unit vector that is not spatially-dependent,

$$\left(\vec{A}\cdot\vec{\nabla}\right)\hat{\Omega}=0, \tag{A.37}$$

and

$$\vec{A}\times\left(\vec{\nabla}\times\hat{\Omega}\right)=0. \tag{A.38}$$

Thus, a simplified version of the vector identity in Equation A.36 can be substituted into the integral, such that

$$\int_{4\pi}\hat{\Omega}\left[\hat{\Omega}\cdot\vec{\nabla}\left(\vec{A}\cdot\hat{\Omega}\right)\right]\,d\Omega=\int_{4\pi}\hat{\Omega}\left[\hat{\Omega}\cdot\left(\hat{\Omega}\cdot\vec{\nabla}\right)\vec{A}+\hat{\Omega}\cdot\left(\hat{\Omega}\times\left(\vec{\nabla}\times\vec{A}\right)\right)\right]\,d\Omega. \tag{A.39}$$

Here, the first dot product with $\hat{\Omega}$ has been distributed across the substituted vector calculus identity.

Now consider the term $\hat{\Omega}\cdot\left(\hat{\Omega}\times\left(\vec{\nabla}\times\vec{A}\right)\right)$. By definition, $\hat{\Omega}\times\left(\vec{\nabla}\times\vec{A}\right)$ will produce a vector that is orthogonal to $\hat{\Omega}$. Thus, the dot product between the resultant vector and $\hat{\Omega}$ will, again by definition, be 0. Therefore Equation A.39 reduces to

$$\int_{4\pi}\hat{\Omega}\left[\hat{\Omega}\cdot\vec{\nabla}\left(\vec{A}\cdot\hat{\Omega}\right)\right]\,d\Omega=\int_{4\pi}\hat{\Omega}\left[\hat{\Omega}\cdot\left(\hat{\Omega}\cdot\vec{\nabla}\right)\vec{A}\right]\,d\Omega. \tag{A.40}$$

Now, note that, in spherical coordinates, [44]

$$\hat{\Omega}=\hat{r}, \tag{A.41}$$

and [39]

$$\vec{\nabla}=\frac{\partial}{\partial r}\,\hat{r}\;+\;\frac{1}{r}\frac{\partial}{\partial\theta}\,\hat{\theta}\;+\;\frac{1}{r\sin\theta}\frac{\partial}{\partial\varphi}\,\hat{\varphi}. \tag{A.42}$$

Given these definitions, the integral in Equation A.40 can be simplified to

$$\int_{4\pi}\hat{\Omega}\left[\hat{\Omega}\cdot\vec{\nabla}\left(\vec{A}\cdot\hat{\Omega}\right)\right]\,d\Omega=\int_{4\pi}\hat{\Omega}\,\frac{\partial A_r}{\partial r}\,d\Omega, \tag{A.43}$$

where A_r is the $\hat{r}$ component of $\vec{A}$. Since $\frac{\partial A_r}{\partial r}$ is not dependent on θ or φ it can be brought outside the integral, resulting in

$$\int_{4\pi} \hat{\Omega}\left[\hat{\Omega}\cdot\vec{\nabla}\left(\vec{A}\cdot\hat{\Omega}\right)\right]\,d\Omega = \frac{\partial A_r}{\partial r}\int_{4\pi}\hat{\Omega}\,d\Omega, \tag{A.44}$$

which has already been shown in Appendix A.2.1 to be equal to 0. Therefore,

$$\int_{4\pi} \hat{\Omega}\left[\hat{\Omega}\cdot\vec{\nabla}\left(\vec{A}\cdot\hat{\Omega}\right)\right]\,d\Omega = 0. \tag{A.45}$$

This is the identity given in Equation 2.44.

A.3 Homogeneous Optical Properties from k

As defined in Equation 2.73, the variable k, which governs the propagation of an oscillating diffuse photon density wave due to a frequency domain source term, is given by

$$k \equiv \sqrt{\frac{v\mu_a + \imath\omega}{D}}. \tag{A.46}$$

As discussed in Section 2.4.3, real and imaginary parts of k can be determined from measurements of the fluence amplitude and phase offset at multiple source detector separations. These values can then be used to calculate the homogeneous optical properties of the medium. First, k_r and k_i can be derived from the definition of k in Equation A.46 by examining k^2, where

$$k^2 = \frac{v\mu_a + \imath\omega}{D}. \tag{A.47}$$

Then, this term can be rewritten in the polar representation of complex numbers [9] as

$$k^2 = \sqrt{\frac{v^2\mu_a^2+\omega^2}{D^2}}\exp\left[\imath\arctan\left(\frac{\omega}{v\mu_a}\right)\right]. \tag{A.48}$$

Then, by taking the square root of Equation A.48 and converting k back to the Cartesian representation of complex numbers [9], k can be written as

$$k = \left[\frac{v^2\mu_a^2+\omega^2}{D^2}\right]^{1/4}\exp\left[\frac{\imath}{2}\arctan\left(\frac{\omega}{v\mu_a}\right)\right] \tag{A.49}$$

$$= \left[\frac{v^2\mu_a^2+\omega^2}{D^2}\right]^{1/4}\cos\left[\frac{1}{2}\arctan\left(\frac{\omega}{v\mu_a}\right)\right] + \imath\left[\frac{v^2\mu_a^2+\omega^2}{D^2}\right]^{1/4}\sin\left[\frac{1}{2}\arctan\left(\frac{\omega}{v\mu_a}\right)\right]. \tag{A.50}$$

Therefore the real and imaginary parts of k are

$$k_r = \left[\frac{v^2\mu_a^2+\omega^2}{D^2}\right]^{1/4}\cos\left[\frac{1}{2}\arctan\left(\frac{\omega}{v\mu_a}\right)\right]; \tag{A.51}$$

$$k_i = \left[\frac{v^2\mu_a^2 + \omega^2}{D^2}\right]^{1/4} \sin\left[\frac{1}{2}\arctan\left(\frac{\omega}{v\mu_a}\right)\right]. \tag{A.52}$$

The trigonometric functions in Equations A.51 and A.52 can be simplified using the identities [5]

$$\cos(\arctan x) = \frac{1}{\sqrt{1+x^2}}, \tag{A.53}$$

$$\sin(\arctan x) = \frac{x}{\sqrt{1+x^2}}, \tag{A.54}$$

and the half-angle formulae [5] for both sine and cosine. This results in the following expressions for k_r and k_i

$$k_r = \left(\frac{v\mu_a}{2D}\right)^{1/2}\left[\left(1+\left(\frac{\omega}{v\mu_a}\right)^2\right)^{1/2}+1\right]^{1/2}; \tag{A.55}$$

$$k_i = \left(\frac{v\mu_a}{2D}\right)^{1/2}\left[\left(1+\left(\frac{\omega}{v\mu_a}\right)^2\right)^{1/2}-1\right]^{1/2}. \tag{A.56}$$

These are the representations of k_r and k_i seen in Equations 2.79 and 2.80.

The next step is to derive expressions for the optical properties μ_a and μ_s' in terms of k_r and k_i. First, for simplicity, write the polar representation of k (Equation A.49) as

$$k = Ae^{\imath\, b}, \tag{A.57}$$

where

$$A = \left[\frac{v^2\mu_a^2 + \omega^2}{D^2}\right]^{1/4}; \tag{A.58}$$

$$b = \frac{1}{2}\arctan\left(\frac{\omega}{v\mu_a}\right). \tag{A.59}$$

Then, given the relationship between the polar and Cartesian representations of k [9],

$$k_r = A\,\cos b\,; \tag{A.60}$$

$$k_i = A\,\sin b\,. \tag{A.61}$$

The first step to solve for μ_a is to write the following quantity, given Equations A.60 and A.61,

$$\frac{k_r}{k_i} - \frac{k_i}{k_r} = \frac{\cos b}{\sin b} - \frac{\sin b}{\cos b} \tag{A.62}$$

$$= \frac{\cos^2 b - \sin^2 b}{\cos b\,\sin b}. \tag{A.63}$$

Then, given the double-angle formulae for sine and cosine [5], this quantity can be rewritten as

$$\frac{k_r}{k_i} - \frac{k_i}{k_r} = \frac{2\cos(2b)}{\sin(2b)}. \tag{A.64}$$

Finally, using the arctangent identities in Equations A.53 and A.54 and the definition of b in Equation A.59, the expression can be written as

$$\frac{k_r}{k_i} - \frac{k_i}{k_r} = \frac{2v\mu_a}{\omega}, \tag{A.65}$$

and thus, μ_a can be written as

$$\mu_a = \frac{\omega}{2v}\left[\frac{k_r}{k_i} - \frac{k_i}{k_r}\right]. \tag{A.66}$$

This is the expression for μ_a given in Equation 2.81.

In order to derive the expression for μ_s', first start with the term

$$k_r^2 - k_i^2 = A^2\left[\cos^2 b - \sin^2 b\right] \tag{A.67}$$

$$= A^2\cos(2b). \tag{A.68}$$

Equation A.68 takes advantage of the double-angle formula for cosine [5]. Then, using the definition of A and b in Equations A.58 and A.59, as well as the arctangent identity in Equation A.53, the quantity can be written as

$$k_r^2 - k_i^2 = \frac{v\mu_a}{D}. \tag{A.69}$$

By using the definition of the diffusion coefficient D (Equation 2.52) and performing some algebraic manipulation, μ_s' can then be expressed as

$$\mu_s' = \frac{k_r^2 - ki^2}{3\mu_a} - \mu_a. \tag{A.70}$$

Substituting the definition of μ_a from Equation A.66 into the denominator yields

$$\mu_s' = \frac{2v}{3\omega}\, k_i\, k_r - \mu_a. \tag{A.71}$$

This is the expression for μ_s' in Equation 2.82. Since, under the assumptions required for the diffusion equation to be valid, $\mu_a \ll \mu_s'$, the μ_a term can usually be dropped from Equation A.71 for an accurate approximation of μ_s'. For an exact solution, the value of μ_a in terms of k_r and k_i from Equation A.66 can again be substituted into the full expression.

A.4 Fourier Transform for Time Domain Solution

The Green's function solution to the time domain diffusion equation is simply the Fourier transform of the Green's function solution to the frequency domain diffusion equation. This is true regardless of tissue geometry and boundary conditions.

In the infinite homogeneous geometry, the frequency domain Green's function G can be written as

$$G(\vec{r},\vec{r}_s) = \frac{v}{4\pi\, D\,|\vec{r}-\vec{r}_s|} e^{-k|\vec{r}-\vec{r}_s|}, \tag{A.72}$$

where $\vec{r}_s$ is the source position. This is the Green's function solution associated with Equation 2.74. Here k, as defined in Equation 2.73, is $\sqrt{\frac{v\mu_a+\imath\omega}{D}}$. The time domain Green's function g will be the Fourier transform of Equation A.72, such that

$$g(\vec{r},\vec{r}_s,t,t_s) = \frac{1}{2\pi}\int_{-\infty}^{\infty} G(\vec{r},\vec{r}_s)\exp\left[\imath\omega\,(t-t_s)\right]d\omega, \tag{A.73}$$

and, therefore, with Equation A.72 substituted in for G,

$$g(\vec{r},\vec{r}_s,t,t_s) = \frac{1}{2\pi}\int_{-\infty}^{\infty} \frac{v}{4\pi\, D\,|\vec{r}-\vec{r}_s|}\exp\left[-k|\vec{r}-\vec{r}_s|\right]\exp\left[\imath\omega\,(t-t_s)\right]d\omega. \tag{A.74}$$

First, note that the $\frac{v}{4\pi\, D\,|\vec{r}-\vec{r}_s|}$ term is not dependent on ω and can be taken outside the integral. Next, perform a variable substitution using the defined value of k, where

$$k = \sqrt{\frac{v\mu_a+\imath\omega}{D}}. \tag{A.75}$$

It follows from this substitution that

$$\imath\omega = Dk^2 - v\mu_a, \tag{A.76}$$

$$d\omega = -2\imath D\,k\,dk. \tag{A.77}$$

After moving all ω-independent terms outside the integral, this substitution results in

$$g(\vec{r},\vec{r}_s,t,t_s) = \frac{-\imath Dv}{4\pi^2\, D\,|\vec{r}-\vec{r}_s|}\exp\left[-v\mu_a\,(t-ts)\right]\int_{-\infty}^{\infty} k\,\exp\left[D\,(t-t_s)\,k^2 - |\vec{r}-\vec{r}_s|k\right]dk. \tag{A.78}$$

Completing the square of the exponent inside the integral by adding and subtracting the term $\frac{|\vec{r}-\vec{r}_s|^2}{4D(t-t_s)}$ further simplifies the equation to

$$g(\vec{r},\vec{r}_s,t,t_s) = \frac{-\imath Dv}{4\pi^2\, D\,|\vec{r}-\vec{r}_s|}\exp\left[-\frac{|\vec{r}-\vec{r}_s|^2}{4D\,(t-t_s)} - v\mu_a\,(t-ts)\right] \int_{-\infty}^{\infty} k\,\exp\left[\left(\sqrt{D\,(t-t_s)}k - \frac{|\vec{r}-\vec{r}_s|}{\sqrt{4D\,(t-t_s)}}\right)^2\right]dk. \tag{A.79}$$

A second variable substitution for the exponent in the integral can be made, such that

$$-u^2 = \left(\sqrt{D\,(t-t_s)}k - \frac{|\vec{r}-\vec{r}_s|}{\sqrt{4D\,(t-t_s)}}\right)^2. \tag{A.80}$$

From this substitution, it follows that

$$k = \frac{1}{\sqrt{D\left(t - t_s\right)}} \left(\frac{|\vec{r} - \vec{r}_s|}{\sqrt{4D\left(t - t_s\right)}} - \imath u \right), \tag{A.81}$$

$$dk = \frac{\imath}{\sqrt{D\left(t - t_s\right)}}\, du. \tag{A.82}$$

Substituting these three relations into Equation A.79 yields

$$g(\vec{r}, \vec{r}_s, t, t_s) = \frac{Dv}{4\pi^2\, D\,|\vec{r} - \vec{r}_s|} \frac{1}{D\left(t - t_s\right)} \exp\left[-\frac{|\vec{r} - \vec{r}_s|^2}{4D\left(t - t_s\right)} - v\mu_a\left(t - ts\right) \right] \int_{-\infty}^{\infty} \left[\frac{|\vec{r} - \vec{r}_s|}{\sqrt{4D\left(t - t_s\right)}} - \imath\, u \right] e^{-u^2}\, du. \tag{A.83}$$

It can now be noted that the $u \exp\left[-u^2\right]$ term is an odd function, and therefore, its integral from $-\infty$ to ∞ is 0 [39]. The other term inside the integral is simply a constant multiplied by a Gaussian, and thus, it reduces to the constant times $\sqrt{\pi}$ [127]. Thus, with only algebraic manipulation, Equation A.83 reduces to

$$g(\vec{r}, \vec{r}_s, t, t_s) = \frac{v}{\left(4\pi D\left(t - t_s\right)\right)^{3/2}} \exp\left[-\frac{|\vec{r} - \vec{r}_s|^2}{4D\left(t - t_s\right)} - v\mu_a\left(t - t_s\right) \right]. \tag{A.84}$$

This is the Green's function for the fluence expression in Equation 2.85; therefore, the frequency and time domain Green's functions have been shown to be a Fourier transform pair.

A.5 Semi-Infinite Homogeneous Green's Function

As discussed in Section 2.5.3, the semi-infinite homogeneous Green's function solution to the diffusion equation can be determined using the method of images and the partial-flux boundary condition [49; 22]. With the method of images, the total semi-infinite Green's function solution G_{SI} in cylindrical coordinates can be written as the sum of the infinite geometry Green's function and a correction term as follows

$$G_{SI} = G_I(\rho, z) + G_C(\rho, z), \tag{A.85}$$

where

$$G_I(\rho, z) = \frac{v}{4\pi D r_1} \exp\left[-k r_1\right], \tag{A.86}$$

$$r_1 \equiv \sqrt{\left(z - l_{tr}\right)^2 + \rho^2}. \tag{A.87}$$

Here, G_I is the infinite homogeneous Green's function for an isotropic point source at position $(\rho = 0, z = l_{tr})$, and G_C is an as-yet-undetermined correction term. The partial-flux boundary condition, as given in Equation 2.100, is

$$\Phi(\rho, z = 0, t) = z_b \frac{\partial \Phi(\rho, z = 0, t)}{\partial z}. \tag{A.88}$$

Given Equation A.85, this boundary condition can be written as

$$[G_I + G_C]_{z=0} = z_b \left[\frac{\partial G_I}{\partial z} + \frac{\partial G_C}{\partial z} \right]_{z=0}. \tag{A.89}$$

Taking the derivative of of G_I with respect to z results in the following relationship:

$$\left[\frac{\partial G_C}{\partial z} - \frac{G_C}{z_b} \right]_{z=0} = - \left[\frac{\partial G_I}{\partial z} - \frac{G_I}{z_b} \right]_{z=0} \tag{A.90}$$

$$= \left[\frac{v}{4\pi D r_1^2} \exp\left[-k r_1\right] \left(\frac{z - l_{tr}}{r_1} + k(z - l_{tr}) + \frac{r_1}{z_b} \right) \right]_{z=0}. \tag{A.91}$$

Remembering that r_1 is dependent on z, the $z = 0$ condition can now be implemented, such that

$$\left[\frac{\partial G_C}{\partial z} - \frac{G_C}{z_b} \right]_{z=0} = \frac{v}{4\pi D \left(l_{tr}^2 + \rho^2\right)} \exp\left[-k\sqrt{l_{tr}^2 + \rho^2} \right] \left[\frac{\sqrt{l_{tr}^2 + \rho^2}}{z_b} - \frac{l_{tr}}{\sqrt{l_{tr}^2 + \rho^2}} - k l_{tr} \right]. \tag{A.92}$$

Now, consider an image source that occurs at position $(\rho = 0, z = -l_{tr})$ and is thus a mirror image of the real source about the $z = 0$ interface. An infinite homogeneous Green's function for this source will have the form

$$G_I^{im}(\rho, z) = \frac{v}{4\pi D r_2} \exp\left[-k r_2\right], \tag{A.93}$$

where

$$r_2 \equiv \sqrt{\left(z + l_{tr}\right)^2 + \rho^2}. \tag{A.94}$$

Then, it can be shown via derivation of G_I^{im} with respect to z that, for $z = 0$,

$$\left[\frac{\partial G_I^{im}}{\partial z} + \frac{G_I^{im}}{z_b} \right]_{z=0} = \frac{v}{4\pi D \left(l_{tr}^2 + \rho^2\right)} \exp\left[-k\sqrt{l_{tr}^2 + \rho^2} \right] \left[\frac{\sqrt{l_{tr}^2 + \rho^2}}{z_b} - \frac{l_{tr}}{\sqrt{l_{tr}^2 + \rho^2}} - k l_{tr} \right]. \tag{A.95}$$

The right hand side of this equation is equal to the right hand side of Equation A.92, and thus the partial-flux boundary condition is satisfied when

$$\frac{\partial G_C}{\partial z} - \frac{G_C}{z_b} = \frac{\partial G_I^{im}}{\partial z} + \frac{G_I^{im}}{z_b}. \tag{A.96}$$

Therefore, solving Equation A.96 for G_C will provide a Green's function solution for the semi-infinite homogeneous medium. The first step to solve this equation is to multiply both sides by

e^{-z/z_b} and to recognize that these terms can be rewritten using the partial integral with respect to z of the combined G and exponential terms as

$$\frac{\partial}{\partial z}\left[G_C e^{-z/z_b}\right] = \frac{\partial}{\partial z}\left[G_I^{im} e^{-z/z_b}\right] + \frac{2}{z_b} G_I^{im} e^{-z/z_b}. \tag{A.97}$$

Then, with a variable change of $z \rightarrow z'$, integration of both sides over $z' = z$ to $z' = \infty$, and substitution for G_I^{im} (Equation A.93), the equation can be expressed as

$$\int_z^\infty \frac{\partial}{\partial z'}\left[G_C \exp\left[-z'/z_b\right]\right] dz' = \int_z^\infty \frac{\partial}{\partial z'}\left[\frac{v \exp\left[-(k\sqrt{(z'+l_{tr})^2+\rho^2} + z/z_b\right)}{4\pi D\sqrt{(z'+l_{tr})^2+\rho^2}}\right] dz' +$$
$$\frac{2}{z_b}\int_z^\infty \frac{v \exp\left[-(k\sqrt{(z'+l_{tr})^2+\rho^2} + z/z_b\right)}{4\pi D\sqrt{(z'+l_{tr})^2+\rho^2}}\, dz'. \tag{A.98}$$

The left hand side and first term on the right hand side are simple to integrate, leaving

$$-G_C \exp\left[-z/z_b\right] = -\frac{v \exp\left[-(k\sqrt{(z+l_{tr})^2+\rho^2} + z/z_b\right)}{4\pi D\sqrt{(z+l_{tr})^2+\rho^2}} + \tag{A.99}$$
$$\frac{2}{z_b}\int_z^\infty \frac{v \exp\left[-(k\sqrt{(z'+l_{tr})^2+\rho^2} + z'/z_b\right)}{4\pi D\sqrt{(z'+l_{tr})^2+\rho^2}}\, dz'. \tag{A.100}$$

Finally performing a variable substitution, such that $u = z' - z$, results in

$$G_C = \frac{v}{4\pi D r_2} e^{-kr_2} - \frac{2}{z_b}\int_0^\infty \frac{v e^{-u/z_b}}{4\pi D\sqrt{(u+z+l_{tr})^2+\rho^2}} \exp\left[-k\sqrt{(u+z+l_{tr})^2+\rho^2}\right] du. \tag{A.101}$$

This is the correction term for the semi-infinite Green's function solution under the partial-flux boundary condition given in Equation 2.108. The first term represents an image source at position $z = -l_{tr}$, and the second term represents a continuous line of image sinks with amplitudes falling to 0 as z goes to ∞.

A.6 Rytov Solution for Heterogeneous Medium

The frequency domain diffusion equation can be solved for heterogeneous media where the perturbation from a homogeneous medium is small (see Section 2.6.1). In this case, the optical properties can be represented as

$$\mu_a(\vec{r}) = \mu_a^o + \delta\mu_a(\vec{r}), \tag{A.102}$$

$$D(\vec{r}) = D^o + \delta D(\vec{r}). \tag{A.103}$$

Here, μ_a^o and D^o are the homogeneous absorption and diffusion coefficients, respectively, while $\delta\mu_a$ and δD are the small, spatially-dependent perturbations in the optical properties. With the Rytov approximation, the AC term of the photon fluence U is written as

$$U(\vec{r}) = U_o\, U_{sc} \tag{A.104}$$

$$= e^{\phi_o}\, e^{\phi_{sc}} = e^{\phi_o + \phi_{sc}}, \tag{A.105}$$

where $U_o = e^{\phi_o}$ is the solution to the homogeneous medium diffusion equation, in which $\mu_a = \mu_a^o$ and $D = D^o$. $U_{sc} = e^{\phi_{sc}}$ is the perturbative, or scattering, correction to the homogeneous medium solution due to the optical property perturbations.

As a reminder, the homogeneous medium diffusion equation is

$$\nabla^2 U_o(\vec{r}, \vec{r}_s) - \frac{v\mu_a^o + \imath\omega}{D^o} U_o(\vec{r}, \vec{r}_s) = -v\, B\, \delta(\vec{r}, \vec{r}_s). \tag{A.106}$$

Here $\vec{r}_s$ is the position of the modulated point source, and B is a constant term representing the source profile. The diffusion equation for the heterogeneous medium can then be expressed as

$$\nabla \cdot \left[\left(D^o + \delta D(\vec{r})\right) \nabla \left(U_o(\vec{r}, \vec{r}_s) U_{sc}(\vec{r}, \vec{r}_s)\right)\right] - \left[v\left(\mu_a^o + \delta\mu_a(\vec{r})\right) + \imath\omega\right] \left(U_o(\vec{r}, \vec{r}_s) U_{sc}(\vec{r}, \vec{r}_s)\right) = -v\, B\, \delta(\vec{r}, \vec{r}_s). \tag{A.107}$$

Henceforth, the explicit reference to the dependence of U_o, U_{sc}, $\delta\mu_a$, and δD on $\vec{r}$ and $\vec{r}_s$ will be dropped for notational simplicity. Note that μ_a^o and D^o are independent of $\vec{r}$. Next, distributing the derivatives across all terms and dividing by D^o results in

$$\left(\nabla^2 U_o\right) U_{sc} + 2\left(\nabla U_o\right) \nabla U_s + U_o \nabla^2 U_{sc} + \left(\nabla F\right)\left(\nabla U_o\right) U_{sc} + \left(\nabla F\right) U_o \nabla U_{sc} + F\left(\nabla^2 U_o\right) U_{sc} + 2\, F\left(\nabla U_o\right) \nabla U_{sc} + F U_o \nabla^2 U_{sc} - \left[\frac{v\mu_a^o + v\delta\mu_a + \imath\omega}{D^o}\right] U_o U_{sc} = -\frac{vB}{D^o}\delta(\vec{r}, \vec{r}_s), \tag{A.108}$$

where F is defined as

$$F \equiv \frac{\delta D}{D^o}. \tag{A.109}$$

Then, given the exponential definition of U_{sc} (see Equation A.105), the derivatives of U_{sc} can be written in terms of ϕ_{sc}, such that

$$\nabla U_{sc} = \left(\nabla \phi_{sc}\right) U_{sc}, \tag{A.110}$$

$$\nabla^2 U_{sc} = \left(\nabla^2 \phi_{sc}\right) U_{sc} + \left(\nabla \phi_{sc}\right)^2 U sc. \tag{A.111}$$

Equations A.110 and A.111 can be substituted into Equation A.108, and then both sides of the equation can be divided by U_{sc}, leaving

$$\nabla^2 U_o + 2\left(\nabla U_o\right)\nabla\phi_{sc} + U_o\nabla^2\phi_{sc} + U_o\left(\nabla\phi_{sc}\right)^2 + \left(\nabla F\right)\nabla U_o + \left(\nabla F\right)U_o\nabla\phi_{sc} + F\nabla^2 U_o + 2F\left(\nabla U_o\right)\nabla\phi_{sc} + FU_o\nabla^2\phi_{sc} + FU_o\left(\nabla\phi_{sc}\right)^2 - \left[\frac{v\mu_a^o + v\delta\mu_a + \imath\omega}{D^o}\right]U_o = -\frac{vB}{D^o U_{sc}(\vec{r}=\vec{r}_s)}\delta(\vec{r},\vec{r}_s). \quad \text{(A.112)}$$

Note that the remaining U_{sc} term is multiplied by a delta function at position $\vec{r} = \vec{r}_s$, *i.e.*, the source position; therefore U_{sc} is evaluated only at $\vec{r} = \vec{r}_s$. At the source position, there is no difference between the fluence for the heterogeneous medium and the fluence in the homogeneous medium. Thus, $U_{sc}(\vec{r} = \vec{r}_{sc}) = 1$, *i.e.*, $U(\vec{r} = \vec{r}_s) = U_o$.

With this formulation, the terms from the homogeneous medium diffusion equation (Equation A.106) can be canceled. Also the following vector calculus identity [39]

$$\nabla^2\left(U_o\phi_{sc}\right) = \left(\nabla^2 U_o\right)\phi_{sc} + U_o\nabla^2\phi_{sc} + 2\left(\nabla U_o\right)\nabla\phi_{sc} \quad \text{(A.113)}$$

can be used to rewrite the $2\left(\nabla U_o\right)\nabla\phi_{sc} + U_o\nabla^2\phi_{sc}$ terms in Equation A.112. This results in the relation

$$\nabla^2\left(U_o\phi_{sc}\right) - \left(\nabla^2 U_o\right)\phi_{sc} = -U_o\left(\nabla\phi_{sc}\right)^2 - \left(\nabla F\right)\nabla U_o - \left(\nabla F\right)U_o\nabla\phi_{sc} - F\nabla^2 U_o - 2F\left(\nabla U_o\right)\nabla\phi_{sc} - FU_o\nabla^2\phi_{sc} - FU_o\left(\nabla\phi_{sc}\right)^2 + HU_o, \quad \text{(A.114)}$$

where

$$H \equiv \frac{v\delta\mu_a}{D^o}. \quad \text{(A.115)}$$

Next, given the homogeneous diffusion equation (Equation A.106), it is apparent that, for all positions $\vec{r} \neq \vec{r}_s$

$$\nabla^2 U_o = k^2 U_o, \quad \text{(A.116)}$$

where

$$k^2 \equiv \frac{v\mu_a^o + \imath\omega}{D^o}. \quad \text{(A.117)}$$

Substituting Equation A.116 into Equation A.114 results in a Helmholtz-like equation of the form

$$\left(\nabla^2 - k^2\right)\left(U_o\phi_{sc}\right) = -U_o\left(\nabla\phi_{sc}\right)^2 - \left(\nabla F\right)\nabla U_o - \left(\nabla F\right)U_o\nabla\phi_{sc} - F\nabla^2 U_o - 2F\left(\nabla U_o\right)\nabla\phi_{sc} - FU_o\nabla^2\phi_{sc} - FU_o\left(\nabla\phi_{sc}\right)^2 + HU_o. \quad \text{(A.118)}$$

The right hand side of this equation can be considered a source term, allowing for the application of Green's theorem to solve for $U_o\phi_{sc}$ at a specific detector position $\vec{r}_d$. In this case, the Green's function solution to this equation will be of the form

$$G \equiv G(\vec{r} - \vec{r}_d). \tag{A.119}$$

Using Green's theorem [9], $U_o\phi_{sc}$ can then be written as

$$\begin{aligned} U_o\phi_{sc} = \\ -\int G \Big[& U_o \left(\nabla\phi_{sc}\right)^2 + \left(\nabla F\right)\nabla U_o + F\nabla^2 U_o + \left(\nabla F\right) U_o \nabla\phi_{sc} + \\ & F U_o \nabla^2\phi_{sc} + F U_o \left(\nabla\phi_{sc}\right)^2 + 2F\left(\nabla U_o\right)\nabla\phi_{sc} - H U_o \Big]\, d^3r. \end{aligned} \tag{A.120}$$

Green's first identity of vector calculus can be used to simplify this equation. This identity relates an integral over the volume of a domain to an integral over the surface of the domain [9], such that

$$\int_V \left[\varphi\nabla^2\psi + \left(\nabla\varphi\right)\nabla\psi\right] d^3r = \oint_S \varphi\,\hat{n}\cdot\nabla\psi\, d^2r. \tag{A.121}$$

Here, φ and ψ are generic functions and $\hat{n}$ is the normal vector on the surface S. Equation A.120 can be simplified if this identity is applied twice: once with $\varphi = GF$ and $\psi = U_o$ and once with $\varphi = GFU_o$ and $\psi = \phi_{sc}$. The resulting simplified equation is

$$\begin{aligned} U_o\phi_{sc} = \\ -\int \Big[& G U_o \left(\nabla\phi_{sc}\right)^2 - \left(\nabla G\right) F\nabla U_o + GF\left(\nabla U_o\right)\nabla\phi_{sc} - \\ & \left(\nabla G\right) F U_o \nabla\phi_{sc} + GF U_o \left(\nabla\phi_{sc}\right)^2 - GH U_o \Big]\, d^3r. \end{aligned} \tag{A.122}$$

Note that both surface integrals from the Green's first identity substitutions went to zero because this solution is for the infinite geometry. Thus, the surface of the volume is at $\vec{r} = \infty$, and the fluence at that surface is 0. In order to apply this infinite geometry solution to bounded geometries, the boundary conditions and image source methods from Section 2.5 are used.

Further simplification of this equation requires the small perturbation approximation in the following forms:

1. Since the perturbation in the fluence is small, $G(\vec{r} - \vec{r}_d) \approx G_o(\vec{r} - \vec{r}_d)$, where G_o is the homogeneous medium Green's function. Therefore, U_o, which is dependent on $\vec{r}_s$, is simply the convolution of a constant term with G_o, which is dependent on $\vec{r}_d$. Thus, given that this solution is symmetric with respect to the source and detector,

$$\int \left(\nabla G\right) F U_o \nabla\phi_{sc}\, d^3r = \int GF\left(\nabla U_o\right)\nabla\phi_{sc}\, d^3r, \tag{A.123}$$

and these two terms cancel in Equation A.122.

2. Because the perturbations in the scattering and the fluence are small, $F \ll 1$ and $(\nabla\phi_{sc})^2 \ll (\nabla G)\,\nabla U_o$. Therefore, the two terms that contain $(\nabla\phi_{sc})^2$ can be approximated as 0.

These two approximations leave the following simplified equation:

$$U_o\phi_{sc} = \int (\nabla G)\, F \nabla U_o \, d^3r + \int G H U_o \, d^3r. \tag{A.124}$$

Finally, in practice, the optical properties and fluence will be calculated over a discrete grid of voxels; therefore, these integrals should become summations. Discretizing Equation A.124, dividing through by U_o, and substituting in the definitions of F and H, results in an expression for ϕ_{sc} at a detector position $\vec{r}_d$ due to a source at position $\vec{r}_s$ of the form

$$\phi_{sc}(\vec{r}_s,\vec{r}_d) = \sum_{n=1}^{N_n}\left[\frac{U_o(\vec{r}_n,\vec{r}_s)G_o(\vec{r}_n-\vec{r}_d)v\,\Delta V}{D^o U_o(\vec{r}_s,\vec{r}_d)}\delta\mu_a(\vec{r}_n) + \frac{(\nabla U_o(\vec{r}_n,\vec{r}_s)\cdot\nabla G_o(\vec{r}_n-\vec{r}_d)v\,\Delta V}{D^o U_o(\vec{r}_s,\vec{r}_d)}\delta D(\vec{r}_n)\right]. \tag{A.125}$$

Here, n is the index of a discrete voxel, or node, in the volume, N_n is the total number of voxels, ΔV is the volume of a single voxel, and $\vec{r}_n$ is the position of the n^{th} voxel. Because this reconstruction of the optical properties will be performed across many voxels and will utilize multiple source-detector pairs, Equation A.125 is actually a matrix equation of the form

$$\begin{bmatrix}\phi_{sc}(\vec{r}_{s_1},\vec{r}_{d_1})\\ \phi_{sc}(\vec{r}_{s_2},\vec{r}_{d_2})\\ \vdots\\ \vdots\\ \vdots\\ \phi_{sc}(\vec{r}_{s_M},\vec{r}_{d_M})\end{bmatrix} = \begin{bmatrix} W^A_{1,1} & \dots & W^A_{1,N} & W^S_{1,1} & \dots & W^S_{1,N}\\ W^A_{2,1} & \dots & W^A_{2,N} & W^S_{2,1} & \dots & W^S_{2,N}\\ \vdots & & \vdots & \vdots & & \vdots\\ \vdots & & \vdots & \vdots & & \vdots\\ \vdots & & \vdots & \vdots & & \vdots\\ W^A_{M,1} & \dots & W^A_{M,N} & W^S_{M,1} & \dots & W^S_{M,N}\end{bmatrix}\begin{bmatrix}\delta\mu_a(\vec{r}_{n_1})\\ \vdots\\ \delta\mu_a(\vec{r}_{n_N})\\ \delta D(\vec{r}_{n_1})\\ \vdots\\ \delta D(\vec{r}_{n_N})\end{bmatrix}. \tag{A.126}$$

Here, $\vec{r}_{s_i}$ and $\vec{r}_{d_i}$ are the positions for the source and detector, respectively, that make up the i^{th} source-detector pair, r_{n_j} is the position of the j^{th} voxel, M is the number of source-detector pairs, N is the number of voxels, and the absorption weight factor $W^A_{i,j}$ and scattering weight factor $W^S_{i,j}$ are defined as

$$W^A_{i,j} \equiv \frac{U_o(\vec{r}_{n_j},\vec{r}_{s_i})G_o(\vec{r}_{d_i}-\vec{r}_{n_j})v\,\Delta V}{D^o U_o(\vec{r}_{s_i},\vec{r}_{d_i})}, \tag{A.127}$$

$$W^S_{i,j} \equiv \frac{\left(\nabla U_o(\vec{r}_{n_j},\vec{r}_{s_i})\right)\left(\nabla G_o(\vec{r}_{d_i}-\vec{r}_{n_j})\right)v\,\Delta V}{D^o U_o(\vec{r}_{s_i},\vec{r}_{d_i})}. \tag{A.128}$$

These three equations are Equations 2.129, 2.130, and 2.131 found in Section 2.6.1.

Bibliography

[1] *Molecular Oncology of Breast Cancer*. Jones and Bartlett Publishers Sudbury, MA (2005).

[2] *Molecular Pathology and Diagnostics of Cancer*. Cancer Growth and Progression. Springer 2014 edition edition (2014).

[3] Matlab 2015a (2015).

[4] Invasive breast cancer (2017).

[5] M. Abramowitz and I. A. Stegun. *Handbook of mathematical functions : with formulas, graphs and mathematical tables*. Dover books on advanced mathematics. Dover Publications New York 9th dover printing, with additional corr. edition (1973).

[6] B. J. Ackerson, R. L. Dougherty, N. M. Reguigui, and U. Nobbman. Correlation transfer: application of radiative transfer solution methods to photon correlation problems. *J Thermophys Heat Tr* **6**, 577–588 (1992).

[7] M. L. Ah-See, A. Makris, N. J. Taylor, M. Harrison, P. I. Richman, R. J. Burcombe, J. J. Stirling, J. A. d'Arcy, D. J. Collins, M. R. Pittam, D. Ravichandran, and A. R. Padhani. Early changes in functional dynamic magnetic resonance imaging predict for pathologic response to neoadjuvant chemotherapy in primary breast cancer. *Clin Cancer Res* **14**(20), 6580–9 (2008).

[8] P. G. Anderson, S. Kalli, A. Sassaroli, N. Krishnamurthy, S. S. Makim, R. A. Graham, and S. Fantini. Optical mammography in patients with breast cancer undergoing neoadjuvant chemotherapy: individual clinical response index. *Acad Radiol* **24**(10), 1240–1255 (2017).

[9] G. B. Arfken and H.-J. Weber. *Mathematical methods for physicists*. Elsevier Academic Amsterdam ; London 6th edition (2005).

[10] S. R. Arridge. Photon-measurement density functions. part i: analytical forms. *Appl Optics* **34**(31), 7395–7409 (1995).

[11] S. R. Arridge, M. Cope, and D. T. Delpy. The theoretical basis for the determination of optical pathlengths in tissue: temporal and frequency analysis. *Phys Med Biol* **37**(7), 1531–1560 (1992).

[12] S. R. Arridge and J. C. Hebden. Optical imaging in medicine. ii. modelling and reconstruction. *Phys Med Biol* **42**(5), 841–853 (1997).

[13] S. R. Arridge and W. R. Lionheart. Nonuniqueness in diffusion-based optical tomography. *Opt Lett* **23**(11), 882–884 (1998).

[14] S. R. Arridge and J. C. Schotland. Optical tomography: forward and inverse problems. *Inverse Probl* **25**(12), 123010 (2009).

[15] S. R. Arridge and M. Schweiger. Photon-measurement density functions. part 2: finite-element-method calculations. *Appl Optics* **34**(34), 8026–8037 (1995).

[16] S. R. Arridge and M. Schweiger. A gradient-based optimisation scheme for optical tomography. *Opt Express* **2**, 213 (1998).

[17] S. R. Arridge, M. Schweiger, M. Hiraoka, and D. T. Delpy. A finite element approach to modelling photon transport in tissue. *Med Phys* **20**(2), 299–309 (1993).

[18] S. Avril, J. Muzic, R. F., D. Plecha, B. J. Traughber, S. Vinayak, and N. Avril. 18f-fdg pet/ct for monitoring of treatment response in breast cancer. *J Nucl Med* **57 Suppl 1**, 34S–9S (2016).

[19] M. Ayers, W. F. Symmans, J. Stec, A. I. Damokosh, E. Clark, K. Hess, M. Lecocke, J. Metivier, D. Booser, N. Ibrahim, V. Valero, M. Royce, B. Arun, G. Whitman, J. Ross, N. Sneige, G. N. Hortobagyi, and L. Pusztai. Gene expression profiles predict complete pathologic response to neoadjuvant paclitaxel and fluorouracil, doxorubicin, and cyclophosphamide chemotherapy in breast cancer. *J Clin Oncol* **22**(12), 2284–93 (2004).

[20] F. S. Azar, K. Lee, A. Khamene, R. Choe, A. Corlu, S. D. Konecky, F. Sauer, and A. G. Yodh. Standardized platform for coregistration of nonconcurrent diffuse optical and magnetic resonance breast images obtained in different geometries. *J Biomed Opt* **12**(5), 051902 (2007).

[21] R. Baierlein. *Thermal physics*. Cambridge University Press Cambridge (1999).

[22] W. B. Baker. *Optical Cerebral Blood Flow Monitoring of Mice to Men*. PhD thesis University of Pennsylvania (2015).

[23] H. Y. Ban. *Spatially-dense, multi-spectral, frequency-domain diffuse optical tomography of breast cancer*. PhD thesis University of Pennsylvania (2016).

[24] H. Y. Ban, D. R. Busch, S. Pathack, F. A. Moscatelli, M. Machida, J. C. Schotland, V. A. Markel, and A. G. Yodh. Diffuse optical tomography in the presence of a chest wall. *J Biomed Opt* **18**(2), 026016–026016 (2013).

[25] H. Y. Ban, M. Schweiger, V. C. Kavuri, J. M. Cochran, L. Xie, D. R. Busch, J. Katrasnik, S. Pathak, S. H. Chung, K. Lee, R. Choe, B. J. Czerniecki, S. R. Arridge, and A. G. Yodh. Heterodyne frequency-domain multispectral diffuse optical tomography of breast cancer in the parallel-plane transmission geometry. *Med Phys* **43**(7), 4383 (2016).

[26] A. Behrooz, H. M. Zhou, A. A. Eftekhar, and A. Adibi. Total variation regularization for 3d reconstruction in fluorescence tomography: experimental phantom studies. *Appl Opt* **51**(34), 8216–27 (2012).

[27] H. C. Berg. *Random walks in biology*. Princeton University Press expanded edition edition (1993).

[28] B. J. Berne and R. Pecora. *Dynamic light scattering with applications to chemistry, biology, and physics*. Krieger Malabar, FL (1990).

[29] D. A. Berry, K. A. Cronin, S. K. Plevritis, D. G. Fryback, L. Clarke, M. Zelen, J. S. Mandelblatt, A. Y. Yakovlev, J. D. Habbema, E. J. Feuer, I. Cancer, and C. Surveillance Modeling Network. Effect of screening and adjuvant therapy on mortality from breast cancer. *N Engl J Med* **353**(17), 1784–92 (2005).

[30] F. Bevilacqua, A. J. Berger, A. E. Cerussi, D. Jakubowski, and B. J. Tromberg. Broadband absorption spectroscopy in turbid media by combined frequency-domain and steady-state methods. *Appl Optics* **39**(34), 6498–507 (2000).

[31] R. B. Bird, W. E. Stewart, E. N. Lightfoot, Alumni, and F. M. B. Fund. *Transport phenomena*. J. Wiley New York rev. 2nd edition (2007).

[32] D. A. Boas. *Diffuse photon probes of structural and dynamical properties of turbid media: theory and biomedical applications*. PhD thesis University of Pennsylvania (1996).

[33] D. A. Boas, L. E. Campbell, and A. G. Yodh. Scattering and imaging with diffusing temporal field correlations. *Phys Rev Lett* **75**(9), 1855–1858 (1995).

[34] D. A. Boas, A. M. Dale, and M. A. Franceschini. Diffuse optical imaging of brain activation: approaches to optimizing image sensitivity, resolution, and accuracy. *Neuroimage* **23 Suppl 1**, S275–S288 (2004).

[35] D. A. Boas and A. K. Dunn. Laser speckle contrast imaging in biomedical optics. *J Biomed Opt* **15**(1), 011109 (2010).

[36] D. A. Boas, M. A. Oleary, B. Chance, and A. G. Yodh. Scattering of diffuse photon density waves by spherical inhomogeneities within turbid media: analytic solution and applications. *P Natl Acad Sci USA* **91**(11), 4887–4891 (1994).

[37] D. A. Boas, S. Sakadzic, J. Selb, P. Farzam, M. A. Franceschini, and S. A. Carp. Establishing the diffuse correlation spectroscopy signal relationship with blood flow. *Neurophotonics* **3**(3), 031412 (2016).

[38] D. A. Boas and A. G. Yodh. Spatially varying dynamical properties of turbid media probed with diffusing temporal light correlation. *J Opt Soc Am A* **14**(1), 192–215 (1997).

[39] M. L. Boas. *Mathematical methods in the physical sciences*. John Wiley Hoboken, N.J. 3rd edition (2006).

[40] G. Bonadonna, G. N. Hortobagyi, and A. M. Gianni. *Textbook of breast cancer : a clinical guide to therapy*. Dunitz London 2nd edition (2001).

[41] G. Boverman, E. L. Miller, A. Li, Q. Zhang, T. Chaves, D. H. Brooks, and D. A. Boas. Quantitative spectroscopic diffuse optical tomography of the breast guided by imperfect a priori structural information. *Phys Med Biol* **50**(17), 3941–3956 (2005).

[42] N. Boyd, L. Martin, S. Chavez, A. Gunasekara, A. Salleh, O. Melnichouk, M. Yaffe, C. Friedenreich, S. Minkin, and M. Bronskill. Breast-tissue composition and other risk factors for breast cancer in young women: a cross-sectional study. *Lancet Oncol* **10**(6), 569 – 580 (2009).

[43] R. W. Boyd. *Nonlinear optics*. Academic Press Amsterdam ; London 3rd edition (2008).

[44] H. Bradt. *Astronomy methods : a physical approach to astronomical observations*. Cambridge University Press Cambridge (2004).

[45] J. E. Brazy. Cerebral oxygen monitoring with near-infrared spectroscopy: clinical application to neonates. *J Clin Monitor* **7**(4), 325–334 (1991).

[46] B. Brooksby, S. Jiang, H. Dehghani, B. W. Pogue, K. D. Paulsen, C. Kogel, M. Doyley, J. B. Weaver, and S. P. Poplack. Magnetic resonance-guided near-infrared tomography of the breast. *Rev Sci Instrum* **75**, 5262 (2004).

[47] B. Brooksby, S. Jiang, H. Dehghani, B. W. Pogue, K. D. Paulsen, J. Weaver, C. Kogel, and S. P. Poplack. Combining near-infrared tomography and magnetic resonance imaging to study in vivo breast tissue: implementation of a laplacian-type regularization to incorporate magnetic resonance structure. *J Biomed Opt* **10**(5), 051504 (2005).

[48] W. Brown, editor. *Dynamic light scattering: the method and some applications*. Monographs on the Physics and Chemistry of Materials. New Yrok: Clarendon Press (1993).

[49] G. Bryan. An application of the method of images to the conduction of heat. *Proc London Math Soc* **22**, 424–430 (1891).

[50] E. M. Buckley, N. M. Cook, T. Durduran, M. N. Kim, C. Zhou, R. Choe, G. Q. Yu, S. Shultz, C. M. Sehgal, D. J. Licht, P. H. Arger, M. E. Putt, H. Hurt, and A. G. Yodh. Cerebral hemodynamics in preterm infants during positional intervention measured with diffuse correlation spectroscopy and transcranial doppler ultrasound. *Opt Express* **17**(15), 12571–12581 (2009).

[51] E. M. Buckley, D. Hance, T. Pawlowski, J. Lynch, F. B. Wilson, R. C. Mesquita, T. Durduran, L. K. Diaz, M. E. Putt, D. J. Licht, M. A. Fogel, and A. G. Yodh. Validation of diffuse correlation spectroscopic measurement of cerebral blood flow using phase-encoded velocity mapping magnetic resonance imaging. *J Biomed Opt* **17**(3), 037007 (2012).

[52] D. R. Busch. *Computer-aided, multi-modal, and Compression diffuse optical studies of breast tissue*. PhD thesis University of Pennsylvania (2011).

[53] D. R. Busch, R. Choe, T. Durduran, D. H. Friedman, W. B. Baker, A. D. Maidment, M. A. Rosen, M. D. Schnall, and A. G. Yodh. Blood flow reduction in breast tissue due to mammographic compression. *Acad Radiol* **21**(2), 151–61 (2014).

[54] D. R. Busch, R. Choe, T. Durduran, and A. G. Yodh. Towards non-invasive characterization of breast cancer and cancer metabolism with diffuse optics. *PET Clin* **8**(3) (2013).

[55] D. R. Busch, R. Choe, M. A. Rosen, W. Guo, T. Durduran, M. D. Feldman, C. Mies, B. J. Czerniecki, J. Tchou, A. Demichele, M. D. Schnall, and A. G. Yodh. Optical malignancy

parameters for monitoring progression of breast cancer neoadjuvant chemotherapy. *Biomed Opt Express* **4**(1), 105–21 (2013).

[56] D. R. Busch, W. Guo, R. Choe, T. Durduran, M. D. Feldman, C. Mies, M. A. Rosen, M. D. Schnall, B. J. Czerniecki, J. Tchou, A. DeMichele, M. E. Putt, and A. G. Yodh. Computer aided automatic detection of malignant lesions in diffuse optical mammography. *Med Phys* **37**(4), 1840–9 (2010).

[57] P. Carmeliet and R. K. Jain. Angiogenesis in cancer and other diseases. *Nature* **407**, 249–257 (2000).

[58] H. S. Carslaw and J. C. Jaeger. *Conduction of heat in solids*. Clarendon Oxford 2nd edition (1986).

[59] A. Cerussi, D. Hsiang, N. Shah, R. Mehta, A. Durkin, J. Butler, and B. J. Tromberg. Predicting response to breast cancer neoadjuvant chemotherapy using diffuse optical spectroscopy. *Proc Natl Acad Sci U S A* **104**(10), 4014–9 (2007).

[60] A. Cerussi, N. Shah, D. Hsiang, A. Durkin, J. Butler, and B. J. Tromberg. In vivo absorption, scattering, and physiologic properties of 58 malignant breast tumors determined by broadband diffuse optical spectroscopy. *J Biomed Opt* **11**(4), 044005 (2006).

[61] A. E. Cerussi, V. W. Tanamai, D. Hsiang, J. Butler, R. S. Mehta, and B. J. Tromberg. Diffuse optical spectroscopic imaging correlates with final pathological response in breast cancer neoadjuvant chemotherapy. *Philos Trans A Math Phys Eng Sci* **369**(1955), 4512–30 (2011).

[62] B. Chabner and D. L. Longo. *Cancer chemotherapy and biotherapy : principles and practice*. Wolters Kluwer/Lippincott Williams & Wilkins Health Philadelphia 5th edition (2011).

[63] B. Chance, M. Cope, E. Gratton, N. Ramanujam, and B. Tromberg. Phase measurement of light absorption and scatter in human tissue. *Rev Sci Instrum* **69** (1998).

[64] B. Chance, M. T. Dait, C. Zhang, T. Hamaoka, and F. Hagerman. Recovery from exercise-induced desaturation in the quadriceps muscles of elite competitive rowers. *Am J Physiol* **262**(3 Pt 1), C766–C775 (1992).

[65] B. Chance, J. S. Leigh, H. Miyake, D. S. Smith, S. Nioka, R. Greenfeld, M. Finander, K. Kaufmann, W. Levy, and M. Young. Comparison of time-resolved and -unresolved measurements of deoxyhemoglobin in brain. *P Natl Acad Sci USA* **85**(14), 4971–4975 (1988).

[66] B. Chance, S. Nioka, J. Kent, K. McCully, M. Fountain, R. Greenfeld, and G. Holtom. Time-resolved spectroscopy of hemoglobin and myoglobin in resting and ischemic muscle. *Anal Biochem* **174**(2), 698–707 (1988).

[67] B. Chance, S. Nioka, J. Zhang, E. F. Conant, E. Hwang, S. Briest, S. G. Orel, M. D. Schnall, and B. J. Czerniecki. Breast cancer detection based on incremental biochemical and physiological properties of breast cancers: a six-year, two-site study. *Acad Radiol* **12**(8), 925–933 (2005).

[68] S. Chandrasekhar. Stochastic problems in physics and astronomy. *Rev Mod Phys* **15**(1), 1–89 (1943).

[69] C. Cheung, J. P. Culver, K. Takahashi, J. H. Greenberg, and A. G. Yodh. In vivo cerebrovascular measurement combining diffuse near-infrared absorption and correlation spectroscopies. *Phys Med Biol* **46**, 2053–2065 (2001).

[70] R. Choe, A. Corlu, K. Lee, T. Durduran, S. D. Konecky, M. Grosicka-Koptyra, S. R. Arridge, B. J. Czerniecki, D. L. Fraker, A. DeMichele, B. Chance, M. A. Rosen, and A. G. Yodh. Diffuse optical tomography of breast cancer during neoadjuvant chemotherapy: A case study with comparison to mri. *Med Phys* **32**(4), 1128–1139 (2005).

[71] R. Choe and T. Durduran. Diffuse optical monitoring of the neoadjuvant breast cancer therapy. *IEEE J Sel Top Quant* **18**(4), 1367–1386 (2012).

[72] R. Choe, S. D. Konecky, A. Corlu, K. Lee, T. Durduran, D. R. Busch, S. Pathak, B. J. Czerniecki, J. Tchou, D. L. Fraker, A. Demichele, B. Chance, S. R. Arridge, M. Schweiger, J. P. Culver, M. D. Schnall, M. E. Putt, M. A. Rosen, and A. G. Yodh. Differentiation of benign and malignant breast tumors by in-vivo three-dimensional parallel-plate diffuse optical tomography. *J Biomed Opt* **14**(2), 024020 (2009).

[73] R. Choe, M. E. Putt, P. M. Carlile, T. Durduran, J. M. Giammarco, D. R. Busch, K. W. Jung, B. J. Czerniecki, J. Tchou, M. D. Feldman, C. Mies, M. A. Rosen, M. D. Schnall, A. DeMichele, and A. G. Yodh. Optically measured microvascular blood flow contrast of malignant breast tumors. *PLoS One* **9**(6), e99683 (2014).

[74] B. Chu. *Laser light scattering, basic principles and practice.* Academic New York (1991).

[75] J. M. Cochran, D. R. Busch, A. Leproux, Z. Zhang, T. D. O'Sullivan, A. E. Cerussi, P. M. Carpenter, R. Mehta, D. Roblyer, K. D. Paulsen, B. Pogue, S. Jiang, P. A. Kaufman, C. S.

H., M. Schnall, B. S. Snyder, N. Hylton, S. A. Carp, S. J. Isakoff, D. Mankoff, B. J. Tromberg, and A. G. Yodh. Tissue oxygen saturation predicts response to breast cancer neoadjuvant chemotherapy within 10 days of treatment. *J Biomed Opt* , In Submission (2018).

[76] J. M. Cochran, S. H. Chung, A. Leproux, W. B. Baker, D. R. Busch, A. M. DeMichele, J. Tchou, B. J. Tromberg, and A. G. Yodh. Longitudinal optical monitoring of blood flow in breast tumors during neoadjuvant chemotherapy. *Phys Med Biol* **62**(12), 4637–4653 (2017).

[77] A. Corlu. *Multi-spectral and fluorescence diffuse optical tomography of breast cancer*. PhD thesis University of Pennsylvania (2007).

[78] A. Corlu, R. Choe, T. Durduran, K. Lee, M. Schweiger, E. M. C. Hillman, S. R. Arridge, and A. G. Yodh. Diffuse optical tomography with spectral constraints and wavelength optimization. *Appl Optics* **44**, 2082–2093 (2005).

[79] A. Corlu, T. Durduran, R. Choe, M. Schweiger, E. M. Hillman, S. R. Arridge, and A. G. Yodh. Uniqueness and wavelength optimization in continuous-wave multispectral diffuse optical tomography. *Opt Lett* **28**(23), 2339–41 (2003).

[80] J. P. Culver, R. Choe, M. J. Holboke, L. Zubkov, T. Durduran, A. Slemp, V. Ntziachristos, B. Chance, and A. G. Yodh. Three-dimensional diffuse optical tomography in the parallel plane transmission geometry: evaluation of a hybrid frequency domain/continuous wave clinical system for breast imaging. *Med Phys* **30**, 235–247 (2003).

[81] J. P. Culver, V. Ntziachristos, M. J. Holboke, and A. G. Yodh. Optimization of optode arrangements for diffuse optical tomography: A singular-value analysis. *Opt Lett* **26**, 701–703 (2001).

[82] M. Cutler. Transillumination as an aid in the diagnosis of breast lesions. *Surg Gynecol Obstet* **48**, 721–29 (1929).

[83] H. Dehghani, B. Brooksby, K. Vishwanath, B. W. Pogue, and K. D. Paulsen. The effects of internal refractive index variation in near-infrared optical tomography: a finite element modelling approach. *Phys Med Biol* **48**(16), 2713–2727 (2003).

[84] H. Dehghani, M. E. Eames, P. K. Yalavarthy, S. C. Davis, S. Srinivasan, C. M. Carpenter, B. W. Pogue, and K. D. Paulsen. Near infrared optical tomography using nirfast: Algorithm for numerical model and image reconstruction. *Int J Numer Meth Bio* **25**(6), 711–732 (2009).

[85] S. Del Bianco, F. Martelli, and G. Zaccanti. Penetration depth of light re-emitted by a diffusive medium: theoretical and experimental investigation. *Phys Med Biol* **47**(23), 4131–4144 (2002).

[86] E. R. DeLong, D. M. DeLong, and D. L. Clarke-Pearson. Comparing the areas under two or more correlated receiver operating characteristic curves: a nonparametric approach. *Biometrics* **44**(3), 837–45 (1988).

[87] D. T. Delpy, M. Cope, P. van der Zee, S. Arridge, S. Wray, and J. Wyatt. Estimation of optical pathlength through tissue from direct time of flight measurement. *Phys Med Biol* **33**(12), 1433–1442 (1988).

[88] B. Deng, M. Lundqvist, Q. Fang, and S. A. Carp. Impact of errors in experimental parameters on reconstructed breast images using diffuse optical tomography. *Biomed Opt Express* **9**(3), 1130–1150 (2018).

[89] C. E. DeSantis, J. Ma, A. Goding Sauer, L. A. Newman, and A. Jemal. Breast cancer statistics, 2017, racial disparity in mortality by state. *CA Cancer J Clin* **67**(6), 439–448 (2017).

[90] M. W. Dewhirst, H. Kimura, S. W. Rehmus, R. D. Braun, D. Papahadjopoulos, K. Hong, and T. W. Secomb. Microvascular studies on the origins of perfusion-limited hypoxia. *Brit J Cancer Suppl* **27**, S247–S251 (1996).

[91] M. Diop, K. Verdecchia, T. Y. Lee, and K. St Lawrence. Calibration of diffuse correlation spectroscopy with a time-resolved near-infrared technique to yield absolute cerebral blood flow measurements. *Biomed Opt Express* **2**(7), 2068–2081 (2011).

[92] L. Dougherty, G. Isaac, M. A. Rosen, L. W. Nunes, P. J. Moate, R. C. Boston, M. D. Schnall, and H. K. Song. High frame-rate simultaneous bilateral breast dce-mri. *Magn Reson Med* **57**(1), 220–5 (2007).

[93] R. L. Dougherty, B. J. Ackerson, N. M. Reguigui, F. Dorri-Nowkoorani, and U. Nobbmann. Correlation transfer: development and application. *J Quant Spectrosc Ra* **52**, 713–727 (1994).

[94] M. Dowsett, I. Smith, J. Robertson, L. Robison, I. Pinhel, L. Johnson, J. Salter, A. Dunbier, H. Anderson, Z. Ghazoui, T. Skene, A. Evans, R. A'Hern, A. Iskender, M. Wilcox, and J. Bliss. Endocrine therapy, new biologicals, and new study designs for presurgical studies in breast cancer. *J Natl Cancer Inst Monogr* **2011**(43), 120–3 (2011).

[95] H. K. Dressman, C. Hans, A. Bild, J. A. Olson, E. Rosen, P. K. Marcom, V. B. Liotcheva, E. L. Jones, Z. Vujaskovic, J. Marks, M. W. Dewhirst, M. West, J. R. Nevins, and K. Blackwell. Gene expression profiles of multiple breast cancer phenotypes and response to neoadjuvant chemotherapy. *Clin Cancer Res* **12**(3 Pt 1), 819–26 (2006).

[96] A. K. Dunn, A. Devor, H. Bolay, M. L. Andermann, M. A. Moskowitz, A. M. Dale, and D. A. Boas. Simultaneous imaging of total cerebral hemoglobin concentration, oxygenation, and blood flow during functional activation. *Opt Lett* **28**(1), 28–30 (2003).

[97] T. Durduran. *Noninvasive measurements of tissue hemodynamics with hybrid diffuse optical methods*. PhD thesis University of Pennsylvania (2004).

[98] T. Durduran, R. Choe, W. B. Baker, and A. G. Yodh. Diffuse optics for tissue monitoring and tomography. *Rep Prog Phys* **73**(7) (2010).

[99] T. Durduran, R. Choe, J. P. Culver, L. Zubkov, M. J. Holboke, J. Giammarco, B. Chance, and A. G. Yodh. Bulk optical properties of healthy female breast tissue. *Phys Med Biol* **47**, 2847–2861 (2002).

[100] T. Durduran, R. Choe, G. Yu, C. Zhou, J. C. Tchou, B. J. Czerniecki, and A. G. Yodh. Diffuse optical measurement of blood flow in breast tumors. *Opt Lett* **30**(21), 2915–7 (2005).

[101] T. Durduran, G. Yu, M. G. Burnett, J. A. Detre, J. H. Greenberg, J. Wang, C. Zhou, and A. G. Yodh. Diffuse optical measurement of blood flow, blood oxygenation, and metabolism in a human brain during sensorimotor cortex activation. *Opt Lett* **29**(15), 1766–8 (2004).

[102] M. E. Eames, J. Wang, B. W. Pogue, and H. Dehghani. Wavelength band optimization in spectral near-infrared optical tomography improves accuracy while reducing data acquisition and computational burden. *J Biomed Opt* **13**(5), 054037 (2008).

[103] C. H. Edwards and D. E. Penney. *Differential Equations & Linear Algebra*. Pearson Upper Saddle River, NJ third edition (2010).

[104] A. T. Eggebrecht, B. R. White, S. L. Ferradal, C. Chen, Y. Zhan, A. Z. Snyder, H. Dehghani, and J. P. Culver. A quantitative spatial comparison of high-density diffuse optical tomography and fmri cortical mapping. *Neuroimage* **61**(4), 1120–8 (2012).

[105] F. El-Ghussein, M. A. Mastanduno, S. Jiang, B. W. Pogue, and K. D. Paulsen. Hybrid photomultiplier tube and photodiode parallel detection array for wideband optical spectroscopy of the breast guided by magnetic resonance imaging. *J Biomed Opt* **19**(1), 011010 (2014).

[106] L. C. Enfield, A. P. Gibson, N. L. Everdell, D. T. Delpy, M. Schweiger, S. R. Arridge, C. Richardson, M. Keshtgar, M. Douek, and J. C. Hebden. Three-dimensional time-resolved optical mammography of the uncompressed breast. *Appl Optics* **46**(17), 3628–3638 (2007).

[107] L. J. Esserman, D. A. Berry, M. C. Cheang, C. Yau, C. M. Perou, L. Carey, A. DeMichele, J. W. Gray, K. Conway-Dorsey, M. E. Lenburg, M. B. Buxton, S. E. Davis, L. J. van't Veer, C. Hudis, K. Chin, D. Wolf, H. Krontiras, L. Montgomery, D. Tripathy, C. Lehman, M. C. Liu, O. I. Olopade, H. S. Rugo, J. T. Carpenter, C. Livasy, L. Dressler, D. Chhieng, B. Singh, C. Mies, J. Rabban, Y. Y. Chen, D. Giri, A. Au, and N. Hylton. Chemotherapy response and recurrence-free survival in neoadjuvant breast cancer depends on biomarker profiles: results from the i-spy 1 trial (calgb 150007/150012; acrin 6657). *Breast Cancer Res Tr* **132**(3), 1049–62 (2012).

[108] L. J. Esserman, D. A. Berry, A. DeMichele, L. Carey, S. E. Davis, M. Buxton, C. Hudis, J. W. Gray, C. Perou, C. Yau, C. Livasy, H. Krontiras, L. Montgomery, D. Tripathy, C. Lehman, M. C. Liu, O. I. Olopade, H. S. Rugo, J. T. Carpenter, L. Dressler, D. Chhieng, B. Singh, C. Mies, J. Rabban, Y. Y. Chen, D. Giri, L. van 't Veer, and N. Hylton. Pathologic complete response predicts recurrence-free survival more effectively by cancer subset: results from the i-spy 1 trial–calgb 150007/150012, acrin 6657. *J Clin Oncol* **30**(26), 3242–9 (2012).

[109] O. Falou, H. Soliman, A. Sadeghi-Naini, S. Iradji, S. Lemon-Wong, J. Zubovits, J. Spayne, R. Dent, M. Trudeau, J. F. Boileau, F. C. Wright, M. J. Yaffe, and G. J. Czarnota. Diffuse optical spectroscopy evaluation of treatment response in women with locally advanced breast cancer receiving neoadjuvant chemotherapy. *Transl Oncol* **5**(4), 238–46 (2012).

[110] Q. Fang, S. A. Carp, J. Selb, G. Boverman, Q. Zhang, D. B. Kopans, R. H. Moore, E. L. Miller, D. H. Brooks, and D. A. Boas. Combined optical imaging and mammography of the healthy breast: optical contrast derived from breast structure and compression. *IEEE T Med Imaging* **28**(1), 30–42 (2009).

[111] Q. Fang, J. Selb, S. A. Carp, G. Boverman, E. L. Miller, D. H. Brooks, R. H. Moore, D. B. Kopans, and D. A. Boas. Combined optical and x-ray tomosynthesis breast imaging. *Radiology* **258**(1), 89–97 (2011).

[112] S. Fantini, M. A. Franceschini, J. B. Fishkin, B. Barbieri, and E. Gratton. Quantitative determination of the absorption spectra of chromophores in strongly scattering media: a light-emitting-diode based technique. *Appl Opt* **33**(22), 5204–13 (1994).

[113] T. J. Farrell, M. S. Patterson, and B. Wilson. A diffusion theory model of spatially resolved, steady-state diffuse reflectance for the noninvasive determination of tissue optical properties in vivo. *Med Phys* **19**(4), 879–888 (1992).

[114] P. Farzam and T. Durduran. Multidistance diffuse correlation spectroscopy for simultaneous estimation of blood flow index and optical properties. *J Biomed Opt* **20**(5), 55001 (2015).

[115] T. Fawcett. An introduction to roc analysis. *Pattern Recogn Lett* **27**(8), 861–874 (2006).

[116] L. D. Feldman, G. N. Hortobagyi, A. U. Buzdar, F. C. Ames, and G. R. Blumenschein. Pathological assessment of response to induction chemotherapy in breast cancer. *Cancer Res* **46**(5), 2578–81 (1986).

[117] J. Feng, S. Jiang, J. Xu, Y. Zhao, B. W. Pogue, and K. D. Paulsen. Multiobjective guided priors improve the accuracy of near-infrared spectral tomography for breast imaging. *J Biomed Opt* **21**(9), 90506 (2016).

[118] A. Fick. Uber die messung des blutquantums in der hertzvent rikeln. *Sitzber Physik Med Ges Wurzburg* **36** (1870).

[119] J. Folkman. Angiogenesis in cancer, vascular, rheumatoid and other disease. *Nat Med* **1**(1), 27–31 (1995).

[120] M. A. Franceschini, K. T. Moesta, S. Fantini, G. Gaida, E. Gratton, H. Jess, W. W. Mantulin, M. Seeber, P. M. Schlag, and M. Kaschke. Frequency-domain techniques enhance optical mammography: initialclinical results. *P Natl Acad Sci USA* **94**(12), 6468–6473 (1997).

[121] P. B. Garcia-Allende, K. Radrich, P. Symvoulidis, J. Glatz, M. Koch, K. M. Jentoft, J. Ripoll, and V. Ntziachristos. Uniqueness in multispectral constant-wave epi-illumination imaging. *Opt Lett* **41**(13), 3098–101 (2016).

[122] A. Garofalakis, A. Dubois, B. Thézé, B. Czarny, B. Tavitian, and F. Ducongé. Fusion of [18 f] fdg pet with fluorescence diffuse optical tomography to improve validation of probes and tumor imaging. *Mol Imaging Biol* , 1–10 (2012).

[123] R. J. Gaudette, D. H. Brooks, C. A. DiMarzio, M. E. Kilmer, E. L. Miller, T. Gaudette, and D. A. Boas. A comparison study of linear reconstruction techniques for diffuse optical tomographic imaging of absorption coefficient. *Phys Med Biol* **45**(4), 1051–1070 (2000).

[124] C. P. Gonatas, M. Ishii, J. S. Leigh, and J. C. Schotland. Optical diffusion imaging using a direct inversion method. *Phys Rev E Stat Phys Plasmas Fluids Relat Interdiscip Topics* **52**(4), 4361–4365 (1995).

[125] A. M. Gonzalez-Angulo, B. T. Hennessy, F. Meric-Bernstam, A. Sahin, W. Liu, Z. Ju, M. S. Carey, S. Myhre, C. Speers, L. Deng, R. Broaddus, A. Lluch, S. Aparicio, P. Brown, L. Pusztai, W. F. Symmans, J. Alsner, J. Overgaard, A. L. Borresen-Dale, G. N. Hortobagyi, K. R. Coombes, and G. B. Mills. Functional proteomics can define prognosis and predict pathologic complete response in patients with breast cancer. *Clin Proteom* **8**(1), 11 (2011).

[126] J. W. Goodman. *Speckle Phenomena in Optics: Theory and Applications* volume 1. (2007).

[127] D. Griffiths. *Introduction to quantum mechanics*. Addison-Wesley (2005).

[128] R. A. J. Groenhuis, H. A. Ferwerda, and J. J. Ten Bosch. Scattering and absorption of turbid materials determined from reflection measurements. 1: Theory. *Appl Optics* **22**(16), 2456–2462 (1983).

[129] D. Grosenick, H. Wabnitz, H. H. Rinneberg, K. T. Moesta, and P. M. Schlag. Development of a time-domain optical mammograph and first in vivo applications. *Appl Optics* **38**(13), 2927–2943 (1999).

[130] M. Guven, B. Yazici, X. Intes, and B. Chance. Diffuse optical tomography with a priori anatomical information. *Phys Med Biol* **50**(12), 2837 (2005).

[131] L. A. Habel, A. M. Capra, N. S. Achacoso, A. Janga, L. Acton, B. Puligandla, and C. P. Quesenberry. Mammographic density and risk of second breast cancer after ductal carcinoma in situ. *Cancer Epidem Biomar* **19**(10), 2488–2495 (2010).

[132] J. A. Hanley and B. J. McNeil. The meaning and use of the area under a receiver operating characteristic (roc) curve. *Radiology* **143**(1) (1982).

[133] P. Hansen. Analysis of discrete ill-posed problems by means of the l-curve. *SIAM Rev* **34**, 561–580 (1992).

[134] P. Hansen and D. O'Leary. The use of the l-curve in the regularization of discrete ill-posed problems. *SIAM J Sci Comput* **14**, 1487–1503 (1993).

[135] R. C. Haskell, L. O. Svaasand, T. T. Tsay, T. C. Feng, M. S. McAdams, and B. J. Tromberg. Boundary conditions for the diffusion equation in radiative-transfer. *J Opt Soc Am* **11(10)**, 2727–2741 (1994).

[136] T. Hastie, R. Tibshirani, and J. Friedman. *The elements of statistical learning: data mining, inference, and prediction*. Springer Series in Statistics. Springer Science & Business Media second edition (2008).

[137] E. Hecht. *Optics*. Addison Wesley San Francisco ; London 4th edition (2002).

[138] M. A. Helvie, L. K. Joynt, R. L. Cody, L. J. Pierce, D. D. Adler, and S. D. Merajver. Locally advanced breast carcinoma: accuracy of mammography versus clinical examination in the prediction of residual disease after chemotherapy. *Radiology* **198**(2), 327–32 (1996).

[139] M. Hockel and P. Vaupel. Tumor hypoxia: definitions and current clinical, biologic, and molecular aspects. *J Natl Cancer I* **93**(4), 266–76 (2001).

[140] M. J. Holboke, B. J. Tromberg, X. Li, N. Shah, J. Fishkin, D. Kidney, J. Butler, B. Chance, and A. G. Yodh. Three-dimensional diffuse optical mammography with ultrasound localization in a human subject. *J Biomed Opt* **5**, 237–247 (2000).

[141] D. W. Hosmer, S. Lemeshow, and R. X. Sturdivant. Applied logistic regression (2013).

[142] D. Hsiang, N. Shah, H. Yu, M. Y. Su, A. Cerussi, J. Butler, C. Baick, R. Mehta, O. Nalcioglu, and B. Tromberg. Coregistration of dynamic contrast enhanced mri and broadband diffuse optical spectroscopy for characterizing breast cancer. *Technol Cancer Res T* **4**(5), 549–58 (2005).

[143] O. Humbert, J. M. Riedinger, C. Charon-Barra, A. Berriolo-Riedinger, I. Desmoulins, V. Lorgis, S. Kanoun, C. Coutant, P. Fumoleau, A. Cochet, and F. Brunotte. Identification of biomarkers including 18fdg-pet/ct for early prediction of response to neoadjuvant chemotherapy in triple-negative breast cancer. *Clin Cancer Res* **21**(24), 5460–8 (2015).

[144] N. M. Hylton, J. D. Blume, W. K. Bernreuter, E. D. Pisano, M. A. Rosen, E. A. Morris, P. T. Weatherall, C. D. Lehman, G. M. Newstead, S. Polin, H. S. Marques, L. J. Esserman, and M. D. Schnall. Locally advanced breast cancer: Mr imaging for prediction of response to neoadjuvant chemotherapy–results from acrin 6657/i-spy trial. *Radiology* **263**(3), 663–72 (2012).

[145] X. Intes, C. Maloux, M. Guven, B. Yazici, and B. Chance. Diffuse optical tomography with physiological and spatial a priori constraints. *Phys Med Biol* **49**(12), N155 (2004).

[146] X. Intes, J. Ripoll, Y. Chen, S. Nioka, A. G. Yodh, and B. Chance. In vivo continuous-wave optical breast imaging enhanced with indocyanine green. *Med Phys* **30**(6), 1039–1047 (2003).

[147] D. Irwin, L. Dong, Y. Shang, R. Cheng, M. Kudrimoti, S. D. Stevens, and G. Yu. Influences of tissue absorption and scattering on diffuse correlation spectroscopy blood flow measurements. *Biomed Opt Express* **2**(7), 1969–85 (2011).

[148] S. L. Jacques. Optical properties of biological tissues: a review. *Phys Med Biol* **58**(11), R37–61 (2013).

[149] F. Jaillon, S. E. Skipetrov, J. Li, G. Dietsche, G. Maret, and T. Gisler. Diffusing-wave spectroscopy from head-like tissue phantoms: influence of a non-scattering layer. *Opt Express* **14**(22), 10181–10194 (2006).

[150] R. K. Jain. Normalization of tumor vasculature: an emerging concept in antiangiogenic therapy. *Science* **307**(5706), 58–62 (2005).

[151] V. Jain, E. M. Buckley, D. J. Licht, J. M. Lynch, P. J. Schwab, M. Y. Naim, N. A. Lavin, S. C. Nicolson, L. M. Montenegro, A. G. Yodh, and F. W. Wehrli. Cerebral oxygen metabolism in neonates with congenital heart disease quantified by mri and optics. *J Cerebr Blood F Met* **34**(3), 380–8 (2014).

[152] A. A. Jazaeri, C. S. Awtrey, G. V. Chandramouli, Y. E. Chuang, J. Khan, C. Sotiriou, O. Aprelikova, C. J. Yee, K. K. Zorn, M. J. Birrer, J. C. Barrett, and J. Boyd. Gene expression profiles associated with response to chemotherapy in epithelial ovarian cancers. *Clin Cancer Res* **11**(17), 6300–10 (2005).

[153] M. Jermyn, J. Mercier, K. Aubertin, J. Desroches, K. Urmey, J. Karamchandiani, E. Marple, M. C. Guiot, F. Leblond, and K. Petrecca. Highly accurate detection of cancer in situ with intraoperative, label-free, multimodal optical spectroscopy. *Cancer Res* **77**(14), 3942–3950 (2017).

[154] S. Jiang, B. W. Pogue, C. M. Carpenter, S. P. Poplack, W. A. Wells, C. A. Kogel, J. A. Forero, L. S. Muffly, G. N. Schwartz, K. D. Paulsen, and P. A. Kaufman. Evaluation of breast tumor response to neoadjuvant chemotherapy with tomographic diffuse optical spectroscopy: case studies of tumor region-of-interest changes. *Radiology* **252**(2), 551–60 (2009).

[155] F. F. Jobsis. Noninvasive, infrared monitoring of cerebral and myocardial oxygen sufficiency and circulatory parameters. *Science* **198**(4323), 1264–1267 (1977).

[156] F. Jobsis-Vander Vliet. Non-invasive, near infrared monitoring of cellular oxygen sufficiency in vivo. *Adv Exp Med Bio* **191**, 833–841 (1985).

[157] D. K. Joseph, T. J. Huppert, M. A. Franceschini, and D. A. Boas. Diffuse optical tomography system to image brain activation with improved spatial resolution and validation with functional magnetic resonance imaging. *Appl Optics* **45**(31), 8142–8151 (2006).

[158] M. N. Kim, T. Durduran, S. Frangos, B. L. Edlow, E. M. Buckley, H. E. Moss, C. Zhou, G. Q. Yu, R. Choe, E. Maloney-Wilensky, R. L. Wolf, M. S. Grady, J. H. Greenberg, J. M. Levine, A. G. Yodh, J. A. Detre, and W. A. Kofke. Noninvasive measurement of cerebral blood flow and blood oxygenation using near-infrared and diffuse correlation spectroscopies in critically brain-injured adults. *Neurocrit Care* **12**(2), 173–180 (2010).

[159] S. D. Konecky, G. Y. Panasyuk, K. Lee, V. A. Markel, A. G. Yodh, and J. C. Schotland. Imaging complex structures with diffuse light. *Opt Express* **16**(7), 5048–5060 (2008).

[160] L. Kostakoglu, F. Duan, M. O. Idowu, P. R. Jolles, H. D. Bear, M. Muzi, J. Cormack, J. P. Muzi, D. A. Pryma, J. M. Specht, L. Hovanessian-Larsen, J. Miliziano, S. Mallett, A. F. Shields, D. A. Mankoff, and A. I. Team. A phase ii study of 3'-deoxy-3'-18f-fluorothymidine pet in the assessment of early response of breast cancer to neoadjuvant chemotherapy: Results from acrin 6688. *J Nucl Med* **56**(11), 1681–9 (2015).

[161] C. L. Lawson and R. J. Hanson. *Solving least squares problems*. Society for Industrial Mathematics (1995).

[162] P. A. Lemieux and D. J. Durian. Investigating non-gaussian scattering processes by using nth-order intensity correlation functions. *J Opt Soc Am A* **16**(7), 1651–1664 (1999).

[163] A. Leproux, A. E. Cerussi, W. Tanamai, A. F. Durkin, M. Compton, E. Gratton, and B. J. Tromberg. Impact of contralateral and ipsilateral reference tissue selection on self-referencing differential spectroscopy for breast cancer detection. *J Biomed Opt* **16**(11), 116019 (2011).

[164] A. Leproux, A. Durkin, M. Compton, A. E. Cerussi, E. Gratton, and B. J. Tromberg. Assessing tumor contrast in radiographically dense breast tissue using diffuse optical spectroscopic imaging (dosi). *Breast Cancer Res* **15**(5), R89 (2013).

[165] A. Leproux, Y. M. Kim, J. W. Min, C. E. McLaren, W. P. Chen, T. D. O'Sullivan, S. H. Lee, P. S. Chung, and B. J. Tromberg. Differential diagnosis of breast masses in south korean premenopausal women using diffuse optical spectroscopic imaging. *J Biomed Opt* **21**(7), 74001 (2016).

[166] A. Leproux, T. D. O'Sullivan, A. E. Cerussi, A. Durkin, B. Hill, N. M. Hylton, A. G. Yodh, S. A. Carp, D. A. Boas, S. Jiang, K. D. Paulsen, B. W. Pogue, D. M. Roblyer, W. T. Yang, and

B. J. Tromberg. Performance assessment of diffuse optical spectroscopic imaging instruments in a 2-year multicenter breast cancer trial. *J Biomed Opt* **22**(12), 121604 (2017).

[167] K. Levenberg. A method for the solution of certain non-linear problems in least squares. *Q Appl Math* **2**, 164 (1944).

[168] A. Li, J. Liu, W. Tanamai, R. Kwong, A. E. Cerussi, and B. J. Tromberg. Assessing the spatial extent of breast tumor intrinsic optical contrast using ultrasound and diffuse optical spectroscopy. *J Biomed Opt* **13**(3), 030504 (2008).

[169] A. Li, E. L. Miller, M. E. Kilmer, T. J. Brukilacchio, T. Chaves, J. Stott, Q. Zhang, T. Wu, M. Chorlton, R. H. Moore, D. B. Kopans, and D. A. Boas. Tomographic optical breast imaging guided by three-dimensional mammography. *Appl Optics* **42**(25), 5181–5190 (2003).

[170] Z. Li, W. B. Baker, A. B. Parthasarathy, T. S. Ko, D. Wang, S. Schenkel, T. Durduran, G. Li, and A. G. Yodh. Calibration of diffuse correlation spectroscopy blood flow index with venous-occlusion diffuse optical spectroscopy in skeletal muscle. *J Biomed Opt* **20**(12), 125005 (2015).

[171] J. M. Lynch, E. M. Buckley, P. J. Schwab, D. R. Busch, B. D. Hanna, M. E. Putt, D. J. Licht, and A. G. Yodh. Noninvasive optical quantification of cerebral venous oxygen saturation in humans. *Acad Radiol* **21**(2), 162–7 (2014).

[172] F. C. MacKintosh and S. John. Diffusing-wave spectroscopy and multiple-scattering of light in correlated random-media. *Phys Rev B* **40**(4), 2383–2406 (1989).

[173] D. A. Mankoff, L. K. Dunnwald, J. R. Gralow, G. K. Ellis, E. K. Schubert, J. Tseng, T. J. Lawton, H. M. Linden, and R. B. Livingston. Changes in blood flow and metabolism in locally advanced breast cancer treated with neoadjuvant chemotherapy. *J Nucl Med* **44**(11), 1806–14 (2003).

[174] V. A. Markel, J. A. O'Sullivan, and J. C. Schotland. Inverse problem in optical diffusion tomography. iv. nonlinear inversion formulas. *J Opt Soc Am A* **20**(5), 903–912 (2003).

[175] V. A. Markel and J. C. Schotland. Inverse problem in optical diffusion tomography. i. fourier-laplace inversion formulas. *J Opt Soc Am A* **18**(6), 1336–1347 (2001).

[176] V. A. Markel and J. C. Schotland. Symmetries, inversion formulas, and image reconstruction for optical tomography. *Phys Rev E* **70**(5 Pt 2), 056616 (2004).

[177] M. A. Mastanduno, J. Xu, F. El-Ghussein, S. Jiang, H. Yin, Y. Zhao, K. E. Michaelsen, K. Wang, F. Ren, B. W. Pogue, and K. D. Paulsen. Sensitivity of mri-guided near-infrared spectroscopy clinical breast exam data and its impact on diagnostic performance. *Biomed Opt Express* **5**(9), 3103–15 (2014).

[178] M. A. Mastanduno, J. Xu, F. El-Ghussein, S. Jiang, H. Yin, Y. Zhao, K. Wang, F. Ren, J. Gui, B. W. Pogue, and K. D. Paulsen. Mr-guided near-infrared spectral tomography increases diagnostic performance of breast mri. *Clin Cancer Res* **21**(17), 3906–12 (2015).

[179] T. O. McBride, B. W. Pogue, S. Jiang, U. L. Osterberg, K. D. Paulsen, P. McCullagh, and J. A. Nelder. A parallel-detection frequency-domain near-infrared tomography system for hemoglobin imaging of the breast in vivo. *Rev Sci Instrum* , 1817–1824 (2001).

[180] G. M. McDermott, A. Welch, R. T. Staff, F. J. Gilbert, L. Schweiger, S. I. Semple, T. A. Smith, A. W. Hutcheon, I. D. Miller, I. C. Smith, and S. D. Heys. Monitoring primary breast cancer throughout chemotherapy using fdg-pet. *Breast Cancer Res Tr* **102**(1), 75–84 (2007).

[181] S. Meisamy, P. J. Bolan, E. H. Baker, R. L. Bliss, E. Gulbahce, L. I. Everson, M. T. Nelson, T. H. Emory, T. M. Tuttle, D. Yee, and M. Garwood. Neoadjuvant chemotherapy of locally advanced breast cancer: predicting response with in vivo 1h mr spectroscopy–a pilot study at 4 t. *Radiology* **233**(2), 424–31 (2004).

[182] R. C. Mesquita, T. Durduran, G. Yu, E. M. Buckley, M. N. Kim, C. Zhou, R. Choe, U. Sunar, and A. Yodh. Direct measurement of tissue blood flow and metabolism with diffuse optics. *Philos T Roy Soc A* **369**(1955), 4390–4406 (2011).

[183] K. E. Michaelsen, V. Krishnaswamy, L. Shi, S. Vedantham, S. P. Poplack, A. Karellas, B. W. Pogue, and K. D. Paulsen. Calibration and optimization of 3d digital breast tomosynthesis guided near infrared spectral tomography. *Biomed Opt Express* **6**(12), 4981–91 (2015).

[184] J. R. Mourant, T. Fuselier, J. Boyer, T. M. Johnson, and I. J. Bigio. Predictions and measurements of scattering and absorption over broad wavelength ranges in tissue phantoms. *Appl Optics* **36**(4), 949–957 (1997).

[185] K. Nie, L. Shi, Q. Chen, X. Hu, S. K. Jabbour, N. Yue, T. Niu, and X. Sun. Rectal cancer: Assessment of neoadjuvant chemoradiation outcome based on radiomics of multiparametric mri. *Clin Cancer Res* **22**(21), 5256–5264 (2016).

[186] A. M. Nilsson, C. Sturesson, D. L. Liu, and S. Andersson-Engels. Changes in spectral shape of tissue optical properties in conjunction with laser-induced thermotherapy. *Appl Opt* **37**(7), 1256–67 (1998).

[187] S. Nioka, M. Miwa, S. Orel, M. Shnall, M. Haida, S. Zhao, and B. Chance. Optical imaging of human breast cancer. *Adv Exp Med Bio* **361**, 171–9 (1994).

[188] S. Nioka, Y. Yung, M. Shnall, S. Zhao, S. Orel, C. Xie, B. Chance, and L. Solin. Optical imaging of breast tumor by means of continuous waves. *Adv Exp Med Bio* **411**, 227–232 (1997).

[189] G. R. Norman and D. L. Streiner. *Biostatistics: the bare essentials*. BC. Decker Inc. (2000).

[190] V. Ntziachristos and B. Chance. Accuracy limits in the determination of absolute optical properties using time-resolved nir spectroscopy. *Med Phys* **28**(6), 1115–1124 (2001).

[191] V. Ntziachristos, A. H. Hielscher, A. G. Yodh, and B. Chance. Diffuse optical tomography of highly heterogeneous media. *IEEE T Med Imaging* **20**, 470–478 (2001).

[192] V. Ntziachristos, X. H. Ma, and B. Chance. Time-correlated single photon counting imager for simultaneous magnetic resonance and near-infrared mammography. *Rev Sci Instrum* **69**(12), 4221–4233 (1998).

[193] V. Ntziachristos, A. G. Yodh, M. D. Schnall, and B. Chance. Mri-guided diffuse optical spectroscopy of malignant and benign breast lesions. *Neoplasia* **4**, 347–354 (2002).

[194] S. Oh, A. B. Milstein, C. A. Bouman, and K. J. Webb. A general framework for nonlinear multigrid inversion. *IEEE T Image Process* **14**(1), 125–140 (2005).

[195] M. A. O'Leary. *Imaging with diffuse photon density waves*. PhD thesis University of Pennsylvania (1996).

[196] M. A. O'Leary, D. A. Boas, B. Chance, and A. G. Yodh. Refraction of diffuse photon density waves. *Phys Rev Lett* **69**, 2658–2661 (1992).

[197] M. A. O'Leary, D. A. Boas, B. Chance, and A. G. Yodh. Experimental images of heterogeneous turbid media by frequency-domain diffusing-photon tomography. *Opt Lett* **20**, 426–428 (1995).

[198] T. D. O'Sullivan, A. Leproux, J. H. Chen, S. Bahri, A. Matlock, D. Roblyer, C. E. McLaren, W. P. Chen, A. E. Cerussi, M. Y. Su, and B. J. Tromberg. Optical imaging correlates

with magnetic resonance imaging breast density and reveals composition changes during neoadjuvant chemotherapy. *Breast Cancer Res* **15**(1), R14 (2013).

[199] M. Pagliazzi, S. K. V. Sekar, L. Colombo, E. Martinenghi, J. Minnema, R. Erdmann, D. Contini, A. D. Mora, A. Torricelli, A. Pifferi, and T. Durduran. Time domain diffuse correlation spectroscopy with a high coherence pulsed source: in vivo and phantom results. *Biomed Opt Express* **8**(11), 5311–5325 (2017).

[200] S. H. Park, W. K. Moon, N. Cho, J. M. Chang, S. A. Im, I. A. Park, K. W. Kang, W. Han, and D. Y. Noh. Comparison of diffusion-weighted mr imaging and fdg pet/ct to predict pathological complete response to neoadjuvant chemotherapy in patients with breast cancer. *Eur Radiol* **22**(1), 18–25 (2012).

[201] M. S. Patterson, S. Andersson-Engels, B. C. Wilson, and E. K. Osei. Absorption spectroscopy in tissue-simulating materials: a theoretical and experimental study of photon paths. *Appl Opt* **34**(1), 22–30 (1995).

[202] M. S. Patterson, B. Chance, and B. C. Wilson. Time resolved reflectance and transmittance for the noninvasive measurement of tissue optical-properties. *Appl Optics* **28**(12), 2331–2336 (1989).

[203] M. S. Patterson, J. D. Moulton, B. C. Wilson, K. W. Berndt, and J. R. Lakowicz. Frequency-domain reflectance for the determination of the scattering and absorption properties of tissue. *Appl Optics* **30**(31), 4474–4476 (1991).

[204] K. D. Paulsen and H. Jiang. Spatially varying optical property reconstruction using a finite element diffusion equation approximation. *Med Phys* **22**(6), 691–701 (1995).

[205] K. D. Paulsen and H. Jiang. Enhanced frequency-domain optical image reconstruction in tissues through total-variation minimization. *Appl Opt* **35**(19), 3447–58 (1996).

[206] M. S. Pepe. *The statistical evaluation of medical tests for classification and prediction*. Oxford statistical science series. Oxford University Press Oxford (2003).

[207] A. Pifferi, P. Taroni, A. Torricelli, F. Messina, and R. Cubeddu. Four-wavelength time-resolved optical mammography in the 680-980-nm range. *Opt Lett* **28**(13), 1138–1140 (2003).

[208] A. Pifferi, A. Torricelli, L. Spinelli, D. Contini, R. Cubeddu, F. Martelli, G. Zaccanti, A. Tosi, A. D. Mora, F. Zappa, and S. Cova. Time-resolved diffuse reflectance using small source-detector separation and fast single-photon gating. *Phys Rev Lett* **100**(13), 138101 (2008).

[209] D. J. Pine, D. A. Weitz, P. M. Chaikin, and E. Herbolzheimer. Diffusing wave spectroscopy. *Phys Rev Lett* **60**(12), 1134–1137 (1988).

[210] B. Pogue, M. Testorf, T. McBride, U. Osterberg, and K. Paulsen. Instrumentation and design of a frequency-domain diffuse optical tomography imager for breast cancer detection. *Opt Express* **1**(13), 391–403 (1997).

[211] B. W. Pogue, S. C. Davis, F. Leblond, M. A. Mastanduno, H. Dehghani, and K. D. Paulsen. Implicit and explicit prior information in near-infrared spectral imaging: accuracy, quantification and diagnostic value. *Philos Trans A Math Phys Eng Sci* **369**(1955), 4531–57 (2011).

[212] B. W. Pogue, T. O. McBride, J. Prewitt, U. L. Osterberg, and K. D. Paulsen. Spatially variant regularization improves diffuse optical tomography. *Appl Opt* **38**(13), 2950–61 (1999).

[213] B. W. Pogue and M. S. Patterson. Frequency-domain optical absorption spectroscopy of finite tissue volumes using diffusion theory. *Phys Med Biol* **39**, 1157–1180 (1994).

[214] E. Polak and G. Ribiére. Note sur la convergence des méthodes de directions conjuguées. *Rev Fr Inform Rech O* **16**, 35–43 (1969).

[215] S. A. Prahl and S. L. Jacques. Optical properties spectra (2012).

[216] G. Ramirez, A. R. Proctor, K. W. Jung, T. T. Wu, S. Han, R. R. Adams, J. Ren, D. K. Byun, K. S. Madden, E. B. Brown, T. H. Foster, P. Farzam, T. Durduran, and R. Choe. Chemotherapeutic drug-specific alteration of microvascular blood flow in murine breast cancer as measured by diffuse correlation spectroscopy. *Biomed Opt Express* **7**(9), 3610–3630 (2016).

[217] P. Rastogi, S. J. Anderson, H. D. Bear, C. E. Geyer, M. S. Kahlenberg, A. Robidoux, R. G. Margolese, J. L. Hoehn, V. G. Vogel, S. R. Dakhil, D. Tamkus, K. M. King, E. R. Pajon, M. J. Wright, J. Robert, S. Paik, E. P. Mamounas, and N. Wolmark. Preoperative chemotherapy: updates of national surgical adjuvant breast and bowel project protocols b-18 and b-27. *J Clin Oncol* **26**(5), 778–85 (2008).

[218] H. Rinneberg, D. Grosenick, K. T. Moesta, H. Wabnitz, J. Mucke, G. Wübbeler, R. Macdonald, and P. Schlag. Detection and characterization of breast tumours by time-domain scanning optical mammography. *Opto-Electron Rev* **16**(2), 147–162 (2008).

[219] J. Ripoll. Derivation of the scalar radiative transfer equation from energy conservation of maxwell's equations in the far field. *J Opt Soc Am A Opt Image Sci Vis* **28**(8), 1765–75 (2011).

[220] D. Roblyer, S. Ueda, A. Cerussi, W. Tanamai, A. Durkin, R. Mehta, D. Hsiang, J. A. Butler, C. McLaren, W. P. Chen, and B. Tromberg. Optical imaging of breast cancer oxyhemoglobin flare correlates with neoadjuvant chemotherapy response one day after starting treatment. *Proc Natl Acad Sci U S A* **108**(35), 14626–31 (2011).

[221] R. Rouzier, C. M. Perou, W. F. Symmans, N. Ibrahim, M. Cristofanilli, K. Anderson, K. R. Hess, J. Stec, M. Ayers, P. Wagner, P. Morandi, C. Fan, I. Rabiul, J. S. Ross, G. N. Hortobagyi, and L. Pusztai. Breast cancer molecular subtypes respond differently to preoperative chemotherapy. *Clin Cancer Res* **11**(16), 5678–85 (2005).

[222] S. Rummel, M. T. Hueman, N. Costantino, C. D. Shriver, and R. E. Ellsworth. Tumour location within the breast: Does tumour site have prognostic ability? *Ecancermedicalscience* **9**, 552 (2015).

[223] A. Y. Sajjadi, S. J. Isakoff, B. Deng, B. Singh, C. M. Wanyo, Q. Fang, M. C. Specht, L. Schapira, B. Moy, A. Bardia, D. A. Boas, and S. A. Carp. Normalization of compression-induced hemodynamics in patients responding to neoadjuvant chemotherapy monitored by dynamic tomographic optical breast imaging (dtobi). *Biomed Opt Express* **8**(2), 555–569 (2017).

[224] F. E. W. Schmidt, M. E. Fry, J. C. Hebden, and D. T. Delpy. A 32-channel time-resolved instrument for medical optical tomography. *Rev Sci Instrum* **71**(1), 256–265 (2000).

[225] J. C. Schotland, J. C. Haselgrove, and J. S. Leigh. Photon hitting density. *Appl Optics* **32**(4), 448–453 (1993).

[226] A. Schuster. Radiation through a foggy atmosphere. *Astrophys J* **21**, 1 (1905).

[227] M. Schweiger and S. Arridge. The toast++ software suite for forward and inverse modeling in optical tomography. *J Biomed Opt* **19**(4), 040801 (2014).

[228] M. Schweiger, S. R. Arridge, and D. T. Delpy. Application of the finite element method for the forward and inverse problem in optical tomography. *J Math Imaging Vis* **3**(3), 263–283 (1993).

[229] M. Schweiger, S. R. Arridge, and I. Nissila. Gauss-newton method for image reconstruction in diffuse optical tomography. *Phys Med Biol* **50**(10), 2365–86 (2005).

[230] N. Shah, A. E. Cerussi, D. Jakubowski, D. Hsiang, J. Butler, and B. J. Tromberg. Spatial variations in optical and physiological properties of healthy breast tissue. *J Biomed Opt* **9**(3), 534–40 (2004).

[231] Y. Shang and G. Yu. A nth-order linear algorithm for extracting diffuse correlation spectroscopy blood flow indices in heterogeneous tissues. *Appl Phys Lett* **105**(13), 133702 (2014).

[232] A. M. Siegel, J. J. A. Marota, and D. A. Boas. Design and evaluation of a continous-wave diffuse optical tomography system. *Opt Express* **4**, 287–298 (1999).

[233] R. L. Siegel, K. D. Miller, and A. Jemal. Cancer statistics, 2017. *CA Cancer J Clin* **67**(1), 7–30 (2017).

[234] H. P. Sinn and H. Kreipe. A brief overview of the who classification of breast tumors, 4th edition, focusing on issues and updates from the 3rd edition. *Breast Care (Basel)* **8**(2), 149–54 (2013).

[235] G. W. Sledge, E. P. Mamounas, G. N. Hortobagyi, H. J. Burstein, P. J. Goodwin, and A. C. Wolff. Past, present, and future challenges in breast cancer treatment. *J Clin Oncol* **32**(19), 1979–86 (2014).

[236] H. Soliman, A. Gunasekara, M. Rycroft, J. Zubovits, R. Dent, J. Spayne, M. J. Yaffe, and G. J. Czarnota. Functional imaging using diffuse optical spectroscopy of neoadjuvant chemotherapy response in women with locally advanced breast cancer. *Clin Cancer Res* **16**(9), 2605–14 (2010).

[237] H. K. Song and L. Dougherty. K-space weighted image contrast (kwic) for contrast manipulation in projection reconstruction mri. *Magn Reson Med* **44**(6), 825–32 (2000).

[238] H. K. Song and L. Dougherty. Dynamic mri with projection reconstruction and kwic processing for simultaneous high spatial and temporal resolution. *Magn Reson Med* **52**(4), 815–24 (2004).

[239] L. Spinelli, A. Torricelli, A. Pifferi, P. Taroni, G. Danesini, and R. Cubeddu. Characterization of female breast lesions from multi-wavelength time-resolved optical mammography. *Phys Med Biol* **50**(11), 2489–502 (2005).

[240] S. Srinivasan, B. W. Pogue, B. Brooksby, S. Jiang, H. Dehghani, C. Kogel, W. A. Wells, S. P. Poplack, and K. D. Paulsen. Near-infrared characterization of breast tumors in vivo using spectrally-constrained reconstruction. *Technol Cancer Res T* **4**(5), 513–26 (2005).

[241] U. Sunar, H. Quon, T. Durduran, J. Zhang, J. Du, C. Zhou, G. Yu, R. Choe, A. Kilger, R. Lustig, L. Loevner, S. Nioka, B. Chance, and A. G. Yodh. Noninvasive diffuse optical measurement of blood flow and blood oxygenation for monitoring radiation therapy in patients with head and neck tumors: a pilot study. *J Biomed Opt* **11**(6), 064021 (2006).

[242] J. Sutin, B. Zimmerman, D. Tyulmankov, D. Tamborini, K. C. Wu, J. Selb, A. Gulinatti, I. Rech, A. Tosi, D. A. Boas, and M. A. Franceschini. Time-domain diffuse correlation spectroscopy. *Optica* **3**(9), 1006–1013 (2016).

[243] P. Taroni, D. Comelli, A. Pifferi, A. Torricelli, and R. Cubeddu. Absorption of collagen: effects on the estimate of breast composition and related diagnostic implications. *J Biomed Opt* **12**(1), 014021 (2007).

[244] P. Taroni, A. Pifferi, E. Salvagnini, L. Spinelli, A. Torricelli, and R. Cubeddu. Seven-wavelength time-resolved optical mammography extending beyond 1000 nm for breast collagen quantification. *Opt Express* **17**(18), 15932–15946 (2009).

[245] J. R. Taylor. *An introduction to error analysis*. University Science Books (1997).

[246] A. Tikhonov. On the stability of inverse problems. *Dokl Akad Nauk+* **39**, 195–8 (1943).

[247] N. V. Tkachenko. *Optical spectroscopy : methods and instrumentations*. Elsevier Amsterdam ; London (2006).

[248] B. J. Tromberg, A. Cerussi, N. Shah, M. Compton, A. Durkin, D. Hsiang, J. Butler, and R. Mehta. Imaging in breast cancer: diffuse optics in breast cancer: detecting tumors in pre-menopausal women and monitoring neoadjuvant chemotherapy. *Breast Cancer Res* **7**(6), 279–85 (2005).

[249] B. J. Tromberg, Z. Zhang, A. Leproux, T. D. O'Sullivan, A. E. Cerussi, P. Carpenter, R. S. Mehta, D. Roblyer, W. Yang, K. D. Paulsen, B. W. Pogue, S. Jiang, P. Kaufman, A. G. Yodh, S. H. Chung, M. Schnall, B. S. Snyder, N. Hylton, D. A. Boas, S. A. Carp, S. J. Isakoff, and D. Mankoff. Predicting responses to neoadjuvant chemotherapy in breast cancer: Acrin 6691 trial of diffuse optical spectroscopic imaging (dosi). *Cancer Res* (2016).

[250] S. Ueda, D. Roblyer, A. Cerussi, A. Durkin, A. Leproux, Y. Santoro, S. Xu, T. D. O'Sullivan, D. Hsiang, R. Mehta, J. Butler, and B. J. Tromberg. Baseline tumor oxygen saturation correlates with a pathologic complete response in breast cancer patients undergoing neoadjuvant chemotherapy. *Cancer Res* **72**(17), 4318–28 (2012).

[251] S. J. Vinnicombe, A. D. MacVicar, R. L. Guy, J. P. Sloane, T. J. Powles, G. Knee, and J. E. Husband. Primary breast cancer: mammographic changes after neoadjuvant chemotherapy, with pathologic correlation. *Radiology* **198**(2), 333–40 (1996).

[252] D. Wang, A. B. Parthasarathy, W. B. Baker, K. Gannon, V. Kavuri, T. Ko, S. Schenkel, Z. Li, Z. Li, M. T. Mullen, J. A. Detre, and A. G. Yodh. Fast blood flow monitoring in deep tissues with real-time software correlators. *Biomed Opt Express* **7**(3), 776–97 (2016).

[253] J. Wang, S. Jiang, Z. Li, R. M. diFlorio Alexander, R. J. Barth, P. A. Kaufman, B. W. Pogue, and K. D. Paulsen. In vivo quantitative imaging of normal and cancerous breast tissue using broadband diffuse optical tomography. *Med Phys* **37**(7), 3715–24 (2010).

[254] L. V. Wang and H. I. Wu. *Biomedical optics: principles and imaging* volume 13 of *J Biomed Opt*. Wiley (2008).

[255] X. Wang, B. W. Pogue, S. Jiang, H. Dehghani, X. Song, S. Srinivasan, B. A. Brooksby, K. D. Paulsen, C. Kogel, S. P. Poplack, and W. A. Wells. Image reconstruction of effective mie scattering parameters of breast tissue in vivo with near-infrared tomography. *J Biomed Opt* **11**(4), 041106 (2006).

[256] R. V. Warren, J. Cotter, G. Ganesan, L. Le, J. P. Agustin, B. Duarte, K. Cutler, T. O'Sullivan, and B. J. Tromberg. Noninvasive optical imaging of resistance training adaptations in human muscle. *J Biomed Opt* **22**(12), 1–9 (2017).

[257] L. Wasserman. *All of Statistics: A Concise Course in Statistical Inference*. Springer Texts in Statistics. Springer New York (2005).

[258] B. C. Wilson, E. M. Sevick, M. S. Patterson, and B. Chance. Time-dependent optical spectroscopy and imaging for biomedical applications. *P IEEE* **80**(6), 918–930 (1992).

[259] L. Wu, W. Wan, X. Wang, Z. Zhou, J. Li, L. Zhang, H. Zhao, and F. Gao. Shape-parameterized diffuse optical tomography holds promise for sensitivity enhancement of fluorescence molecular tomography. *Biomed Opt Express* **5**(10), 3640–59 (2014).

[260] P. K. Yalavarthy, B. W. Pogue, H. Dehghani, and K. D. Paulsen. Weight-matrix structured regularization provides optimal generalized least-squares estimate in diffuse optical tomography. *Med Phys* **34**(6), 2085–98 (2007).

[261] Y. Yamashita, A. Maki, and H. Koizumi. Wavelength dependence of the precision of noninvasive optical measurement of oxy-, deoxy-, and total-hemoglobin concentration. *Med Phys* **28**(6), 1108–14 (2001).

[262] Y. Yang, H. Liu, X. Li, and B. Chance. Low-cost frequency-domain photon migration instrument for tissue spectroscopy, oximetry, and imaging. *Opt Eng* **36**, 1562–1569 (1997).

[263] T. Yates, J. C. Hebden, A. Gibson, N. Everdell, S. R. Arridge, and M. Douek. Optical tomography of the breast using a multi-channel time-resolved imager. *Phys Med Biol* **50**(11), 2503–2517 (2005).

[264] H. S. Yazdi, T. D. O'Sullivan, A. Leproux, B. Hill, A. Durkin, S. Telep, J. Lam, S. S. Yazdi, A. M. Police, R. M. Carroll, F. J. Combs, T. Stromberg, A. G. Yodh, and B. J. Tromberg. Mapping breast cancer blood flow index, composition, and metabolism in a human subject using combined diffuse optical spectroscopic imaging and diffuse correlation spectroscopy. *J Biomed Opt* **22**(4), 45003 (2017).

[265] E. Yeh, P. Slanetz, D. B. Kopans, E. Rafferty, D. Georgian-Smith, L. Moy, E. Halpern, R. Moore, I. Kuter, and A. Taghian. Prospective comparison of mammography, sonography, and mri in patients undergoing neoadjuvant chemotherapy for palpable breast cancer. *Am J Roentgenol* **184**(3), 868–77 (2005).

[266] A. G. Yodh and D. A. Boas. Functional imaging with diffusing light. In *Biomedical Photonics* pages 34–40. CRC Press (2003).

[267] A. G. Yodh and B. Chance. Spectroscopy and imaging with diffusing light. *Phys Today* , 34–39 (1996).

[268] A. G. Yodh, D. J. Pine, P. D. Kaplan, M. H. Kao, and N. Georgiades. Speckle fluctuations and their use as probes of dense random media. *Mol Cryst Liq Cryst Sci Technol - Sec B.: Nonlinear Optics* **3**, 149–160 (1992).

[269] G. Yu. Near-infrared diffuse correlation spectroscopy in cancer diagnosis and therapy monitoring. *J Biomed Opt* **17**(1), 010901 (2012).

[270] Q. Zhang, T. J. Brukilacchio, A. Li, J. J. Stott, T. Chaves, E. Hillman, T. Wu, M. Chorlton, E. Rafferty, R. H. Moore, D. B. Kopans, and D. A. Boas. Coregistered tomographic x-ray and optical breast imaging: initial results. *J Biomed Opt* **10**(2), 024033 (2005).

[271] X. Zhang, V. Toronov, and A. Webb. Simultaneous integrated diffuse optical tomography and functional magnetic resonance imaging of the human brain. *Opt Express* **13**(14), 5513–5521 (2005).

[272] Y. Zhao, W. R. Burger, M. Zhou, E. B. Bernhardt, P. A. Kaufman, R. R. Patel, C. V. Angeles, B. W. Pogue, K. D. Paulsen, and S. Jiang. Collagen quantification in breast tissue using a 12-wavelength near infrared spectral tomography (nirst) system. *Biomed Opt Express* **8**(9), 4217–4229 (2017).

[273] C. Zhou, R. Choe, N. Shah, T. Durduran, G. Yu, A. Durkin, D. Hsiang, R. Mehta, J. Butler, A. Cerussi, B. J. Tromberg, and A. G. Yodh. Diffuse optical monitoring of blood flow and oxygenation in human breast cancer during early stages of neoadjuvant chemotherapy. *J Biomed Opt* **12**(5), 051903 (2007).

[274] Q. Zhu, T. Durduran, V. Ntziachristos, M. Holboke, and A. G. Yodh. Imager that combines near-infrared diffusive light and ultrasound. *Opt Lett* **24**, 1050–1052 (1999).

[275] Q. Zhu, S. H. Kurtzma, P. Hegde, S. Tannenbaum, M. Kane, M. Huang, N. G. Chen, B. Jagjivan, and K. Zarfos. Utilizing optical tomography with ultrasound localization to image heterogeneous hemoglobin distribution in large breast cancers. *Neoplasia* **7**(3), 263–270 (2005).

[276] Q. Zhu, S. Tannenbaum, P. Hegde, M. Kane, C. Xu, and S. H. Kurtzman. Noninvasive monitoring of breast cancer during neoadjuvant chemotherapy using optical tomography with ultrasound localization. *Neoplasia* **10**(10), 1028–40 (2008).

[277] Q. Zhu, S. Tannenbaum, and S. H. Kurtzman. Optical tomography with ultrasound localization for breast cancer diagnosis and treatment monitoring. *Surg Oncol Clin N Am* **16**, 307–321 (2007).

[278] R. Ziegler, T. Nielsen, T. Koehler, D. Grosenick, O. Steinkellner, A. Hagen, R. Macdonald, and H. Rinneberg. Nonlinear reconstruction of absorption and fluorescence contrast from measured diffuse transmittance and reflectance of a compressed-breast-simulating phantom. *Appl Optics* **48**(24), 4651–62 (2009).

[279] O. C. Zienkiewicz and R. L. Taylor. *The Finite Element Method*. McGraw-Hill London 4th edition (1987).

[280] B. B. Zimmermann, B. Deng, B. Singh, M. Martino, J. Selb, Q. Fang, A. Y. Sajjadi, J. Cormier, R. H. Moore, D. B. Kopans, D. A. Boas, M. A. Saksena, and S. A. Carp. Multimodal breast cancer imaging using coregistered dynamic diffuse optical tomography and digital breast tomosynthesis. *J Biomed Opt* **22**(4), 46008 (2017).